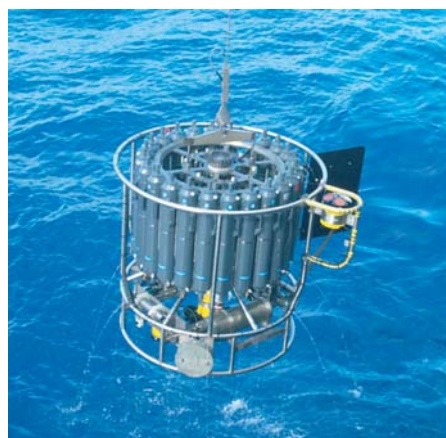




Simulating the early Holocene eastern  
Mediterranean sapropel formation using an  
ocean biogeochemical model

Rosina Grimm



## Hinweis

Die Berichte zur Erdsystemforschung werden vom Max-Planck-Institut für Meteorologie in Hamburg in unregelmäßiger Abfolge herausgegeben.

Sie enthalten wissenschaftliche und technische Beiträge, inklusive Dissertationen.

Die Beiträge geben nicht notwendigerweise die Auffassung des Instituts wieder.

Die "Berichte zur Erdsystemforschung" führen die vorherigen Reihen "Reports" und "Examensarbeiten" weiter.



## Notice

*The Reports on Earth System Science are published by the Max Planck Institute for Meteorology in Hamburg. They appear in irregular intervals.*

*They contain scientific and technical contributions, including Ph. D. theses.*

*The Reports do not necessarily reflect the opinion of the Institute.*

*The "Reports on Earth System Science" continue the former "Reports" and "Examensarbeiten" of the Max Planck Institute.*

## Anschrift / Address

Max-Planck-Institut für Meteorologie  
Bundesstrasse 53  
20146 Hamburg  
Deutschland

Tel.: +49-(0)40-4 11 73-0  
Fax: +49-(0)40-4 11 73-298  
Web: [www.mpimet.mpg.de](http://www.mpimet.mpg.de)

## Layout:

Bettina Diallo, PR & Grafik

Titelfotos:

vorne:

Christian Klepp - Jochem Marotzke - Christian Klepp

hinten:

Clotilde Dubois - Christian Klepp - Katsumasa Tanaka

Simulating the early Holocene eastern  
Mediterranean sapropel formation using an  
ocean biogeochemical model

Rosina Grimm

aus Memmingen

Hamburg 2012

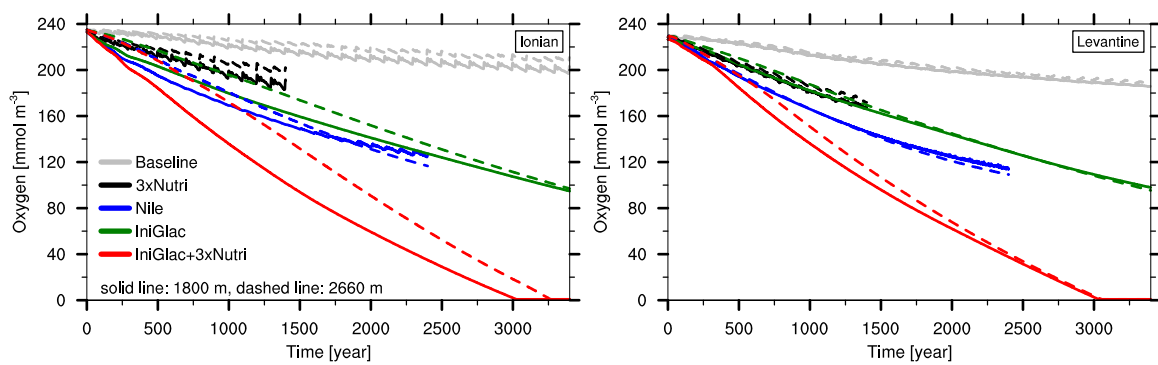
Rosina Grimm  
Max-Planck-Institut für Meteorologie  
Bundesstrasse 53  
20146 Hamburg

Als Dissertation angenommen  
vom Department Geowissenschaften der Universität Hamburg

auf Grund der Gutachten von  
Prof. Dr. Gerhard Schmiedl  
und  
Dr. Ernst Maier-Reimer

Hamburg, den 11. Juli 2012  
Prof. Dr. Jürgen Oßenbrügge  
Leiter des Departments für Geowissenschaften

# Simulating the early Holocene eastern Mediterranean sapropel formation using an ocean biogeochemical model



Rosina Grimm

Hamburg 2012



## Abstract

The early Holocene sapropel S1 is an organic-rich sediment layer. The S1 was deposited under oxygen-depleted deep water conditions, which evolved as a consequence of a stagnating deep water circulation and/or enhanced biological productivity. Commonly, both of these processes were inferred to be triggered by an enhanced humidity over the broader Mediterranean area, in particular, by the increased strength of the African monsoon during the African humid period (AHP) providing strongly enhanced Nile runoff and nutrient load. However, the exact mechanisms leading to S1 formation are still being debated. Using a set of model simulations we show that neither enhanced biological productivity fueled by increased riverine nutrient input, nor an AHP climatic induced stagnating deep water circulation combined with enhanced biological productivity can explain S1 formation. The main reasons are: (i) A purely enhanced biological productivity cannot overcome the effect of a continuous deep ventilation, thus, a stagnating deep water circulation is a prerequisite for S1 formation. (ii) The pre-sapropel period is characterized by low particulate organic carbon (POC) sediment burial flux, hence, the S1 formation involves no particularly strong riverine induced eutrophication scenario. (iii) The time frame required for complete oxygen depletion within the stagnating deep water circulation exceeds the time span between the beginning of the AHP and the onset of the S1 oxygen deficiency, therefore, the AHP climate is not the cause of S1 formation. Furthermore, it has been proposed that during the last glacial-interglacial transition time substantial freshening and warming of the Mediterranean upper ocean established a stable density stratification, preventing deep water ventilation. We show that imposing the climatic signals of the last glacial-interglacial transition triggers a deep water stagnation, which is persistent over the entire 3.4 kyr of simulation. Under an oligotrophic regime, the simulated sediment is in accordance with pre-sapropel sediment core POC burial fluxes. No deep water anoxia develops in the short time frame of this simulation relative to the temporal extent of the deglaciation period. The trend of the oxygen consumption suggests that it takes at least 6.5 kyr until deep water anoxia evolves. The simulated trend of the strength of the deep water stagnation indicates that a restrengthening of the density stratification, for instance, through an additional freshwater input, is required to meet the reconstructed spatial extent and duration of the S1 deposition. An examination of records of epibenthic deep-sea foraminifera  $\delta^{18}\text{O}$  supports our findings, and indicates that the stagnation of the deep circulation started  $\sim 6$  kyr before the onset of the S1 deposition.

Here we show, for the first time, by means of ocean biogeochemical modeling that the sapropel S1 formation cannot be explained through the AHP climate, but that it was triggered by the climatic changes associated with the last glacial-interglacial transition.



# Contents

|          |  |           |
|----------|--|-----------|
| <b>1</b> | <b>Introduction</b>  | <b>7</b>  |
| 1.1      | Motivation and research questions . . . . .                    | 7         |
| 1.2      | Thesis Outline . . . . .                                       | 11        |
| <b>2</b> | <b>Methods: Models, regional setup and boundary conditions</b> | <b>13</b> |
| 2.1      | The Max Planck Institute ocean model . . . . .                 | 13        |
| 2.2      | The Hamburg ocean carbon cycle model . . . . .                 | 13        |
| 2.3      | Regional model setup . . . . .                                 | 15        |
| 2.4      | Boundary conditions . . . . .                                  | 16        |
| 2.4.1    | Atmospheric forcing . . . . .                                  | 16        |
| 2.4.2    | The open boundary to the Atlantic Ocean . . . . .              | 16        |
| 2.4.3    | Rivers . . . . .   | 17        |
| 2.5      | Initial conditions . . . . .                                   | 19        |
| <b>3</b> | <b>The pre-industrial Mediterranean Sea</b>                    | <b>21</b> |
| 3.1      | Motivation . . . . .   | 21        |
| 3.2      | Experimental setup . . . . .                                   | 21        |
| 3.3      | Results . . . . .  | 22        |
| 3.3.1    | General circulation . . . . .                                  | 22        |
| 3.3.1.1  | Upper ocean circulation . . . . .                              | 22        |
| 3.3.1.2  | Intermediate and deep water formation . . . . .                | 24        |
| 3.3.2    | Nutrient cycle . . . . .                                       | 34        |
| 3.3.3    | Biological productivity . . . . .                              | 37        |
| 3.3.4    | Oxygen cycle . . . . .   | 40        |
| 3.3.4.1  | Sensitivity of deep water oxygenation . . . . .                | 41        |
| 3.3.5    | Sediment . . . . .   | 44        |
| 3.3.5.1  | Sediment particulate organic carbon burial flux . . . . .      | 44        |
| 3.3.5.2  | Sediment pore water $\delta^{13}\text{C}$ isotopes . . . . .   | 46        |
| 3.4      | Summary . . . . .  | 49        |

## CONTENTS

|          |  |            |
|----------|--|------------|
| <b>4</b> | <b>The early Holocene sapropel formation</b>   | <b>51</b>  |
| 4.1      | Motivation . . . . .   | 51         |
| 4.2      | Experimental design . . . . .  | 53         |
| 4.3      | Results . . . . .  | 54         |
| 4.3.1    | General circulation . . . . .  | 54         |
| 4.3.1.1  | Upper ocean circulation . . . . .  | 55         |
| 4.3.1.2  | Intermediate water and mixed layer . . . . .   | 55         |
| 4.3.1.3  | Deep water . . . . .   | 62         |
| 4.3.2    | Nutrient cycle . . . . .   | 79         |
| 4.3.3    | Biological productivity . . . . .  | 82         |
| 4.3.4    | Oxygen cycle . . . . .   | 86         |
| 4.3.4.1  | The time evolution of deep water oxygen . . . . .  | 86         |
| 4.3.4.2  | The dynamical evolution of oxygen minimum zones . . . . .  | 91         |
| 4.3.4.3  | The onset of deep water anoxia . . . . .   | 97         |
| 4.3.5    | Sediment . . . . .   | 103        |
| 4.3.5.1  | Sediment particulate organic carbon burial flux . . . . .  | 103        |
| 4.3.5.2  | Sediment pore water $\delta^{13}\text{C}$ isotopes . . . . .   | 109        |
| 4.4      | Discussion and Summary . . . . .   | 115        |
| 4.4.1    | Uncertainties in simulating the sapropel S1 formation . . . . .  | 119        |
| <b>5</b> | <b>Conclusions and Outlook</b>   | <b>123</b> |
| 5.1      | Conclusions . . . . .  | 123        |
| 5.2      | Outlook . . . . .  | 126        |
|          | <b>List of Abbreviations</b>   | <b>127</b> |
| <b>A</b> | <b>Appendix</b>  | <b>129</b> |
| A.1      | Sensitivity of the deep water circulation to the mixing parameterization . . . . .                     | 129        |
| A.1.1    | Additional remarks: Sensitivity of the deep water circulation to the mixing parameterization . . . . . | 134        |
| A.2      | Additional remarks: General circulation . . . . .  | 136        |
|          | <b>Bibliography</b>  | <b>141</b> |
|          | <b>Acknowledgements</b>  | <b>155</b> |

# Chapter 1

## Introduction

### 1.1 Motivation and research questions

During the last 5 million years, the Mediterranean marine system responded particularly sensitive to climate change, documented by the repeated occurrence of organic-rich sediment layers, the sapropels (Ollausson 1961; Cita et al. 1977; Vergnaud-Grazzini et al. 1977; Thunell et al. 1984; Cramp and O'Sullivan 1999). Sapropel formation implies the preservation of organic matter under oxygen-depleted deep water conditions (Schmiedl et al. 1998). The most recent sapropel S1 was deposited between 6.5–10 kyr BP (Mercone et al. 2000; Schmiedl et al. 2010).

The present-day Mediterranean Sea is characterized by excess evaporation over precipitation and river runoff. The freshwater deficit establishes an anti-estuarine type circulation with fresher surface water inflow and more saline water outflow through the Strait of Gibraltar. Deep water formation in the eastern and western basin provides the basic ventilation mechanism for the deep sea. The biological productivity of the open sea is among the lowest observed (Bethoux 1989), caused by the anti-estuarine circulation and the low riverine nutrient supply, establishing a very oligotrophic regime. Consequently, the deep Mediterranean upper sediment commonly contains low organic carbon contents of around 0.1–0.2% (e.g., De Lange et al. 2008; Mercone et al. 2000). Thus, compared to the present-day Mediterranean Sea, the deposition of the S1 sediment layer, with organic carbon contents of 0.2–2% (e.g., Rohling 1994; De Lange et al. 2008; Mercone et al. 2000), indicates strong changes of the general circulation and/or biological productivity.

Despite the large scientific community working on the eastern Mediterranean sapropel formation, until now, there is no general agreement on the mechanisms leading to the S1 formation. Different theories have been invoked explaining the evolution of the S1 deep water oxygen deficiency. According to the stagnation theory a weakening/shutdown of the thermohaline deep water ventilation leads to the development of a deep water oxygen deficiency, which enhances the preservation of the deep-sea sediment organic carbon (e.g. Sachs and Repeta 1999; Moodley et al. 2005; Möbius et al. 2010). Alternatively, an enhanced biological productivity has been considered as the

main cause of an increased oxygen consumption through the remineralization of the enhanced carbon flux, which consequently preserved the organic carbon in the sediment (e.g. Calvert et al. 1992; Kemp et al. 1999; Martinez-Ruiz et al. 2000). Finally, a considerable number of studies suggested a combination of both processes (e.g. Rohling and Gieskes 1989; Howell and Thunell 1992; Rohling 1994; Strohle and Krom 1997; Stratford et al. 2000; Bianchi et al. 2006; Emeis et al. 2000). These controversies about the basic mechanism leading to S1 formation motivates our first research question:

- Is the sapropel S1 formation caused by an enhanced biological productivity, or is a stagnating deep water circulation a prerequisite?

It is widely accepted that climate driven changes supported the required riverine nutrient input and/or freshwater supply inducing the enhanced biological productivity and/or stagnating deep water circulation (e.g., Rohling 1994). The timing of the Quaternary sapropel sequence, including S1, is correlated with orbital induced variations in insolation, in particular, the minimum in precession cycle, which potentially induced an intensification of the monsoon over tropical Africa (Rossignol-Strick et al. 1982; Rossignol-Strick 1985; Prell and Kutzbach 1987; Hilgen 1991). The last precessionally induced amplification of the northern Hemisphere seasonal insolation occurred between  $\sim 15$ –6 kyr BP (Kutzbach and Street-Perrott 1985), and has significantly enhanced the African monsoon circulation between 14.8–5.5 kyr BP, the so called African humid period (AHP) (DeMenocal et al. 2000). Traditionally, the AHP, in particular the monsoon-fed enhanced Nile runoff, was used to explain the source of freshwater and nutrient supply, provoking S1 formation (e.g., Rohling 1994).

A considerable number of studies also find evidence for an enhanced freshwater supply from the northern borderlands through enhanced precipitation (Shaw and Evans 1984; Rossignol-Strick 1987; Cramp et al. 1988; Kallel et al. 1997; Rossignol-Strick 1999; Kallel et al. 2000; Kotthoff et al. 2008; Spötl et al. 2010), and the melting of the Rhodope mountain glaciers (Ehrmann et al. 2007). Also the opening of the Strait of Bosphorus, which occurred either before (Lane-Serff et al. 1997) or during (Sperling et al. 2003) the S1 deposition enhanced the freshwater and nutrient flux to the eastern Mediterranean Sea.

Numerous physical ocean-only modeling studies have provided valuable insight into the response of the eastern Mediterranean circulation under various imposed, and over time constant, freshwater forcings. Myers et al. (1998), Myers (2002), Meijer and Dijkstra (2009), and Adloff (2011) showed that with increasing freshwater input rates to the eastern Mediterranean Sea, the resulting strength of the deep water stagnation is increased. Furthermore, it was reported that the origin of the source of enhance freshwater regulates the strength of the density stratification. Meijer and Tuenter (2007) found that an increase of the freshwater input from the northern borderlands, and enhanced precipitation over the Mediterranean Sea, are of similar or greater importance

## 1.1 MOTIVATION AND RESEARCH QUESTIONS

for the strength of the stratification than that increase of the Nile discharge. Adloff (2011) showed that an enhanced runoff from the Po river resulted in a stronger deep water stagnation than that of an increased precipitation, the reconnection with the Black Sea, or an increased runoff from the Nile river. Until now, however, there is no clear statement whether a freshwater induced stagnation is a plausible scenario for S1 formation, since the simulations are either highly idealized, or rather too short to be conclusive, or the deep water stagnation too weak on the relevant time scales. In addition, all of these physical ocean-only modeling studies disregard the effects of the organic carbon, nutrient and oxygen cycling, which are the crucial processes when trying to assess the plausibility of a scenario. Until now, only two ocean biogeochemical studies focused on S1 formation. Both studies concluded that S1 formation requires a stagnating deep water circulation combined with a particularly strong eutrophication scenario. However, both of these studies analyzed the biogeochemical response under a static ocean circulation, (Stratford et al. (2000) ran a biogeochemical model coupled “off-line” to a stagnating circulation field of a perpetual year derived from a general circulation model, while Bianchi et al. (2006) used a one-dimensional ecosystem model), which does not allow for conclusions on the stability of a freshwater induced stagnation over time.

Since the Quaternary sapropel sequence shows a strong correlation to distinct minima in the precession cycle, there is a strong argument that the AHP climate is the main factor explaining S1 formation (Rossignol-Strick 1985). Based on this hypothesis we pose our next question:

- Is the climate of the African humid period (AHP), implying a particularly enhanced Nile river discharge and nutrient load, a plausible scenario explaining the sapropel S1 formation?

The climatic changes associated with the last glacial-interglacial transition were also proposed to trigger a stagnating deep water circulation and S1 formation (Thunell and Williams 1989; Troelstra et al. 1991; Béthoux and Pierre 1999). The deglaciation started at around 21.5 kyr BP (Shakun et al. 2012). Until the onset of the Holocene, the last glacial-interglacial transition was characterized by a global warming of around  $\sim 3^\circ\text{C}$  (Shakun et al. 2012), melting of the Laurentide and Fennoscandian ice sheets,  $\sim 100\text{ m}$  sea level rise, and correspondingly a freshening of the Atlantic Ocean (Fairbanks 1989). Since the last glacial maximum (LGM) was considerable cooler (Hayes et al. 2005; Mikolajewicz 2011) and the lower sea level accumulated highly saline water in the Mediterranean Sea (Rohling and Bryden 1994; Bryden and Stommel 1984; Thunell and Williams 1989; Mikolajewicz 2011), the Mediterranean deep water was considerable denser during the LGM than during the early Holocene. Under the rising sea-level the exchange rate at the Strait of Gibraltar increased, which decreased the salinity gradient between the Mediterranean Sea and the Atlantic Ocean, so overall

the freshening effect for the Mediterranean Sea exceeded the rate of freshening in the Atlantic Ocean (Rohling and Bryden 1994; Bryden and Stommel 1984). Since the deep water has a longer residence time than the upper ocean, the deep water properties possibly lagged behind the changes at the surface, which possibly triggered a vertical density stratification inhibiting deep water formation.

Two modeling studies focused on the effect of the climatic changes of the last glacial-interglacial transition with respect to S1 formation: Matthiesen and Haines (2003) simulated the glacial-interglacial transition and found strong changes in the vertical stratification of the Mediterranean Sea in response to the meltwater pulses 1A and 1B (Fairbanks 1989). Adloff (2011) simulated a continuous freshening of 0.014 psu per century of the Atlantic inflow, and reported a persistent poorly ventilated state of the eastern Mediterranean Sea. Since both of these studies disregard the effects of the organic carbon and oxygen cycling, they could not draw conclusions on the S1 formation. This motivates our next research question:

- Did the climatic changes associated with the last glacial-interglacial transition period trigger the sapropel S1 formation?

Overall, the uncertainties in the initial climate perturbation(s) and the required nutrient regime seem large when trying to explain the S1 formation. Therefore, we ask:

- What are the main uncertainties in simulating the formation of the sapropel S1?

Despite the uncertainties in the evolution of the deep water oxygen deficiency, the onset of the S1 deposition is well constrained to occur synchronously, basin-wide, below 1800 m depth (Mercone et al. 2000; De Lange et al. 2008; Schmiedl et al. 2010). Ocean biogeochemical simulations show a downward propagation of an anoxic oxygen minimum zone (OMZ) from intermediate depth down to the seafloor, with the downward propagation velocity depending on the circulation scenario and external nutrient input (Stratford et al. 2000; Bianchi et al. 2006). This motivates our last research question:

- Can we infer from the reconstructed temporal and spatial synchronous onset of the sapropel S1 deep water oxygen deficiency a circulation and/or nutrient regime that governs this pattern?

In this thesis, we present time slice simulations using a regional ocean biogeochemical model including a sediment module, forced with daily atmospheric data derived from global climate model simulations for the pre-industrial and 9 kyr BP time slice. Through the simulation of the pre-industrial time slice we infer the model's capabilities and inabilities in simulating the large-scale circulation and biogeochemical cycles with respect to the coarse resolution atmospheric forcing. To simulate the sapropel S1

formation, we impose low and high latitude climatic signals of the late Pleistocene to mid Holocene, as well as various riverine nutrient regimes, and focus on the oceanic and biogeochemical response in the eastern Mediterranean Sea. We aim to constrain the plausibility of our simulations by examining the required time frame for complete oxygen depletion, by the spatial extent of the S1 oxygen deficiency, and by the comparison of our simulated sediment with sediment core observations for the time prior and during the S1 deposition.

## 1.2 Thesis Outline

In chapter 2 we give an overview of the models, the regional model setup for the Mediterranean Sea, and the imposed boundary conditions.

In chapter 3 we analyze the pre-industrial eastern Mediterranean general circulation, biogeochemical cycles and sediment. Through a comparison of our simulation results to observations we gain an understanding of the uncertainties in simulating the large-scale thermohaline circulation and biogeochemical cycles, which arise by forcing the regional model with a coarse resolution atmospheric dataset.

In chapter 4 we analyze scenarios for sapropel S1 formation. We give a broad process understanding of the major mechanisms leading to the development of the S1 oxygen deficiency. We discuss the results in terms of their plausibility to explain the S1 formation.

Chapter 5 closes the thesis with the main conclusions, and gives perspectives for future research.



## Chapter 2

# Methods: Models, regional setup and boundary conditions

### 2.1 The Max Planck Institute ocean model

The Max Planck Institute ocean model (MPIOM) is a z-coordinate global ocean general circulation model (GCM) based on the primitive equations for a hydrostatic Boussinesq fluid with a free surface (Marsland et al. 2003). Scalar and vector variables are formulated on an orthogonal curvilinear C-grid (Arakawa and Lamb 1977). The model includes isopycnal diffusion of the thermohaline fields following Griffies (1998). For the vertical eddy viscosity and diffusion the Richardson-number dependent scheme of Pacanowski and Philander (1981) is applied. Since the Pacanowski-Philander scheme in its classical form underestimates the turbulent mixing close to the surface, an additional wind mixing parameterization is included. In the presence of static instability, convective overturning is parametrized by greatly enhanced vertical diffusion to a value of  $0.05 \text{ m}^2 \text{ s}^{-1}$ . Heat fluxes at the surface are calculated using standard bulk-formulas with prescribed atmospheric forcing and modeled SST. Freshwater fluxes are calculated from prescribed precipitation and river runoff, and evaporation is calculated interactively from latent heat flux.

### 2.2 The Hamburg ocean carbon cycle model

The Hamburg ocean carbon cycle model (HAMOCC5) is coupled online to the ocean general circulation model MPIOM, running with the same vertical and horizontal resolution and the same time step. The biogeochemical tracers are transported with the same advection scheme as the thermohaline fields of MPIOM. HAMOCC is based on nutrients (dissolved phosphate, dissolved nitrate, dissolved iron), dissolved oxygen, phytoplankton, zooplankton, dissolved organic carbon (DOC), and particulate organic carbon (POC) as key variables for the organic cycling. The key variables for the chemical aspect are dissolved inorganic carbon (DIC), alkalinity, and dissolved silica (Maier-Reimer et al. 2005). The model contains a sediment module following Heinze

et al. (2003) including opal, silt, POC, and calcium carbonate. In the frame of this study new processes were introduced into the model:

A semi-refractory DOC pool, which is remineralized to dissolved phosphate and nitrate with a 10-year decay rate using a constant Redfield ratio C:N:P of 122:16:1.

The POC pools was differentiated into a slow sinking (advected) dead phyto- and zooplankton, and fast sinking (not advected) zooplankton fecal pellets pool. Both size classes are remineralized with a constant rate  $r$ , and each class has its own sinking velocity  $w$ , set to constant values of  $1.5 \text{ m d}^{-1}$  and  $25 \text{ m d}^{-1}$ . The POC flux  $F$  at stationary at any depth  $z$  (referenced to  $z_0$ ) is then given by

$$F(z) = wPOC(z_0)e^{-\frac{rz}{w}} = F_0e^{-\frac{rz}{w}}. \quad (2.1)$$

In the sediment, we introduced a bottom-water temperature ( $T(-H)$ ) dependent remineralization rate  $r_{sed}$  [ $\text{kmol}^{-1} \text{O}_2 \text{ m}^3 \text{ s}^{-1}$ ] through introducing a quadratic function given by

$$r_{sed} = T(-H)^2 4.8 \times 10^{-5} + 1.2 \times 10^{-3}, \quad (2.2)$$

for  $T(-H) \geq 0.$ , otherwise  $T(-H) = 0.$

$r_{sed}$  mimics the Q10=2 rule between approximately  $4^\circ\text{C}$  to  $14^\circ\text{C}$  and Q10=4 between  $14^\circ\text{C}$  to  $24^\circ\text{C}$ .

To account for the erosion of particles in the sediment, we introduce a physical sediment erosion following Lavelle et al. (1984). The erosion rate is dependent on the fluid motion given by

$$E = \alpha|\tau|^\eta, \quad (2.3)$$

where  $\tau$  is the fluid bottom stress [ $\text{dyne cm}^{-2}$ ],  $\alpha$  the erosion rate normalization [ $\text{g cm}^{-2} \text{ s}^{-1}$ ]. The bottom stress is related to the free stream velocity  $U$  by

$$\tau = \rho C_D |U|U, \quad (2.4)$$

where  $C_D$  is the drag coefficient and was set to a value of  $1.6 \times 10^{-3}$ .  $\rho$  is the fluid density ( $\rho = 1.0 \text{ g cm}^{-3}$ ). We chose  $\eta = 1.25$  and  $\alpha = 1.0 \times 10^{-6}$ . We only allow for erosion in the first sediment layer. In addition, the erosion rate  $E$  is weighed by the thickness of the bottom water layer, since with increasing water depth the bottom layer thickness increases. In the case of stronger erosion than sedimentation, the sediment is refilled from below with coarse grained not erodible sand. In case the bottom velocity is lower than  $0.01 \text{ m s}^{-1}$  erosion is not applied. Eroded POC is added to the slow sinking advected POC pool, which allows for a lateral displacement of the POC. Similarly, eroded atmospheric dust can be laterally displaced.

## 2.3 Regional model setup

We use a regional version of the ocean general circulation model MPIOM, which covers the entire Mediterranean, the Black Sea and a small part of the Atlantic Ocean (Mikolajewicz 2011; Adloff et al. 2011), with an horizontal resolution of around 20 km, and 46 levels in the vertical, of which 8 levels are in the uppermost 100 m and 17 levels in the uppermost 500 m. The bathymetry has been derived from ETOPO5 (1988). During the early Holocene the sea level on average stood  $\sim 20$  m lower than today. To account for the sea level reduction, we reduce the depth of each grid box by adding the anomalies from the ICE-5G reconstructions (Peltier 2004) between present-day and the early Holocene topography to the standard topography. Consequently, the model sill depth of the Strait of Gibraltar is reduced from 256 m to 241 m, and the Bosphorus with the model depth of 12 m is closed. Thus, the Black Sea is not included in the early Holocene simulations. The timing of the reconnection with the Black Sea has been a matter of debate, and until now, there is no general agreement whether the reconnection occurred before or during S1 formation (Aksu et al. 2002; Ryan et al. 1997; Sperling et al. 2003; Soulet et al. 2011). Figure 2.1 shows the early Holocene eastern Mediterranean bathymetry.

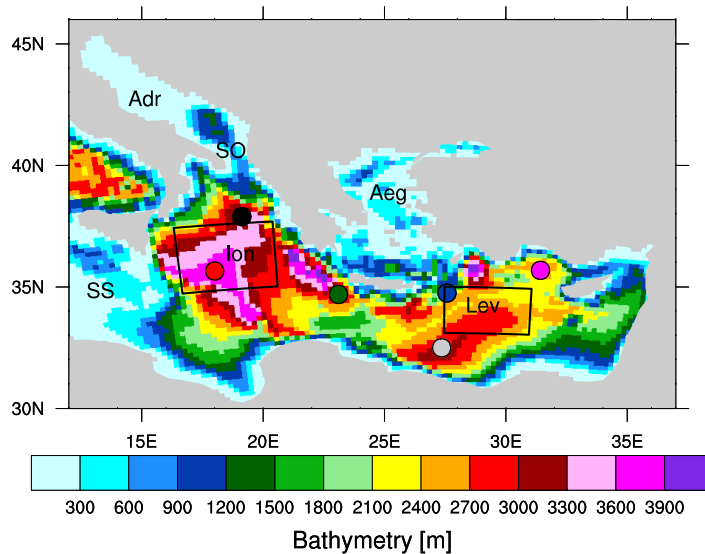


Figure 2.1: Early Holocene bathymetry. Adr: Adriatic Sea, Aeg: Aegean Sea, Ion: Ionian Sea, Lev: Levantine Sea, SO: Strait of Otranto, SS: Strait of Sicily. The boxes indicate the areas over which we average results for the Ionian and Levantine Sea if not otherwise stated. The dots represent certain locations used in several other figures (black: North Ionian, red: Deep Ionian, green: Cretan, blue: Rhodes, grey: Southern Levantine, pink: Cyprus).

## 2.4 Boundary conditions

### 2.4.1 Atmospheric forcing

We run two global climate model time slice simulations, one for the pre-industrial (PR), and one for the Holocene insolation maximum (HIM) (9 kry BP) climate, to derive an atmospheric dataset of the same spatial and temporal resolution for both time slices.

The global climate model simulations were performed with the atmosphere-ocean-dynamical vegetation model ECHAM5/MPI-OM/LPJ for the corresponding time slices. The atmospheric general circulation model ECHAM5 (Roeckner et al. 2003) has been run in a horizontal resolution of T31 with 19 vertical levels. The global ocean general circulation model MPIOM (Marsland et al. 2003) has a curvilinear grid with poles over Greenland and Antarctica, with a horizontal resolution of about  $3^\circ$  and 40 vertical levels. The dynamical vegetation model LPJ has the same horizontal resolution as the atmospheric model ECHAM5. The PR time slice simulation was run with an atmospheric  $CO_2$  concentration of 280 ppm, and insolation corresponding to the year 1950. For the HIM time slice simulation, the insolation was adjusted to the Earth's orbital configuration of the early Holocene, the atmospheric  $pCO_2$  was reduced to 260 ppm, and the topography was changed in particular to include the major ice sheets following the ICE-5G reconstructions (Peltier 2004). In a previous study Adloff et al. (2011) gave a detailed analysis of the atmospheric forcing, and showed that the regional model forced by this early Holocene atmospheric forcing (9K2 simulation in Adloff et al. (2011)) resulted in a better representation of the upper ocean climate than by using an atmospheric forcing derived from a global model simulation with changes only in insolation as a result of changes in the Earth's orbital parameters.

For both time slices, we derive a 100-year daily data set of near surface air temperature, dew point temperature, wind speed, wind stress, cloud cover, and downward radiative shortwave. The upward longwave radiation is calculated from the model SST. The exact procedure on how the data was derived is detailed in Adloff et al. (2011). The penetration of shortwave radiation into the ocean is taken from the optical water type Ib for the Mediterranean and III for the Black Sea (Jerlov 1976).

### 2.4.2 The open boundary to the Atlantic Ocean

At the western boundary of the Atlantic box a sponge zone encompassing the 5 most western grid boxes with a restoring to temperature and salinity towards monthly climatological hydrography of the World Ocean Atlas (WOA 2009) is used in the regional simulations in order to prescribe the properties of the inflowing Atlantic water. In the area of the sponge zone a restoring towards sea level height of zero is conducted because the Mediterranean is an evaporative basin, and hence, the sea level would continuously sink in the model domain.

Table 2.1: Atlantic Ocean boundary values for nutrients, oxygen and alkalinity (WOA 2009).

| Depth | Phosphate      | Nitrate | Silica | Oxygen | Alkalinity |
|-------|----------------|---------|--------|--------|------------|
| $m$   | $mmol\ m^{-3}$ |         |        |        |            |
| 50    | 0.09           | 1.5     | 1.75   | 230    | 2280       |
| 600   | 0.8            | 14      | 6.45   | 180    | 2280       |

In the HIM forced regional simulations the differences between the HIM and PR simulation with the coarse resolution ESM were added to the monthly climatological values used for the PR forced regional simulation.

The biogeochemical tracers dissolved phosphate, dissolved nitrate, dissolved silica, dissolved oxygen, and alkalinity are restored to climatological concentrations derived from the World Ocean Atlas (WOA 2009) at the western boundary of the Atlantic ocean. We linearly interpolate between values taken at the mixed layer depth of 50 m and the values from the depth of the nutricline at 600 (Table 2.1). Below 600 m depth the values are kept constant. As we have no simulation with the global model including the carbon cycle available, the same nutrient boundary configuration were applied to both, the PR and HIM forced simulation.

### 2.4.3 Rivers

Riverine freshwater input was derived from the UNESCO RivDis database (Vörösmarty et al. 1998). Only for the major rivers (Danube, Nile, Rhone, Po and Ebro) the seasonal cycle of discharge was considered. For the Nile and Ebro we consider discharge rates prior to damming, with mean annual runoff of  $2931\ m^3\ s^{-1}$  and  $410\ m^3\ s^{-1}$ , respectively. For the HIM forced regional simulations we added the differences of the river discharges simulated by the global coupled model to the monthly climatology of river runoff used for the PR forced regional simulation. The river discharge is summarized in Table 2.2.

Table 2.2: Riverine dissolved phosphate, nitrate and silica input, and river discharge for the PR and HIM forced regional simulations. Units for nutrients  $mol\ s^{-1}$ , and for discharge  $m^3\ s^{-1}$ . Note, the refractory DOC pool is not included in the given phosphate and nitrated data.

|           | PR        | HIM  | PR      | HIM   | PR     | HIM    | PR        | HIM   |
|-----------|-----------|------|---------|-------|--------|--------|-----------|-------|
| Region    | Phosphate |      | Nitrate |       | Silica |        | discharge |       |
| Med.      | 33.4      | 39.2 | 892.6   | 947.2 | 2033.6 | 2451.1 | 10950     | 13387 |
| EMed.     | 19.7      | 25.6 | 573.0   | 510.1 | 1153.5 | 1577.8 | 7026      | 9518  |
| WMed.     | 13.8      | 13.5 | 443.7   | 437.1 | 880.2  | 873.3  | 3923      | 3869  |
| Adria     | 7.0       | 6.9  | 313.6   | 308.2 | 479.6  | 474.7  | 3063      | 3029  |
| Nile      | 7.1       | 13.0 | 77.4    | 141.5 | 498.2  | 910.9  | 2931      | 5358  |
| Black Sea | 47.2      |      | 1061.9  |       | 498.2  |        | 10391     |       |

Riverine nutrient flux is simulated for the major dissolved nutrients such as phosphate, nitrate, silica, iron, DIC as well as alkalinity. Moreover, we included a semi-refractory DOC pool, which decays to dissolved phosphate and nitrate using a constant Redfield ratio of C:P:N of 122:1:16 with a decay rate of 10 years. Riverine concentrations of dissolved phosphate, nitrate, and silica were taken from published measurements (Meybeck and Ragu 1996; Ludwig et al. 2003; Nixon 2003; Strobl et al. 2009) and are included in the model as weighted averages of the freshwater runoff of the corresponding time slice simulations. For those rivers, for which no measurements were available, we assigned a mean value of  $1.5 \text{ mmol m}^{-3}$  for dissolved phosphate,  $24 \text{ mmol m}^{-3}$  for dissolved nitrate, and  $170 \text{ mmol m}^{-3}$  for dissolved silica. During the model tuning process, the total nutrient load of dissolved phosphate and nitrate was too low, therefore, we increased each value by 10%. The semi-refractory DOC riverine input was set to be 30% of the dissolved phosphate input. The riverine concentration of DIC was set to a constant value of  $1000 \text{ mmol m}^{-3}$ , and Alkalinity to  $0 \text{ mmol m}^{-3}$ . Table 2.2 summarizes the riverine nutrient influx.

## 2.5 Initial conditions

Table 2.3 summarizes the ocean physical and biogeochemical initial conditions applied to the regional simulations.

Table 2.3: Initial conditions of physical and biogeochemical tracers. Atl: Atlantic Ocean, EMed: eastern Mediterranean Sea, WMed: western Mediterranean Sea, Med: Mediterranean Sea.

| Tracer                            | Initial value       | Region                | Unit            |
|-----------------------------------|---------------------|-----------------------|-----------------|
| Salinity                          | 38                  | Med., Atl.            | psu             |
| Salinity                          | 20                  | Black Sea             | psu             |
| Temperature                       | 20                  | Med., Atl., Black Sea | °C              |
| Phosphate                         | 0.35                | Atl., WMed.           | $mol P m^{-3}$  |
| Phosphate                         | 0.2                 | EMed.                 | $mol P m^{-3}$  |
| Phosphate                         | 3.5                 | Black Sea             | $mol P m^{-3}$  |
| Nitrate                           | 7                   | Med., Atl.            | $mol N m^{-3}$  |
| Nitrate                           | 0.4                 | Black Sea             | $mol N m^{-3}$  |
| Oxygen                            | 185                 | Med., Atl.            | $mol O m^{-3}$  |
| Oxygen                            | 1                   | Black Sea             | $mol O m^{-3}$  |
| Silica                            | 8                   | Med., Atl.            | $mol Si m^{-3}$ |
| Silica                            | 150                 | Black Sea             | $mol Si m^{-3}$ |
| DIC                               | 2270                | Med., Atl., Black Sea | $mol C m^{-3}$  |
| Alkalinity                        | 2370                | Med., Atl., Black Sea | $mol eq m^{-3}$ |
| DOC                               | $10^{-4}$           | Med., Atl., Black Sea | $mol C m^{-3}$  |
| R-DOC                             | $8.2 \cdot 10^{-7}$ | Med., Atl., Black Sea | $mol P m^{-3}$  |
| Iron                              | $0.6 \cdot 10^{-3}$ | Med., Atl., Black Sea | $mol Fe m^{-3}$ |
| Phytoplankton                     | $1 \cdot 10^{-5}$   | Med., Atl., Black Sea | $mol P m^{-3}$  |
| Zooplankton                       | $1 \cdot 10^{-5}$   | Med., Atl., Black Sea | $mol P m^{-3}$  |
| POC (dead phyto- and zooplankton) | $1 \cdot 10^{-8}$   | Med., Atl., Black Sea | $mol P m^{-3}$  |
| POC (zooplankton fecal pellets)   | $1 \cdot 10^{-8}$   | Med., Atl., Black Sea | $mol P m^{-3}$  |
| Calcium carbonate                 | $1 \cdot 10^{-2}$   | Med., Atl., Black Sea | $mol C m^{-3}$  |
| Opal-shells                       | $1 \cdot 10^{-2}$   | Med., Atl., Black Sea | $mol Si m^{-3}$ |
| Dust                              | 1                   | Med., Atl., Black Sea | $mg m^{-3}$     |
| Sediment POC                      | $122 \cdot 10^3$    | Med., Atl., Black Sea | $mol C m^{-3}$  |
| Sediment Calcium carbonate        | $1 \cdot 10^{-2}$   | Med., Atl., Black Sea | $mol C m^{-3}$  |
| Sediment Opal-shells              | $1 \cdot 10^{-2}$   | Med., Atl., Black Sea | $mol Si m^{-3}$ |
| Sediment clay                     | 0                   | Med., Atl., Black Sea | $mg m^{-3}$     |
| Sediment sand                     | 2570                | Med., Atl., Black Sea | $mg m^{-3}$     |



# Chapter 3

## The pre-industrial Mediterranean Sea

### 3.1 Motivation

The regional ocean biogeochemical simulations of the early Holocene sapropel S1 formation are forced with atmospheric data derived from a global climate model of the Holocene insolation maximum (HIM) time slice. This approach, however, might bear large uncertainties, since the Mediterranean Sea reacts very sensitive to atmospheric forcing (Pinardi and Masetti 2000). To assess the uncertainty arising from applying a coarse resolution atmospheric forcing to a regional model, we first force the regional model with an atmospheric dataset of the pre-industrial time slice derived from the same coarse resolution global climate model as is later used for the HIM time slice. We assess the model capability in simulating the large-scale pre-industrial thermohaline circulation and biogeochemical cycles by evaluating the model results with present-day observations. In particular, we focus our analysis of the pre-industrial regional simulation on the processes that are through be be crucial for the S1 formation, such as, water-mass formation, nutrient and oxygen cycling, biological productivity, and sediment organic carbon burial. Through this approach we aim to understand the uncertainty in the predictability of the HIM forced regional simulations arising from the coarse resolution atmospheric forcing.

### 3.2 Experimental setup

The pre-industrial regional simulation (CTRL) was performed using the PR boundary conditions (section 2.4). The CTRL simulation was initialized with homogeneous low density water conditions (Table 2.3). The initialization with the low density water has the advantage that the bottom waters are easily replaced by dense surface water, which allows the model to fully develop the water masses by itself.

After an ocean-only spinup of 500 years we coupled the physical ocean model to the biogeochemical model, which was also initialized with homogeneous water and sediment conditions (Table 2.3). In the year 1501, we increase the vertical resolution of the model from 29 to 46 vertical layers, and run it until the year 100 years (see Appendix A.1

for details). This entire simulation serves as a spinup for the CTRL simulation. We continue the CTRL simulation for another 1000 years. All results presented are inferred from the last 100 years of this simulation if not otherwise stated.

### 3.3 Results

#### 3.3.1 General circulation

The anti-estuarine type general circulation of the pre-industrial Mediterranean Sea is driven by the excess of evaporative losses (E) over the precipitation (P) and river (R) runoff inputs (P-E+R), with fresher surface water inflow and more saline water outflow through the Strait of Gibraltar. A more detailed description of the fresh water budget is given by Adloff et al. (2011). The Mediterranean outflow at Gibraltar consists mainly of intermediate water, formed in the Levantine (LIW), Aegean (AIW), Cretan (CIW) and Ionian Sea (IIW). Due to the shallowness of the Strait of Sicily and Strait of Gibraltar, the eastern Mediterranean deep water (EMDW) formed in the Adriatic Sea (ADW) and the western Mediterranean deep water formed in the Gulf of Lions are effectively separated from each other and the Atlantic ocean.

We constrain our analysis to the eastern Mediterranean only, because first, the sapropel forms in the eastern basin, and second, the deep water formation in the western Mediterranean is rather unrealistically simulated. The deep water formation in the western Mediterranean Sea, occurring in the Gulf of Lions, is very sensitive to the wind stress and thermal forcing. Cold and dry winds channelized through the complex topography of the Rhone Valley and the Pyrenees, usually occurring in strong bursts of a few days duration, induce a strong buoyancy loss of the weakly stratified upper and intermediate waters and cause deep convection processes (Hong et al. 2007; Mertens and Schott 1998). The downscaling of the winds from the coarse resolution global climate model is rather imprecise considering these small-scale wind features. In addition, the thermal forcing seems to warm in the Gulf of Lions, therefore, the buoyancy loss required to initiate deep water formation is overall too low in our regional model. The shallow sill depth of the Strait of Sicily separates the deep western basin effectively from the eastern basin, therefore, the deep western circulation is largely unimportant for the eastern Mediterranean circulation features.

##### 3.3.1.1 Upper ocean circulation

The near-surface circulation of the eastern Mediterranean is illustrated in Figure 3.1. Evaluating the model results with present-day observations (Pinardi and Masetti 2000), we find a good representation of the major circulation features (Fig. 3.1): The Atlantic-Ionian Stream enters the eastern Mediterranean through the Strait of Sicily and propagates as the Mid-Mediterranean Jet into the Levantine basin, while a small part sep-

arates and flows northward towards the Adriatic Sea mainly in late spring to summer. The wind stress (not shown here) and the associated wind stress curl induces the anticyclonic Rhodes gyre in the northern, and the cyclonic Mersa-Matruh gyre in the southern Levantine Sea. Part of the Asia Minor current along the coast of Turkey flows northward into the Aegean, and returns together with the Black Sea outflow along the western Aegean Sea towards the south. The major part of the Asia Minor current flows west, along the northern coast of Crete, and eventually along the Greek and Albanian coast into the Adriatic Sea. In the southern Adriatic Sea a cyclonic gyre is simulated, which is most pronounced in summer and autumn.

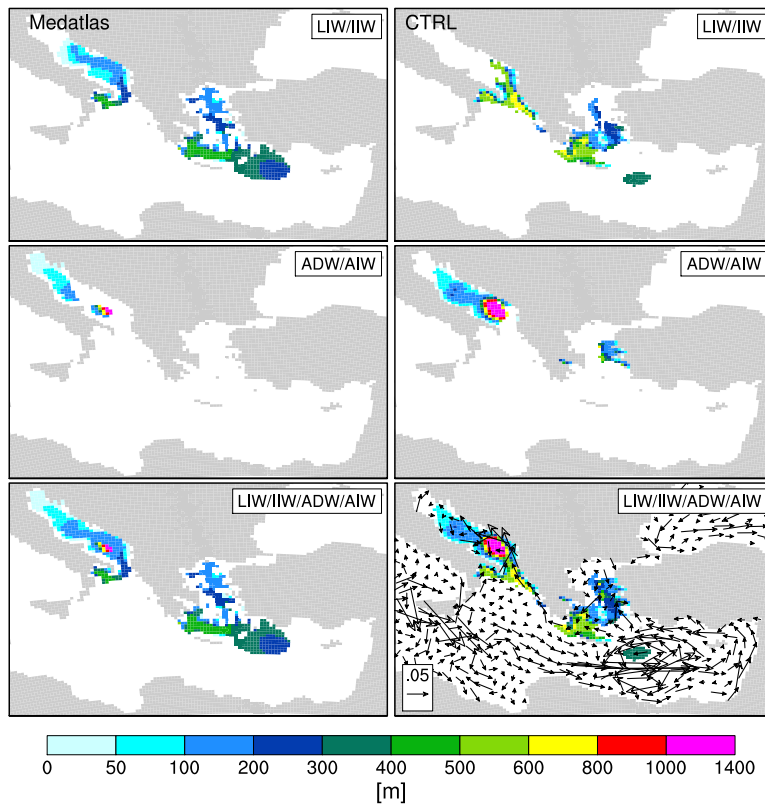


Figure 3.1: Mixed layer depth in February/March derived as detailed in the text for the LIW including the IIW (upper panel), the ADW and AIW (middle panel), and the combined mixed layer depth for all water masses (lower panel) for the Medatlas climatology (left column) and the CTRL simulation averaged over the last 100 years of simulation (right column). Vectors represent both the direction and speed [ $m s^{-1}$ ] of the annual mean circulation in 25 m.

### 3.3.1.2 Intermediate and deep water formation

To assess the locations of intermediate and deep water formation, we first analyze the mixed layer depth in the various sub-basins. Commonly, criteria to assess the mixed layer depth are based upon threshold values for  $\sigma_\Theta$  relative to the surface. However, such criteria are inappropriate to differentiate between predominantly upwelling and downwelling regions. Water formation in the Mediterranean Sea is strongly preconditioned by cyclonic gyres, leading to a doming of isopycnals and to a preconditioning of the water column towards thermal cooling during winter. To assess the areas of water mass formation, we define the intermediate and deep water on isopycnal layers.

Water-mass formation is characterized by the outcropping of isopycnal at the surface. Instead of simply visually defining the outcropping isopycnals, we rather define a common criteria that we can also apply to the early Holocene simulations (section 4.3.1.2). Intermediate water formation should not substantially penetrate the pycnocline, deep water formation must penetrate the pycnocline. The major source of intermediate water formation is in the Levantine Sea, and the major source of deep water formation is in the Adriatic Sea. Thus, we define intermediate water dependent on the stability in the Levantine Sea, and deep water formation dependent on the stability of the Ionian Sea. To determine the pycnocline, we compute the Brunt-Väisälä Frequency  $N$ , which is a measure of water column stability and reaches a maximum at the pycnocline, given by:

$$N^2 = -g\rho_0^{-1}\frac{\partial\rho}{\partial z}. \quad (3.1)$$

To determine the isopycnal range of the intermediate water-mass in the CTRL simulation, we plot the Brunt-Väisälä Frequency versus  $\sigma_\Theta$  of the 100-year mean fields of February/March averaged over the Levantine and Ionian Sea (Fig. 3.2). We define the lower isopycnal of the intermediate water-mass at the  $\sigma_\Theta$  where the Brunt-Väisälä Frequency shows a clear increase of water column stability towards the surface, and we simply add  $0.2\sigma_\Theta$  to the lower boundary to obtain the upper boundary of the isopycnal range (Fig. 3.2). This gives an intermediate water isopycnal range between  $\sigma_\Theta$  28.98 to 29.18, which is slightly higher than the isopycnal ranges of observations ranging between 28.85 to 29.1 (Castellari et al. 2000, and citations therein).

To assess the deep water-mass in the CTRL simulation, the upper isopycnal was defined as the last prominent increase of the Brunt-Väisälä Frequency in the Ionian Sea, since eastern Mediterranean deep water formation should at least penetrate this stability layer. The deep water isopycnal is  $\sigma_\Theta \geq 29.16$ , which is within the range ( $\sigma_\Theta \geq 29.1$ ) given in other studies (Castellari et al. 2000, and citations therein). The defined intermediate and deep isopycnal layers were computed for each year of the last 100 years of simulation. The mixed layer pattern was then derived by computing the depth in which a surface outcropping of the intermediate and deep isopycnal layers occurs in

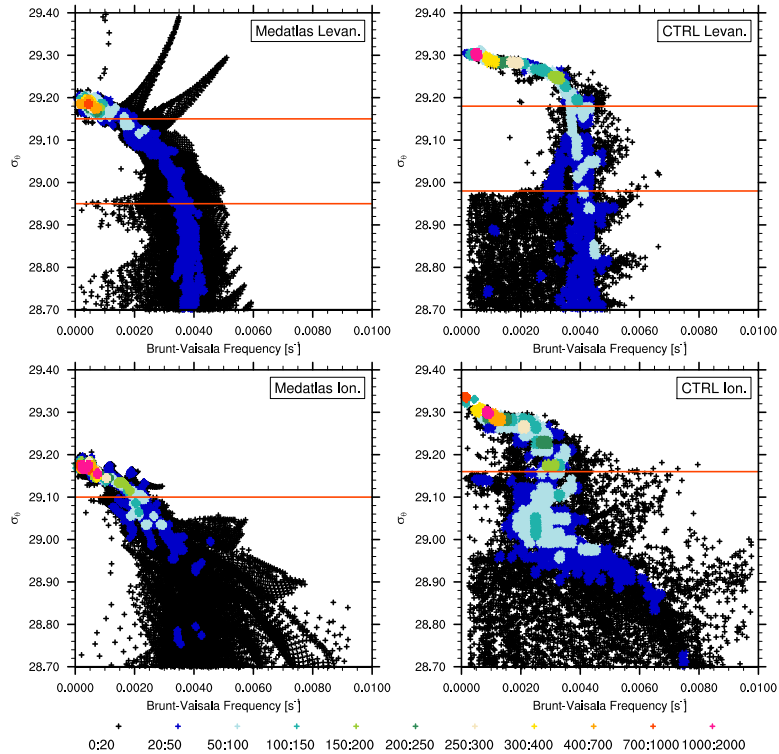


Figure 3.2: Brunt-Väisälä Frequency versus  $\sigma_\Theta$  averaged in February/March. First column Medatlas climatology, second column CTRL simulation. Upper row shows values from Levantine Sea, lower row shows values from Ionian Sea. The red lines indicate the determined intermediate and deep isopycnal ranges. Colors indicate the density of the scatter, determined by counting the number of pairs in squared subsections of 100 equally spaced intervals in the range between 0 to  $0.1 \text{ s}^{-1}$  Brunt-Väisälä Frequency and 28.5 to 29.5  $\sigma_\Theta$ . See text for more details on the isopycnal determination. Note that only a subsection of the total isopycnal range is plotted.

February/March. Since intermediate and deep water formation shows a high temporal variability, for the mixed layer depth we illustrate the intermediate depth only if 40 %, and for the deep water if 60 % of the last 100 years show an outcropping at the surface.

To determine the intermediate water layer in the Medatlas climatology (Medar-Medatlas 2002), we take into account that the high spatial and temporal variability is smoothed due the spatial interpolation of few observations, especially in deeper levels. To asses the degree of smoothing in the Medatlas climatology, we determined the CTRL mixed layer depth also for a climatological field averaged over the last 100 years, and find a reduction of the outcropping of  $\sim 100 \text{ m}$  compared to the mixed layer pattern derived by individual years. Thus, we lower the criteria on isopycnal surface outcropping of the Medatlas climatology by 100 m to obtain the mixed layer depth (compare

to the upper isopycnal depth for actual surface outcropping (Fig. 3.4, k). The deep water layer of the Medatlas climatology was assessed as in the CTRL simulation by the last prominent increase of the Brunt-Väisälä Frequency in the Ionian Sea.

The spatial pattern of LIW, AIW and ADW mixing is similar to the Medatlas climatology (Fig. 3.1) and in general agreement with the mixed layer climatology of D’Ortenzio et al. (2005).

LIW is formed in the area of the Rhodes gyre. The cyclonic gyre strongly preconditions the intermediate water formation through the doming of the isopycnals, bringing dense subsurface water close to the surface, where winter cooling leads to the formation of dense LIW.

The major source of deep water formation is in the southern Adriatic Sea. Figure 3.3 illustrates the meridional overturning stream function across the Adriatic and northern Ionian Sea. The stream function  $\Psi$  gives an indication of the transport of water at different levels/isopycnals, and can be used to assess the meridional location and rate of deep water formation. We compute the meridional stream function on both  $z$ -levels given by

$$\Psi(y, z) = \int_{-H}^z \int_E^W v(x, y, z') dx dz', \quad (3.2)$$

and isopycnal levels given by

$$\Psi(y, \sigma_\Theta) = \int_{\sigma_{\Theta_{max}}}^{\sigma_\Theta} \int_E^W v(x, y, \sigma'_\Theta) dx d\sigma'_\Theta \quad (3.3)$$

$$\text{with } \sigma_\Theta \in \{\sigma_{\Theta_{max}}, \sigma_{\Theta_{max}} - 0.01, \dots, \sigma_{\Theta_{min}} + 0.01, \sigma_{\Theta_{min}}\},$$

with  $v$  representing the annual mean meridional horizontal velocity field at each location  $x, y$  and depth level  $z$  or isopycnal level  $\sigma_\Theta$ ,  $-H$  the bottom of the sea,  $\sigma_{\Theta_{max}}$  the maximum and  $\sigma_{\Theta_{min}}$  the minimum annual mean isopycnal levels,  $E$  the lower bound of the integration in the east, and  $W$  the upper integration bound in the west.

In the northern and middle Adriatic Sea, on average the densest water with  $\sigma_\Theta$  of up to 29.9 forms during winter with temperatures as low as 5.5 °C, indicating shelf deep convection processes (Artegiani et al. 1997) also visible in the Medatlas climatology (Fig. 3.4). This very dense northern Adriatic deep water (NAdDW) flows towards the south, where there is the major location of ADW formation as indicated by the highest transport rates (Fig. 3.3, a, b), and the intensive mixing (Fig. 3.1). The combination of winter surface cooling, wind stirring, entrainment of salt from intermediate layers, and the presence of the permanent cyclonic gyre strongly preconditions open ocean convection and formation of ADW. The ADW is further transported south into the Ionian Sea, where on average it spreads into a depth of  $\sim 1100$  m (Fig. 3.3, a).

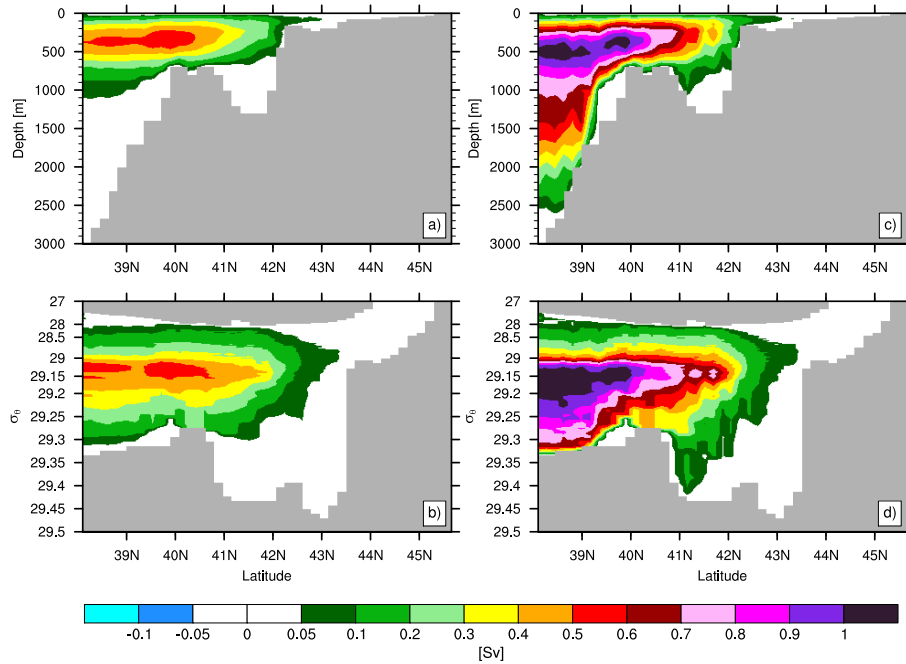


Figure 3.3: Meridional overturning stream function integrated across the Adriatic and northern Ionian Sea for the CTRL simulation. Left column shows the stream function calculated on a 100-year averaged velocity field, right column shows the stream function during one cold winter year (forcing year 24). First row shows the stream function calculated on  $z$ -levels (Eq. 3.2), second row shows the stream function calculated on  $\sigma_\theta$ -levels (Eq. 3.3). The grey colors represents the deepest topography or non occurring densities. Note the nonlinear spacing of the isopycnals and the color bar.

EMDW formation, which implies sinking of ADW into the deep Ionian Sea, occurs only during years with extreme cold winters within the 100-year repeating atmospheric forcing. The density of the newly formed water during a cold winter year is considerably higher, and the transport strongly enhanced compared to the mean state (Fig. 3.3, c, d). While the water flows over the sill of Otranto ( $40^\circ\text{N}$  to  $41^\circ\text{N}$ ) considerable horizontal and vertical mixing occurs, which causes further entrainment of the LIW and overall leads to a density reduction. The strong mixing during the overflow at the Strait of Otranto is probably related to the coarse vertical and horizontal representation of the sill, which does not allow for the simulation of the right bottom dynamics and slantwise convection, similarly, as has been described in other modeling studies (Wu and Haines 1996; Castellari et al. 2000). South of the Otranto sill the entrainment of ambient highly saline water increases the density. During the cold winter, a considerable mixing in the northern Ionian further contributes to southward shift of the maximum transport.

In the central Aegean Sea, the Medatlas climatology and the CTRL simulation show

the formation of very dense water (Fig. 3.4). This type of dense water formation has been described as the Eastern Mediterranean Transient (EMT) (Roether et al. 1996; Klein et al. 1999), which implies that EMDW is no longer formed in the Adriatic Sea but in the Aegean Sea, overflowing the Cretan Arcs and filling the deep Ionian and Levantine Sea. In the CTRL simulation, we do not find highly dense water exiting through the Cretan Arcs and filling the deep basin, indicating that there is no EMT event simulated by the model. Instead, along the pathway towards the Cretan Sea and the Ionian Sea the Aegean dense water loses its high density, probably due to intensive mixing while the water flows over the rough topography of the Aegean Sea. Thus, when exiting through the Cretan Arcs, the water shows no potential to sink into the deep eastern basin. Instead, the simulated Aegean dense water spreads mainly through the western Cretan Arc into the Ionian Sea at intermediate depth.

The CTRL simulation shows significant mixing along the eastern coast of Greece, where there is the formation of IIW, induced through the entrainment of highly saline AIW. In contrast, the Medatlas climatology does not show the formation of IIW, possible because the Aegean dense water sinks to depth and forms EMDW during the EMT.

Table 3.1: Physical and biogeochemical properties of the major water masses. 100 year mean values of indicated properties for LIW averaged over the Levantine Sea, IIW averaged over the Ionian Sea, AIW averaged over the Aegean Sea excluding the Cretan Sea, ADW averaged over the area of the Adriatic Sea with water depth  $\geq 250$  m, EMDW averaged over the area of the Ionian Sea with water depth  $\geq 1800$  m. Water formation rates calculated as 100 year mean of annual maximum of water formed in the Levantine for LIW, Ionian for IIW, Aegean Sea excluding the Cretan Sea for AIW, Adriatic for ADW, and transport below 1000 m across  $38.82^\circ\text{N}$  in the Ionian Sea for EMDW. Phosphate, Nitrate and oxygen concentrations in  $\text{mmol m}^{-3}$ . Abbreviations: D.: Depth, Form.: Formation rate, bot.: bottom.

| Properties             | LIW   |       | IIW   |       | AIW   |       | ADW   |       | EMDW  |        |
|------------------------|-------|-------|-------|-------|-------|-------|-------|-------|-------|--------|
|                        | Meda  | CTRL   |
| Upper $\sigma_\Theta$  | 28.95 | 28.98 | 28.95 | 28.98 | 29.1  | 29.16 | 29.1  | 29.16 | 29.1  | 29.16  |
| Lower $\sigma_\Theta$  | 29.15 | 29.18 | 29.15 | 29.18 |       |       |       |       |       |        |
| D. Min [m]             | 212   | 304   | 232   | 242   | 214   | 87    | 145   | 154   | 479   | 471    |
| D. Max [m]             | 485   | 439   | 720   | 464   | 366   | 291   | 678   | 747   | bot.  | bot.   |
| Form. [Sv]             |       | 0.41  |       | 0.80  |       | 0.30  |       | 0.68  |       | 0.06   |
| T [ $^\circ\text{C}$ ] | 15.1  | 15.2  | 14.1  | 15.0  | 14.1  | 14.1  | 13.5  | 13.7  | 13.5  | 13.8   |
| S [psu]                | 38.9  | 39.1  | 38.7  | 39.0  | 38.9  | 39.0  | 38.7  | 38.9  | 38.7  | 39.0   |
| Phosphate              | 0.15  | 0.14  | 0.16  | 0.12  | 0.16  | 0.09  | 0.17  | 0.09  | 0.18  | 0.21   |
| Nitrate                | 3.0   | 2.8   | 4.1   | 2.48  | 1.33  | 1.89  | 4.23  | 2.37  | 4.56  | 4.29   |
| Oxygen                 | 207.4 | 222.4 | 199.4 | 228.2 | 234.1 | 227.4 | 209.1 | 237.0 | 192.4 | 218.34 |

The main characteristics of the water masses are summarized in Table 3.1 and illustrated in Figure 3.4. The modeled LIW disperses mainly west towards Crete, where it splits south and north into two branches, with most of the flow to the north and

towards the Cretan Sea. In the Cretan Sea, the LIW again splits into a western and northern branch, with most of the flow towards the west. The AIW flows south along the eastern side of the Cyclades Islands to the Cretan Sea, where it intrudes the LIW. The increase in salinity and temperature in the northeastern Cretan Sea (Fig. 3.4, b) is the result of the upper layer inflow of LIW to compensate the extra bottom outflow of the denser AIW. Jointly the highly saline LIW/AIW flows around the Cyclades Islands into the western Cretan Sea. Since this area receives relatively fresh surface water entering from the Black Sea, the water formed in the southwestern Aegean is fresher and cooler than the water formed in the central eastern Aegean and the LIW, as can be seen by the northwest to southeast salinity and temperature gradient in the Strait of Antikythera (Fig. 3.4, b, f). These dense intermediate water masses then flow jointly along the coast of Greece towards the northeastern Ionian, where the salt entrainment triggers IIW formation. While some of the intermediate water enters the Adriatic Sea on the eastern side, the major part of the intermediate water flows around the western Ionian Sea towards the Strait of Sicily. The southern branch of the LIW in the area of the Rhodes gyre initially turns to the south of Crete and flows east, with some part flowing into the Mersa-Matruh gyre, while the major part flows towards the east and finally around the south of Cyprus and along the coast of Turkey towards the southern Aegean Sea, where it joins the northern branch of the LIW. The newly formed ADW flows out through the Strait of Otranto along the western boundary into the Ionian Sea, and if dense enough it sinks to depth and forms EMDW.

To assess the general overturning circulation of the eastern Mediterranean Sea, we compute the zonal overturning stream function, given by

$$\Psi(x, z) = \int_{-H}^z \int_N^S u(x, y, z') dy dz', \quad (3.4)$$

with  $u(x, y, z)$  representing the annual mean zonal horizontal velocity field at each location  $x, y$  and depth level  $z$ ,  $-H$  the bottom of the sea,  $N$  the lower bound of the integration in the north, and  $S$  the upper integration bound in the south.

We integrate the zonal overturning stream function over the entire Mediterranean Sea (Fig. 3.5). The zonal overturning circulation is characterized by two main cells; The upper anti-estuarine circulation cell with water flowing into the Mediterranean Sea through the Strait of Gibraltar and the Strait of Sicily further into the eastern Mediterranean, and the return flow at intermediate depth. The second cell illustrates the deep anti-clockwise circulation, and is only seen in the eastern Mediterranean. While on the 100-year average the deep circulation cell is only weakly established (0.1 Sv) in the upper 500 m to 800 m, during the cold winter with strong EMDW formation the cell rapidly expands down to the deepest layers with a maximum transport of up to 0.5 Sv. This clearly demonstrates that deep water formation events take place during selective

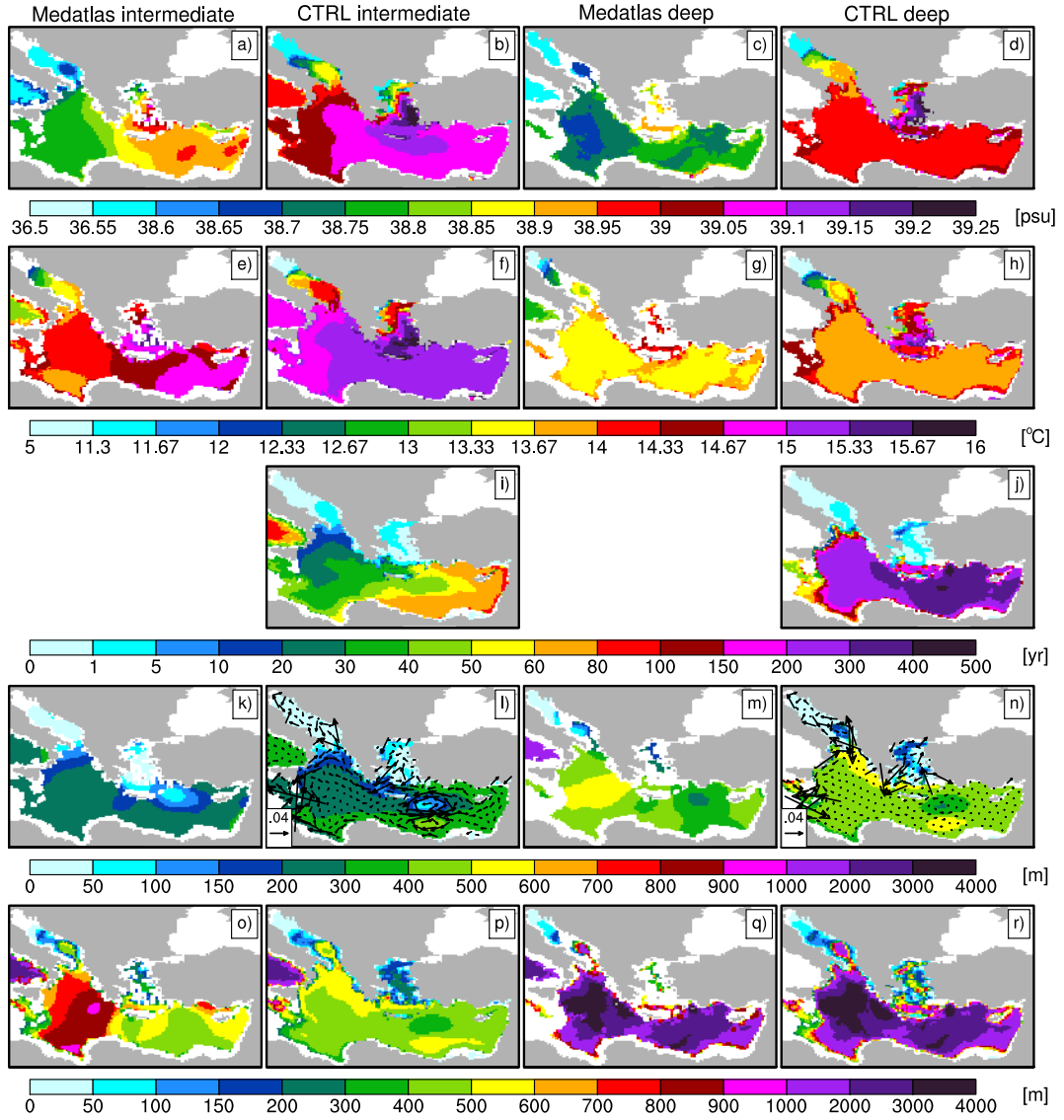


Figure 3.4: Properties of the intermediate water and deep water averaged in February/March over the last 100 years of simulation for the CTRL, and on the climatological February/March field of the Medatlas. a) to d) salinity; e) to h) temperature; i) to j) apparent water age; k) to n) upper depth of water mass; o) to r) lower depth of water mass. Isopycnals for Medatlas intermediate water (first column):  $\sigma_{\Theta}$  28.95 to 29.15; CTRL intermediate water (second column):  $\sigma_{\Theta}$  28.98 to 29.18; Medatlas deep water (third column):  $\sigma_{\Theta} \geq 29.1$ ; CTRL deep water (fourth column):  $\sigma_{\Theta} \geq 29.16$ ; The vectors in l), n) represent both the direction and speed [ $m s^{-1}$ ] of the circulation averaged over the depth of the isopycnal layer.

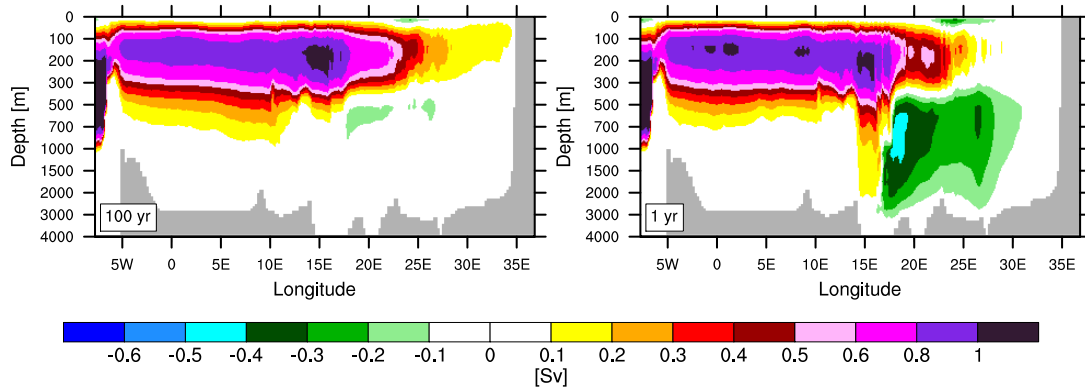


Figure 3.5: Zonal overturning stream function (Eq. 3.2) integrated across the Mediterranean Sea. Calculations are based on a 100-year annual mean velocity field (left), and one a one year velocity field of a very cold winter year (right) (forcing year 24). The grey colors represents the deepest topography. Note the nonlinear spacing of the depth levels and the color bar.

years, and that they rapidly ventilate the entire deep eastern Mediterranean Sea.

In the Rhodes gyre the salinity of the LIW is 39.1 psu, which is in good agreement with climatological estimates ranging between 38.85 to 39.15 psu (Castellari et al. 2000, and citations therein), and around 0.2 psu saltier than the Medatlas climatology. Also the LIW temperature in the Rhodes gyre with 15.3 °C is in good agreement with observations ranging between 14.5 °C and 16.4 °C (Castellari et al. 2000, and citations therein), however, warmer than the Medatlas climatology. Highest salinities within the intermediate water layer are simulated in the central eastern Aegean Sea, with salinities of up to 39.3 psu, around 0.3 psu higher than the Medatlas. The strongest discrepancy between the Medatlas climatology and the CTRL simulation is within the Ionian Sea for both salinity and temperature. To a large extent this discrepancy might be explained by the spreading of the saline LIW/AIW/CIW into the Ionian Sea in the CTRL simulation, while in the Medatlas the Aegean dense water sinks to depth, which can be seen by the deepening of the isopycnal layer in Figure 3.4, o. Also, especially in the central and southern Ionian, observations are sparse and the Medatlas climatology shows highest statistical errors in this area (Medar-Medatlas 2002).

To assess the strength of mixing and correspondingly physical ventilation, we introduce the apparent water age tracer  $age_M$  in the model. This tracer increases its value linearly with time  $t$  in all locations  $i, j$ , and in all depth levels  $z$ , except for the surface

$z_{surface}$ , where it is kept at zero,

$$\begin{aligned} \frac{d}{dt}age_M(i, j, z, t) &= 1, \\ age_M(i, j, z_{surface}, t) &= 0. \end{aligned} \quad (3.5)$$

The  $age_M$  shows youngest water in the Aegean and Adriatic Sea (Fig. 3.4 i, j). The intermediate water in the area of the Rhodes gyre is relatively younger than the  $age_M$  of the surrounding Levantine, however, older than in the AIW, IIW, ADW formation sites. This water age pattern indicates the doming of the isopycnals in the Rhodes gyre, bringing older dense water towards the surface, which facilitates the subsequent formation of LIW. The simulated deep water shows a progressive aging from west to east, indicating the EMDW flow path.

The relatively fresher tongue of water spreading from the Adriatic into the Ionian Sea illustrates the (sinking) pathway of the ADW. Overall, however, both the temperature and salinity of the deep water are higher than observed, which is a surface signal resulting from the atmospheric forcing and subsequently propagated into the deep ocean via mixing. The Medatlas climatology shows the spreading of deep water through the western and eastern Cretan arcs into the deep Ionian, which possibly indicates the EMT, filling the deep eastern Mediterranean with relatively warm and salty water.

### 3.3.1.2.1 Intermediate and deep water formation rates

The water formation rates were calculated by the annual maximum volume of water formed within the  $\sigma_\Theta$  range of the intermediate and deep water in the corresponding sub-basins (Fig. 3.6, Table 3.1).

The mean LIW formation rate is 0.41 Sv. The interannual variability is large, ranging between 0 to 1.8 Sv. Using the same procedure to calculate the LIW formation rate Lascaratos et al. (1993) derived 1.0 Sv from a climatologically forced mixed layer model, and Castellari et al. (2000) calculated the LIW formation rate to range between 0.5 to 5.8 Sv using an ocean general circulation model forced with different temporal resolutions of the NCEP atmospheric forcing data and a set of air-sea heat flux bulk formulas for the period 1980-1988. A mean formation rate ranging between 0 Sv to 1.4 Sv with a mean value of 0.77 Sv was simulated by Pinardi and Masetti (2000) for the period between 1978 to 1993.

The mean AIW formation rate is 0.3 Sv with values ranging between 0.0 and 0.75 Sv. Dense water formation in the Aegean Sea was modeled by Beuvier et al. (2010) for the period between 1961 to 2000. Their results show Aegean dense water formation rates with  $\sigma_\Theta \geq 29.3$  of up to 0.48 Sv during the EMT in 1993, and around half of it during the cold winters of 1972 and 1976. This shows, that our model simulates several years with EMT like dense water formation. However, as stated above, the model does not form deep water of Aegean origin, such as observed during the EMT, since the water

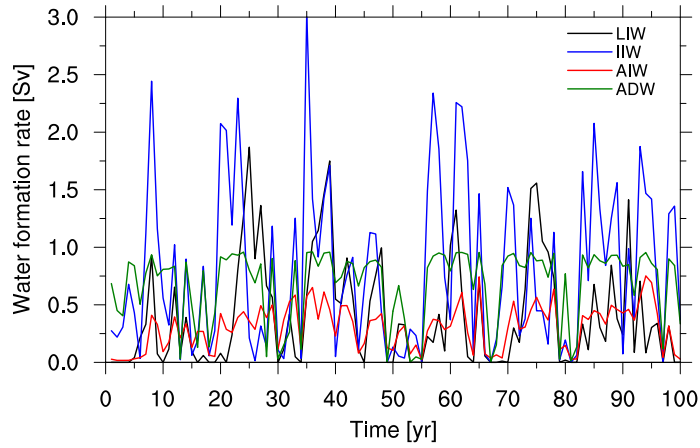


Figure 3.6: Annual maximum LIW, AIW, IIW and ADW formation rate of the CTRL simulation over the last 100 years of simulation.

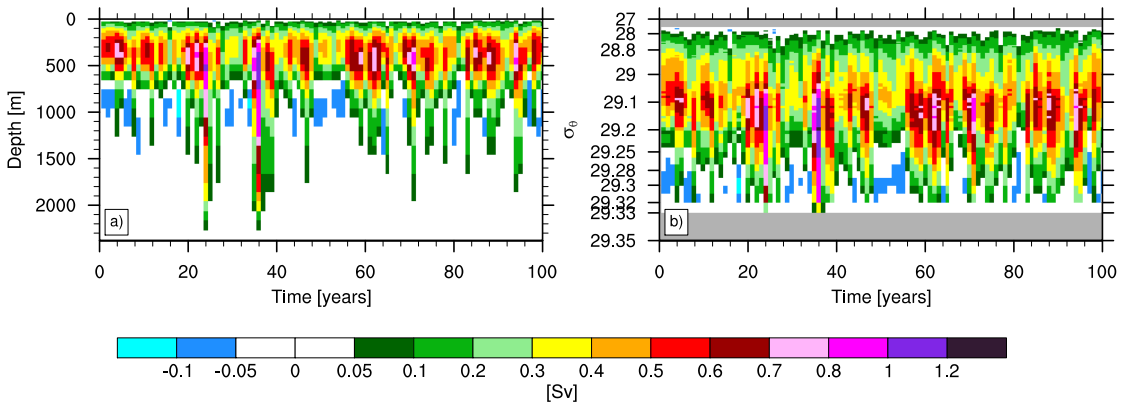


Figure 3.7: Hovmöller diagram of the annual mean water transport rate in the northern Ionian Sea at 38.82 °N for the last 100 years of simulation. a) calculated on z-levels (Eq. 3.2), b) calculated on  $\sigma_\theta$ -level (Eq. 3.3). The grey colors represents non occurring densities. Note the nonlinear color scale and the spacing of the isopycnals.

loses its high density due to intensive mixing while overflowing the rough topography of the Aegean and Cretan Sea.

Within the repeating 100-year cycle of atmospheric forcing annual maximum LIW formation occurs mostly in February, and AIW, IIW and ADW formation mostly occurs in March. There is a 10 to 15 year cyclicity of the maximum LIW, IIW, and more weakly pronounced also in the AIW and ADW formation rate, which are correlated with the air temperature. This climate variability might point towards the variability of large-scale atmospheric pressure patterns such as the North Atlantic Oscillation (NAO). Wallace and Gutzler (1981) showed, that positive values of the NAO-Index coincide with low air temperature over the Aegean Sea and the Levantine basin, with winds having a strong northerly component and warm winters over the western MED. Thus, a positive NAO-Index might favor a larger water formation rate.

The simulated ADW within the 100-year cycle of atmospheric forcing shows in most years a formation rate of 0.97 Sv, indicating a complete mixing of the entire Adriatic volume. However, even a complete mixing of the Adriatic Sea does not imply the formation of EMDW. To assess the EMDW formation rate we additionally compute the overturning stream function on both  $z$ -levels (Eq. 3.2) and  $\sigma_\theta$ -levels (Eq. 3.3) for the last 100-years of simulation. Figure 3.7 shows the annual mean transport rate on a transect spanning between Italy and Greece at 38.8°N. It can be seen that only selective years show a transport below 1500 m, with the annual maximum transport rates of 0.48 Sv and 0.68 Sv below 1500 m in the years 24 and 36 of the atmospheric forcing. On the isopycnal levels, these two very cold years show transport rates of 0.62 and 0.82 below the 29.31  $\sigma_\theta$ -level, while the 100-year mean transport below this isopycnal is 0.04 Sv. Overall, the very large amplitude of the interannual variability of the EMDW formation rate highlights the variability of the circulation and water mass structure. This large variability makes it rather difficult to compare the mean modeled EMDW formation rate to observations indicating a  $\sim 0.3$  Sv formation rate (Schlitzer et al. 1991; Roether and Schlitzer 1991; Lascaratos 1993).

### 3.3.2 Nutrient cycle

The present-day entire Mediterranean Sea is an oligotrophic system, resulting from the anti-estuarine circulation and the low riverine and atmospheric nutrient input. The biological productivity, in particular of the eastern Mediterranean Sea, is among the lowest observed (McGill 1969; Bethoux 1989). At the surface nutrient-depleted MAW enters the Mediterranean Sea, propagates to the eastern basin, and at depth nutrient-enriched water flows out.

The annual budget of total phosphate is shown in Table 3.2. The external nutrient input is largely balanced by the outflow at the Strait of Sicily, while only a little amount of the total phosphate is buried in the sediment.

Table 3.2: Annual total phosphate budget [ $mol s^{-1}$ ] of the eastern Mediterranean for the CTRL simulation calculated over the last 100 years of simulation. Export production at 113 m depth averaged over the area of the eastern Mediterranean Sea.

|                             | [ $mol s^{-1}$ ] |
|-----------------------------|------------------|
| Rivers                      | 25.6             |
| Net inflow Black Sea        | 19.1             |
| Net outflow Sicily          | 40.5             |
| Net flux water and sediment | 4.2              |
| Net flux sediment           | -1.9             |
| Net grain                   | 2.3              |
| Export production           | 113.8            |

In a depth below 100 m the modeled profile of dissolved phosphate concentration of the CTRL simulation compares well with the observational data (Fig. 3.8). In the first 100 m, the modeled phosphate concentrations of  $0.01$  to  $0.03 mmol m^{-3}$  is too low when compared to the mean concentration of the plotted observed data, however, it is still in the range of the observed variability. In fact, phosphate concentrations up to a depth of 80 to 100 m have been observed to be close to or even under the detection limit with concentrations ranging between  $0.01$  to  $0.03 mmol m^{-3}$  (Yacobi et al. 1995; Ediger and Yilmaz 1996; Kress and Herut 2001; Moutin and Raimbault 2002).

For a spatial representation of the nutrient distribution, we show the phosphate concentrations within the intermediate and deep water (Fig. 3.9) on the isopycnal surfaces as defined in section 3.3.1.2, and summarize the water mass characteristics in Table 3.1. The modeled intermediate phosphate concentrations of the CTRL are in good agreement with the Medatlas. In general, areas of intermediate and deep water formation appear phosphate depleted due to the surface outcropping of isopycnals into shallow levels with little nutrient concentrations. Compared to the Medatlas the model simulates intermediate water formation in the northeastern Ionian with correspondingly low phosphate concentrations. In the southern Levantine Sea, the slightly higher phosphate concentrations compared to the Medatlas result from the too strongly simulated strength of the anticyclonic Mersa-Matruh gyre, and thus, downwelling and subduction of the isopycnals into greater depth with higher nutrient concentrations, as shown in the maximum depth of the intermediate isopycnals in Figure (3.4 o, p). In the Ionian Sea and the eastern Levantine Sea, the Medatlas climatology shows higher phosphate concentration, mostly related to the deeper position of the intermediate isopycnals in this area. The northern Aegean Sea is strongly affected by the nutrient-rich inflow from the Black Sea.

The CTRL as well as the Medatlas climatology show a pronounced west-east gradient of increasing phosphate in the deep water (Fig. 3.9). This gradient is established by the deep water flowing from the Ionian into the Levantine Sea, continuously accumulating

### CHAPTER 3 THE PRE-INDUSTRIAL MEDITERRANEAN SEA

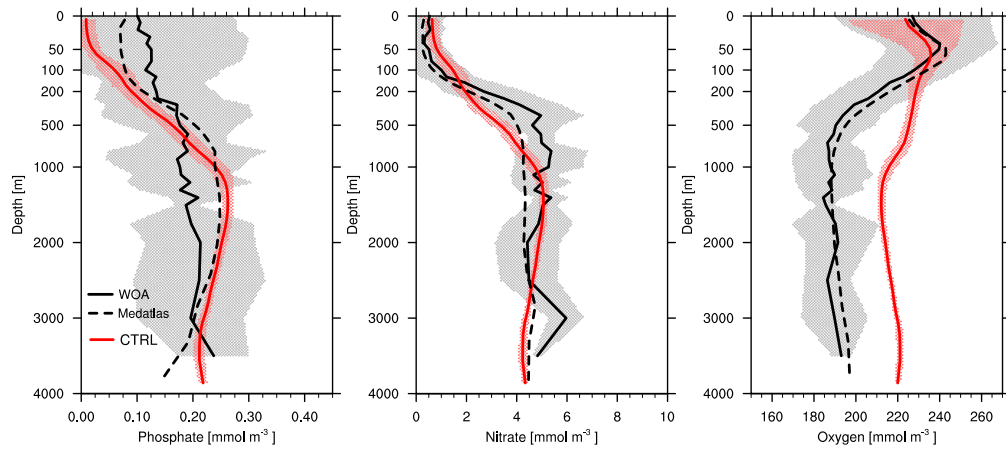


Figure 3.8: Dissolved phosphate, dissolved nitrate, and dissolved oxygen concentration averaged over the Ionian and Levantine Sea. The shaded grey area display 2x standard deviation around the mean of the WOA climatology, and the shaded red area 2x standard deviation around the mean of the CTRL of last 100 years of simulation. Note the nonlinear depth scale.

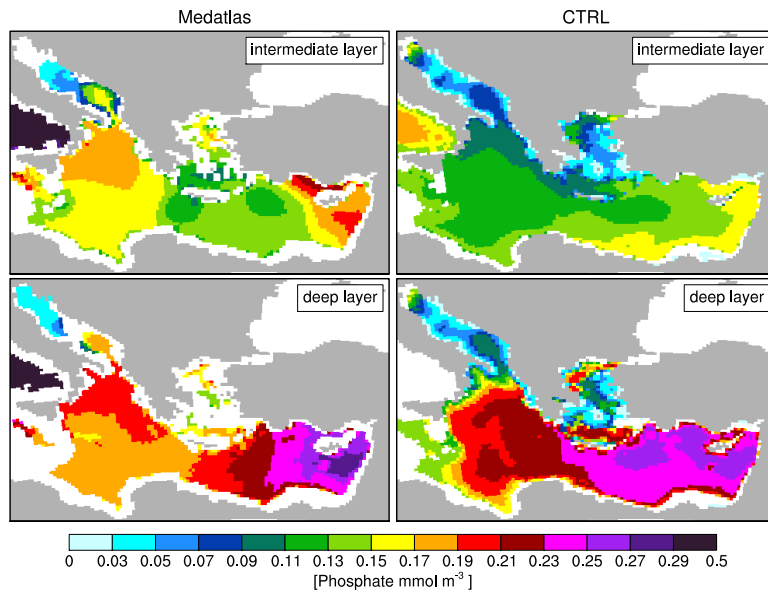


Figure 3.9: Dissolved phosphate within the intermediate and deep water of the Medatlas winter climatology and the CTRL simulation averaged in February/March for the intermediate and deep isopycnal layers as defined in section 3.3.1.2.

nutrients through organic matter remineralization.

The averaged profile of dissolved nitrate concentrations of the CTRL simulation is in good agreement with the observations (Fig. 3.8), with slightly higher nitrate concentrations in the upper 150 m and slightly lower concentrations between 200 m and 800 m.

### 3.3.3 Biological productivity

On a seasonal timescale, primary production is a function of the availability of light and nutrients. The nutrient availability is dependent on the physical advection/diffusion of nutrients from the deep ocean to the euphotic zone, the external nutrient input through rivers, and the recycling of nutrients within the upper ocean. Also the atmosphere is a source of nutrients through dust desorption (e.g. Ridame and Guieu 2002; Bartoli et al. 2005; Herut et al. 2005), however, this process is not simulated by the model. Since only the export production reaches the deep ocean and determines deep oxygen consumption and sediment carbon fluxes, we mainly focus on export production rather than primary production.

The geographical distribution of annual and seasonal POC export is shown in Figure 3.10. Areas of higher production are localized in the eastern Levantine, the Adriatic Sea, the northwestern Ionian Sea, the Strait of Sicily, and the Aegean Sea.

The high export production in the eastern Levantine and the Adriatic Sea is largely fueled by the high riverine nutrient input of the Nile and Po rivers. In the Aegean Sea, high export production is supported by the nutrient-rich surface waters entering the eastern Mediterranean through the Bosphorus. The inflowing nutrient-rich water from the Black Sea is mixed with the AIW, and circulates along the coast of Greece towards the northeastern Ionian and Adriatic Sea. During spring, the intermediate water formation along the coast of Greece fuels high biological production, indicated by the continuous, yet, decreasing export production along the flow pathway of the intermediate water masses towards the northern Ionian. In the western Ionian, the high export production is fueled by nutrients, which are up-welled by Ekman suction, resulting from the predominantly south-westerly winds during late spring to early summer. The enhanced POC export production in the Strait of Sicily is related to coastal upwelling of nutrient enriched outflowing intermediate and deep water. In contrast, in the open ocean areas of the Ionian and Levantine Sea export production is rather low.

In spring, as soon as there is sufficient light the phytoplankton bloom develops, resulting in highest export production. In summer, when there is the highest light availability, we find enhanced phytoplankton concentrations in a depth between 50 m and 60 m basin-wide, with highest concentrations in the Ionian and eastern Levantine Sea in the CTRL simulation, indicating a deep chlorophyll maximum (DCM) (Fig.

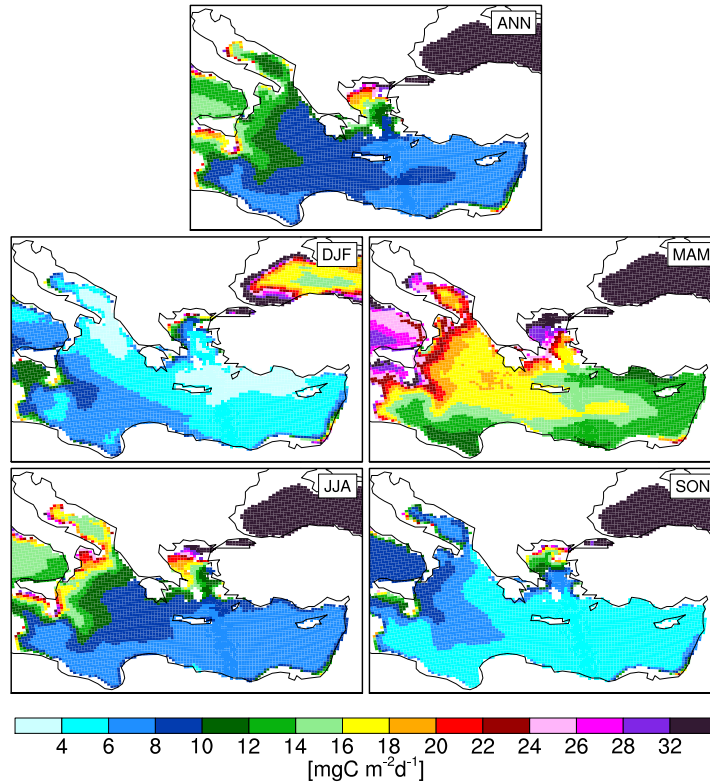


Figure 3.10: Annual mean (ANN), winter (DJF), spring (MAM), summer (JJA), and autumn (SON) POC export production in 113 m. Note the nonlinear color scale. Export production in the Black Sea is on average  $74 \text{ mgC m}^{-2} \text{ d}^{-1}$ .

3.11). In the present-day eastern Mediterranean a DCM is typically observed in a depth between 80 m and 120 m (Krom et al. 1992; Salihoglu et al. 1990; Yacobi et al. 1995; Herut 2000). However, several observational studies have reported that the DCM occurs not in the depth of maximum abundance of cells nor carbon biomass (Yacobi et al. 1995; Zohary and Robarts 1998; Psarra et al. 2000). Instead, these studies report that a DCM is measured because of the light adaption of deep phytoplankton communities to sub-optimal light conditions, which leads to a higher chlorophyll concentration and correspondingly a higher carbon-to-chlorophyll ratio (Hense and Beckmann 2008; Wang et al. 2008). Figure 3.11 shows the DCM derived with a constant carbon-to-chlorophyll ratio of 60. The investigation of a variable vertical profile of the carbon-to-chlorophyll ratio in the eastern Mediterranean is beyond the scope of this thesis.

The simulated annual mean export production at a depth of 113 m in the eastern Mediterranean Sea ranges between  $6.7$  to  $57.4 \text{ mgC m}^{-2} \text{ d}^{-1}$  with an average of  $9.9 \text{ mgC m}^{-2} \text{ d}^{-1}$ . Our results are within the range of observations and other model-

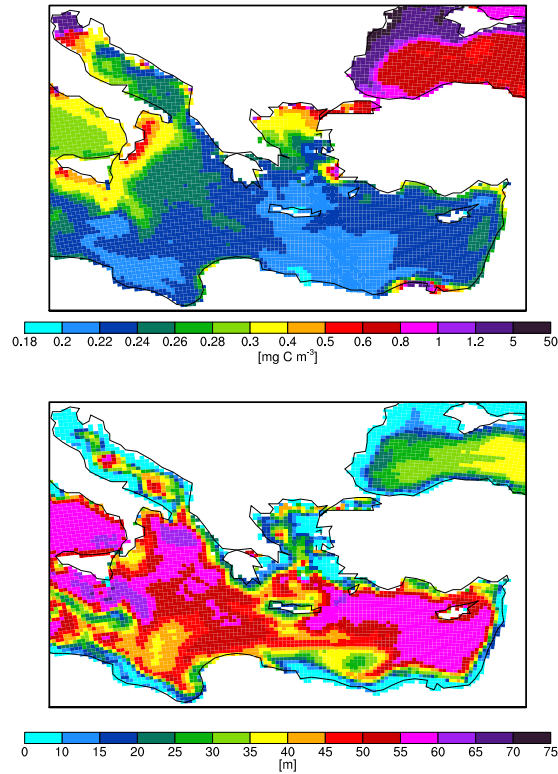


Figure 3.11: Chlorophyll concentration at the depth of the summer (JJA) DCM (upper panel); Depth of DCM (lower panel). Units converted using a carbon/chlorophyll ratio of 1:60. Note the nonlinear color scale.

ing studies. For instance Bethoux (1989) estimated the export production of POC to range between 16 and  $32 \text{ mgC m}^{-2} \text{ d}^{-1}$ , Moutin and Raimbault (2002) measured POC export flux to range between 3.5 and  $28.5 \text{ mgC m}^{-2} \text{ d}^{-1}$  in the eastern Mediterranean in 200 m depth between May and June 1996. In 100 m depth, Stratford et al. (2000) modeled an annual mean export flux of  $10 \text{ mgC m}^{-2} \text{ d}^{-1}$  for the present-day circulation.

The seasonal cycle of the modeled POC flux at a depth of 1450 m and 2616 m averaged over the last 100 years of simulation compared to sediment trap measurements for the Ierapetra Deep sediment trap station near Crete (Möbius et al. 2010) is shown in Figure 3.12. The deep POC flux peaks during summer, between May and June in 1530 m, and between June and July in 2616 m. The time delay between the seasonal peak in export production at depth is a consequence of the time needed for sinking. The total variance in the sediment trap observations is much higher than in the model, with a considerable number of observations being higher than the modeled POC fluxes.

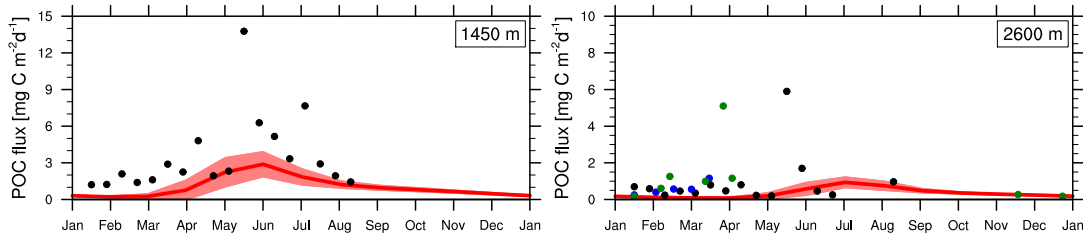


Figure 3.12: POC flux at 1450 m and 2600 m depth averaged over a small area in the southeast of Crete. Red line indicates the mean of 100 year of simulation, the red shaded area displays 2 standard deviation around the mean. Dots represent measurements from the Mediterranean Ierapetra Deep sediment trap station southeast of Crete. Dots in the 1450 m panel represent sediment trap measurements from 1508 m, dots in the 2600 m panel represent sediment trap measurements in 2689 m (black dots), 2720 m (blue dots), 2560 m (green dots). Observations were taken from Möbius et al. (2010), measured during three periods covering three to seven month from early 1999 to summer 2007. Note the different y-axes scales between the two panels.

Nonetheless, since we are aiming in modeling the pre-industrial climate, and therefore assume no anthropogenic fertilization neither through the atmosphere nor through rivers, we regard the modeled POC fluxes as reasonable.

### 3.3.4 Oxygen cycle

Sources and sinks of dissolved oxygen in the water column are determined by both biogeochemical processes and physical mixing. Sources of oxygen are the dissolution of oxygen by air-sea gas exchange and the release of oxygen by photosynthesis. In the case of surface layer over saturation, air-sea gas exchange leads to an evasion of oxygen into the atmosphere. Ocean mixing transports surface oxygen into the interior of the ocean, where the oxygen is consumed by remineralization of organic matter fallout within the water column and the sediment.

The oxygen profile of the eastern Mediterranean shows a maximum at a depth of  $\sim 50$  m (Fig. 3.8), in the climatological fields as well as in the CTRL simulation. Down to a depth of 200 m the modeled oxygen concentrations are within the range of observations, while below they are significantly higher.

Figure 3.13 shows the oxygen concentrations within the intermediate and deep water. The CTRL simulation shows a strong oxygenation at the locations of intermediate and deep water formation e.g. in the Rhodes Gyre, the Aegean, the northwestern Ionian, and the Adriatic Sea, and the subsequent spreading of oxygen along the intermediate flow path. The Adriatic is the source of deep oxygenation via deep water formation. The spreading of the deep water into the Ionian and Levantine Sea can be clearly seen by the west-east gradient of decreasing oxygen along its pathway (Fig. 3.13).

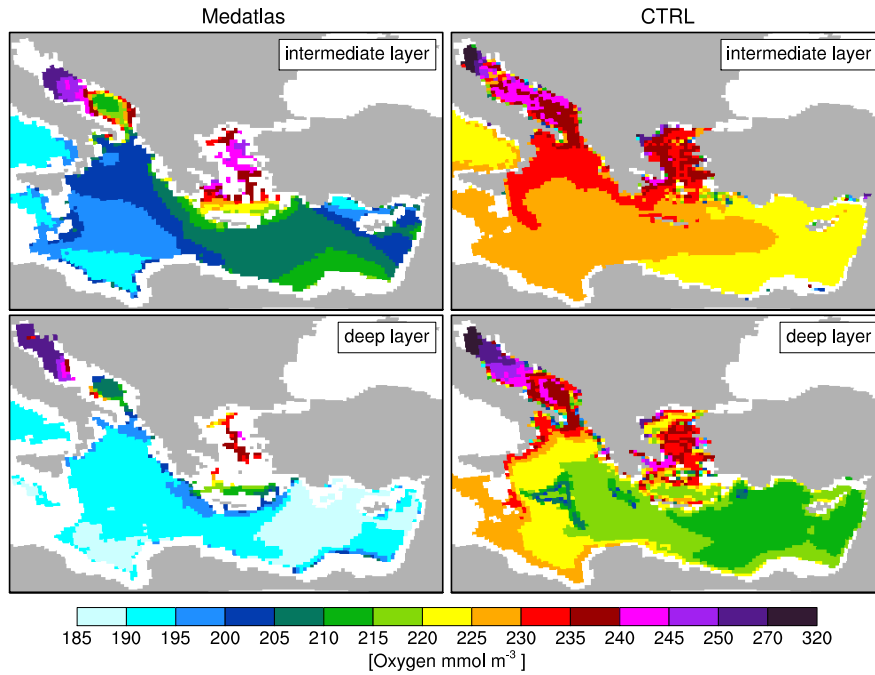


Figure 3.13: Dissolved oxygen within the intermediate and deep water of the Medatlas winter climatology and the CTRL simulation averaged in February/March for the intermediate and deep isopycnal layers as defined in section 3.3.1.2.

The strongest difference between the CTRL and the Medatlas climatology is within the deep water, with oxygen concentrations of up to  $30 \text{ mmol m}^{-3}$  higher than the climatological fields. However, since the general phosphate profile as well as the export production of organic material (section 3.3.3) and the sedimentation of organic material (section 3.3.5) are well within the range of observations, the high simulated oxygen concentrations cannot be attributed to a generally too low biological oxygen consumption by remineralization of POC. Thus, the dissolution of oxygen and physical mixing must lead to the too high oxygen concentrations in the CTRL simulation. In the following, we analyze the rate of over-oxygenation of the deep eastern Mediterranean Sea in response to the strong oxygenation of the Adriatic Sea.

#### 3.3.4.1 Sensitivity of deep water oxygenation

In this section we quantify the rate of deep water oxygenation in the eastern Mediterranean Sea as a function of the oxygen content of the Adriatic Sea. Therefore, we perform two model simulations, both with a lower vertical resolution of 29 levels compared to the 46 levels of the CTRL simulation. The CTRL29 was simulated with the same boundary conditions as the CTRL simulation. After 2000 years of simulation we

split the OxyRestAdria experiment, in which we re-set the oxygen concentration of the Adriatic Sea to a maximum concentration of  $205 \text{ mmol m}^{-3}$  below 208 m at each model time-step. The maximum oxygen concentration was chosen according to the southern Adriatic depth profile of Manca et al. (2004).

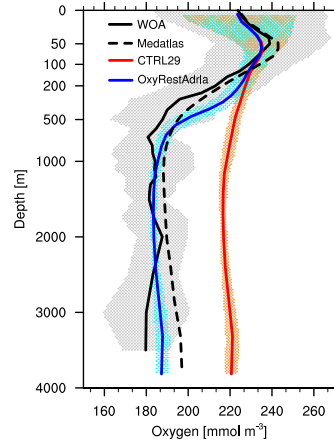


Figure 3.14: Annual mean dissolved oxygen concentration averaged over the Ionian and Levantine Sea. The shaded grey area display  $\pm 2$  standard deviation around the mean of the WOA climatology, the shaded red area  $\pm 2$  standard deviation around the mean of the CTRL29 of last 100 years of simulation, and the light blue shaded area  $\pm 2$  standard deviation around the mean over the CTRL29 of last 100 years of simulation. Note the nonlinear depth scale.

Figure 3.14 shows the oxygen concentration profile of the sensitivity experiments compared to the CTRL29 simulation and observational datasets, and Figure 3.15 the time evolution of the deep water ventilation. To approach an equilibrium within this sensitivity experiment it takes around 1200 years of simulation. Below 600 m depth, the oxygen concentration is well within the range of observations, clearly indicating that the oxygenation of the Adriatic is overestimated by the model due to intensive mixing as described in section 3.3.1.2. Nonetheless, between 150 and 500 m the simulated oxygen concentration is up to  $\sim 20 \text{ mmol m}^{-3}$  higher than observed (Fig. 3.16). The source of the intermediate oxygenation is the AIW spreading mainly through the western Cretan Arc into the Ionian Sea (Fig. 3.16). The reasons for this strong intermediate oxygenation by the AIW are most likely the same as in the Adriatic, with considerable mixing occurring while the water flows of the complex topography of the Aegean Sea and the western Cretan Arc into the Ionian.

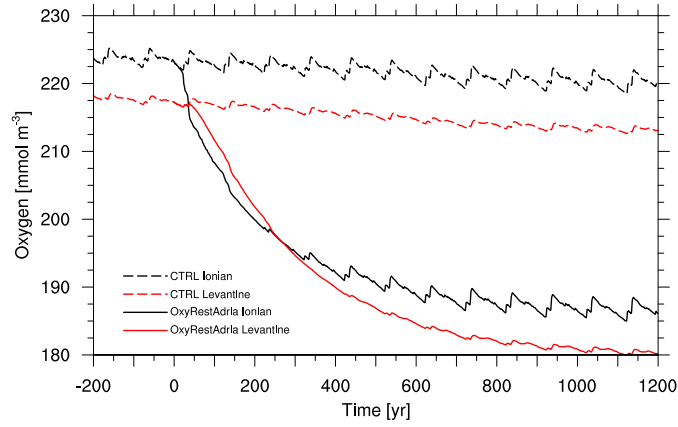


Figure 3.15: Dissolved oxygen concentration averaged over the Ionian and Levantine Sea below 1841 m for the CTRL29 and OxyRestAdria simulations. We initialize the OxyRestAdria experiment from the CTRL29 in the year 2000, illustrated as year 0 in this context.

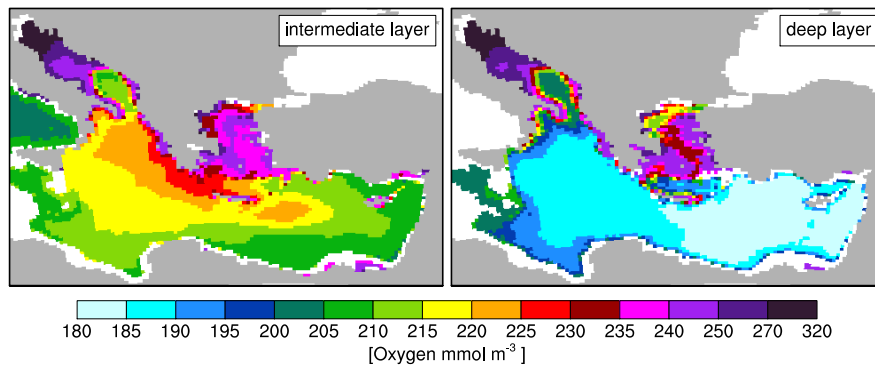


Figure 3.16: Dissolved oxygen within the intermediate and deep water of the OxyRestAdria simulation averaged in February/March for the intermediate and deep isopycnal layers as defined in section 3.3.1.2.

### 3.3.5 Sediment

#### 3.3.5.1 Sediment particulate organic carbon burial flux

The POC burial flux is determined by the strength of the biological export production and the remineralization of POC export flux in the water column and the sediment. Under the same sunlight conditions, the strength of the export production is determined by the availability of nutrients. In the model two POC size classes are simulated; A slower sinking dead phyto- and zooplankton pool, and a faster sinking zooplankton fecal pellets pool. The POC flux in the water column is proportional to the constant remineralization rate and the constant sinking velocity of the individual POC pools (Eq. 2.1). The deeper the water column, the longer the POC particles are subjected to remineralization. Thus, deep-sea sediments receive usually a smaller POC flux than shelf areas. In the sediment, the bacterial remineralization rate is enhanced in warmer waters, and reduced with decreasing pore water oxygen concentrations. Moreover, the remineralization of POC in the sediment is enhanced through erosive sediment resuspension, which depends on the strength of the bottom water flow.

Figure 3.17 shows the geographical distribution of POC burial flux in the sediment compared to sediment core derived observations. In general, the deep ocean areas show lower burial fluxes than areas of intermediate depth, which is the result of the generally lower production in the open ocean areas and the longer time of the POC particles in the well oxygenated water column while sinking. The POC burial flux of the deep ocean areas is in good agreement with the sediment core observations. Lowest burial fluxes are simulated in the marginal areas, in particular in the Adriatic Sea, Aegean Sea, the Sicilian-Tunisian Platform and the Nile delta zone. The model simulates a too strong erosion in these areas. The coarse horizontal and vertical resolution of the model involves a poor or missing representation of canyon systems, which in reality influence the water flow along the shelf margins by channelizing the bottom water flow, which modulates the amount of particle erosion. Moreover, we do not simulate the influx of lithogenic material from rivers, which would cover the top sediment layer with coarser grained lithogenic material, and therefore, protect the fine grained POC from erosion and repeating re-suspension.

Figure 3.18 compares the observed versus the modeled POC burial flux. To account for the temporal as well as the small-scale variability, we illustrate the  $\pm 1$  standard deviation of the interannual variability within the last 100 years of simulation, as well as the maximum small-scale spatial variation within a 2 x 2 gridbox window around the core location. For the observations we account for the maximum variability within the 0 to 1 kyr BP time slice. The temporal variability and spatial-small scale variability of the simulations overweights by far the temporal variability within the sediment core time slice observations, and is highest in the shallower locations. While for most locations the modeled variability is within the range of observations, in particular the core locations

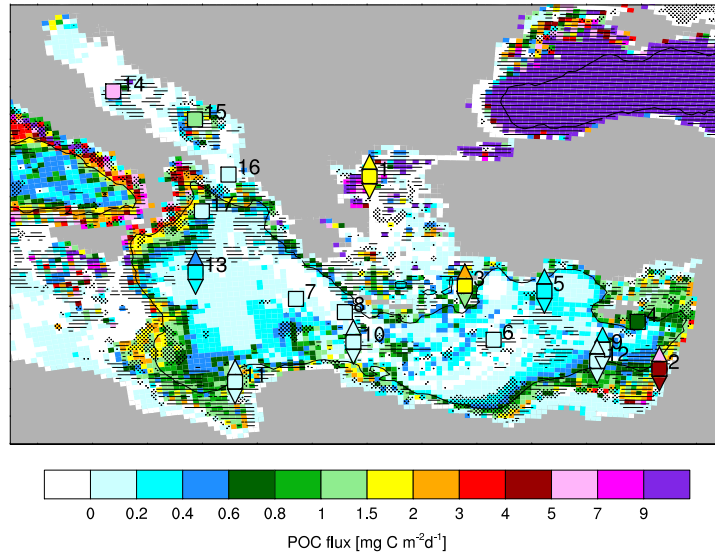


Figure 3.17: Sediment POC burial flux averaged over the last 100 years of simulation superimposed with POC burial fluxes derived from sediment cores. Squares show mean values, triangle pointing upward maximum and triangles pointing downward minimum of the sediment core data averaged between 0–1 kyr BP. The black line represents the 1500 m contour line. Line shaded regions show areas where the trend of POC burial is on average lower than  $-0.05 \text{ mgC m}^{-2} \text{ d}^{-1}$  over the last 500 years of simulation, and point shades areas where this trend is higher than  $0.05 \text{ mgC m}^{-2} \text{ d}^{-1}$ . Sediment core labels for reference in Figure 3.18. Core labels for allocation of cores in Figure 3.18. Sediment core data taken from the sites GeoB7608-1 (Bahr 2007), ODP site 160-970 (Meyers and Bernasconi 2009), MD84-641 (Fontugne and Calvert 1992), BC19 and SL114 (Slomp et al. 2002), Geo-Tü SL119 (Milker et al. 2006), Geo-Tü SL114 (Schmidt 2007), Geo-Tü SL148, Geo-Tü SL112, Geo-Tü SL123 (Kuhnt 2008), ODP site 160-964A (Gallego-Torres et al. 2007) SL 71, #569, #563, #562 (Möbius et al. 2010).

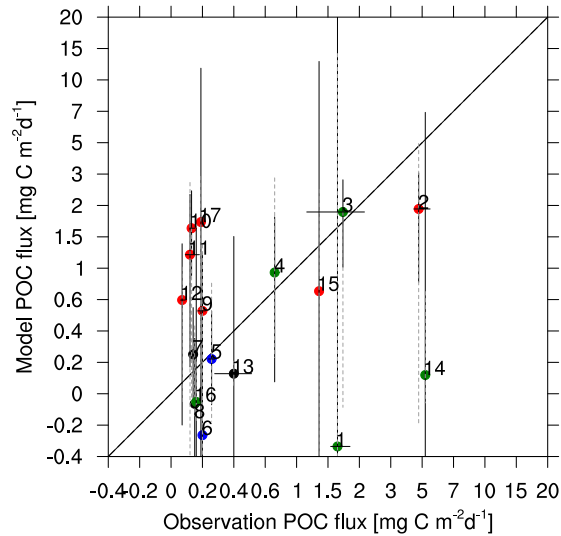


Figure 3.18: Sediment core POC burial flux versus modeled POC burial flux. Points represent averaged observed flux of the sediment cores between 0 to 1 kyr BP versus 100-year averaged fluxes of the model. Black horizontal lines represent the maximum temporal variation of the observations between 0 to 1 kyr BP. The black vertical lines shows  $\pm 1$  standard deviation of the interannual variability within the last 100 years of simulation. Grey dashed vertical lines represent the maximum small-scale spatial variation of mean values within a  $2 \times 2$  gridbox window around the original core location. Colors indicate the water depth of the model gridbox at the core locations: green  $< 1000$  m,  $1000 \text{ m} \leq$  red  $< 2000$  m,  $2000 \text{ m} \leq$  blue  $< 3000$  m, black  $\geq 3000$  m. Sediment core labels as in Figure 3.17. Note the nonlinear axes scales, and that the plot size does not always cover the full data range of the temporal and spatial variations of model results on every point.

between 1000 m and 2000 m are overestimated by the model. However, in these depth regions the model shows a considerable drift toward lower fluxes (Fig. 3.17).

### 3.3.5.2 Sediment pore water $\delta^{13}\text{C}$ isotopes

The distribution of  $\delta^{13}\text{C}$  in dissolved inorganic carbon (DIC) is controlled by a combination of biological and thermodynamic processes. Air-sea gas exchange influences the isotopic composition of the inorganic carbon, with an equilibrium fractionation of  $-6.5 \text{ ‰}$  in our model setup. On the other hand, biological uptake of  $\text{CO}_2$  in the form of organic matter removes preferentially the light  $^{12}\text{C}$  carbon with a modeled fixed equilibrium fractionation set to  $-20 \text{ ‰}$ , resulting in an isotopic enrichment of the residual inorganic carbon. Remineralization of the organic matter releases the  $^{12}\text{C}$  back into the inorganic reservoir. Thus, the biological pump creates an isotopic gradient, with  $\delta^{13}\text{C}$  DIC enriched surface water and  $\delta^{13}\text{C}$  DIC depleted deep water.

Benthic foraminifera calcify in contact with ambient pore water, and thus, record the bottom water  $\delta^{13}\text{C}$  DIC depending on the specific microhabitat (epifaunal or infaunal) (Schmiedl et al. 2004). Therefore, the  $\delta^{13}\text{C}$  DIC provides information on the past carbon cycling and has widely been used to reconstruct past changes of deep water properties and organic matter fluxes (Vergnaud-Grazzini and Pierre 1991; Kuhnt et al. 2008; Schilman et al. 2001).

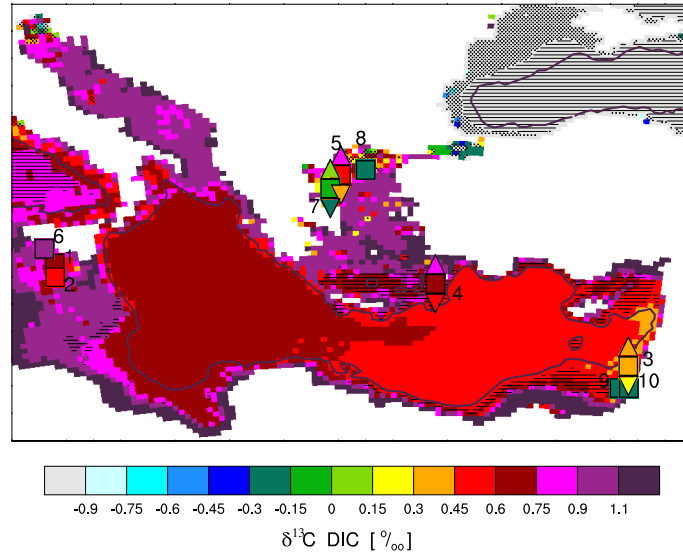


Figure 3.19: Sediment pore water  $\delta^{13}\text{C}$  DIC averaged between 1.2–2 cm depth superimposed with observed  $\delta^{13}\text{C}$  of shallow infaunal benthic *Uvigerina mediterranea* of sediment cores between 0 and 1 kyr BP. Squares show mean values, triangle pointing upward maximum and triangles pointing downward minimum  $\delta^{13}\text{C}$  DIC of the time slice observations. The black line represents the 1500 m contour line. Line shaded regions show areas where the trend of  $\delta^{13}\text{C}$  DIC values is on average lower than  $-0.02\text{‰}$  over the last 500 years of simulation, and point shades areas where this trend is higher than  $0.02\text{‰}$ . Sediment core labels for reference in Figure 3.20. Core labels for allocation of cores in Figure 3.20. Sediment core data taken from sites: Geo-Tü SL148, Geo-Tü SL112, Geo-Tü SL123 (Kuhnt 2008), SL78, MC517 (Schmiedl unpublished data), Ga-110, Ga-111, (Schilman et al. 2001, 2003) SL-31 (Abu-Zied 2001).

Figure 3.19 shows the  $\delta^{13}\text{C}$  DIC of sediment pore water superimposed with observations of the corresponding time slices. Compared to the simulated surface  $\delta^{13}\text{C}$  DIC (not shown), the modeled sediment pore water  $\delta^{13}\text{C}$  DIC is  $\sim 0.7\text{‰}$  lower, indicating the effect of the biological pump. EMDW formed in the Adriatic flows along the bottom towards the Levantine and continuously accumulates  $^{12}\text{C}$  through the remineralization of organic matter fallout from the surface. Thus, there is a west-east gradient of decreasing  $\delta^{13}\text{C}$  DIC in the sediment pore water. In the area of the Nile plume along the Israeli, Lebanese and Syrian coast, the additional higher carbon fluxes to the sediment

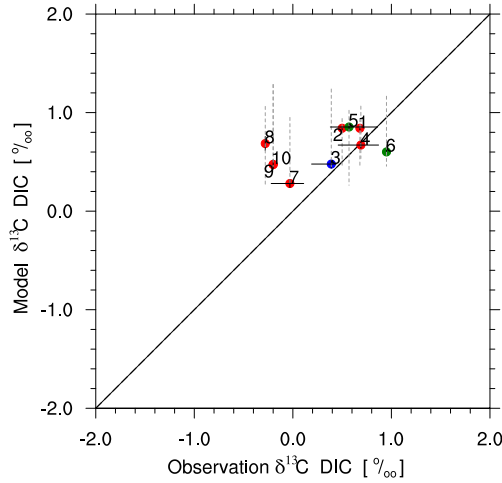


Figure 3.20: Observed  $\delta^{13}\text{C}$  of shallow infaunal benthic *Uvigerina mediterranea* versus modeled sediment pore water  $\delta^{13}\text{C}$  DIC averaged between 1.2–2 cm depth. Points show averaged observed  $\delta^{13}\text{C}$  of benthic foraminifera in the sediment cores between 0 to 1 kyr BP versus 100-year averaged  $\delta^{13}\text{C}$  DIC of the model. Black horizontal lines represent the maximum temporal variation of the observations between 0 to 1 kyr BP. Black vertical lines represent  $\pm 2$  standard deviation of the interannual variability within the last 100 years of simulation. Grey dashed vertical lines represent the maximum small-scale spatial variation of 100-year mean modeled values within a  $2 \times 2$  gridbox window around the original core location. Colors indicate the water depth of the model gridbox at the core locations: green  $< 500$  m,  $500 \text{ m} \leq \text{red} < 1000$  m,  $1000 \text{ m} \leq \text{blue} < 1500$  m. Sediment core labels as in Figure 3.19.

depletes the pore water  $\delta^{13}\text{C}$  DIC. The northern Aegean shows a high biological production, with high organic matter fallout, remineralization and related  $\delta^{13}\text{C}$  depletion. Due to the inflowing  $^{13}\text{C}$  depleted surface water from the Black Sea, mixing in the northern Aegean can only moderately increase the relatively low  $\delta^{13}\text{C}$  DIC values in the sediment. The deep sea areas of the eastern Mediterranean Sea is in equilibrium, however, areas below 1500 m depth in particular in the eastern Levantine and southern Aegean Sea show a drift towards lower  $\delta^{13}\text{C}$  DIC values. In contrast, in the Black Sea in the shallow areas the  $\delta^{13}\text{C}$  DIC values are mostly increasing, while at depth they show a trend towards stronger  $\delta^{13}\text{C}$  DIC depletion.

The modeled pore water  $\delta^{13}\text{C}$  DIC values seem reasonable compared to the observations, even though the observations only cover the marginal areas (Fig. 3.20) with only one core site in the eastern Levantine (Geo-Tü SL112 water depth 892 m, label 3) showing a model depth of 1284 m. While the temporal variability within the 100-year model time slice is very small, the small-scale variability in these coastal areas is very high. Also the observations show a rather high variability. The sparse data coverage concentrated on marginal areas with steep  $\delta^{13}\text{C}$  gradients is rather unsuitable for a

model-observation comparison.

### 3.4 Summary

We have simulated the pre-industrial Mediterranean ocean circulation and biogeochemical cycles using a regional ocean general circulation model coupled to a biogeochemical model including a sediment module, and forced it by atmospheric data derived from a coarse resolution global climate model. We assessed the capability of the model to simulate the large-scale general circulation and biogeochemical cycles under the coarse atmospheric forcing through a validation with observations. Through this approach, we gain an understand of the uncertainty in the predictability of the sapropel simulations, which are performed by the same method of imposing atmospheric data derived from the same coarse resolution global climate model of the Holocene insolation maximum (HIM) time slice (Chapter 4).

The model reproduces the intermediate and deep water formation processes of the present-day Mediterranean Sea. Moreover, the model shows a good representation of the nutrient-cycling in the intermediate and deep layers. The seasonal particulate organic carbon (POC) export production and POC flux through the water column are well simulated. Also the deep-sea sediment POC burial flux is in good accordance with observations. Due to the well representation of the large scale thermohaline circulation and biogeochemical cycles, we are confident that the approach of forcing a regional model with coarse resolution atmospheric data derived from a global climate simulation can also be applied to the HIM time slice in order to simulate the sapropel S1 formation.

Despite the generally well representation of the large-scale features, there are problems encountered, all related to the relatively coarse resolution of the atmospheric forcing and/or the regional model setup:

- The deep water formation in the western Mediterranean Sea is poorly simulated by the model because the western Mediterranean deep water formation is very sensitive to small-scale wind features and thermal forcing. Both atmospheric features are not captured by the atmospheric forcing derived from the coarse resolution global climate model. Since the shallow depth of the Strait of Sicily separates the deep western basin effectively from the eastern basin, the deep western circulation is unimportant for the eastern Mediterranean circulation features. Therefore, we confidently constrain our analyzes to the eastern basin only, and we also do so for the HIM forced simulations.
- The model shows problems in simulating the right bottom dynamics, the slantwise convection, and the bottom flow within narrow channels. Intensive mixing occurs in the simulation while the water flows over the sill of the Strait of Otranto towards

the deep Ionian Sea, which leads to an over-oxygenation during the simulated ADW formation, and correspondingly an over-oxygenation of the newly formed EMDW. For the simulation of the sapropel formation, at least under a stagnating deep water circulation preventing the formation of EMDW, this model limitation becomes irrelevant.

- The physical sediment erosion of POC within the marginal areas, in particular, the Adriatic Sea, Aegean Sea, the Sicilian-Tunisian Platform and the Nile delta zone is strongly overestimated. Owing to the coarse resolution of the model, topographic features, such as slopes and canyons modulating the bottom water flow, are poorly represented. In addition, the simplicity of the model does not account for riverine sedimentation processes covering the top sediment with coarse grain material, which protects the fine grained POC from physical erosion. The too strongly simulated erosion along the marginal areas does not significantly affect the nutrient nor the oxygen cycling. The deep sea sediment POC burial flux is well captured by the model. Therefore, we constrain our analyzes and interpretation of the HIM forced simulations to the deep-sea areas.

## Chapter 4

# The early Holocene sapropel formation

### 4.1 Motivation

Sapropel S1 formation implies the evolution of a deep water oxygen deficiency in the eastern Mediterranean Sea. With a set of model experiments we aim to identify plausible scenarios leading to S1 formation. 'Plausible' in this context implies that the simulated scenarios should be in accordance with the sediment observations prior and during S1 deposition, and the evolution of deep water anoxia should occur within a realistic time frame. Knowledge about the required timescale for complete oxygen depletion can give rise to the climatic event that has triggered the onset of the S1 formation. In general, the oxygen concentration is a function of the strength of the physical deep water ventilation and the biological oxygen utilization through remineralization of organic matter.

There are large uncertainties concerning the temporal evolution of the deep water oxygen depletion. Estimates of the time frame required for complete deep water oxygen depletion range from 400 years (Myers and Rohling 2000) to 640 years (Rohling 1994) to 1000–1500 years (Schmiedl et al. 2010) to 2100 years (Howell and Thunell 1992) to ~5000 years (Troelstra et al. 1991). Previous biogeochemical model studies showed that the evolution of the S1 oxygen depletion requires less than 2000 years, and was caused by a stagnating deep water circulation combined with a significantly enhanced external nutrient input (Stratford et al. 2000; Bianchi et al. 2006). However, the eutrophication scenarios imposed in these modeling studies contradict the reconstructed oligotrophic conditions throughout the glacial-interglacial transition period (Kuhnt et al. 2007). Given these indications for a basin-wide oligotrophic marine environment, the time for the evolution of the deep water oxygen deficiency probably exceeds the 2000 years suggested by biogeochemical model simulations (Stratford et al. 2000; Bianchi et al. 2006).

This controversy motivates us to perform a simple oxygen budget calculation to obtain a rough estimate of the potential time scale for S1 formation. If we assume that the pre-sapropel particulate organic carbon (POC) export production was characterized by a similar oligotrophy as in the present-day eastern Mediterranean Sea, we can estimate

the time needed to deplete the entire deep water oxygen. In chapter 3, we presented a simulation of the pre-industrial eastern Mediterranean Sea. From this simulation we can obtain the POC flux to the deep ocean. Assuming that below 1500 m depth the complete POC flux ( $1.55 \text{ mgC m}^{-2} \text{ d}^{-1}$ ) is remineralized consuming oxygen, and a mean depth of the deep eastern Mediterranean Sea of 3000 m, we can estimate the oxygen consumption rate

$$1.55 \frac{\text{mgC}}{\text{m}^2 \text{d}} \times \frac{1}{12} \frac{\text{mmolC}}{\text{mgC}} \times \frac{1}{122} \frac{P}{C} \times 172 \frac{\text{O}_2}{P} / 1500 \text{ m} = 0.044 \frac{\text{mmolO}_2}{\text{m}^3 \text{yr}}.$$

Assuming that prior to the onset of the stagnation the deep eastern Mediterranean was well-ventilated with an oxygen concentration of  $200 \text{ mmol m}^{-3}$ , we can derive the time frame for complete oxygen consumption below 1500 m

$$200 \frac{\text{mmolO}_2}{\text{m}^3} / 0.044 \frac{\text{mmolO}_2}{\text{m}^2 \text{yr}} = 4545 \text{ yr}.$$

This simple calculation implies a 100% stagnating deep water circulation, which is rather implausible. Next, we introduce a small background diffusion of  $0.5 \times 10^{-5} \text{ m}^2 \text{ s}^{-1}$  to parametrize the effect of eddy diffusion. We determine the diffusive oxygen flux by assuming a diffusive ventilation of the deep ocean with an oxygen concentration of  $200 \text{ mmol m}^{-3}$

$$200 \frac{\text{mmolO}_2}{\text{m}^3} \times 0.5 \times 10^{-5} \frac{\text{m}^2}{\text{s}} / 1500 \text{ m} = 21 \frac{\text{mmolO}_2}{\text{m}^2 \text{yr}}.$$

Distributing the oxygen flux over the entire 1500 m height of the deep stagnating water column, we obtain the diffusive ventilation rate

$$21 \frac{\text{mmolO}_2}{\text{m}^2 \text{yr}} / 1500 \text{ m} = 0.014 \frac{\text{mmolO}_2}{\text{m}^3 \text{yr}}.$$

We infer the time frame for the evolution of deep water anoxia by

$$200 \frac{\text{mmolO}_2}{\text{m}^3} / (0.044 \frac{\text{mmolO}_2}{\text{m}^3 \text{yr}} - 0.014 \frac{\text{mmolO}_2}{\text{m}^3 \text{yr}}) = 6667 \text{ yr}.$$

Overall this might imply that under an oligotrophic regime even in a completely stagnating ocean the time required to develop deep water anoxia is considerably longer than previously assumed. Potentially, this further implies that the widely proposed enhanced Nile river runoff during the African humid period (AHP) might not be the climatic event triggering the deep water stagnation, since the AHP started at 14.8 kyr BP, which would give in total only 4800 years for the development of the S1 deep water anoxia starting at 10 kyr BP. Overall, this simple budget calculation favors the hypothesis that the deep water oxygen depletion started earlier in time than the AHP climate, and was possibly triggered by the climatic changes associated with the glacial-interglacial transition period.

In this chapter, we analyze the most commonly proposed mechanisms for S1 formation, which involve an enhanced biological productivity and/or a stagnating deep

water circulation. We focus on the oceanic and biogeochemical response under a purely eutrophicated production regime, the AHP climate, as well as an oligotrophic and eutrophic realization of the climatic changes associated with the glacial-interglacial transition. We separate the relative importance of the general circulation and the biogeochemical cycles with respect to S1 formation. We analyze the dynamical evolution of the oxygen deficiency in space and time during the pre-sapropel and sapropel time, and discuss the results with respect to observations. Finally, we compare our modeled sediment with observations to further constrain the plausibility of our simulated scenarios.

## 4.2 Experimental design

The simulations were designed to cover the full range of the sapropel forming hypotheses, with the purpose to distinctly separate the role of the general circulation and the biogeochemical cycles (Table 4.1).

First, we performed the early Holocene Baseline simulation, which incorporates no explicit perturbation, thus, it resembles an oligotrophic well-ventilated control simulation for the Holocene insolation maximum (HIM) climate. In order to distinguish the climatic control on the thermohaline circulation, we performed two deep water stagnation experiments. The Nile experiment mimics the climatic conditions of the AHP, with an additional Nile runoff of  $9000 \text{ m}^3 \text{ s}^{-1}$  (Baseline Nile runoff:  $5358 \text{ m}^3 \text{ s}^{-1}$ ). The IniGlac simulation incorporates the signal of the climatic changes associated with the last glacial-interglacial transition period, in that it was initialized from the Baseline experiment by imposing the temperature ( $-3^\circ\text{C}$ ) and salty ( $+1.5 \text{ psu}$ ) change between the LGM and the early Holocene, with the values adapted after Mikolajewicz (2011).

To investigate the role of nutrients in establishing and holding a deep water oxygen depletion, we introduced a set of riverine nutrient input scenarios. We implemented the default riverine nutrient load to be proportional to the river runoff (Table 2.2). Consequently, the Nile experiment, with its enhanced runoff, receives a larger riverine nutrient load. For phosphate, this corresponds to an additional flux of  $34.7 \text{ mol s}^{-1}$  by the Nile river, comparable to nearly a doubling of the default nutrient load for the entire eastern Mediterranean Sea. In addition, we introduced two highly eutrophic riverine nutrient regimes, the 3xNutri and IniGlac+3xNutri, for which we tripled the default riverine nutrient load of each river draining into the Mediterranean Sea. The 3xNutri experiment is coupled with the Baseline circulation field, thus, it resembles the sapropel forming theory of an enhanced biological productivity under a well-ventilated ocean circulation. The IniGlac+3xNutri resembles the hypothesis of a combined stagnating deep water circulation and enhanced biological productivity.

The Baseline simulation was initialized with the same homogeneous low density water conditions as the pre-industrial CTRL simulation (Table 2.3). After an ocean-only

Table 4.1: Summary of the model experiments. See Table 2.2 for default HIM riverine nutrient load. 1600 years of spinup are not included in the given simulation period of the Baseline experiment.

| Experiment      | Imposed physical perturbation  | Imposed riverine nutrients | Simulation period [years] |
|-----------------|--------------------------------|----------------------------|---------------------------|
| Baseline        |                                | default HIM                | 3400                      |
| 3xNutri         |                                | 3 x default HIM            | 1400                      |
| Nile            | runoff Nile $+9000 m^3 s^{-1}$ | default HIM + extra Nile   | 2400                      |
| IniGlac         | $-3^\circ C$ , $+1.5$ psu      | default HIM runoff         | 3400                      |
| IniGlac+3xNutri | $-3^\circ C$ , $+1.5$ psu      | 3 x default HIM            | 3400                      |

spinup of 500 years we coupled the physical ocean model to the biogeochemical model, which was also initialized with homogeneous water and sediment conditions (Table 2.3). The coupled ocean biogeochemical model was run until the year 1500 for the Baseline simulation. At the year 1501, we increased the vertical resolution of the Baseline experiment from 29 to 46 vertical layers (see Appendix A.1 for details), and integrated it for an additional 100 years. This entire 1600 years of simulation served as a spinup for the early Holocene simulations. At the end of the spinup simulation, we initialized all perturbation experiments from the Baseline simulation, and integrated them for another 1400 years for the 3xNutri, 2400 years for the Nile, and 3400 years for the Baseline, IniGlac and IniGlac+3xNutri experiments.

## 4.3 Results

### 4.3.1 General circulation

The general circulation is the driving force for the redistribution of nutrients and oxygen within the water column. In this section, we focus on the strength of the circulation under the Baseline, Nile and IniGlac scenarios, with the aim to understand the large-scale processes which determine the resulting biogeochemical cycles and the development of a deep water oxygen deficiency.

This section is organized as follows: In the first part, we analyze the upper ocean circulation, and in the second part, we focus on the intermediate water mass characteristics and formation rate. Both the upper and intermediate circulation mainly determine the nutrient cycling in the euphotic zone, and consequently regulate spatial and temporal patterns of the biological productivity. In the third part, we focus on the deep water circulation and the strength of the deep water formation, which determines the deep water ventilation, and thus, it is the most crucial process for the development of the deep water anoxia during S1 deposition.

The analyzes of the CTRL simulation showed unrealistic low deep water formation

rate in the Gulf of Lions in the western Mediterranean, resulting from the coarse resolution atmospheric forcing (Chapter 3). Therefore, we doubt the validity of the model for the western Mediterranean. Since the deep western circulation is unimportant for the eastern Mediterranean circulation features due to the effective separation of the deep basins by the shallow Strait of Sicily, and because the sapropel occurred in the eastern basin only, we constrain our analysis to the eastern Mediterranean Sea.

#### 4.3.1.1 Upper ocean circulation

The main upper ocean circulation features in the early Holocene simulations (Fig. 4.1) are rather similar to the pre-industrial CTRL simulation (section 3.3.1.1). Compared to the CTRL simulation, the Baseline experiment shows an intensification of the Atlantic-Ionian Stream, the Mid-Mediterranean Jet, the Rhodes gyre, the Mersa-Matruh gyre, and the Asia-Minor current. The Atlantic-Ionian Stream and the Mid-Mediterranean Jet show a small displacement towards the south compared to the CTRL. The Nile simulation shows the same features as the Baseline simulation, however, the strength of the circulation, in particular of the Atlantic-Ionian Stream and the Mid-Mediterranean Jet, is reduced, while the Rhodes gyre and the Asia Minor current show an intensification. In the IniGlac simulation, the strength of the circulation is entirely reduced compared to the Baseline simulation. In particular, the strength of the Rhodes gyre and the Mersa-Matruh gyre in the entire upper 235 m shows the strongest difference to the Baseline simulation, while below all circulation features show an intensification compared to the Baseline simulation (Fig. A.6, A.7, A.8, A.9).

The strengthening of the near-surface currents in the Baseline simulation with respect to the CTRL simulation might be explained by the enhanced wind during the early Holocene. Since all early Holocene simulations are forced with the same atmospheric dataset, the changes in the strength of the upper ocean circulation features between the simulations point towards effects of the vertical stratification.

#### 4.3.1.2 Intermediate water and mixed layer

The locations of water formation in the early Holocene circulation scenarios remain rather similar to the locations in the pre-industrial CTRL simulation, with intermediate water formation in the Levantine, Aegean and northern Ionian Sea, and deep water formation in the Adriatic Sea.

The enhanced seasonal cycle with cooler winters and warmer summers leads to a net cooling of the early Holocene simulations with respect to the pre-industrial CTRL simulation. The winter cooling penetrates deeper into the ocean via winter mixing, while the summer warming is limited to the upper  $\sim 30$  m due to the strong summer stratification (Adloff et al. 2011). In addition, the lower sea level of the early Holocene leads to an accumulation of salt in the global ocean as well as the Mediterranean. Due to the

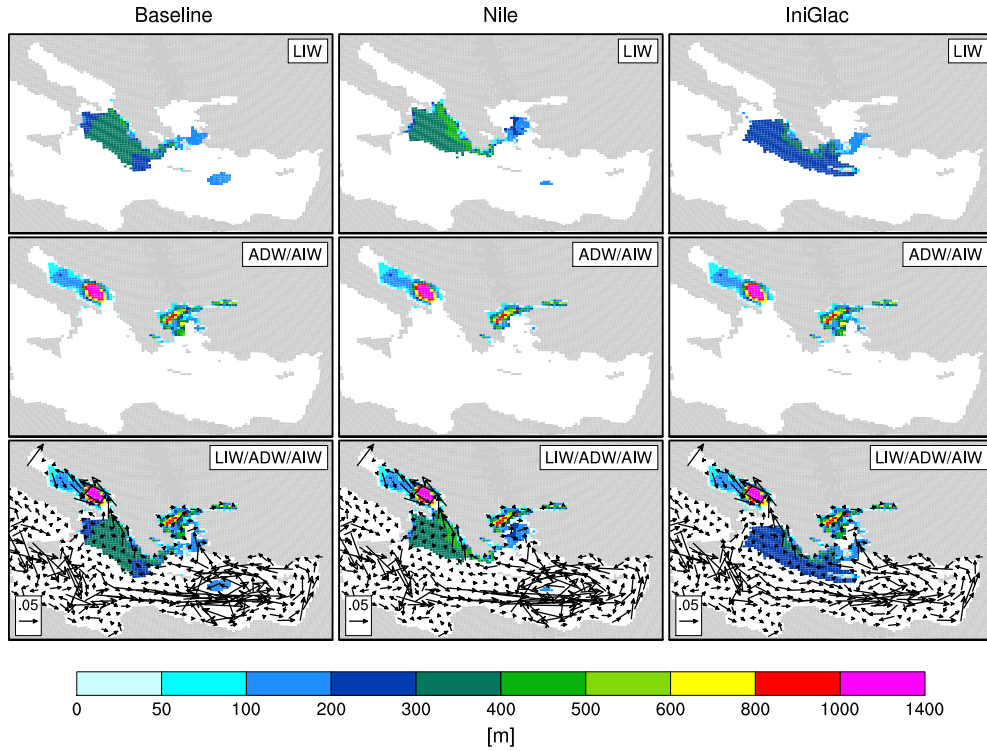


Figure 4.1: Mixed layer depth in February/March derived as detailed in the text for the LIW including the IIW (upper panel), the ADW and AIW (middle panel), and the combined mixed layer depth for all water masses (lower panel). Vectors represent both the direction and speed [ $m s^{-1}$ ] of the annual mean circulation at 25m depth. Results are averaged over the last 100 years of simulation.

lower temperature and the higher salinity the water in the early Holocene simulations is considerably denser than in the pre-industrial CTRL simulation. The shallowing of the thermocline, and the enhanced Nile runoff and corresponding relatively higher freshening of the Levantine compared to the CTRL simulation, leads to a shallowing of the pycnocline, in particular in the Levantine Sea in all early Holocene circulation scenarios (Fig. 4.3).

The mixed layer depth pattern of the early Holocene simulations was assessed by the same methods as was applied for the CTRL simulation (section 3.3.1.2). Figure 4.2 shows the  $\sigma_{\theta}$  versus Brunt-Väisälä Frequency for the individual experiments in the Levantine and Ionian Sea, and the subsequently determined intermediate and deep isopycnal layers.

As a consequence of the shallower pycnocline, intermediate water formation in the Rhodes gyre is reduced in all early Holocene simulations compared to the CTRL simu-

lation (compare Fig. 3.1 and Fig. 4.1). Similarly to the CTRL simulation, considerable mixing occurs in the northeastern Ionian Sea and central Aegean Sea within the intermediate layer of all early Holocene experiments. In all experiments, mixing in the Ionian Sea occurs over a much larger area compared to the CTRL, essentially affecting the entire northern Ionian Sea, and is strongest developed in the Nile experiment. In contrast, the Nile experiment shows slightly reduced mixing in the Rhodes gyre compared to the Baseline. The reduced LIW formation in the Nile experiment results from the strong freshening through the increased Nile river runoff. However, the intensified Rhodes gyre compensates much of this freshening effect, since it preconditions mixing more efficiently, through the doming of the isopycnals, which brings the weakly stratified water in the center of the gyre close to the surface (Marshall and Schott 1999). In contrast, the IniGlac experiment shows mixing all around the Island of Crete. The mixing in the Rhodes gyre completely ceases in the IniGlac experiment, which is attributed to the weakened strength of the cyclonic Rhodes gyre.

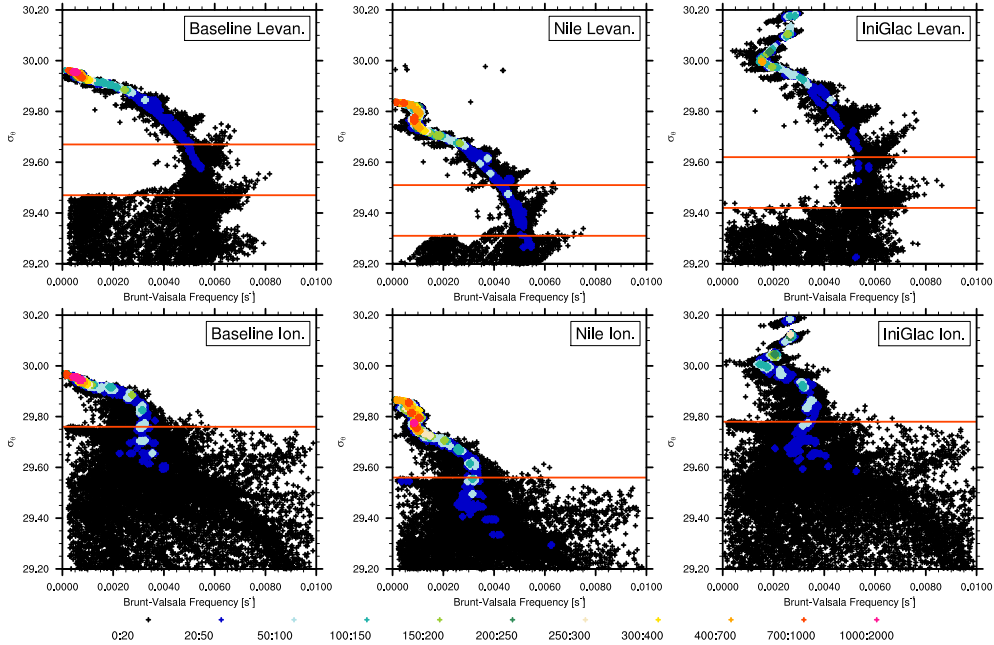


Figure 4.2: Brunt-Väisälä Frequency versus  $\sigma_\theta$  averaged in February/March over the last 100 years of simulation. First column shows Baseline, second column shows Nile, and third column shows IniGlac experiment. Upper row shows values from Levantine Sea. Lower row shows values from Ionian Sea. The red lines indicate the determined intermediate and deep isopycnals. Colors indicate the density of the scatter, determined by counting the number of pairs in squared subsections of 100 equally spaced intervals in the range between 0 to  $0.1 s^{-1}$  Brunt-Väisälä Frequency and 29.2 to  $30.2 \sigma_\theta$ . See text for more details on the isopycnal determination. Note that only a subsection of the total isopycnal range is plotted.

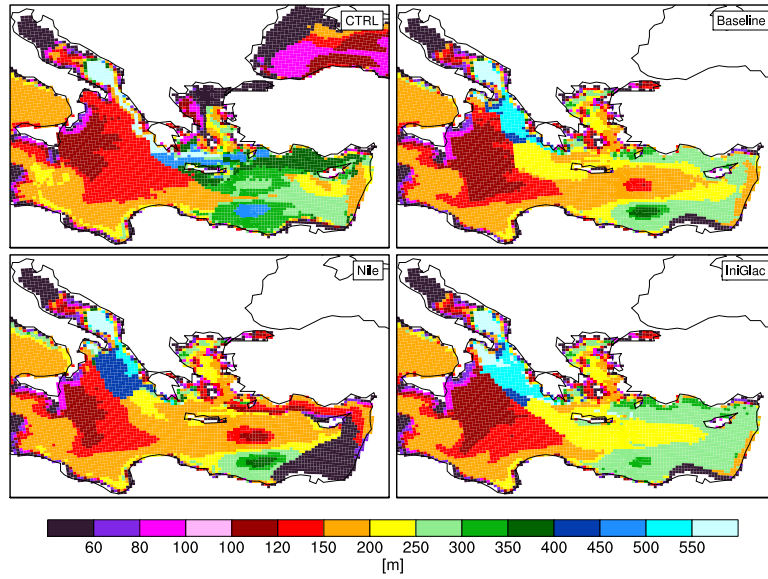


Figure 4.3: Depth of pycnocline in February/March derived by the maximum of the Brunt-Väisälä Frequency averaged over the last 100 years of simulation.

Highly dense water forms in the Adriatic and northern Aegean Sea. Aegean dense water formation, predominantly occurring in the central Aegean in the pre-industrial CTRL simulation, is shifted towards the northern Aegean Sea in the early Holocene simulations. The missing relatively fresh inflow from the Black Sea leads to an accumulation of high salinities in the northern Aegean in all early Holocene simulations, which favors the formation of highly dense water during winter cooling. However, intensive horizontal and vertical mixing leads to a reduction of  $\sigma_{\Theta}$  while the water flows over the rough topography of the Aegean Sea. Therefore, likewise to the CTRL simulation, there is no EMT event, with EMDW formation in the Aegean Sea, simulated in the early Holocene model experiments. This strong density loss along the dense Aegean water flowpath might be a model artifact due to its coarse horizontal and vertical resolution, while in reality water flows through narrow channels and is less subjected to mixing. In the Adriatic Sea, the combination of winter surface cooling, wind stirring, entrainment of salt from intermediate layers, and the presence of the permanent cyclonic gyre strongly precondition the open ocean deep water convection and formation of ADW. The newly formed ADW flows out through the Strait of Otranto along the western boundary into the Ionian Sea, and if dense enough it sinks to depth and forms EMDW.

The main characteristics of the intermediate water of the early Holocene simulations are summarized in Table 4.2 and illustrated in Figure 4.4. For a better comparison of the water properties in-between the experiments in the horizontal plain, we illustrate

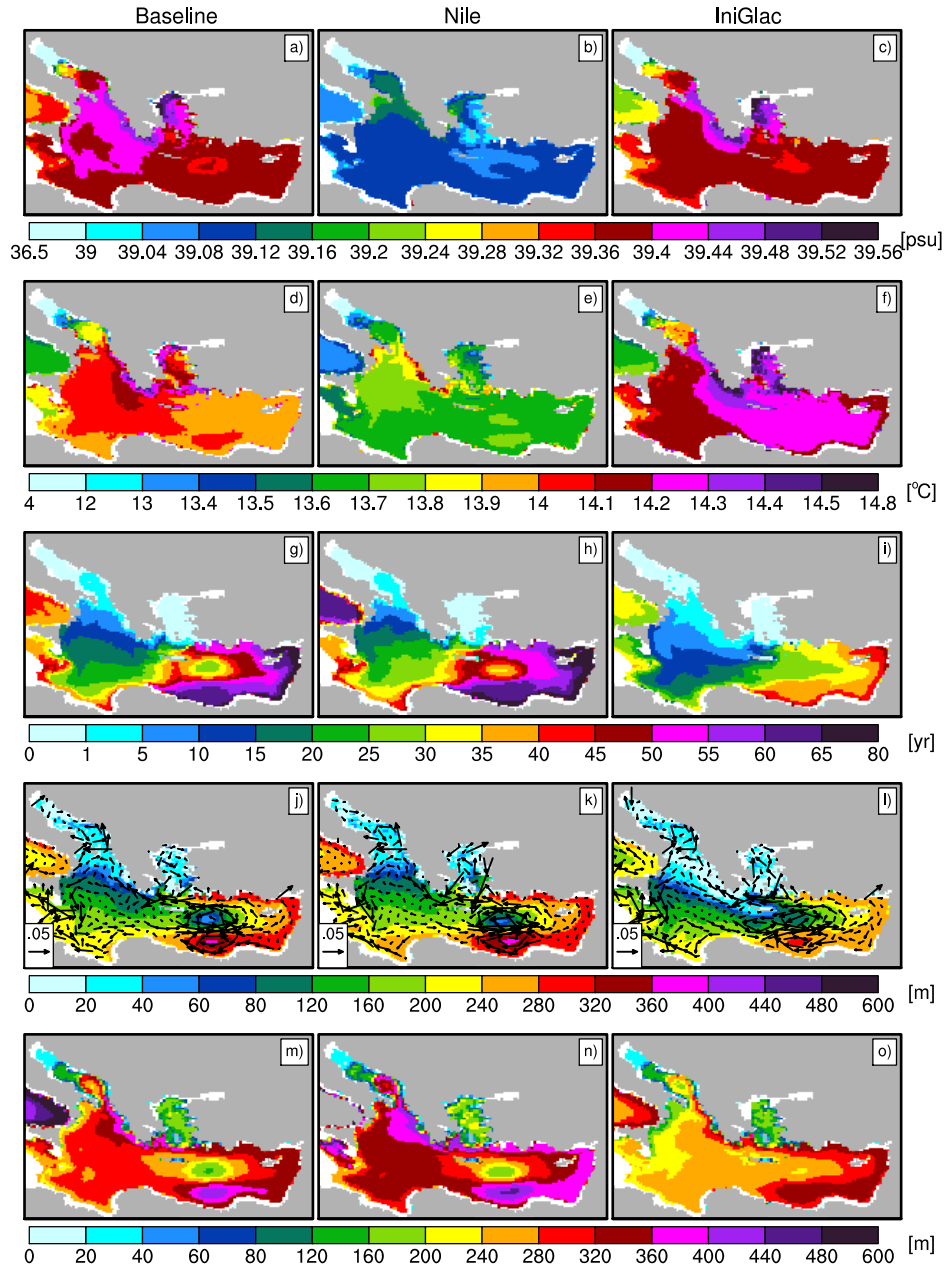


Figure 4.4: Properties of the intermediate water masses averaged in February/March for the last 100 years of simulation of each experiment. a) to c) salinity; d) to f) temperature; g) to i) water age; j) to l) upper depth of intermediate water layer; m) to o) lower depth of intermediate water layer. Isopycnals for Baseline:  $\sigma_{\Theta}$  29.47 to 29.67; Nile:  $\sigma_{\Theta}$  29.31 to 29.51; IniGlac:  $\sigma_{\Theta}$  29.42 to 29.62; The vectors in j), k), l) represent both the direction and speed [ $m s^{-1}$ ] of the circulation averaged over the depth of the isopycnal layer.

Table 4.2: Physical and biogeochemical properties of the major water masses. 100-year mean values of indicated properties averaged over the Levantine Sea for LIW, the Ionian Sea for IIW, the Aegean Sea excluding the Cretan Sea for AIW, the Adriatic Sea with water depth  $\geq 250$  m for ADW, the Ionian Sea with water depth  $\geq 1800$  m for EMDW. Water formation rates calculated as 100-year mean of annual maximum of water formed in the corresponding areas for LIW, IIW, AIW, ADW, and transport below 1500 m across 38.82°N in the Ionian Sea for EMDW. Phosphate, Nitrate and oxygen concentrations in  $mmol\ m^{-3}$ . Abbreviation bot.: bottom.

| Properties            | LIW      |         |       |         |                 | IIW      |         |       |         |                 |
|-----------------------|----------|---------|-------|---------|-----------------|----------|---------|-------|---------|-----------------|
|                       | Baseline | 3xNutri | Nile  | IniGlac | IniGlac+3xNutri | Baseline | 3xNutri | Nile  | IniGlac | IniGlac+3xNutri |
| Upper $\sigma_\theta$ | 29.47    |         | 29.31 | 29.42   |                 | 29.47    |         | 29.31 | 29.42   |                 |
| Lower $\sigma_\theta$ | 29.67    |         | 29.51 | 29.62   |                 | 29.67    |         | 29.51 | 29.62   |                 |
| Depth Min [m]         | 241      |         | 251   | 240     |                 | 148      |         | 162   | 136     |                 |
| Depth Max [m]         | 310      |         | 336   | 300     |                 | 287      |         | 329   | 241     |                 |
| Formation [Sv]        | 0.15     |         | 0.10  | 0.16    |                 | 1.18     |         | 1.39  | 0.84    |                 |
| T [°C]                | 14.0     |         | 13.7  | 14.2    |                 | 14.0     |         | 13.7  | 14.2    |                 |
| S [psu]               | 39.4     |         | 39.0  | 39.4    |                 | 39.4     |         | 39.1  | 39.4    |                 |
| Phosphate             | 0.15     | 0.23    | 0.19  | 0.13    | 0.20            | 0.11     | 0.16    | 0.14  | 0.10    | 0.14            |
| Nitrate               | 2.92     | 4.92    | 3.50  | 2.65    | 4.49            | 2.28     | 3.76    | 2.57  | 2.08    | 3.42            |
| Oxygen                | 228      | 217     | 223   | 230     | 219             | 234      | 228     | 232   | 235     | 229             |
| AIW                   |          |         |       |         |                 |          |         |       |         |                 |
| Properties            | Baseline | 3xNutri | Nile  | IniGlac | IniGlac+3xNutri | Baseline | 3xNutri | Nile  | IniGlac | IniGlac+3xNutri |
| Upper $\sigma_\theta$ | 29.76    |         | 29.56 | 29.78   |                 | 29.76    |         | 29.56 | 29.78   |                 |
| Depth Min [m]         | 38       |         | 58    | 38      |                 | 94       |         | 106   | 101     |                 |
| Depth Max [m]         | 276      |         | 275   | 279     |                 | 730      |         | 725   | 728     |                 |
| Formation [Sv]        | 0.60     |         | 0.42  | 0.60    |                 | 0.74     |         | 0.71  | 0.73    |                 |
| T [°C]                | 12.7     |         | 12.5  | 12.8    |                 | 12.8     |         | 12.7  | 12.7    |                 |
| S [psu]               | 39.6     |         | 39.2  | 39.6    |                 | 39.4     |         | 39.1  | 39.4    |                 |
| Phosphate             | 0.04     | 0.06    | 0.04  | 0.03    | 0.05            | 0.09     | 0.14    | 0.09  | 0.08    | 0.14            |
| Nitrate               | 0.97     | 1.67    | 0.89  | 0.93    | 1.60            | 2.26     | 4.44    | 2.25  | 2.25    | 4.48            |
| Oxygen                | 236      | 237     | 236   | 235     | 236             | 241      | 239     | 241   | 241     | 236             |
| EMDW                  |          |         |       |         |                 |          |         |       |         |                 |
| Properties            | Baseline | 3xNutri | Nile  | IniGlac | IniGlac+3xNutri |          |         |       |         |                 |
| Upper $\sigma_\theta$ | 29.76    |         | 29.56 | 29.78   |                 |          |         |       |         |                 |
| Depth Min [m]         | 388      |         | 395   | 397     |                 |          |         |       |         |                 |
| Depth Max [m]         | bot.     |         | bot.  | bot.    |                 |          |         |       |         |                 |
| Formation [Sv]        | 0.12     |         | 0.08  | 0.02    |                 |          |         |       |         |                 |
| T [°C]                | 12.4     |         | 12.4  | 11.4    |                 |          |         |       |         |                 |
| S [psu]               | 39.4     |         | 39.2  | 40.0    |                 |          |         |       |         |                 |
| Phosphate             | 0.32     | 0.43    | 0.62  | 0.74    | 1.24            |          |         |       |         |                 |
| Nitrate               | 5.97     | 8.89    | 10.73 | 12.71   | 21.12           |          |         |       |         |                 |
| Oxygen                | 208      | 193     | 157   | 137     | 57              |          |         |       |         |                 |

the water properties in 25 m (Fig. A.6), 113 m (Fig. A.7), 197 m (Fig. A.8) and 445 m (Fig. A.9).

The pathway of the intermediate water in the early Holocene simulations is similar to the CTRL (section 3.3.1.2), with a main westward flow (Fig. 4.4). While the Baseline and Nile simulation show a rather similar intermediate circulation, the IniGlac experiment shows a less developed Rhodes gyre partly separated into two gyres, as well as a weakened anti-cyclonic Mersa-Mathru gyre. With increasing depth these circulation features increase in strength compared to the Baseline simulation. Moreover, the IniGlac simulation shows a displacement of the northeastern Ionian flow further away from the coast, which transports the intermediate water more efficiently towards the Strait of Sicily and less towards the Adriatic compared to the Baseline simulation.

As a consequence of the significantly enhanced Nile runoff in the Nile experiment, the entire upper to intermediate water column is on average  $\sim 0.3$  psu fresher than the Baseline simulation. The intermediate temperature of the Nile experiment is cooler in the Rhodes gyre, because the stronger cyclonic circulation brings up the cool deep water more efficiently than the Baseline simulation. This leads to a cooling of  $\sim 0.2^\circ\text{C}$  at a depth below 130 m of the intermediate water spreading through the western Cretan Arc into the Ionian basin. In contrast, the weakened Rhodes gyre in the IniGlac accompanied by a strongly reduced doming of the isopycnals results in a warmer intermediate water mass. In all experiments, the entrainment of the relatively warm and salty intermediate water, formed mainly in the Aegean Sea, into the northern Ionian preconditions intensive mixing during winter.

In the Nile and IniGlac simulation, the highly stratified deep water column prevents the ADW sinking into the deep Ionian Sea. Instead, the cool water of Adriatic origin spreads into the Ionian Sea at intermediate depth.

Along the southern Italian coast and Sicily an upwelling of deep water is visible in all experiments (Fig. A.7 (g, h, i)). This feature differs considerable from the mixing along the eastern Ionian coast, since it shows the upwelling of deep old water. The predominantly westerly winds in this region support coastal upwelling through Ekman suction. In section 4.3.3, we show that this feature leads to especially high biological production, since it brings nutrient-rich deep water into the euphotic zone.

### 4.3.1.3 Deep water

#### 4.3.1.3.1 The strength of the deep water circulation

One way to assess the strength of the stagnation is to compute the Brunt-Väisälä Frequency (Eq. 3.1), which is a measure of the stability of the water column, reaching a maximum at the pycnocline.

Figure 4.5 shows a Hovmöller diagrams of the Brunt-Väisälä Frequency depth profile averaged over the northern Ionian Sea over time. All experiments show the maximum between 20 m and 30 m, which is largely determined by the seasonal thermocline. Even the strong surface salinity reduction in the Nile experiment shows a rather small imprint on the high stability of this layer. A secondary maximum of the Brunt-Väisälä Frequency marks the interface between the relatively salty and warm intermediate water and the cooler and fresher deep water at approximately 500 m. The stagnation scenarios show a third maximum of the Brunt-Väisälä Frequency, which marks the deep water stagnation interface. This deep high stability layer, initially at around 1000 m depth, deepens and weakens with time. Mixing erodes the stability of this layer. In the Nile experiment, the deep stability layer is repeatedly penetrated by the outflow of dense water from the Adriatic Sea. Similar events, however, with a much weaker magnitude and penetration depth, are simulated in the IniGlac experiment. Overall, the IniGlac shows a much more pronounced and over time less weakened deep stability layer compared to the Nile experiment.

In order to understand the stability of a stagnating deep water circulation in space and time, we analyze the EMDW formation within the various circulation scenarios. In particular, we focus on the process of EMDW formation and its formation rate and penetration depth in the Ionian Sea, which determine the stability of the stagnating deep circulation. We compute the meridional overturning stream function across the Adriatic and the northern Ionian Sea (Fig. 4.6). The meridional stream function is a measure of the transport of water at different levels (Eq. 3.2) and isopycnals (Eq. 3.3), and thus, it can be used to assess the meridional location and rate of deep water formation.

In the Baseline simulation, the densest water is formed in the northern and middle Adriatic Sea (NAdDW). The NAdDW flows towards the southern Adriatic, where open ocean convection processes initiate ADW formation. The ADW is transported through the Strait of Otranto into the Ionian Sea. Along the ADW pathway over the sill of Otranto, intensive mixing causes the entrainment of ambient water, and results in a strong density reduction. In the Ionian Sea, the dense water finally spreads into a mean depth of around 1000 m (Fig. 4.6). As in the CTRL simulation, EMDW formation, which implies ADW sinking into the deep Ionian Sea, only occurs during years with especially cool winters within the repeating 100-year cycle of atmospheric forcing. The

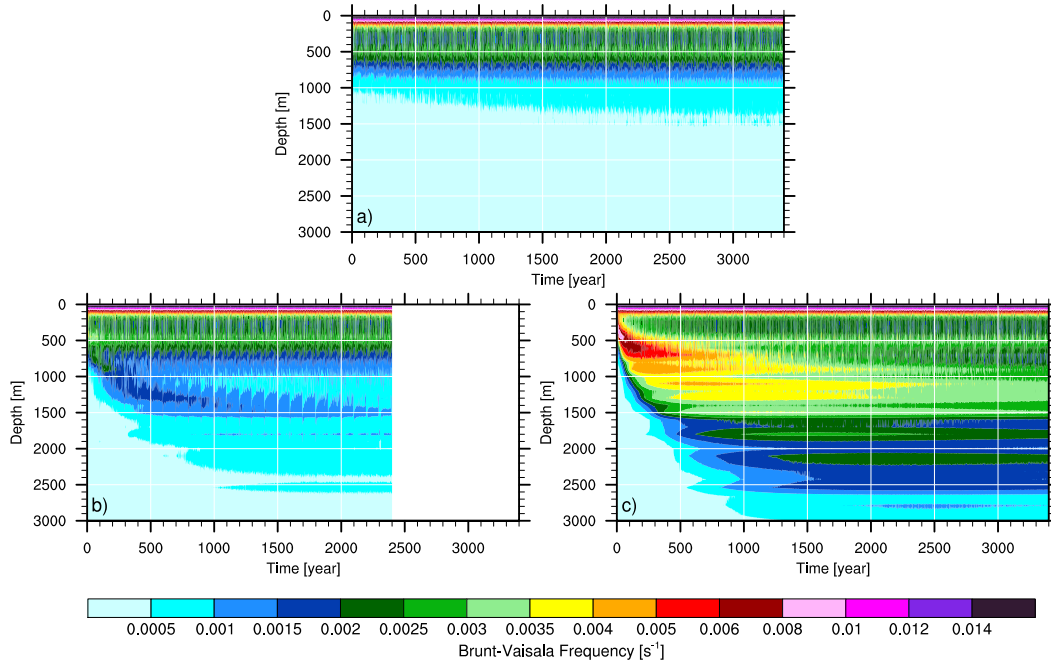


Figure 4.5: Hovmöller diagram of the annual mean Brunt-Väisälä Frequency (Eq. 3.1) averaged over the northern Ionian Sea for the a) Baseline, b) Nile and c) IniGlac experiments. Note the nonlinear color scale.

coolest winter year of the 100-year atmospheric forcing cycle is illustrated in Figure 4.6. During this cold year, the density of the maximum transport cell increases by  $\sim 0.15 \sigma_{\Theta}$  and extends further southward due to a considerable contribution of dense water formation from the northern Ionian Sea. In addition, there is a secondary maximum transport cell with  $\sigma_{\Theta} \geq 29.92$  at around  $39^{\circ}\text{N}$ , resulting from the entrainment of ambient water, which on the one hand, decreases the density and on the other hand, increases the transport. This deep water transport cell follows the bottom topography down to the deep Ionian Sea along the densest isopycnals. This shows that the deep eastern Mediterranean is rapidly ventilated during single EMDW formation events, while on a centennial timescale EMDW formation events are rare.

In the stagnation experiments, the densest water is also formed in the northern and middle Adriatic Sea. However, in the Nile experiment the ADW shows a much lower density than the Baseline simulation, which can be directly attributed to the freshening through the enhanced Nile runoff. This density reduction limits the penetration depth of the ADW outflow south of the Strait of Otranto to  $\sim 800$  m. During the cold winter year, the Nile experiment shows some transport at a maximum depth of  $\sim 1700$  m. This shows that even a strong temperature induced density rise during a cold winter is not

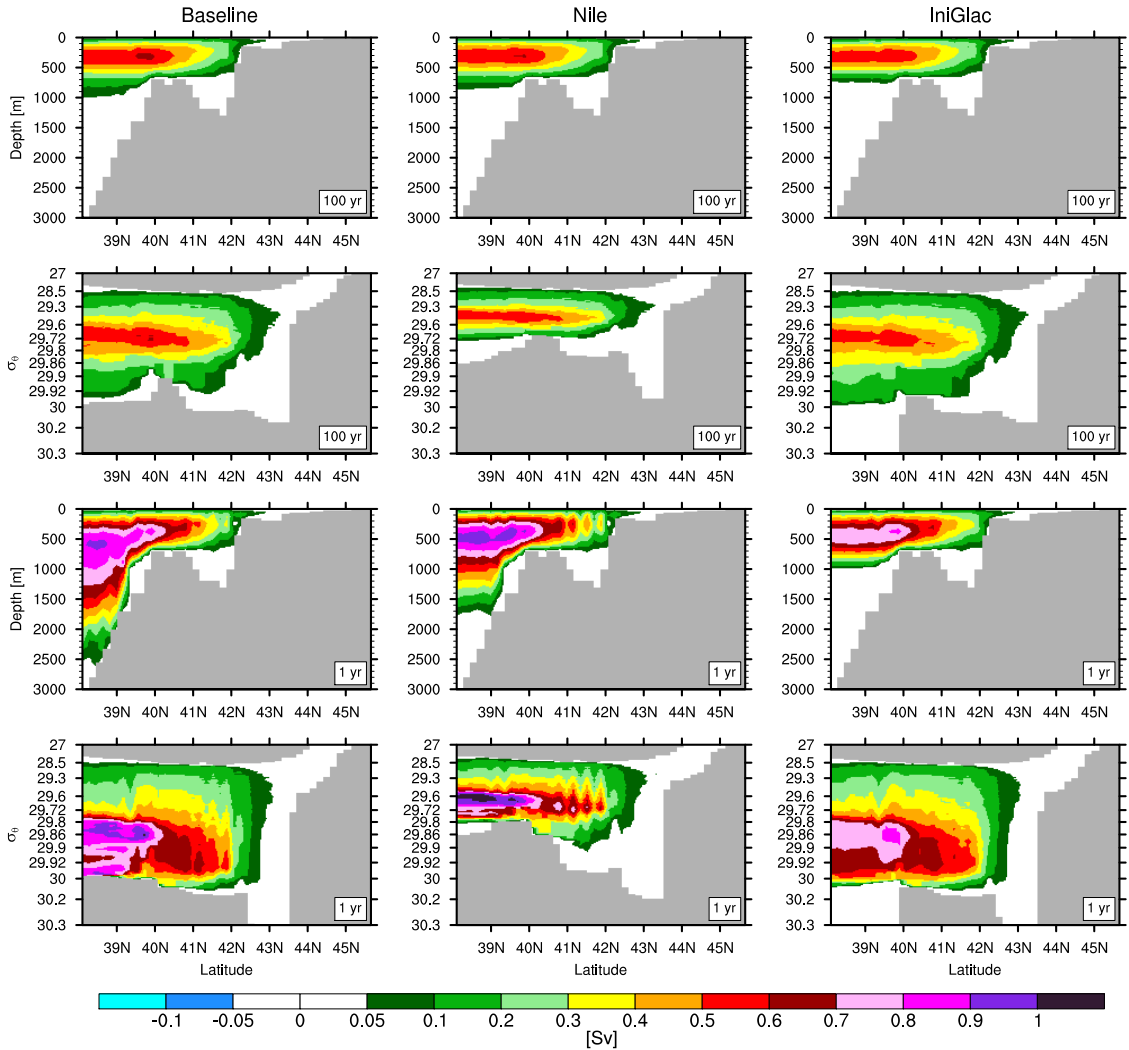


Figure 4.6: Meridional overturning stream function integrated across the Adriatic and northern Ionian Sea for the Baseline (first column), Nile (second column) and IniGlac (third column) simulation. The first and third row show the stream function calculated on z-levels (Eq. 3.2), the second and fourth row on isopycnal levels (Eq. 3.3). The first and second row show calculations based on 100-year mean velocity fields of the years 3301–3400 for the Baseline, 2301–2400 for the Nile, and 3301–3400 for the IniGlac experiments, the third and fourth row show calculations based on annual mean velocity fields of the last very cold winter year (atmospheric forcing year 96) of the corresponding experiments. The grey colors represent the deepest topography or non-occurring densities. Note the nonlinear spacing of the isopycnals and of the color bar.

### 4.3 RESULTS

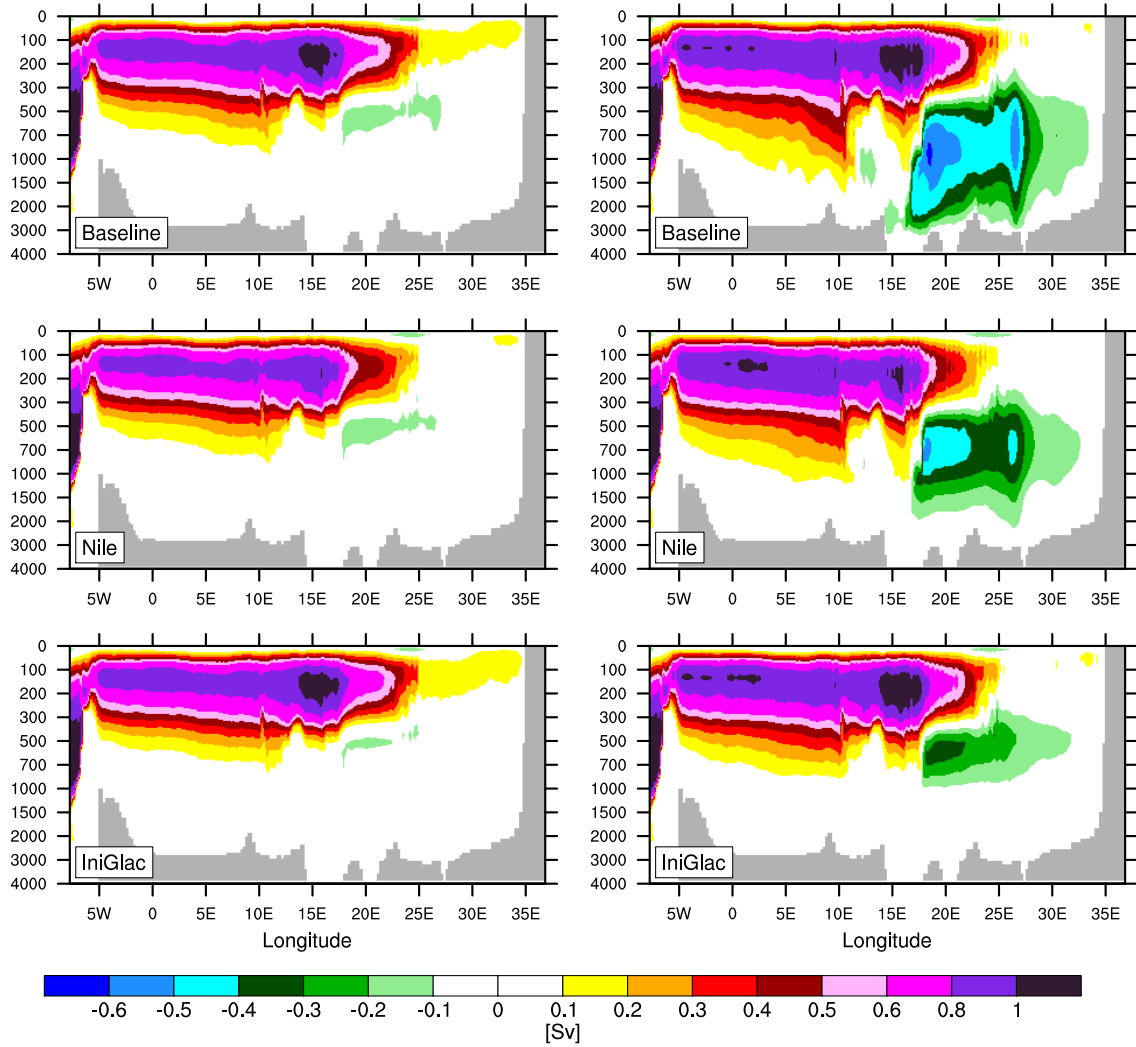


Figure 4.7: Zonal overturning stream function (Eq. 3.4) integrated across the Mediterranean Sea. Calculations are based on annual mean velocity fields (left column) of the years 3301–3400 for the Baseline, 2301–2400 for the Nile , and 3301–3400 for the IniGlac experiments, and annual mean velocity fields of the last very cold winter year (atmospheric forcing year 96) of the corresponding experiments (right column). The grey colors represents the deepest topography. Note the nonlinear spacing of the depth levels and of the color bar.

strong enough to overcome the high density reduction induced by the freshening, and therefore, there is no EMDW formation reaching the bottom of the Ionian Sea.

In the IniGlac experiment, the ADW shows similar densities and formation rates as in the Baseline simulation. Since all of the boundary conditions (riverine freshwater runoff, Atlantic boundary hydrography, and atmospheric forcing) of the IniGlac and Baseline experiment are kept identical, the upper ocean of the IniGlac experiment has equilibrated to a similar state as the Baseline simulation concerning its density properties. In contrast to the Baseline simulation, the density in the deep Ionian Sea is much higher due to the high density initialization. Therefore, the ADW outflow is not dense enough to sink to the deep Ionian Sea to form EMDW, but spreads to a maximum depth of around 1000 m during cold winters.

To gain a better understanding of the general eastern Mediterranean deep water circulation, we compute the zonal overturning stream (Eq. 3.4), integrated over the entire Mediterranean Sea (Fig. 4.7). In the Baseline simulation, the zonal overturning circulation is characterized by two main cells; The upper anti-estuarine circulation cell with water flowing into the Mediterranean Sea through the Strait of Gibraltar and further into the eastern Mediterranean and the return flow at intermediate depth. The anti-clockwise cell illustrates the deep circulation, and is only seen in the eastern Mediterranean. While on the 100-year average the deep circulation cell of the Baseline simulation is only weakly established at  $\sim 400\text{--}800$  m depth, during the cold winters with strong EMDW formation the cell rapidly expands down to the deepest layers, with a maximum transport of up to 0.6 Sv.

Similarly, in the Nile simulation, the zonal overturning stream function is characterized by an upper clockwise and a deeper anti-clockwise circulation cell. The horizontal extent of the upper anti-estuarine cell is limited to the west of Crete ( $25^\circ\text{E}$ ) due to the reduced LIW formation in the Levantine basin induced by the Nile riverine freshening. At depth, the 100-year mean anti-clockwise circulation cell is similarly developed as in the Baseline simulation. Since strong EMDW formation events during cold winters only reach a depth of  $\sim 1700$  m in the Ionian Sea, the newly formed water pushes the water in this depth towards the Levantine Sea, while the deeper eastern Mediterranean remains unaffected.

In the IniGlac experiment, the upper anti-estuarine cell is similarly developed as in the Baseline simulation, indicating that the main features of the upper ocean general circulation are rather similar. At depth, the circulation cells of both the 100-year mean, and even more pronounced the strong EMDW formation year, show a weaker strength ( $\sim 0.4$  Sv) and shallower depth ( $\sim 1000$  m) than the deep cell of the Baseline simulation.

The time evolution of the Brunt-Väisälä Frequency shows that the stability of the deep layers in the stagnation experiments is continuously decreased and its vertical position deepened over time (Fig. 4.5). Therefore, we should expect an increase of

the penetration depth of the dense water transport out of the Adriatic Sea over time in the stagnation experiments. To quantify this EMDW deepening trend, we compute the overturning stream function throughout the entire simulation period, and illustrate a Hovmöller diagram of the transport profile at 38.8°N between Italy and Greece in Figure 4.8 and Figure 4.9. Due to its relatively low stability at depth, the Baseline simulation shows repeating events with high transport rates down to the bottom of the Ionian Sea (Fig. 4.8) at high  $\sigma_\theta$ -levels (Fig. 4.9). The frequency of these events is determined by the occurrence of cold winters in the 100-year repeating atmospheric forcing data. Compared to the CTRL simulation, the frequency of strong EMDW formation events is similar (compare Fig. 3.7 and Figures 4.8, 4.9). While initially the strength of the deep water formation is very high in the Baseline simulation, over the entire time of 3400 years of simulation, a slight weakening of the penetration depth of the EMDW formation events is modeled. This drift results from the decrease of the implicit diffusion of the advection-scheme in this high vertical resolution setup (section A.1). Initially, the dense water rapidly fills the deep eastern Mediterranean Sea and pushes the older deeper water towards the surface. However, with a decreased implicit diffusion, the deep layers slowly become denser, which reduces the penetration depth of the EMDW events. This indicates that on a centennial timescale the Baseline simulation is in equilibrium, while on a millennial timescale the Baseline simulation shows a weak drift towards a less ventilated deep water mass, which is determined by the strength of the vertical diffusion.

Both, the Nile and the IniGlac stagnation experiments show a weakening or complete shut down of the deep transport, while at intermediate depth the strength of the transport is similar to the Baseline simulation. In the Nile experiment, the riverine freshening reduces the density of the deep water formed in the Adriatic, and hence, limits its potential to sink to the deep Ionian Sea. Cross-isopycnal mixing leads to a freshening and thus lightening of the deep layers over time (Fig. 4.9). Consequently, the density gradient between the upper and deep water is progressively eroded (Fig. 4.5), which leads to an increased penetration depth of the dense outflow from the Adriatic Sea over time (Fig. 4.8). This shows that the timescale of the increasing penetration depth of the EMDW formation events (Fig. 4.8) is set by the timescale of the density reduction of the deep layers by cross-isopycnal mixing (Fig. 4.9).

In the IniGlac experiment, the penetration depth of the deep water formation events increases over time, however, with a smaller rate than in the Nile experiment (Fig. 4.8). Likewise to the Nile experiment, the increased penetration depth of the EMDW events in the IniGlac can be attributed to the erosion of the density gradient over time. However, the imposed perturbation of the IniGlac experiment is stronger, and hence, the vertical density gradient stronger than the density gradient created by the freshening in the Nile experiment. Therefore, the IniGlac experiment shows a more stable and persisting stratification over time than the Nile simulation, with no EMDW for-

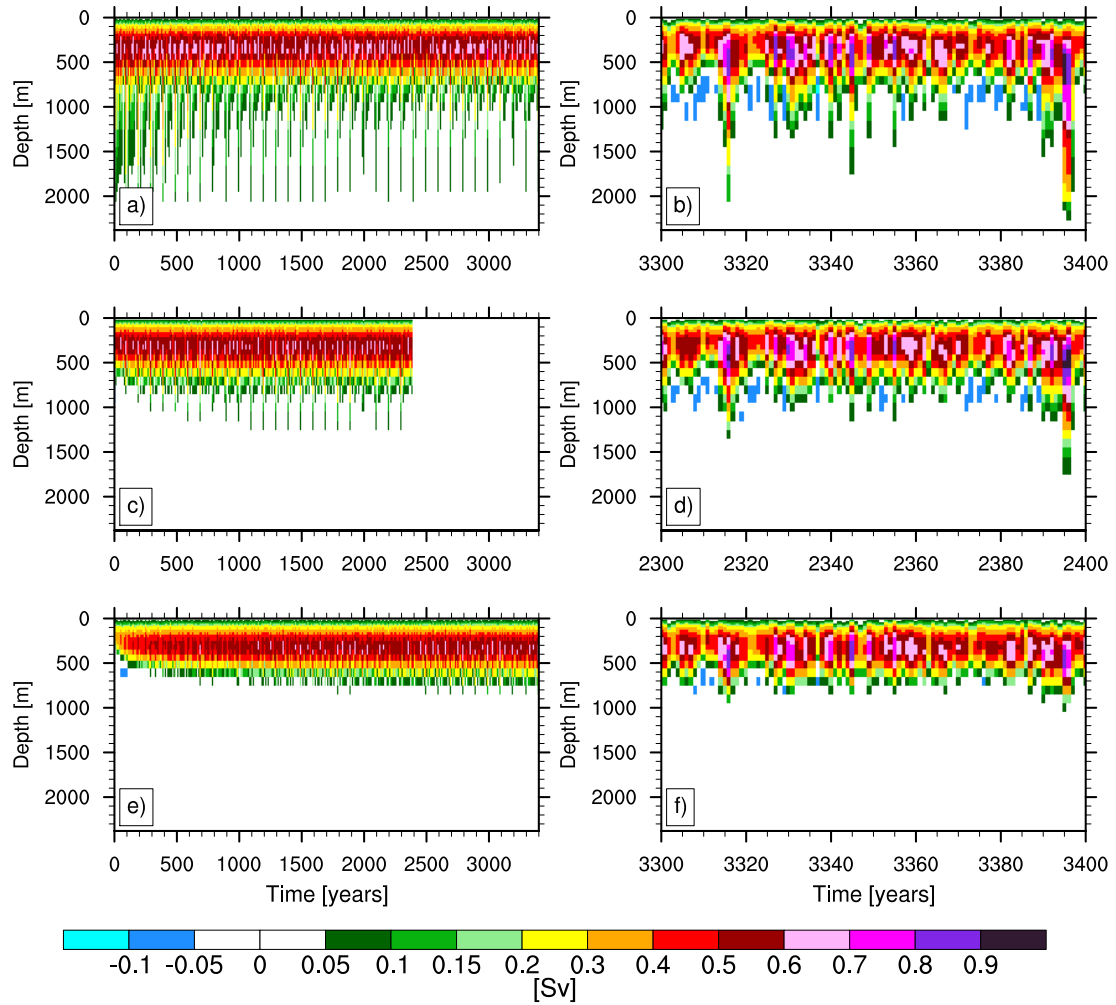


Figure 4.8: Hovmöller diagram of the annual mean water transport rate calculated on z-levels (Eq. 3.2) in the northern Ionian Sea at 38.82 °N for the entire simulation period smoothed with a 10-year running average (left column), and unsmoothed annual mean values of the last 100 years of simulations (right column) for the Baseline (a, b), Nile (c, d) and IniGlac (e, f) experiment. The maximum depth of the transect is given by the maximum depth levels at 2370 m.

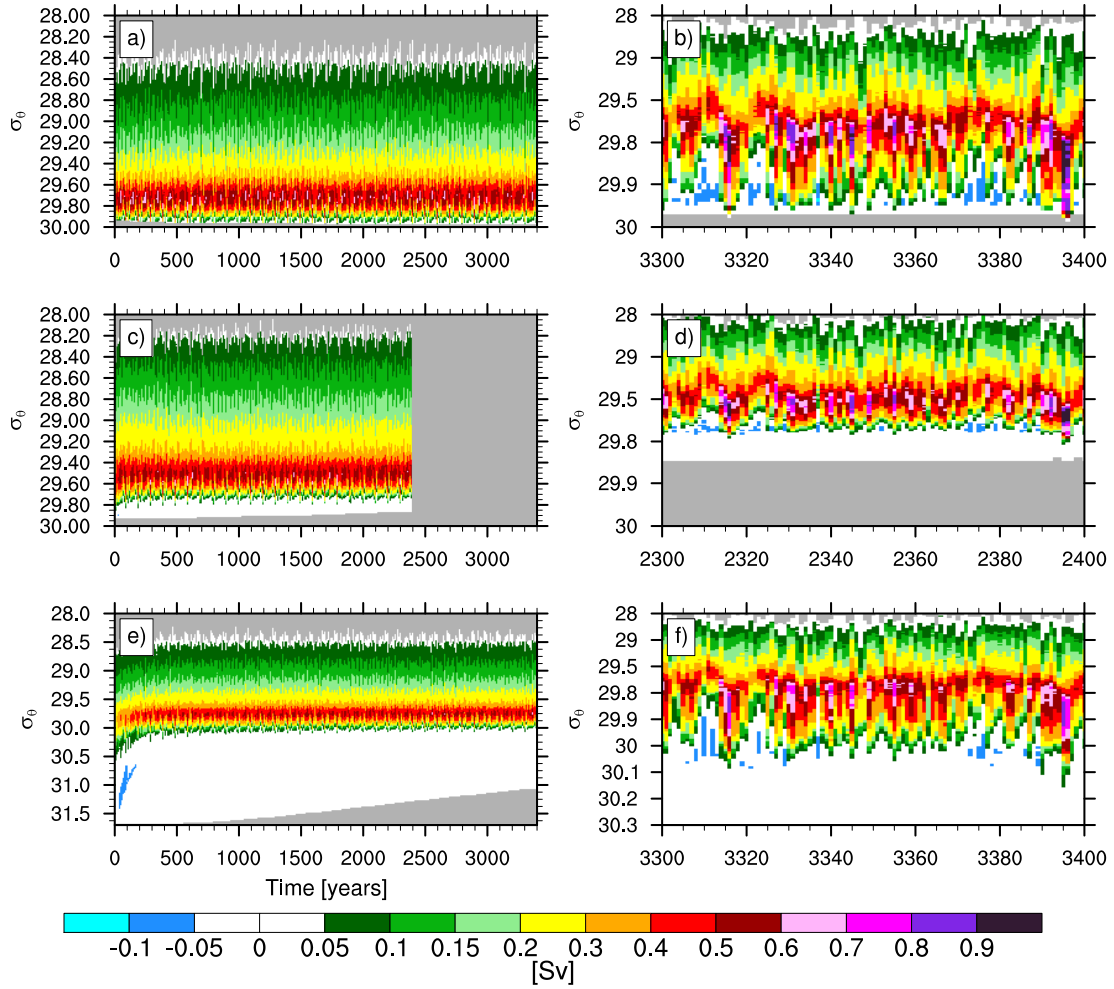


Figure 4.9: Hovmöller diagram of the annual mean water transport rate calculated on isopycnal levels (Eq. 3.3) in the northern Ionian Sea at 38.82°N for the entire simulation period smoothed with a 10-year running average (left column), and unsmoothed annual mean values of the last 100 years of simulations (right column) for the Baseline (a, b), Nile (c, d) and IniGlac (e, f) experiment. The grey colors represents the deepest topography or non occurring densities. Note the different isopycnal spacings.

mation penetrating deeper than 1000 m throughout the simulation period of 3400 years.

In summary, the simulated EMDW formation shows a large interannual variability, which is mainly controlled by the thermal atmospheric forcing. Even though deep water formation events seem rare, they quickly ventilate the entire deep eastern Mediterranean Sea (section 4.3.4). The seasonal penetration depth of the EMDW events is the crucial parameter for the assessment of the strength and stability of a stagnating ocean circulation. In the frame of the simulations, both stagnation experiments show a deepening of the penetration depth of the EMDW formation events with time. The Nile experiment limits the EMDW penetration depth to  $\sim 1700$  m after 2400 years of simulation, and the IniGlac experiment to  $\sim 1000$  m after 3400 years of simulation. The reduction of the strength of stagnation with time is dependent on the strength of the density gradient and the erosion of the density gradient by cross-isopycnal mixing. In general, the erosion of the density gradient by cross-isopycnal mixing is very slow, in the order of millennia, so the strength of the stagnation depends mainly on the initial density gradient. The freshwater induced vertical density gradient in the Nile experiment is weaker developed than in the IniGlac experiment. Since the hydrographic properties of the MAW inflow are unchanged, the saline MAW and the enhanced Nile runoff quickly equilibrate within a few decades to centuries at around  $-0.3$  psu in the Nile experiment with respect to the Baseline simulation. The freshwater induced density gradient inhibits deep convection. Over time, mixing leads to a freshening of the deep layers, which slowly erodes the density gradient, and allows the EMDW formation events to progressively penetrate into greater depth in the Nile experiment. In contrast, the IniGlac experiment shows a much stronger developed density gradient because the warmer early Holocene climate and the hydrography of the MAM inflow considerably differ from the initialized LGM deep water properties. In the framework of the Nile and IniGlac model simulations, cross-isopycnal mixing does not significantly erode the density gradient so that EMDW formation events do not penetrate the deep ocean.

#### 4.3.1.3.2 Sensitivity of the deep water ventilation to the circulation

The sapropel S1 deposition occurred under basin-wide oxygen-depleted deep water conditions. Deep water formation ventilates the deep layers through the transport of oxygen saturated surface water into the deep ocean. In the following, we aim to quantify the role of EMDW formation on the deep ventilation. Since the deep water oxygen concentration is a function of both, physical mixing and biological oxygen consumption, the oxygen concentration cannot be used to understand the pure imprint of the deep water formation on the deep ventilation. Instead, we analyze the  $age_M$  tracer (Eq. 3.5), which shows the imprint of mixing processes, while it is completely independent of biological processes.

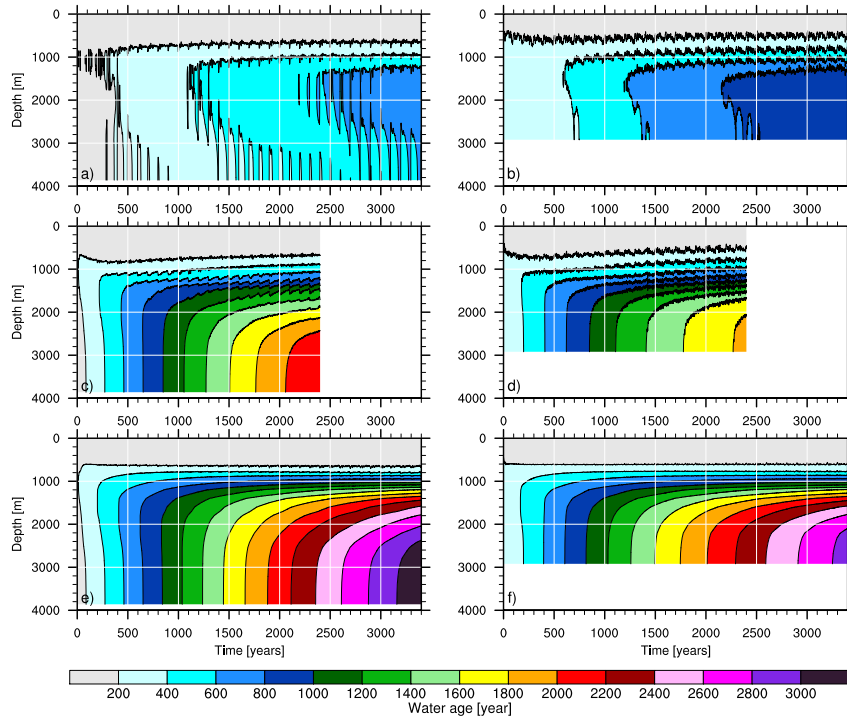


Figure 4.10: Hovmöller diagram of the apparent water age ( $age_M$ , Eq. 3.5) averaged over the Ionian Sea (left column) and Levantine Sea (right column) for the Baseline (a, b), Nile (c, d) and IniGlac (e, f) experiment.

All experiments show an aging of the water below  $\sim 1000$  m depth (Fig. 4.10). In the Baseline simulation, younger upper ocean water repeatedly penetrates down to the deepest layers via deep water formation, with the frequency of these events following the occurrence of cold winters within the 100-year cycle of repeating atmospheric forcing.

On a millennial time scale, deep water formation is reduced in the Baseline simulation (Fig. 4.8), therefore, the deep water progressively ages.

In contrast to the Baseline simulation, the stagnating experiments show a progressive aging of the deep water.

Figure 4.11 shows the fraction of deviation of the water age ( $age_D$ ) (Fig. 4.10) from the perfect stagnation, calculated as

$$age_D(z, t) = \frac{age_T(z, t) - age_M(z, t)}{age_T(z, t)} * 100, \quad (4.1)$$

where  $age_M$  is the modeled water age tracer (Eq. 3.5), and  $age_T$  is the theoretical age the water would have if there was a perfect stagnation (a linear aging of water with

CHAPTER 4 THE EARLY HOLOCENE SAPROPEL FORMATION

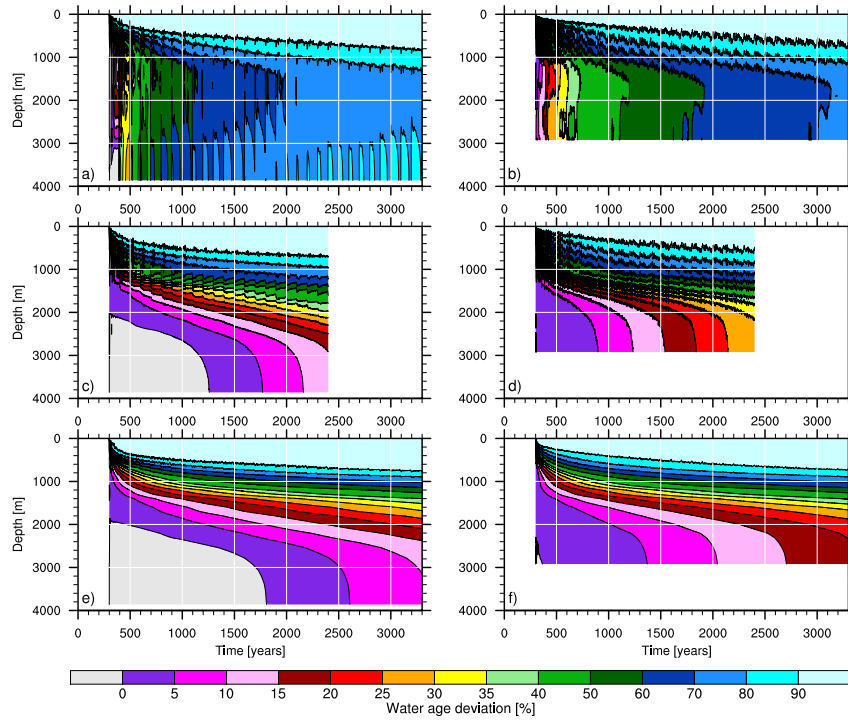


Figure 4.11: Hovmöller diagram of the apparent water age deviation ( $age_D$ ) averaged over the Ionian Sea (left column) and Levantine Sea (right column) for the Baseline (a, b), Nile (c, d) and IniGlac (e, f) experiment. Note the nonlinear color spacing.

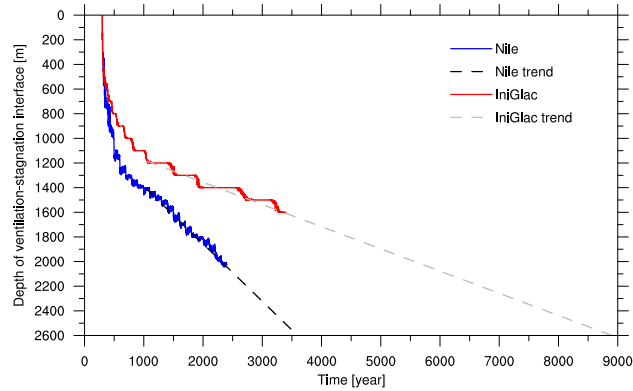


Figure 4.12: Time series of the ventilation-stagnation interface depth (derived as 35% apparent age deviation ( $age_D$ ) averaged over the Ionian Sea) for the Nile and IniGlac simulations. Dashed lines show the linear trend calculated between year 1051 and 2350 for the Nile experiment, and between 1051 and 3350 for the IniGlac experiment.

time). We start this computation with the initial  $age_M(z, 300)$  of each simulation in order to avoid the imprint of the initialization effects. Negative  $age_D$  values indicate that the water age is older than the actual time that has passed, resulting from the mixing of older water from intermediate layers into greater depth. Positive  $age_D$  values indicate the deviation from the perfect stagnation.

With time, the aging of the water is decreased in all experiments. Similarly, the vertical gradient of the  $age_D$  is decreased. The Baseline simulation shows a  $\sim 80\%$  renewal of the deep water masses by the end of the simulation. In the stagnation experiments, the deep water renewal is  $< 20\%$  in the Ionian Sea by the end of the simulations. Assuming that  $age_D \leq 35\%$  indicates a complete stagnation with only little diffusive imprint of younger upper ocean water, and a deviation  $> 35\%$  indicates active mixing processes like convective deep water formation, we can use  $age_D = 35\%$  as a measure for the depth of the boundary between the ventilated and stagnating water masses. Using the time trend of this depth and assuming it is linear over the upper 2600 m, we can extrapolate the future evolution of the depth of the ventilation-stagnation interface. Figure 4.12 shows this time extrapolation. While the Nile experiment shows a complete reventilation of the upper 2600 m after  $\sim 3500$  years, the IniGlac experiment will probably become completely reventilated after  $\sim 9000$  years.

#### 4.3.1.3.3 The internal dynamics of the physical ventilation under different circulation scenarios

There is a clear difference of the aging trends between the Ionian and Levantine Sea in the various circulation scenarios. While in the Baseline simulation, the intermediate deep Levantine Sea shows older water than the Ionian Sea, in the stagnation experiments, this east-west trend is reversed (Fig. 4.10). Here, we focus on the dynamics that establish these trends because it influences the redistribution of deep water oxygen (section 4.3.4.2).

First, we analyze the deep water transport exchange rate between the deep Ionian and Levantine Sea, which determines the horizontal and vertical distribution of tracers, such as oxygen. Therefore, we conducted 6 additional experiments, in which we introduced a new artificial tracer, the water-tracer, which is suitable to trace the deep water masses. We initialized the water-tracer experiments for the Baseline circulation after 3100 years, the Nile experiment after 2100 years, and the IniGlac after 3200 years. At the first time step, the water-tracer field of each circulation scenario was initialized with a high water-tracer concentrations ( $10^9$ ) between 1900 m and 2100 m depth in a  $6 \times 6$  gridbox area in the Ionian, and in the second experiment in the Levantine Sea. Outside of these regions we set the concentration of the water-tracer to 0. The water-tracer does not feedback on the physical circulation field, and is not affected by any processes except for the surface, where its concentration is kept to 0 concentration at each timestep. Therefore, the water-tracer mimics the behavior of oxygen, however,

without the influence of biological processes. The water-tracer can be used to assess the transport capacity of the deep water masses, with higher concentration indicating little mixing with water outside the water-tracer source region, and low concentrations indicating intensive mixing with ambient water and/or surface water. We ran each simulation for 200 years, and display the results averaged over the first and second 100 years of simulation as a vertical transect (Fig. 4.13), with the initialized water-tracer in the Ionian Sea displayed in Figure 4.14, and initialized water-tracer in the Levantine Sea displayed in Figure 4.15.

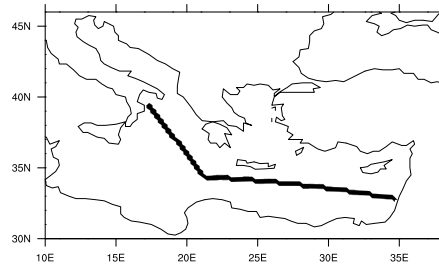


Figure 4.13: Location of the vertical transect spanning from the northern Ionian Sea towards the eastern Levantine Sea.

Strong vertical and horizontal mixing of the Ionian water in the Baseline simulations is indicated by the lowest water-tracer concentrations in the Ionian source region compared to the stagnating Nile and IniGlac experiments. Opposed to the stagnation scenarios, the weakly stratified Ionian Sea in the Baseline simulation dilutes the water-tracer concentration via EMDW formation. The anti-clockwise deep circulation transports the water-tracer into the Levantine Sea, and through the replenishment of the new deep water, the older deep water is pushed upward towards the surface. Since mixing with surface waters reduces the water-tracer concentration, the EMDW formation events, and the upward pushing of the deep and intermediate water, result in an erosion of the water-tracer concentration from below and above. Hence, the water-tracer concentration shows a maximum at intermediate depth (Fig. 4.14).

In the Levantine Sea, the strong vertical mixing and upward pushing of the deep water leads to the lowest water tracer concentration in the Baseline simulation (Fig. 4.15). This partly explains the low transport of the water-tracer concentration from the Levantine towards the Ionian compared to the stagnation experiments. In addition, with increasing strength of stagnation the horizontal circulation and recirculation is strengthened along the horizontal isopycnals (Fig. 4.17). Therefore, the stagnation experiments show a more efficient transport of the water-tracer from the Levantine towards the Ionian Sea. The recirculation in the Ionian Sea is strongly enhanced in the stagnation experiments, in particular, in the IniGlac simulation, which traps the water-

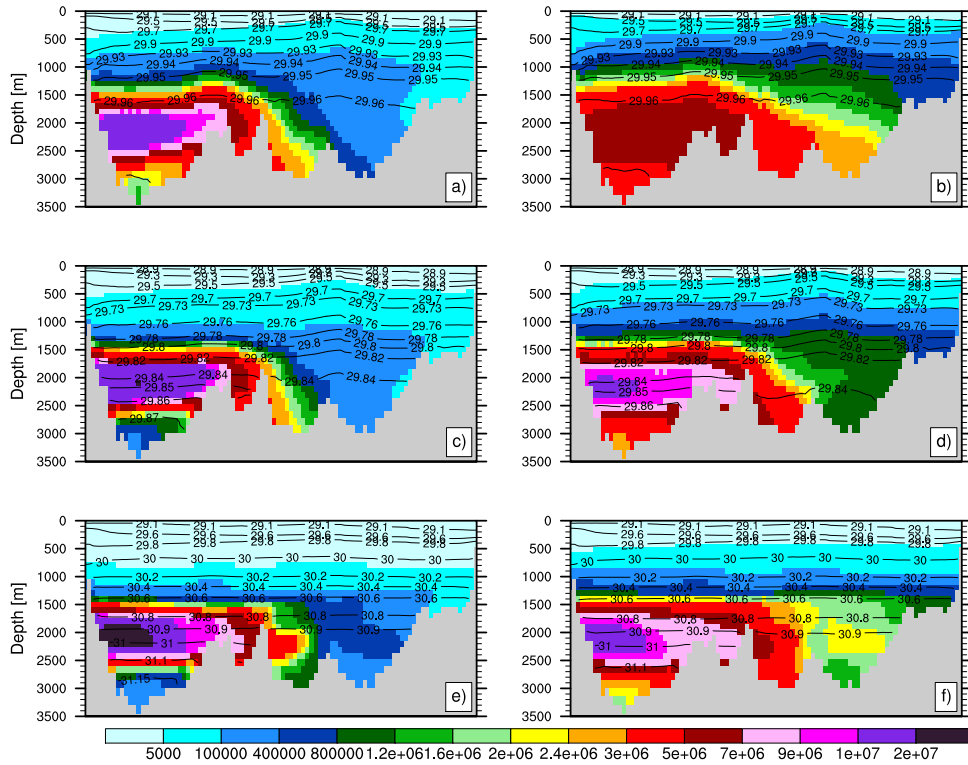


Figure 4.14: Vertical transect of the water-tracer, initialized in the Ionian Sea, spanning through the northern Ionian (left edge) towards the eastern Levantine (right edge) with the transect location shown in Figure 4.13, superimposed with  $\sigma_\Theta$  levels for two successive 100-year averaged time slices of the Baseline (a: year 3101–3200, b: 3201–3300), the Nile (c: year 2101–2200, d: 2201–2300), and the IniGlac (e: 3201–3300, f: 3301–3400) experiment. Note the nonlinear color scale and the coarser spreading of the isopycnals in the upper ocean.

tracer more efficiently in the Ionian Sea. In addition, the stagnation experiments show only a weak diffusive dilution of the deep Ionian water-tracer concentration through the surface. Thus, the water-tracer shows higher concentrations in the Ionian, while in the Levantine the high concentrations are mixed within the weakly stratified deep ocean more effectively. If we would initialize the water tracer synchronously in the Ionian and Levantine Sea, then we should expect highest water-tracer concentrations to accumulate in the Ionian Sea.

Now, as we have assessed the strength of the deep water transport with respect to the imprint of the surface water, we can assess the effect of physical mixing on the deep ventilation by analyzing  $age_D$  in the various circulation scenarios on the same vertical transect (Fig. 4.16). In the Baseline simulation, deep water formed in the Adriatic Sea sinks to the bottom of the Ionian Sea and pushes the deep Ionian water

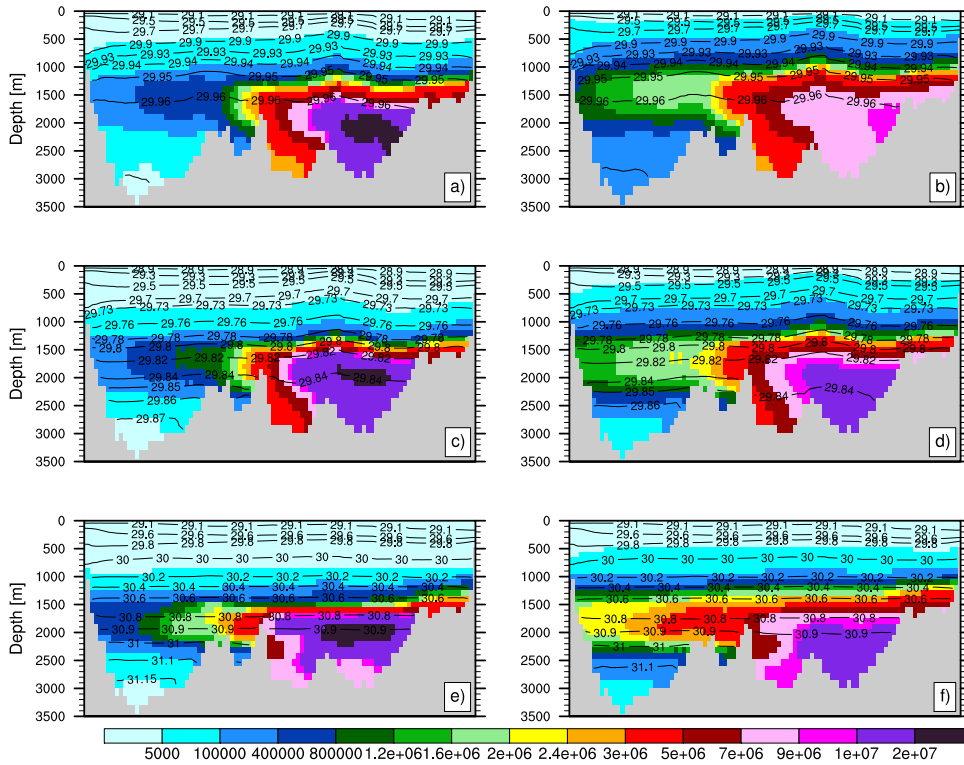


Figure 4.15: Vertical transect of the water-tracer, initialized in the Levantine Sea, spanning through the northern Ionian (left edge) towards the eastern Levantine Sea (right edge) with the transect location shown in Figure 4.13, superimposed with  $\sigma_\Theta$  levels for two successive 100-year averaged time slices of the Baseline (a: year 3101–3200, b: 3201–3300), the Nile (c: year 2101–2200, d: 2201–2300), and the IniGlac (e: 3201–3300, f: 3301–3400) experiment. Note the nonlinear color scale and the coarser spreading of the isopycnals in the upper ocean.

towards the Levantine. Therefore, the deep Ionian Sea receives the youngest water, while the deep Levantine receives a mix of the newly formed EMDW and the older deep Ionian/Levantine water. Overall, the water is thus oldest in the eastern Levantine at intermediate depth.

In the stagnation experiments, the oldest water is found in the deep Ionian Sea, since the well stratified deep Ionian Sea in both stagnation experiments does not allow for the penetration of the dense water outflow from the Adriatic Sea into the deep Ionian Sea. Since the penetration depth of EMDW events is greater in the Nile experiment than in the IniGlac experiment, the vertical gradient of  $age_D$  in the Ionian is eroded more strongly from above in the Nile experiment. The deep Levantine Sea of both stagnation experiments is weakly stratified. Therefore, in the deep Levantine Sea the water is quickly mixed and nearly homogenized. In the Levantine Sea, there is a west-east

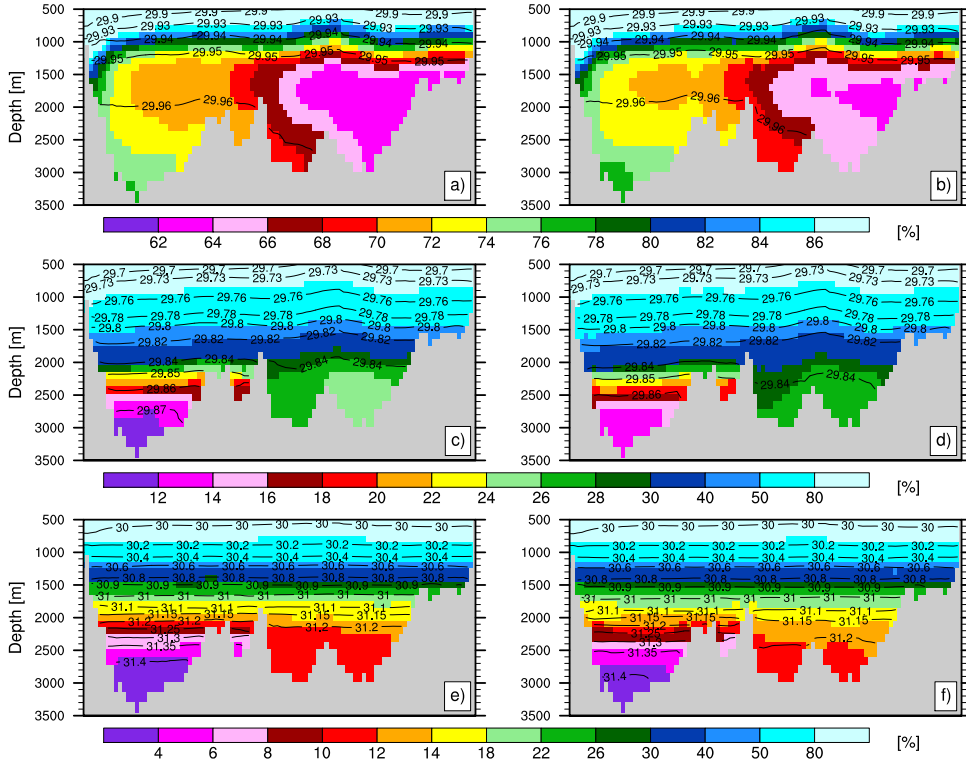


Figure 4.16: Vertical transect of the water age deviation ( $age_D$ ) spanning through the northern Ionian (left edge) towards the eastern Levantine (right edge) with the transect location shown in Figure 4.13, superimposed with  $\sigma_\Theta$  levels for two successive 100-year time slices averaged between the years 2101–2200 and 2201–2300 for the Baseline (a, b), the Nile (c, d), and the IniGlac (e, f) experiments. Note the different color bars between the experiments, and the coarser spreading of the isopycnals in the upper ocean.

gradient of  $age_D$  in the Nile experiment, and a predominantly vertical gradient in the IniGlac experiment. These structurally different gradients are caused by the maximum depth of the deep anti-clockwise circulation cell reaching down to greater depth in the Levantine Sea in the Nile experiment (Fig. 4.7). Along the isopycnals displayed in Figure 4.16 within the time slices,  $age_D$  shows similar values in both basins, resulting from fast mixing along isopycnals and the strong separation of the deep ocean and the well-mixed upper ocean.

In summary, the opposing east-west trends of the water age between the Baseline and the stagnation experiments result from the strength of the deep circulation, which depends on the stratification of the water column. In the Baseline simulation, the entire deep eastern Mediterranean is weakly stratified, allowing the dense water formed in

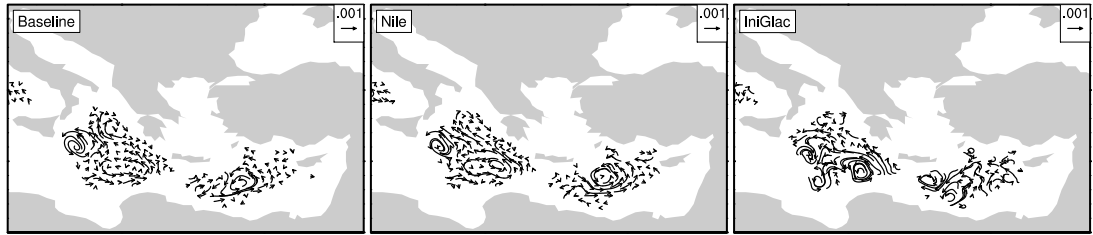


Figure 4.17: Annual mean circulation at 1900 m depth averaged over the last 100 years of simulation in each experiment. Vector represent both speed [ $m s^{-1}$ ] and direction of the circulation.

the Adriatic to penetrate the deep Ionian and Levantine Sea. Therefore, the Levantine shows the oldest water at intermediate depth in the Baseline simulation. In contrast, in the stagnation experiments, the strongly stratified deep Ionian Sea limits the penetration depth of EMDW events, which isolates the deep Ionian Sea where the water continuously ages. In addition, the recirculation within the deep Ionian is strengthened with increasing strength of stagnation, thus, in the Ionian Sea old water is more efficiently trapped in the stagnation experiments.

### 4.3.2 Nutrient cycle

The anti-estuarine circulation, with nutrient-depleted MAW inflow at the surface and nutrient-rich intermediate water outflow, establishes an oligotrophic upper ocean regime in all simulations. The annual budget of total phosphate is shown in Table 4.3.

Table 4.3: Annual total phosphate budget [ $mol\ s^{-1}$ ] of the eastern Mediterranean Sea (Emed). Values are averaged over the simulation years 1301-1400 (1.4 kyr), 2301-2400 (2.4 kyr), and 3301-3400 (3.4 kyr) for the oxygenated pre-sapropel (PS) time. For the anoxic sapropel (S) time values are averaged over the years 3301-3400 (3.4 kyr). Export production in 113m averaged over the eastern Mediterranean, the Ionian and the Levantine Sea.

|                                 | Base<br>-line | 3xNutri | Nile  | IniGlac | IniGlac+<br>3xNutri | IniGlac+<br>3xNutri |
|---------------------------------|---------------|---------|-------|---------|---------------------|---------------------|
|                                 | PS            | PS      | PS    | PS      | PS                  | S                   |
| Rivers Emed                     | 33.3          | 99.8    | 61.6  | 33.3    | 99.8                | 99.8                |
| Net outflux Sicily (1.4 kyr)    | 28.1          | 84.4    | 47.1  | 22.0    | 72.9                |                     |
| Net flux water + sed. (1.4 kyr) | 5.1           | 15.3    | 14.5  | 11.2    | 27.0                |                     |
| Net flux sed. (1.4 kyr)         | -2.5          | -9.7    | -5.7  | -2.7    | -10.1               |                     |
| Net gain Emed (1.4 kyr)         | 2.6           | 5.5     | 8.8   | 8.6     | 16.0                |                     |
| Net outflux Sicily (2.4 kyr)    | 29.8          |         | 51.4  | 24.3    | 78.2                |                     |
| Net flux water + sed. (2.4 kyr) | 3.5           |         | 10.2  | 9.0     | 21.6                |                     |
| Net flux sed. (2.4 kyr)         | -1.7          |         | -5.0  | -2.3    | -9.6                |                     |
| Net gain Emed (2.4 kyr)         | 1.8           |         | 5.2   | 6.6     | 12.0                |                     |
| Net outflux Sicily (3.4 kyr)    | 30.9          |         |       | 25.6    |                     | 81.6                |
| Net flux water + sed. (3.4 kyr) | 2.4           |         |       | 7.6     |                     | 18.1                |
| Net flux sed. (3.4 kyr)         | -1.3          |         |       | -2.2    |                     | -11.0               |
| Net gain Emed (3.4 kyr)         | 1.1           |         |       | 5.5     |                     | 7.1                 |
| Export production (Emed)        | 117.8         | 194.8   | 141.1 | 107.7   | 179.5               | 186.0               |
| Export production (Ionian)      | 64.5          | 94.8    | 70.4  | 60.2    | 87.4                | 91.2                |
| Export production (Levantine)   | 35.3          | 65.7    | 50.8  | 32.2    | 60.4                | 62.1                |

In all simulations, the external nutrient input is largely balanced by the net flux at the Strait of Sicily. Higher nutrient availability translates into higher sediment burial fluxes in the pre-sapropel period, which further increases during the sapropel under the anoxic bottom water conditions. In the tripled riverine nutrient experiments (3xNutri, IniGlac+3xNutri) also the net outflow at the Strait of Sicily is approximately tripled compared to the oligotrophic experiments (Baseline, IniGlac). Over time, in all simulations the net outflux of phosphate at the Strait of Sicily is enhanced, leading to a decreasing flux to the sediment, as well as a decreasing accumulation of nutrients in the water column.

In all experiments, the upper ocean phosphate is depleted over most of the open ocean areas, with a maximum concentration of  $\sim 0.23\ mmol\ m^{-3}$  (Fig. 4.18). Mixing during winter enriches the surface phosphate concentration, which is quickly consumed dur-

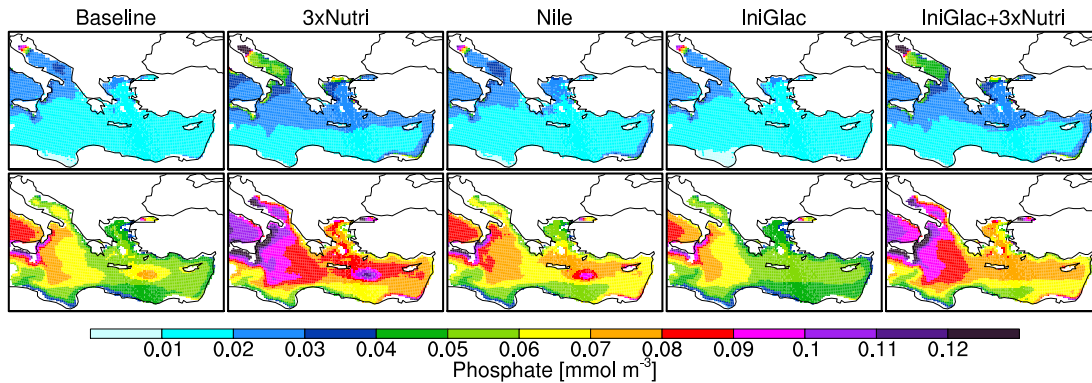


Figure 4.18: Annual mean dissolved phosphate in 35.5 m (upper panel), and 92.5 m (lower panel), averaged over the years 1301-1400 for each model simulation.

ing the spring bloom (not shown). On an annual average, only the tripled riverine nutrient input experiments show relatively high phosphate concentrations in the entire Adriatic Sea at 35.5 m depth. At 92.5 m depth, all experiments show relatively high phosphate concentrations in the western Ionian, which are up-welled mainly through the predominantly south-westerly winds during late spring to early summer, causing Ekman suction of deep nutrient-rich water into the euphotic zone. The well-ventilated Baseline, 3xNutri as well as the stagnating Nile experiment show relatively high phosphate concentration in the center of the Rhodes gyre due to the upward doming of nutrient-rich deep water and the correspondingly shallow pycnocline. The anticyclonic Mersa-Matruh gyre leads to downwelling of nutrient-depleted surface water. The weakly developed Rhodes and Mersa-Matruh gyres in the IniGlac and IniGlac+3xNutri simulations, and correspondingly deeper pycnocline, establish a comparably lower north-south phosphate gradient in the Levantine, and the trapping of the nutrients in the stagnating deep water leads to an overall stronger upper ocean nutrient depletion compared to the Baseline and 3xNutri experiments. In the Nile experiment, the additional nutrient input of the Nile river and the upwelling of nutrients by the strongly developed Rhodes gyre support high nutrient concentrations throughout the eastern Mediterranean Sea. Overall, this shows that the eastern Mediterranean upper ocean nutrient regime is mainly controlled by riverine nutrient input, while in the Levantine Sea a considerably influence of the upwelling of deep nutrients is obvious, which is more effective in the Baseline, 3xNutri and Nile simulations than in the IniGlac and IniGlac+3xNutri simulations with their relatively deep pycnocline and strongly stagnating deep water circulation.

Figure 4.19 shows a Hovmöller diagram of the phosphate concentration. A pronounced nutricline, located at around 800 m to 1200 m, marks the interface between

### 4.3 RESULTS

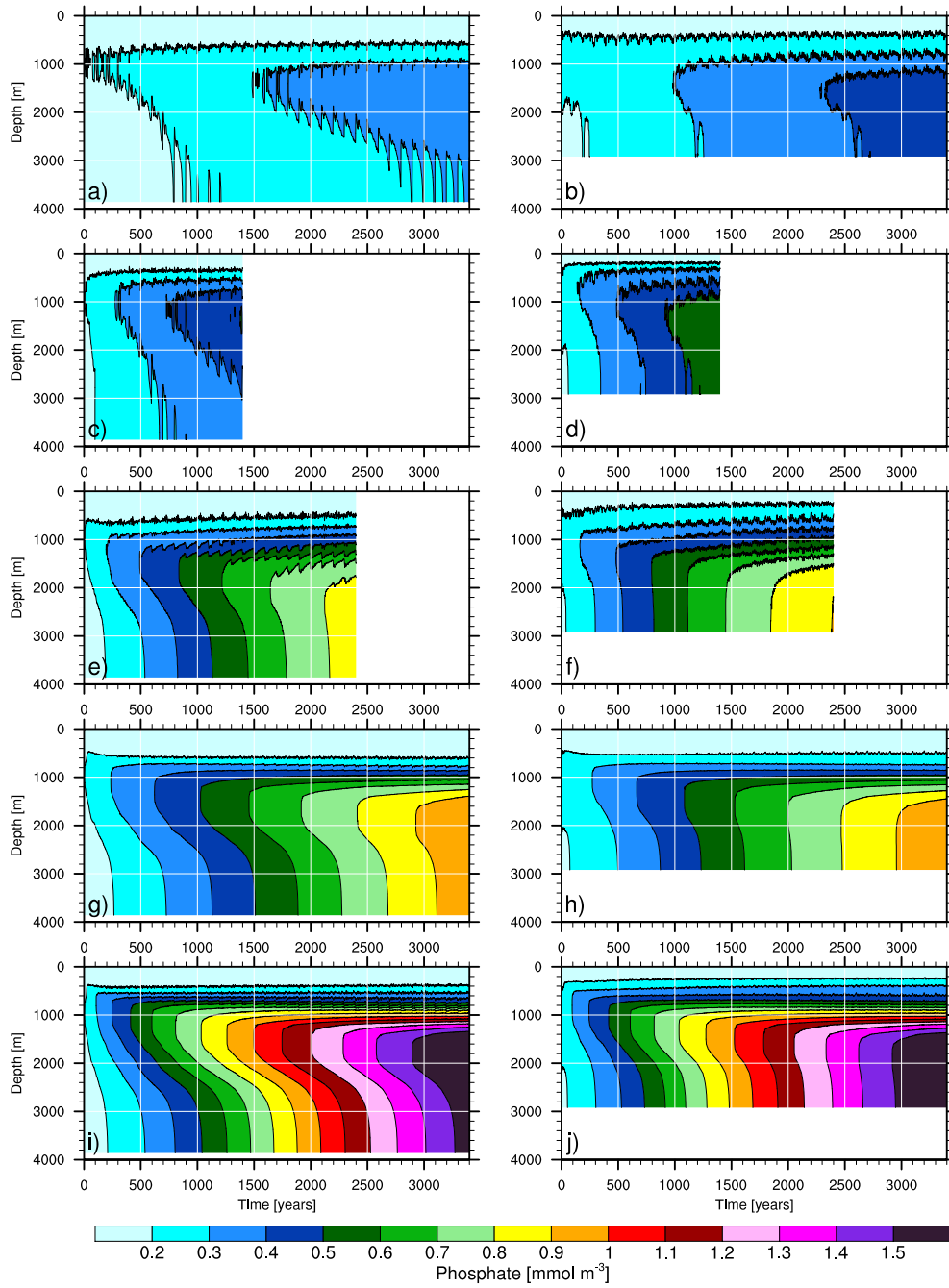


Figure 4.19: Hovmöller diagram of the dissolved phosphate concentrations averaged over the Ionian Sea (left column) and Levantine Sea (right column) for the Baseline (a, b), 3xNutri (c, d), Nile (e, f), IniGlac (g, h) and IniGlac+3xNutri (i, j) experiment.

the well-mixed upper ocean and the deep ocean. At depth, all simulations show a drift towards higher phosphate concentrations. The Baseline and 3xNutri experiment are repeatedly influenced by the EMDW formation, mixing strongly nutrient-depleted water into the deep ocean, and pushes nutrient-rich deep water towards the upper ocean. In contrast, all stagnating experiments show a gradual increase in their deep water phosphate concentrations, resulting from the efficient trapping of nutrients in the deep stagnating water mass.

### 4.3.3 Biological productivity

The strength of particulate organic carbon (POC) export production regulates the rate of deep water oxygen consumption. To determine the large-scale mechanisms leading to the S1 oxygen deficiency, it is essential to understand the mechanisms that are responsible for regional and temporal differences of the biological export production.

The geographical distribution of annual and seasonal POC export production is shown in Figure 4.20. Similar to the pre-industrial CTRL simulation (Fig. 3.10), in all early Holocene simulations export production peaks during spring, when deep mixing ceases and light is sufficient to support high biological production. Also similar to the pre-industrial CTRL simulation, areas of high export production are localized in the eastern Levantine, the Adriatic Sea, the northwestern Ionian Sea, the Strait of Sicily, and the Aegean Sea. The high export production in the eastern Levantine and the Adriatic Sea is largely fueled by the high riverine nutrient input of the Nile and Po. Strong mixing supports high export production in the Aegean and Adriatic Sea. In the western Ionian Sea, the high export production is fueled by nutrients, which are up-welled mainly through Ekman suction.

Compared to the oligotrophic Baseline or IniGlac experiment, the Nile experiment shows an overall increased export production, fueled by the fast distribution of the additional Nile nutrients throughout the entire basin (section 4.3.2). The well-ventilated Baseline and 3xNutri experiments show higher export production than their stagnating counterparts, the IniGlac and IniGlac+3xNutri experiments. On the one hand, the EMDW formation pushes the deep water towards the Levantine, where it diffusively upwells, and on the other hand, the shallower position of the pycnocline and corresponding lifting of the nutricline, both bring deep nutrient-rich water into the euphotic zone. In the IniGlac and IniGlac+3xNutri experiments, deep water formation ceases, nutrients are trapped in the deep stagnating water body (section 4.3.2), and the relatively deep pycnocline (Fig. 4.3) does not allow for a rise of the nutricline into the euphotic zone, leading overall to a decrease of the POC export production.

In summer, when there is the highest light availability, a basin-wide deep chlorophyll maximum (DCM) is simulated between 45 m and 60 m depth (Fig. 4.21), with largest concentrations in the eutrophicated experiments (3xNutri, IniGlac+3xNutri,

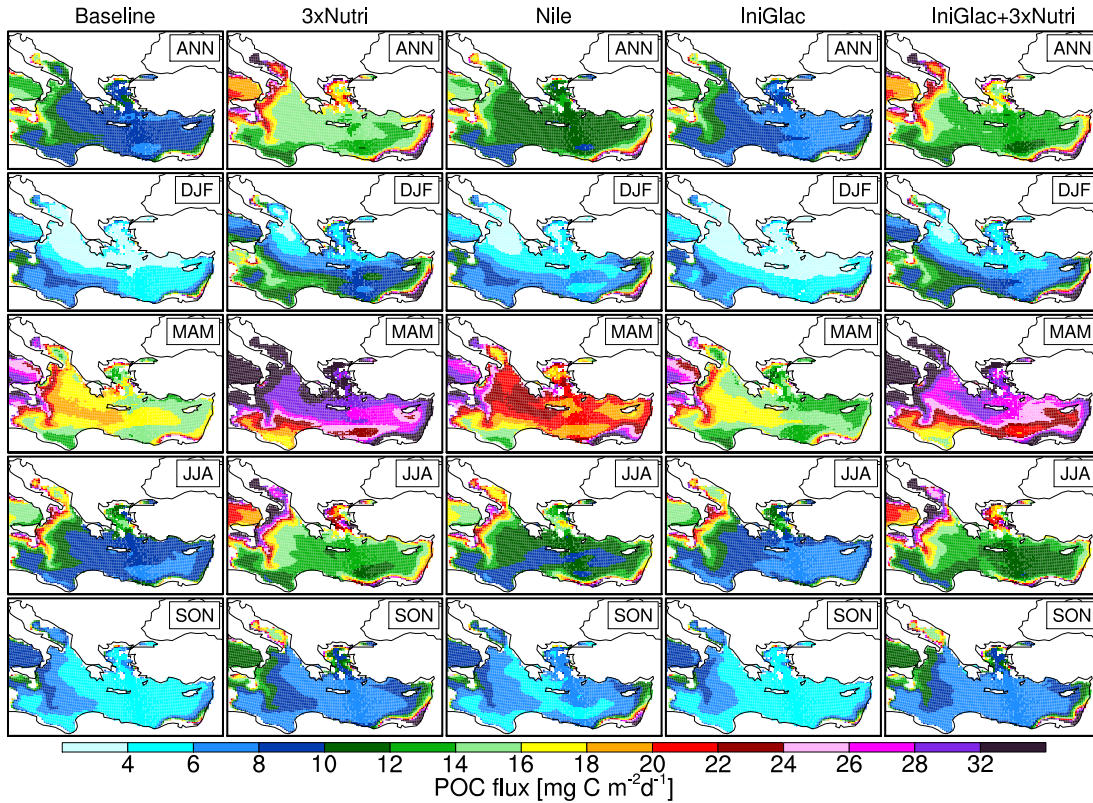


Figure 4.20: Annual mean (ANN), and winter (DJF), spring (MAM), summer (JJA), autumn (SON) POC export production at 113m depth, averaged over the years 1301-1400. Note the nonlinear color scale.

Nile). The strongly reduced LIW formation in the pre-sapropel simulations implies a stronger stratification of the water column, and hence a shoaling of the pycnocline. This shallowing of the pycnocline is hardly enough to support high nutrient concentrations at the base of the euphotic zone. Thus, overall the DCM is rather similar to the CTRL simulations (Fig. 3.11).

The eastern Mediterranean Sea annual mean modeled POC export production of the Baseline simulations is  $10.4 \text{ mgC m}^{-2} \text{ d}^{-1}$ , which is in reasonable agreement with the modeled  $13 \text{ mgC m}^{-2} \text{ d}^{-1}$  at 100 m of Stratford et al. (2000) for a weak anti-estuarine circulation with present-day nutrient input. The trapping of nutrients in the deep layers of the stagnating and oligotrophic IniGlac experiment only slightly reduces the annual mean export production to  $9.8 \text{ mgC m}^{-2} \text{ d}^{-1}$  in the eastern Mediterranean Sea. In contrast, the enhanced nutrient input in the 3xNutri, Nile, IniGlac+3xNutri experiments increases the export production to 17.2 and  $16.5 \text{ mgC m}^{-2} \text{ d}^{-1}$ , respectively. Stratford et al. (2000) reports  $23 \text{ mgC m}^{-2} \text{ d}^{-1}$  for a weak anti-estuarine circulation

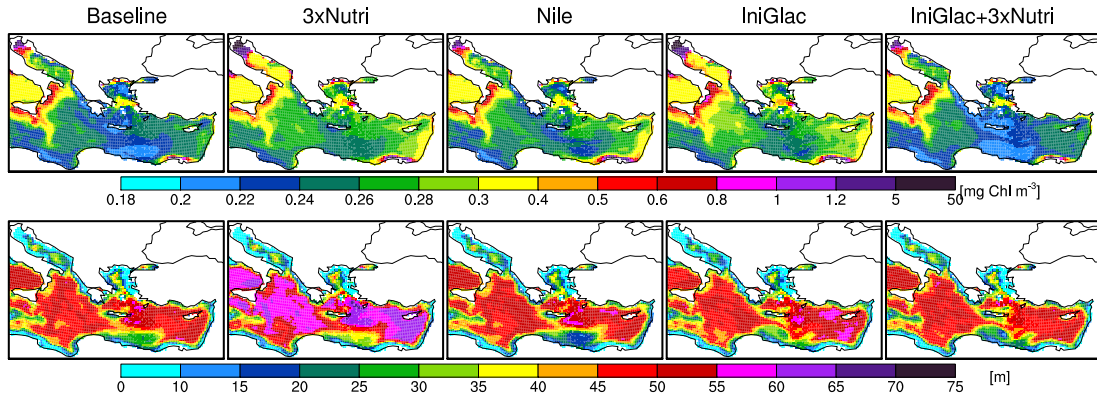


Figure 4.21: Chlorophyll concentration at the depth of the summer (JJA) DCM averaged over the years 1301-1400 (upper panel); Depth of summer DCM (lower panel) averaged over the years 1301-1400. Units converted using a carbon/chlorophyll ratio of 1:60. Note the nonlinear color scale.

with a tripled nutrient input, however, with much of the export concentrated near the coast. In addition, Stratford et al. (2000) reports a secondary maximum in production in autumn due to the onset of convective processes. In all our model simulations, we find an autumn to winter maximum only in the very eastern Levantine in response to the Nile peak runoff during this time. The rather high export production reported by Stratford et al. (2000) might point to other simplifications in their model setup, such as the supply of nutrients evenly between model points contiguous with the coastline. In contrast, we prescribe for each river individual nutrient concentrations at the corresponding river mouth locations and account for seasonal variations at least for the major rivers. Furthermore, Stratford et al. (2000) included an atmospheric phosphate fertilization of  $35 \text{ mol s}^{-1}$  in their model simulations. However, we regard this atmospheric phosphate input as rather implausible, since the major source of atmospheric phosphate would be through desorption from dust particles, but dust deposition has been strongly reduced due to the wetter climate conditions over the Sahara during the AHP (Box et al. 2008).

Figure 4.22 shows time series of the annual mean export production at various locations throughout the eastern Mediterranean. The Baseline simulation shows a rather stable export production throughout the entire period of simulation. The 3xNutri experiment reaches an equilibrium flux after  $\sim 500$  years of simulation. Under the same nutrient regime the stagnating experiments show initially a strong decline of the POC export, and within a few decades a strong increase, which subsequently flattens after a few centuries. The rapidly established deep water stagnation at the beginning of the simulations leads to an initial strong nutrient exhaustion of the upper ocean, since

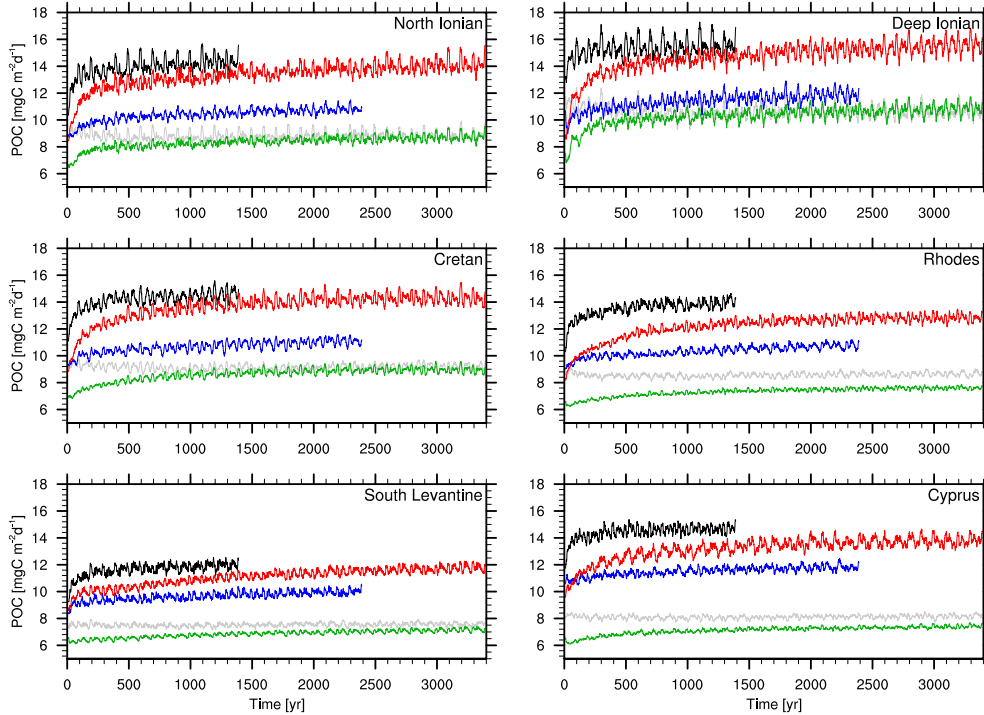


Figure 4.22: POC export flux at 113 m depth at locations as indicated in Figure 2.1. Grey: Baseline, black: 3xNutri, blue: Nile, green: IniGlac, red: IniGlac+3xNutri. Data were smoothed by applying a 20-year running average.

the POC export effectively removes nutrients from the system. The overall continuous increase of the POC export in the stagnation experiments results from the progressively weakening of the stagnation, which enhances the upwelling and mixing of highly nutrient-rich water from the deep ocean into the euphotic layer. This increasing trend is stronger developed in the Ionian compared to the Levantine Sea. In fact, the Cretan, Rhodes and Cyprus locations show a rather stable export production after  $\sim 1500$  years in all stagnating experiments, which indicates that the upwelling of nutrients from the deep ocean and the biological production fueled by these nutrients is in equilibrium at these location. In all simulations, the interannual variability of the export flux is larger in the Ionian compared to the Levantine.

For a tripling of all river nutrient loads under a given circulation scenario, POC export production increases by  $\sim 66\%$ . A strongly stagnating deep water circulation reduces the export production by  $\sim 8\%$  compared to a well-ventilated ocean. In the stagnation experiments, nutrients are trapped in the deep stagnating water body more efficiently than in the well-ventilated experiments, which limits the export production. Under the same circulation field, in the Ionian Sea a tripled riverine nutrient input

increases the export by  $\sim 45\%$ , while in the Levantine Sea the export increases by  $\sim 87\%$ . Since the circulation fields are identical, the different behaviors of the Baseline or IniGlac compared to the 3xNutri or IniGlac+3xNutri experiments in the Ionian and Levantine Sea are mainly caused by the change of the Nile river nutrient load.

#### 4.3.4 Oxygen cycle

In this section, we discuss the processes involved with the deep water oxygen depletion in our simulations. In particular, we address the question whether the sapropel S1 deep water oxygen depletion was induced through a stagnation deep water circulation preconditioned by the AHP climate (Nile experiment), or whether it involved a much longer lasting deep water stagnation preconditioned by the climatic changes associated with the last glacial-interglacial transition period (IniGlac experiment). In addition, we analyze the potential of developing and holding deep water anoxia through enhanced biological production induced through increased riverine nutrient input (3xNutri experiment), also in combination with deep water stagnation scenarios (Nile, IniGlac+3xNutri experiments).

This section is organized as follows. In the first part, we analyze the time evolution of the deep water oxygen under the various climate and nutrient scenarios. In the next part, we focus on the dynamical and biogeochemical processes shaping regional differences of the vertical extend of oxygen minimum zones (OMZ), and their propagation with time. And in the final section, we investigate the processes determining the oxygen cycle during the onset phase of deep water anoxia.

##### 4.3.4.1 The time evolution of deep water oxygen

In this section, we focus on the evolution of the deep water oxygen concentration with respect to the climatic preconditioning of the general circulation, as well as the nutrient regime. In particular, we aim to gain a better insight of the role of nutrients and the strength of the stagnation for the development of deep water anoxia. Finally, we determine the plausibility of our scenarios with respect to the required time frames for the deep water oxygen depletion.

Figure 4.23 shows Hovmöller diagrams of the oxygen concentration, and Figure 4.24 shows time series of the oxygen concentration in 1800 m and 2660 m. All experiments show a trend towards less oxygenated deep water with time, while the upper ocean, to a depth of around 500 m, remains well ventilated.

In the Baseline simulation, on a seasonal timescale, EMDW formation events rapidly oxygenate the deep eastern Mediterranean Sea. The deep water formed in the Adriatic Sea spreads into the deep Ionian and flows at depth towards the Levantine Sea. Hence, the deep Levantine Sea shows a much weaker imprint of the ventilation events. On

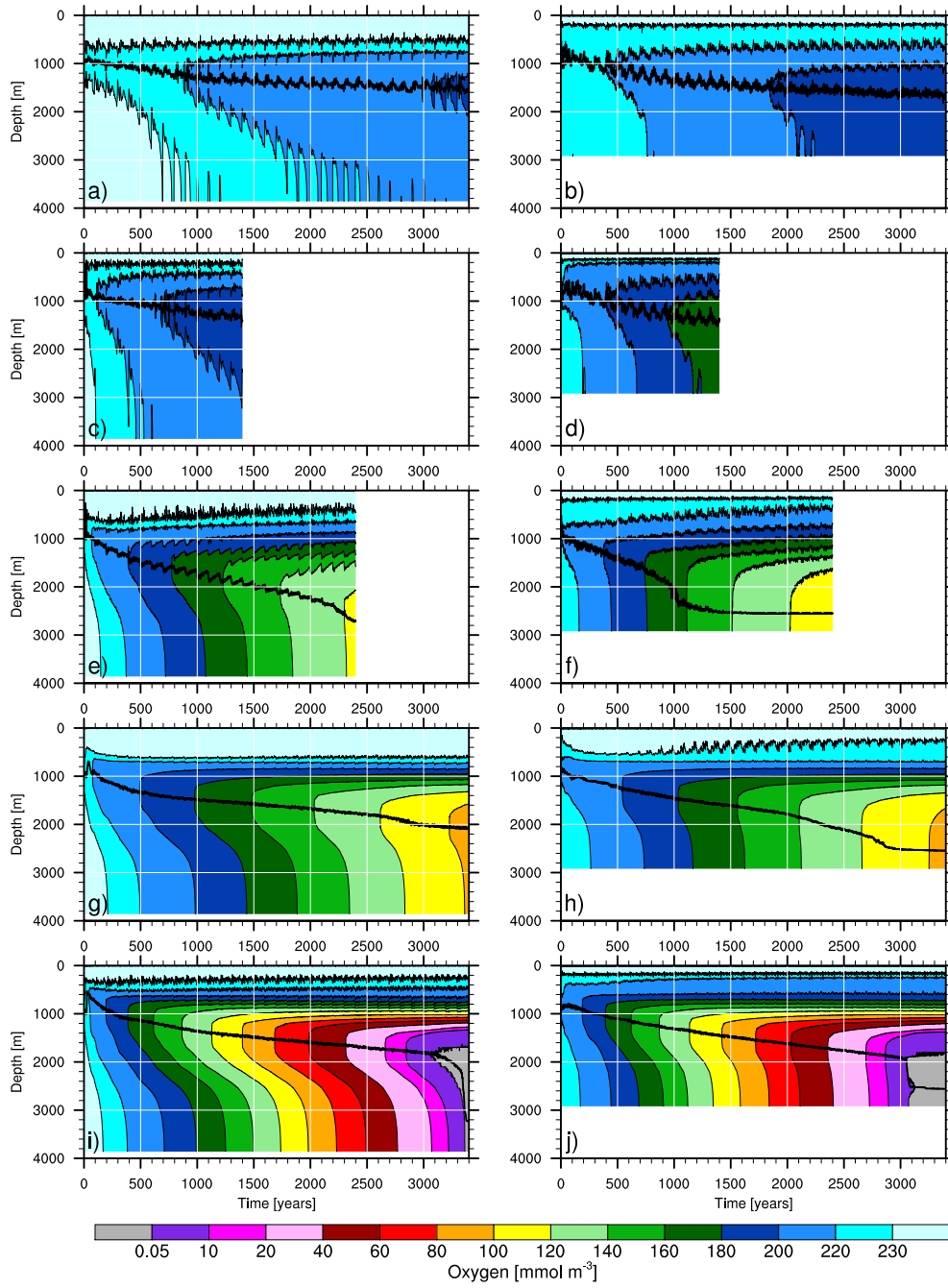


Figure 4.23: Hovmöller diagram of the dissolved oxygen concentration averaged over the Ionian Sea (left column) and Levantine Sea (right column) for the Baseline (a, b), 3xNutri (c, d), Nile (e, f), IniGlac (g, h) and IniGlac+3xNutri (i, j) experiment. The thick black line indicates the depth of the minimum oxygen concentration. Note that the maximum depth of the minimum oxygen concentration corresponds to the mean depth of the averaging areas, which is 3340 m for the Ionian and 2619 m for the Levantine panels. Note the nonlinear color scale.

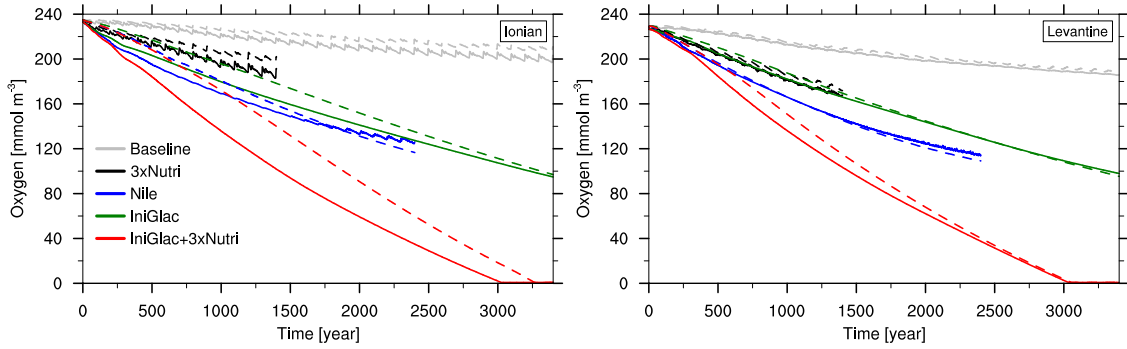


Figure 4.24: Time series of the annual mean dissolved oxygen concentration averaged over the Ionian Sea (left panel) and Levantine Sea (right panel) for the indicated model simulations in 1800 m (solid line) and 2660 m (dashed line).

a millennial timescale, the deep water oxygen concentration in both the Ionian and Levantine Sea shows a drift towards a less oxygenated status. This millennial timescale oxygen drift results from the progressive reduction of the strength of EMDW formation (see section 4.3.1.3.1).

In the 3xNutri experiment, the enhanced biological production leads to an increased biological oxygen utilization compared to the oligotrophic Baseline simulation. However, since the circulation of the 3xNutri experiment is the same as in the Baseline, the deep water is oxygenated via deep water formation. The 3xNutri experiment does not show the potential to utilize the oxygen to a level of oxygen deficiency. In section 3.3.4 we showed that the model overestimates deep oxygenation, resulting from intensive mixing in the southern Adriatic Sea during ADW formation, oversaturating the ADW outflow with oxygen. Thus, also the deep oxygenation of the 3xNutri and Baseline experiments are possibly overestimated.

On the other hand, all stagnation experiments show a gradual deep water oxygen depletion. Since the IniGlac and IniGlac+3xNutri experiment have the same circulation field, the differences between these experiments can be directly attributed to the differences in the biological export production (Fig. 4.22), and the corresponding oxygen consumption by remineralization. Therefore, the higher biological production in the IniGlac+3xNutri experiment results in an overall higher oxygen utilization than the highly oligotrophic IniGlac experiment. By the end of the simulation, the IniGlac+3xNutri experiment develops basin-wide deep water anoxia below  $\sim 1600$  m to 1800 m depth. The Nile experiment shows a weaker strength of the stagnation than the IniGlac simulations, while the biological production ranges in-between the IniGlac and IniGlac+3xNutri experiment (Fig. 4.22). Therefore, the Nile simulation initially utilizes more oxygen than the IniGlac experiment. However, the imprint of the progressive

deepening of the ADW outflow into the Ionian is clearly visible in the intensification of the ventilation events in the time series of the oxygen concentrations at 1800 m depth in the Ionian Sea (Fig. 4.24).

In the framework of the model simulations, only the IniGlac+3xNutri experiment shows the development of deep water anoxia. Nonetheless, all of the perturbations show an oxygen depletion over time, and thus, they show at least initially the potential to develop deep water anoxia. In the following, we focus on the potential timescales until deep water anoxia would be fully developed, with the aim to determine the plausibility of the scenarios with respect to the required time frame for complete oxygen depletion.

Figure 4.25 shows a Hovmöller diagram of the projected time frame until deep water anoxia is developed relative to year 1 (*ptanox*), and Figure 4.26 shows a time series of the *ptanox* at 2000 m depth. *ptanox* was calculated by fitting at each gridbox a linear function between 200-year separated oxygen concentrations, and extrapolating the time until the oxygen concentration would be below  $0.05 \text{ mmol m}^{-3}$  (anoxic). Thus, *ptanox* is only an estimate based on the trends of the modeled oxygen concentrations.

The 3xNutri experiment shows no potential to develop a deep water oxygen deficiency within a reasonable time frame of the early Holocene sapropel formation, since the *ptanox* rapidly increases with values exceeding 11 kyr in the Ionian Sea after 1400 years of simulation. This large projected time frame at the end of the simulation results from the continuous deep ventilation.

The Nile experiment initially indicates to develop anoxic deep water within a few millennia. However, after 2200 years of simulation *ptanox* rapidly rises at 2000 m depth (Fig. 4.26), which is the consequence of the increasing depth penetration of deep water ventilation events (see section 4.3.1.3.1). Therefore, the Nile model simulation most likely does not show the potential to develop deep water oxygen anoxia, if we would continue the simulation.

In contrast, the IniGlac experiment shows an almost linear oxygen depletion over time, with the trend suggesting that this experiment might develop deep water anoxia after  $\sim 6.5$  kyr of simulation. Potentially, after 6.5 kyr the ventilation-stagnation interface of the IniGlac experiment might reach as deep as  $\sim 2200$  m (Fig. 4.12), so that anoxia could only develop below this depth, and be sustained for another 2.5 kyr until complete reventilation might be established after 9 kyr of simulation. This time frame, however, is too short to solely explain the 3.5 kyr of S1 formation.

The IniGlac+3xNutri experiment is throughout the simulation quite stable in its *ptanox* prediction, with a rather small trend of *ptanox* prolongation of around 500 years in 1000 years of simulation. After  $\sim 3000$  years of simulation, the deep water anoxia is developed, which is then the true value of *ptanox*. When again assuming that a complete reventilation will be established after 9000 years, the IniGlac+3xNutri

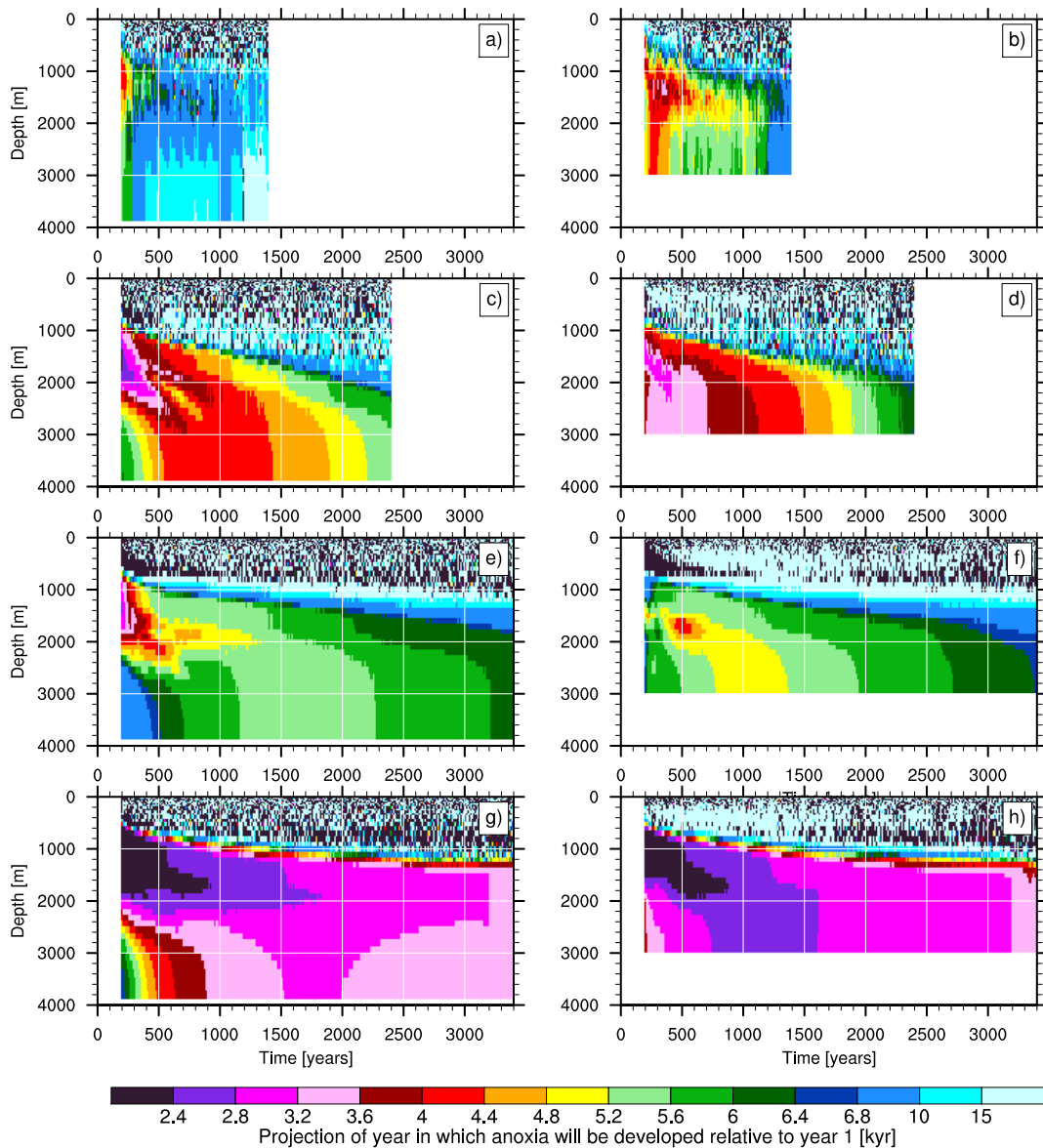


Figure 4.25: Hovmöller diagram of the projected year in which anoxia develops relative to year 1 (*ptanox*) averaged over the Ionian Sea (left column) and the Levantine Sea (right column) for the 3xNutri (a, b), Nile (c, d), IniGlac, (e, f) and IniGlac+3xNutri (g, h). Calculated by using a linear regression between 200 year separated oxygen concentrations, thus, the first 200 years of each simulation are missing.

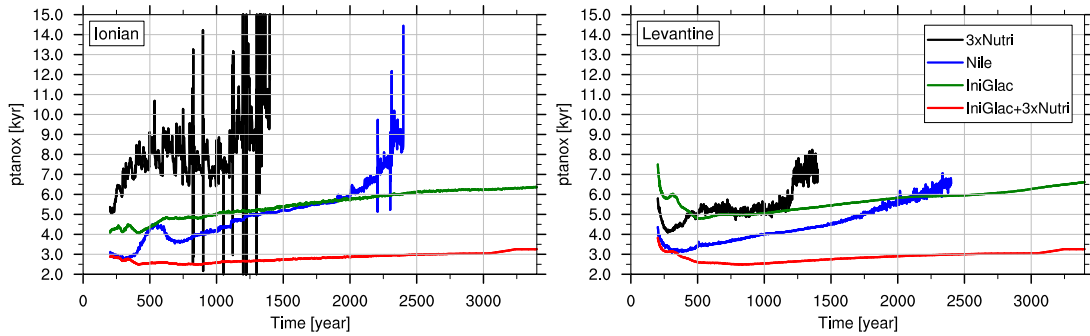


Figure 4.26: Time series of the projected year in which anoxia will be developed relative to the year 1 (*ptanox*) at 2000 m depth averaged over the Ionian Sea (left panel) and the Levantine Sea (right panel) for the indicated model simulations.

possibly will be anoxic for another  $\sim 6000$  years. This projected time frame of the deep water anoxia overestimates the actual time of sapropel deposition, which is only 3.5 kyr. Thus, when only assessing the plausibility of the IniGlac+3xNutri scenario with respect to S1 formation time, the simulation seems either over-eutrophicated, or the stagnation is too strong. In section 4.3.5 we will further assess the plausibility of all scenarios with respect to the simulated sediment.

In summary, the strength of the deep water stagnation is more crucial than the biological production for the development of deep water anoxia. This can be seen when comparing the Nile and IniGlac simulations. The Nile experiment has a weaker strength of the stagnation, however, stronger eutrophication than the IniGlac experiment. The Nile experiment shows no potential to develop deep water anoxia, while the trends of the oxygen consumption and stagnation strength suggest that the IniGlac experiment could potentially develop deep water anoxia. Nonetheless, within a given strength of the deep water stagnation the external nutrient input determines the date for the onset of a deep water oxygen deficiency, which can be seen when comparing the IniGlac and IniGlac+3xNutri experiments.

#### 4.3.4.2 The dynamical evolution of oxygen minimum zones

Proxy records at various depth levels throughout the eastern Mediterranean Sea indicate a basin-wide (De Lange et al. 2008), and depth independent (Schmiedl et al. 2010) synchronous onset of the oxygen deficiency. Therefore, it seems that there was no pronounced OMZ established prior to the onset of the sapropel deposition, but that below 1800 m depth the water column was homogenized with respect to low oxygen concentrations.

All simulations show different behaviors of the deep water oxygen evolution in the

deep Ionian and Levantine Seas with time. In addition, all experiments show an OMZ in the Ionian Sea (Fig. 4.23). In this section, we differentiate the dynamical processes involving ventilation, biological oxygen consumption and internal redistribution of oxygen that control the regional evolution of the simulated OMZs in space and time.

In general, regional differences in the deep water oxygen profile develop through physical ventilation, and circulative redistribution of oxygen, as well as biological oxygen consumption. Previously, we have established the physical mixing potential, and the dynamical transport capacity of the deep water circulation within the various simulated circulation scenarios (section 4.3.1.3.2). Now, we analyze the biological oxygen consumption, so finally we can assess the dynamical evolution of the oxygen profile.

Figure 4.27 shows a vertical transect of the biological oxygen consumption. All experiments show a strong vertical gradient of decreasing biological oxygen consumption with depth, resulting from the continuous remineralization of the sinking POC. Overall, the biological oxygen consumption is enhanced in the eutrophication experiments (3xNutri, IniGlac). In the Nile experiment, the oxygen consumption is enhanced in the Levantine due to the increased Nile river nutrient input fueling high export production. In the IniGlac simulation, the lower POC export translates into lower biological oxygen consumption. With increasing depth the differences between the experiments decrease. In the northern Ionian, the well ventilated Baseline and 3xNutri experiment shows an enhanced biological oxygen consumption, resulting from the EMDW flow along the bottom, resuspending particles from the sediment, which are then resubjected to remineralization in the bottom water. Since there is no, or strongly reduced, EMDW formation in the stagnation experiments, sediment POC resuspension is limited by the reduced strength of the dense-water bottom flow. Nonetheless, the biological production is highest in the northwestern Ionian in all experiments, thus, also the stagnation experiments show overall highest biological oxygen consumption rates in this area. In general, the biological oxygen consumption shows little horizontal variations at depth, with the major differences restricted to the bottom, where sediment erosion enhances the biological oxygen consumption through repeated resuspension of POC from the sediment.

Now, we have differentiated all aspects shaping the oxygen profile, and find that mixing establishes strong vertical oxygen gradients, the deep water transport establishes east-west gradients, and the biological oxygen consumption develops mainly vertical oxygen gradients.

Figure 4.28 shows the oxygen concentration in a transect through the northern Ionian towards the eastern Levantine for two successive 100-year time slices.

In a well ventilated ocean, like in the Baseline and 3xNutri experiment, an OMZ develops at intermediate depth because the deep ocean is continuously ventilated via deep water formation, pushing the older deep water into intermediate depth where the biological oxygen consumption is higher than in the deep ocean. Thus, the transport of

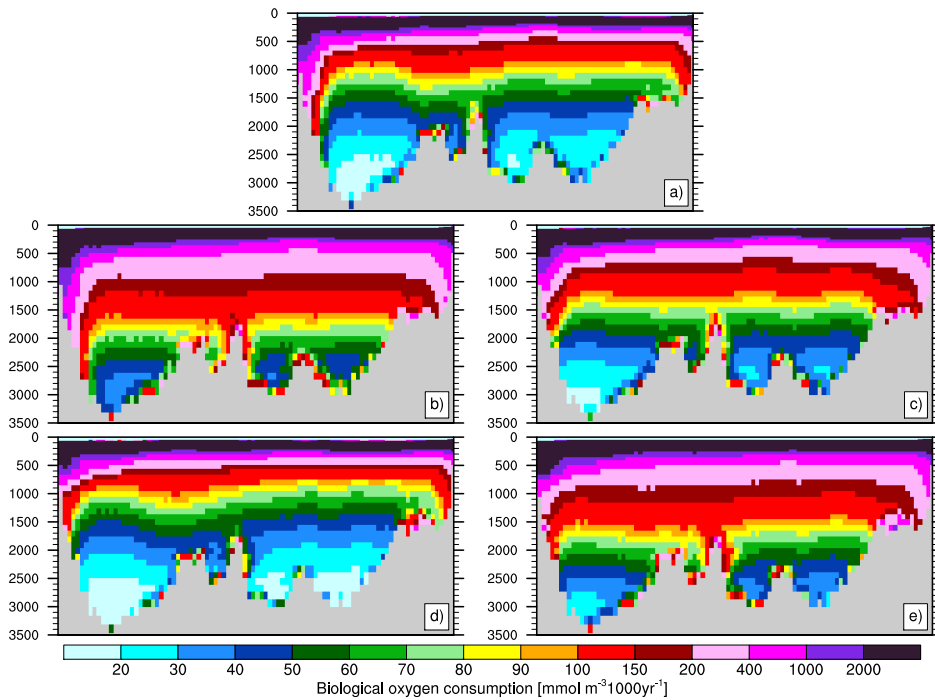


Figure 4.27: Vertical transect of the biological oxygen consumption spanning through the northern Ionian (left edge) towards the eastern Levantine (right edge) with the transect location shown in Figure 4.13, averaged between the simulation years 2301-2400 for the a) Baseline c) Nile d) IniGlac, e) IniGlac+3xNutri, and averaged between the years 1301-1400 for the b) 3xNutri experiment. Note the nonlinear color scale.

deep water from the Ionian towards the Levantine accumulates oxygen-depleted water at intermediate depth, while the vertical oxygen gradient is highest in the Ionian Sea.

Within a moderately stagnating deep water circulation, such as simulated in the Nile experiment, the ventilation is restricted to intermediate depth where the biological oxygen consumption is higher than in the deep ocean. An OMZ can only develop as long as the ventilation front is in shallow position, otherwise ventilation erodes the OMZ from above. The deep water circulation transports the oxygen-depleted intermediate Ionian water towards the Levantine Sea, which establishes a west-east gradient between the Ionian and Levantine Sea.

In the case of a strongly stagnating deep water circulation as simulated in the IniGlac experiments, the deep water mass is effectively separated from the well-ventilated upper ocean. As long as the ventilation-stagnation interface is in a shallow position, the horizontally evenly distributed and vertically strongly decreasing biological oxygen consumption establishes an OMZ at intermediate depth. In the highly stratified Ionian Sea, an OMZ develops since the deep water oxygen gradient is only slowly homogenized

CHAPTER 4 THE EARLY HOLOCENE SAPROPEL FORMATION

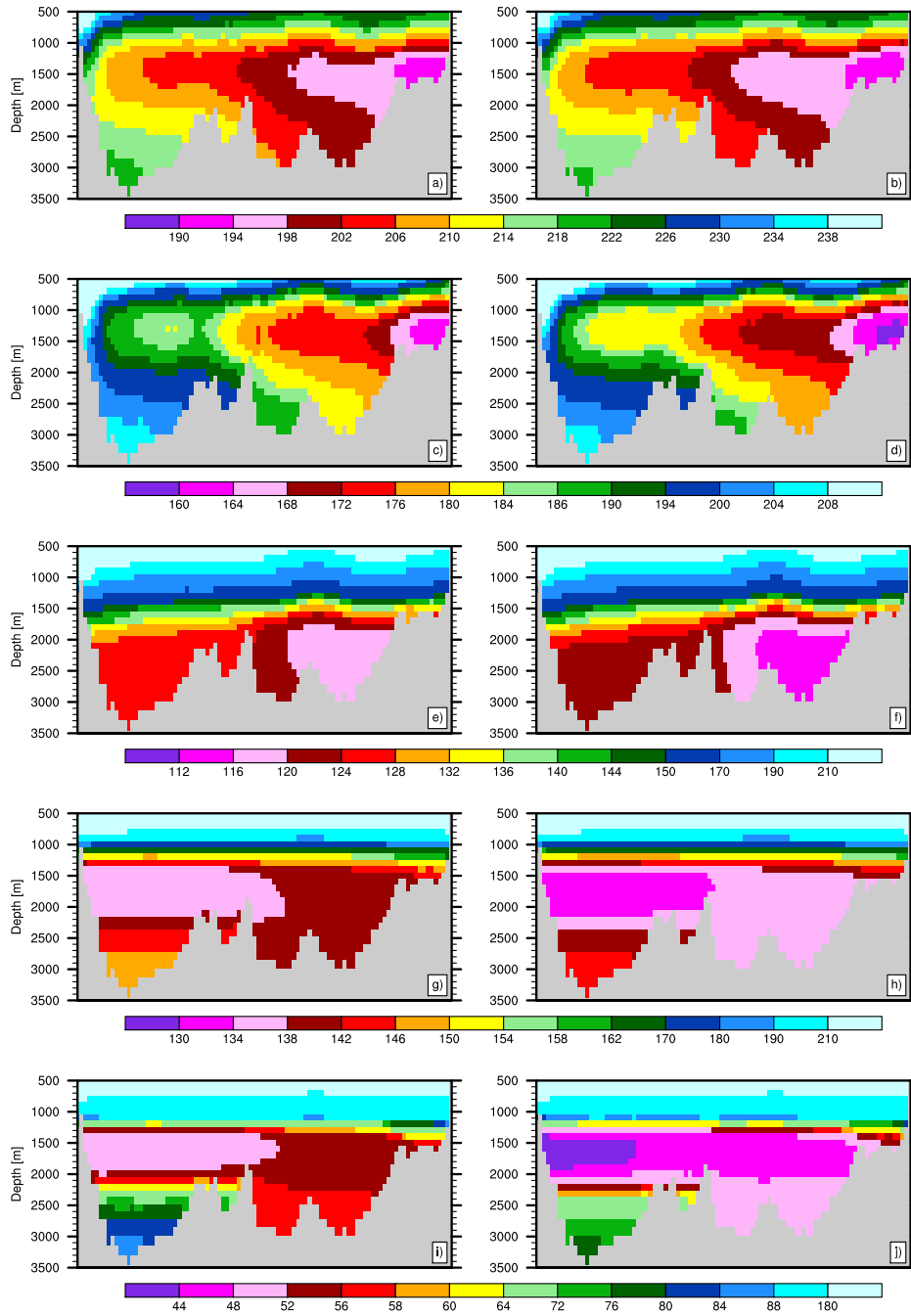


Figure 4.28: Vertical transect of the dissolved oxygen concentration [ $mmol m^{-3}$ ] spanning through the northern Ionian (left edge) towards the eastern Levantine (right edge) with the transect location shown in Figure 4.13, for two successive 100-year averaged time slices of the years 2101-2200 and 2201-2300 for the Baseline (a, b), Nile (e, f), IniGlac (g, h) and IniGlac+3xNutri (i, j), and the years 1101-1200 and 1201-1300 for the 3xNutri (c, d) experiments. Note that every model simulation has its own color bar, however, the color spacing is always  $4 mmol m^{-3}$  for the deep ocean below 1500 m.

through diapycnal mixing, and the recirculation traps the oxygen-depleted water in the Ionian Sea. In contrast, in the weakly stratified deep Levantine Sea, the homogenization of the deep oxygen profile occurs fast, and thus no OMZ evolves.

Between the oligotrophic Baseline/IniGlac and their eutrophicated counterpart scenarios the 3xNutri/IniGlac+3xNutri simulations, the dynamically established horizontal and vertical oxygen gradients are simply enforced in the eutrophication scenarios. The strength of the biological production does not alter the spatial pattern of the dynamically established oxygen gradients, even though in the eutrophicated experiments the major source of nutrient input is shifted to the east, with the strongly enhanced Nile river nutrient input.

In the following, we analyze the time evolution of the vertical extent of the OMZ in the various experiments.

Figure 4.29 shows the difference of the bottom water oxygen concentration ( $O_2(-H)$ ) to the oxygen concentration ( $O_2(z)$ ) over time, which we term the oxygen minimum structure ( $OMS$ )

$$OMS(z) = O_2(-H) - O_2(z). \quad (4.2)$$

The  $OMS$  indicates the gradient of oxygen concentration within the water column. Positive values display the shape and strength of the OMZ, and negative values indicate more oxygenated areas than the bottom layers. Figure 4.30 shows time series of the OMZ oxygen concentration and the maximum  $OMS$  concentrations.

In the Baseline simulation, the  $OMS$  shows a relatively stable vertical extent and constant concentrations in both the Ionian and Levantine basin after around 1000 to 1500 years of simulation. This indicates that the vertical extent of the OMZ is no longer changing and that the shape of the oxygen depth profile is relatively stable, with an OMZ at intermediate depth.

In the 3xNutri experiment, the depth of the maximum  $OMS$  concentration progressively deepens, and the continuous increasing  $OMS$  concentrations indicates the development of a well pronounced OMZ in the Ionian Sea. In the Levantine Sea, the OMZ vertical extent and maximum  $OMS$  concentration show a quasi stabilization after around 1000 years of simulation.

The Nile experiment shows a peak of the maximum  $OMS$  concentration after 400 years in the Ionian Sea, and afterwards a rather linear decrease. Temporal variability of the maximum  $OMS$  concentration continuously decreases in the Nile experiment. On the other hand, the upper branch of the OMZ shows an increasing variability, resulting from the deepening of the EMDW depth penetration, which erodes the OMZ from above. In the Levantine Sea, the maximum  $OMS$  concentration is strongly reduced throughout the simulation of the Nile experiment, and the maximum concentration

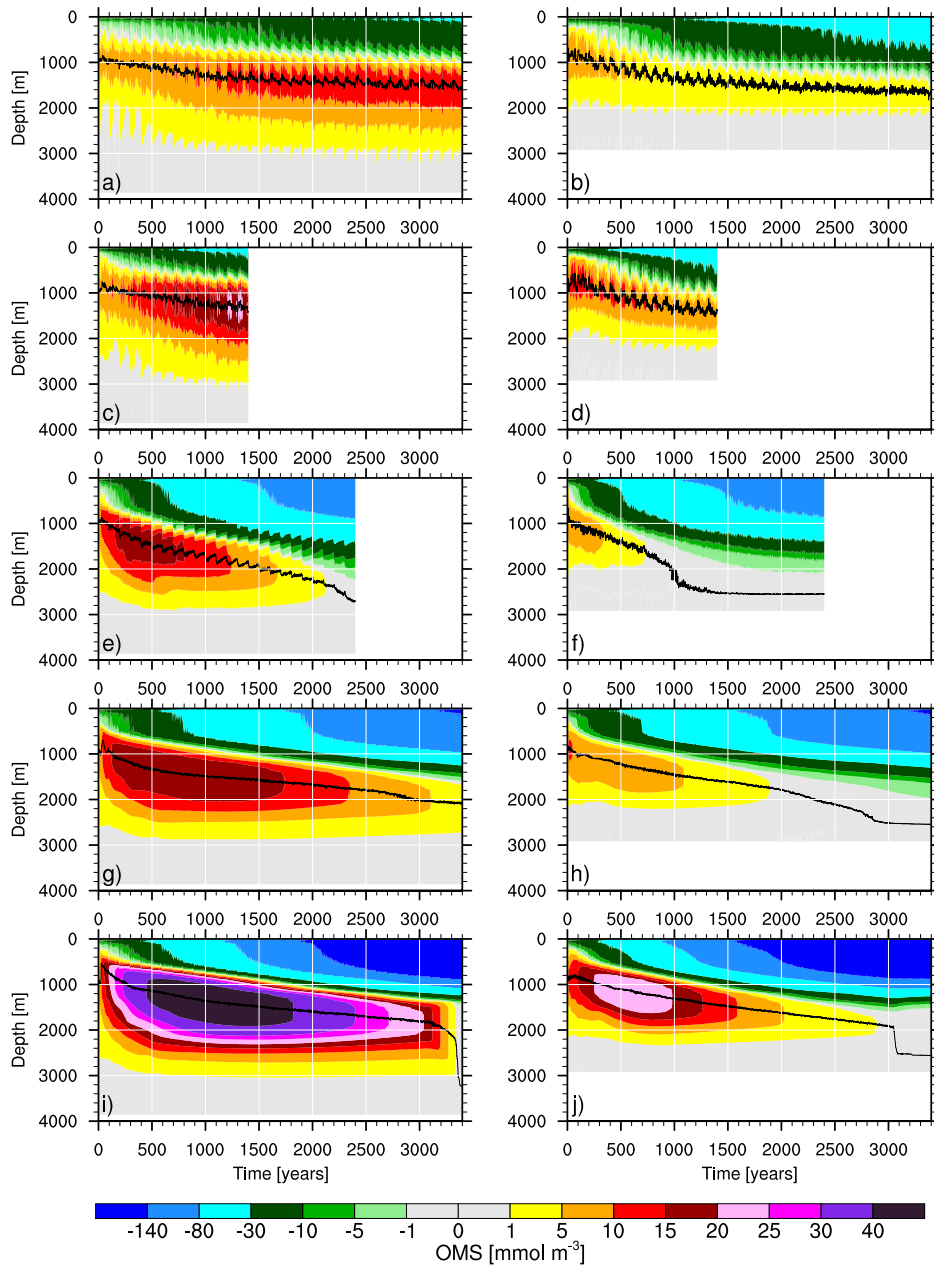


Figure 4.29: Hovmöller diagram of the oxygen minimum structure ( $OMS$ ) (Eq. 4.2) averaged over the Ionian Sea (left column) and the Levantine Sea (right column) for the Baseline (a, b), 3xNutri (c, d), Nile (e, f), IniGlac (g, h) and IniGlac+3xNutri (i, j) experiment. The black line indicates the depth of the maximum  $OMS$  concentration averaged over the basins. Note the nonlinear color scale, and that the maximum depth of the maximum  $OMS$  concentration corresponds to the mean depth of the averaging areas, which is 3340 m for the Ionian and 2619 m for the Levantine panel.

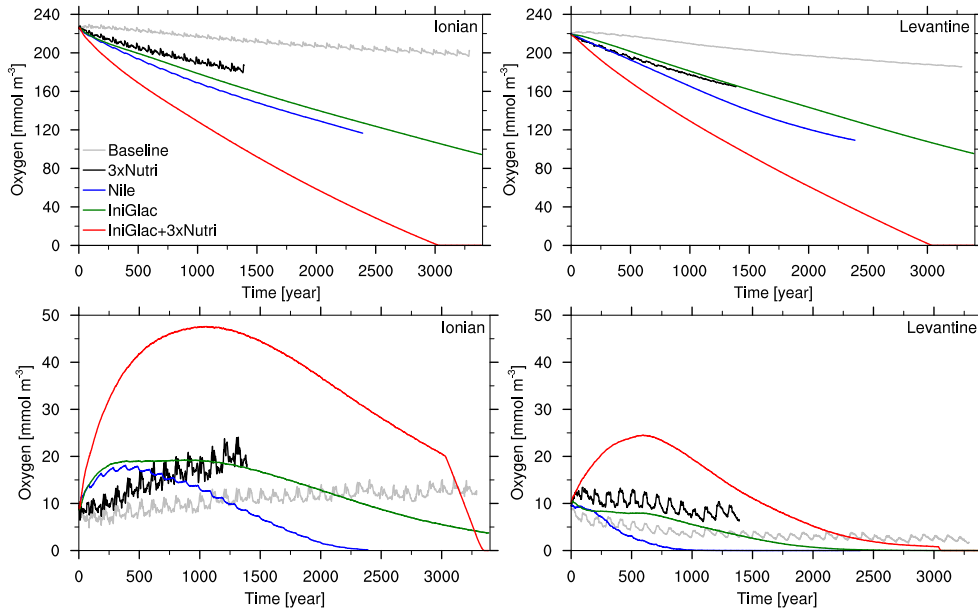


Figure 4.30: Time series of the lowest oxygen concentration averaged over the Ionian and Levantine Sea (upper panel). Time series of the maximum oxygen concentration of the oxygen minimum structure (*OMS*) calculated as explained in the text averaged over the Ionian and the Levantine Sea (lower panel).

reaches the bottom after 1000 years of simulation, which illustrates a completely homogenized oxygen depth profile.

Both, the IniGlac and IniGlac+3xNutri experiment show higher maximum *OMS* concentration peaks in the Ionian Sea compared to the other simulations, indicating the strong effect of a well-stratified deep water column preventing the homogenization of the deep water oxygen. In the IniGlac+3xNutri experiment, the general evolution of the *OMS* concentration is similar to the IniGlac simulation, however, with a strongly amplified maximum *OMS* concentration. As soon as deep water anoxia is developed after  $\sim 3000$  years, the entire depth profile is quickly homogenized until a complete deep water anoxia is established (see section 4.3.4.3, Fig. 4.31). Since the deep Levantine Sea is weakly stratified, the water column is homogenized quickly, and the onset of deep water anoxia occurs synchronously.

#### 4.3.4.3 The onset of deep water anoxia

In this section, we analyze the processes involved with the onset of deep water anoxia. Deep water anoxia is only simulated in the IniGlac+3xNutri experiment, thus, only this experiment is presented.

Figure 4.31 shows Hovmöller diagrams of oxygen during the last 500 years of simulation. In the Ionian Sea, the anoxic OMZ develops in  $\sim 1600$  m to 1700 m and expands towards the bottom within a time frame of around 250 years. In the Levantine Sea, the weakly stratified deep layers allow for a fast homogenization of the deep water. Therefore, the deep Levantine Sea shows a more or less synchronous onset of the deep water anoxia below  $\sim 1700$  m-1800 m. Proxy studies suggest a basin-wide, synchronous, and depth independent onset of anoxia for S1 formation (Mercone et al. 2000; De Lange et al. 2008; Schmiedl et al. 2010). A close inspection of the Ba accumulation (De Lange et al. 2008) and benthic ecosystem collapse (Schmiedl et al. 2010) might suggest a downward expansion of an OMZ. However, within the range of the dating precision ( $\pm 200$  years) such trends are not significant. Strohle and Krom (1997) inferred from proxy records a downward movement of the sapropel with a rate of 1000 m per 200 years. Even though our simulated onset of anoxia is in good accordance with the observations, it is not a robust result, since the onset of anoxia is largely dependent on the position of the ventilation front, which is continuously deepening. Assuming the same circulation field as the IniGlac+3xNutri combined with an even stronger eutrophication scenario, then the oxygen depletion would have been accelerated, the intermediate OMZ would have been more pronounced, and the shallower position of the ventilation front would have led to a shallower position of the onset of anoxia. In turn, a lower nutrient input would have led to an exact synchronous onset, however, the longer time frame required for the onset would also imply a deeper position of the ventilation front under the given circulation scenario.

Figure 4.32 shows the biological oxygen consumption in the various locations. As soon as the OMZ becomes anoxic, the biological consumption of dissolved oxygen is rapidly diminished. Below this anaerobic intermediate layer in the Ionian Sea, the oxygen consumption is slightly enhanced, however, not as high as just above it since anaerobic remineralization decomposes parts of the POC flux within the anoxic layer. In the profile of the Cretan Sea, there is a maximum of the biological oxygen consumption rate at the bottom, which strongly exceeds the rates modeled directly above. These high rates result from the erosion and resuspension of POC particles from the sediment back into the water column. Therefore, the bottom water layer is subjected to an enhanced POC flux from the sediment. Figure 4.33 shows the bottom layer biological oxygen consumption before the onset of deep water anoxia. Highest bottom water oxygen consumption rates are localized in shallow water areas, while in the deep ocean highest rates are localized on small-scale topographic features. Topographic irregularities enhance the bottom-flow fluid stress, which provides the energy for particle resuspension. Owing to the simplicity of our erosion module in the model, the eroded particles are shot up to the pressure point of the gridboxes, which, especially in the deep layers, can comprise several  $10^{th}$  to  $100^{th}$  of meters. In reality, this process of vertical

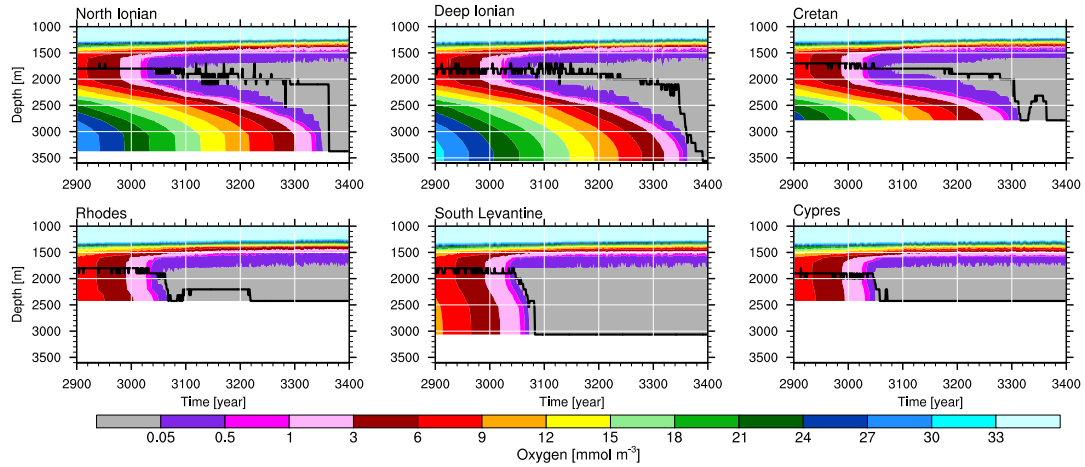


Figure 4.31: Hovmöller diagram of the dissolved oxygen concentration of the IniGlac+3xNutri simulation at the locations depicted in Figure 2.1. The black line indicates the depth of the minimum oxygen concentration. Note the nonlinear color scale.

particle movement by erosion is in the order of centimeters given the relatively small bottom-flow fluid stress in the deep ocean (Lavelle et al. 1984). Therefore, the time that the eroded particles are exposed to the water column remineralization within our model setup is overestimated, especially, in the deep ocean. Nonetheless, in reality, within a non-ventilated deep water circulation, the resuspension of particles might accelerate the development of a thin anoxic bottom water 'blanket'. Several studies have proposed the development of a thin anoxic bottom 'blanket' for sapropel formation, with the proposed mechanisms involving a restricted ventilation and high export production (Casford et al. 2003), with the additional contribution of an enhanced POC sinking velocity (Bianchi et al. 2006). These processes would favor the development of a thin anoxic bottom 'blanket', while the intermediate water would remain oxygenated. We think that the addition of a thin bottom layer in our model configuration might show the potential to develop an anoxic bottom water 'blanket' in all stagnation experiments.

Figure 4.34 shows the POC flux at the various locations. The initial reduction of the modeled POC flux with the onset of anoxia in the year 3040 is related to the contemporaneous occurrence of both aerobic and anaerobic remineralization, which are set to the threshold values of  $\geq 0.05 \text{ mmol m}^{-3}$  and  $\leq 0.5 \text{ mmol m}^{-3}$ , respectively. Therefore, during this overlapping time period the modeled POC remineralization is enhanced, which is not a real anomaly but rather a little model artifact related to the chosen oxygen thresholds for the termination of the aerobic and the onset of the anaerobic remineralization.

CHAPTER 4 THE EARLY HOLOCENE SAPROPEL FORMATION

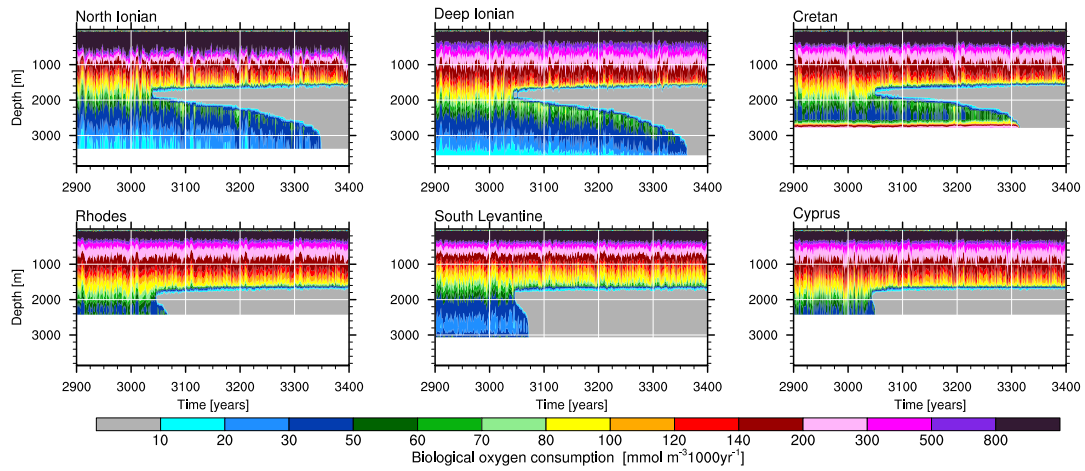


Figure 4.32: Hovmöller diagram of the aerobic biological oxygen consumption of the IniGlac+3xNutri simulation at the locations depicted in Figure 2.1. Note the nonlinear color scale.

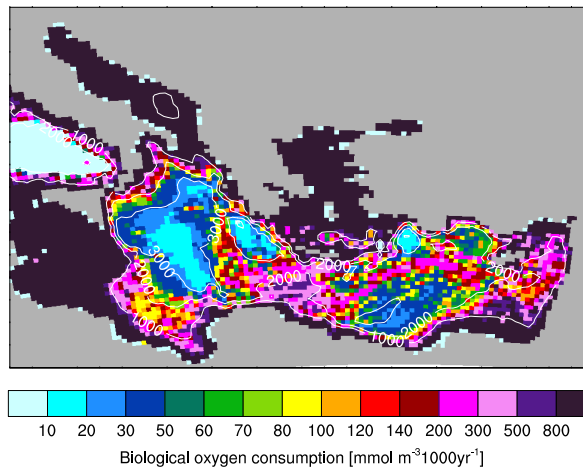


Figure 4.33: Bottom water biological oxygen consumption averaged over the year 3201-3300 of the IniGlac+3xNutri simulation superimposed with topographic contours [m]. Note the nonlinear color scale..

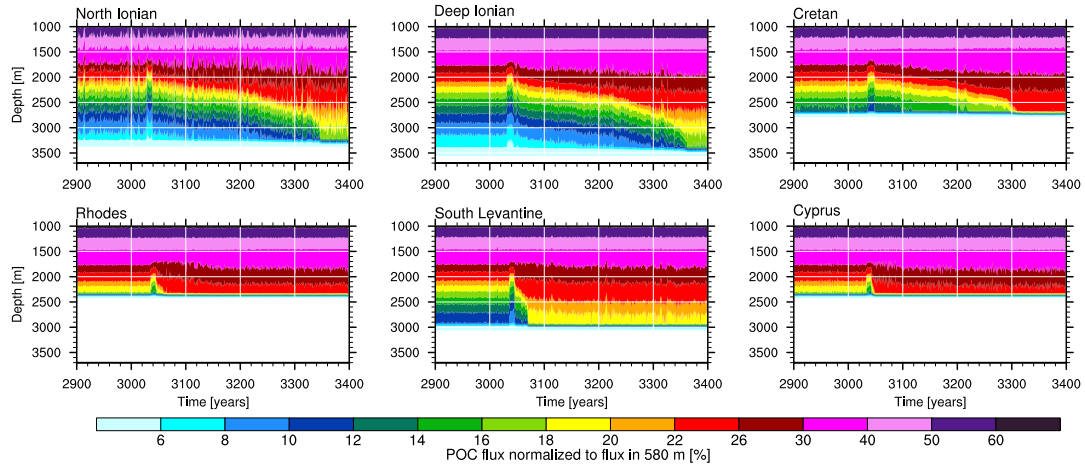


Figure 4.34: Hovmöller diagram of the POC flux normalized to the POC flux in 580 m in the IniGlac+3xNutri simulation at the locations depicted in Figure 2.1. Note the nonlinear color scale.

The profiles of the Northern Ionian, Deep Ionian, and Cretan show a pronounced anoxic OMZ at intermediate depth propagating towards the bottom with time (Fig. 4.31). The reduced remineralization of POC within the intermediate anoxic OMZ results in a higher preservation of the POC flux throughout the OMZ (Fig. 4.34). Therefore, below the anoxic OMZ, the POC flux is only slightly reduced compared to the flux above the OMZ. This process leads to an enhanced POC flux to the sea floor. In the perspective of a sediment core observation, an enhanced POC flux to the sediment might be interpreted as an eutrophication signal before the onset of the sapropel. In fact, in sediment cores of the eastern Mediterranean Sea, such indications have been documented by Kuhnt et al. (2007, 2008) and Schmidt (2007), who found just before the onset of the deep water oxygen deficiency during the earliest Holocene an increase in the benthic foraminiferal numbers (BFN), which indicates enhanced food supply, and thus, a possible eutrophication. However, synchronously the diversity of the benthic foraminifera decreases. While the high BFN might be explained by the enhanced food supply, the low diversity points towards oxygen stress. Overall, many species cannot survive under the extreme oxygen conditions, but a few species profit from the enhanced food supply. If the rise in the BFN would result from an eutrophication signal, then we should expect an increase of the benthic diversity before the benthic ecosystem collapses under the anoxic conditions. Thus, the enhanced POC flux might indicate the development of an anoxic OMZ at intermediate depth, and its fast downward expansion, rather than an eutrophication signal.

## CHAPTER 4 THE EARLY HOLOCENE SAPROPEL FORMATION

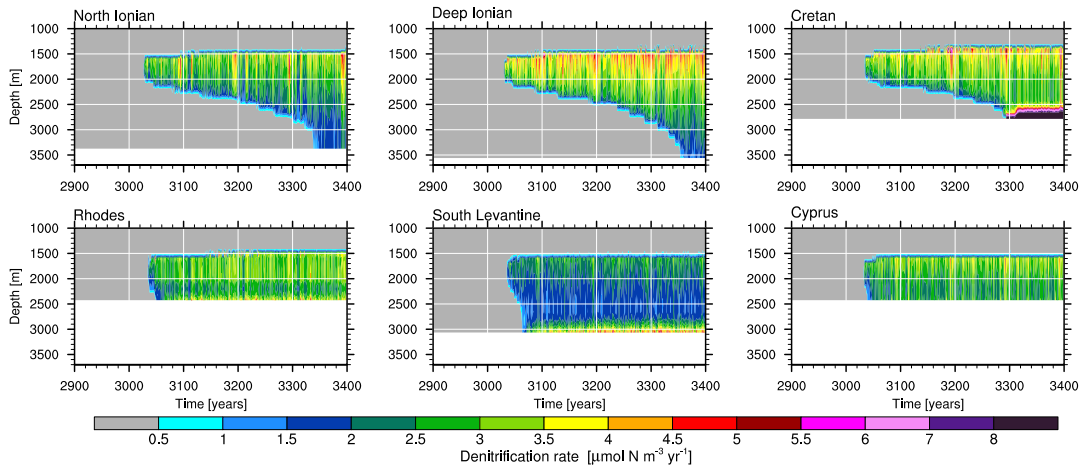


Figure 4.35: Hovmöller diagram of the denitrification rate in the IniGlac+3xNutri simulation at the locations depicted in Figure 2.1. Note the nonlinear color scale.

As soon as there is no oxygen available, POC is remineralized through the processes of denitrification. During the process of denitrification, organic matter, an electron donor, is decomposed by reducing oxidized forms of nitrogen, with a cycle of reducing nitrate ( $\text{NO}_3^-$ ) to nitrite ( $\text{NO}_2^-$ ) to nitric oxide ( $\text{NO}$ ) to nitrous oxide ( $\text{N}_2\text{O}$ ) to dinitrogen ( $\text{N}_2$ ), which, as gas, is released into the atmosphere. The ocean biogeochemical model treats the anaerobic remineralization in the water column and the sediments. For denitrification, however, not all of the intermediate nitrogen forms are resolved, but nitrate is immediately reduced to dinitrogen.

The modeled rate of denitrification is shown in Figure 4.35. The onset of the modeled denitrification occurs as soon as the oxygen concentration falls below the threshold value of  $0.5 \text{ mmol m}^{-3}$ . Thus, the onset of the modeled denitrification is marked by a sharp boundary. The denitrification rate is highest in the upper layers of the anoxic OMZ, since this area receives the highest POC flux. In the profile of the Cretan and Southern Levantine, there is a maximum of the denitrification rate at the bottom, which strongly exceeds the rates modeled in the upper layers of the OMZ. These high rates resemble the same chain of processes as were previously described for the aerobic remineralization, with particle erosion, resuspension, and thus, enhanced denitrification.

The reduction of nitrate by denitrification leads to a decrease of the nitrate concentration. Figure 4.36 shows the evolution of the nitrate and phosphate concentrations for the last 500 years of simulation in the same locations at 1800 m depth. As soon as denitrification starts, the nitrate is used for denitrification, which overall reduces the nitrate concentration. On the other hand, the phosphate concentration continues to rise, however, with a reduced rate since the anaerobic remineralization is less efficient

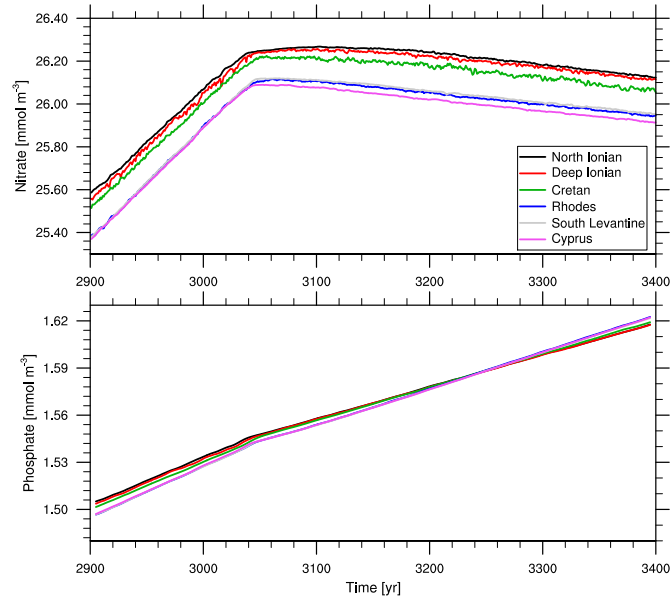


Figure 4.36: Time series of dissolved nitrate (upper panel) and dissolved phosphate (lower panel) at 1800 m depth in the IniGlac+3xNutri simulation at the locations depicted in Figure 2.1.

than the aerobic remineralization.

### 4.3.5 Sediment

In this section we focus on the spatial and temporal patterns of the simulated sediment POC burial flux, as well as the sediment pore water  $\delta^{13}\text{C}$  isotopes, and compare the results with observations of the pre-sapropel and sapropel period. Through this approach we aim to assess the plausibility of the simulated scenarios with respect to S1 formation.

Since a complete deep water oxygen deficiency has only evolved in the IniGlac+3xNutri experiment, we can only compare this experiment with observations from the period of S1 deposition. Given that it takes several millennia to develop deep water anoxia, with the exact timescale depending on the strength of the deep water stagnation and/or biological production, we can still analyze the 3xNutri, Nile and IniGlac experiment in the light of being realistic for the time prior to the onset of the deep water oxygen deficiency.

#### 4.3.5.1 Sediment particulate organic carbon burial flux

The sediment POC burial flux is determined by the strength of the biological export production, the remineralization of POC in the water column and the sediment, and

the strength of erosion, repeated resuspension, transport and remineralization of POC at the sediment-water interface. Section 3.3.5.1 gives a more detailed overview of the individual processes that determine the sediment POC burial flux.

Figure 4.37 shows the sediment POC burial flux over time, and Figure 4.38 shows the last 500 years of the anoxic IniGlac+3xNutri experiment at the same locations.

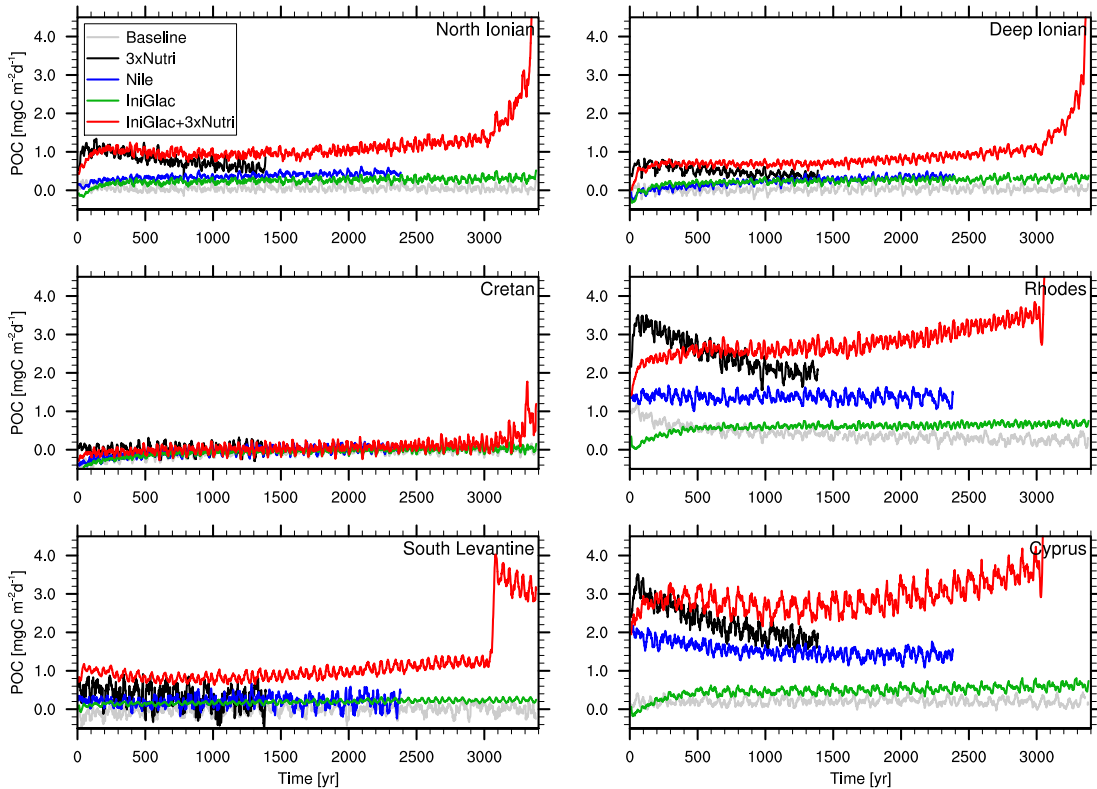


Figure 4.37: Sediment POC burial flux of indicated model experiments over the entire time of simulation at locations as indicated in Figure 2.1. Note that the IniGlac+3xNutri experiment shows fluxes beyond the scale of the plot in the North Ionian, Deep Ionian, Rhodes and Cyprus locations at the end of the simulation. The last 500 years of the IniGlac+3xNutri is shown in more detail in Figure 4.38. Data was smoothed by applying a 20-year running mean.

As soon as the IniGlac+3xNutri experiment develops bottom water anoxia, the POC burial flux increases rapidly since the POC is no longer subjected to aerobic remineralization in the water column and the sediment (Fig. 4.38). In the northern and deep Ionian as well as the Cretan Sea, the IniGlac+3xNutri experiment shows the development of an anoxic OMZ at intermediate depth, which expands towards the bottom within  $\sim 250$  years (section 4.3.4.3). This downward expansion of the anoxic interme-

diate layer slowly increases the POC flux to the sediment in the Ionian and Cretan locations. By the time when the anoxic OMZ reaches the bottom, the POC burial flux increases rapidly by  $\sim 2 \text{ mgC m}^{-2} \text{ d}^{-1}$ , and is then slowly decreases due to anaerobic carbon decomposition in the sediment. (Fig. 4.38).

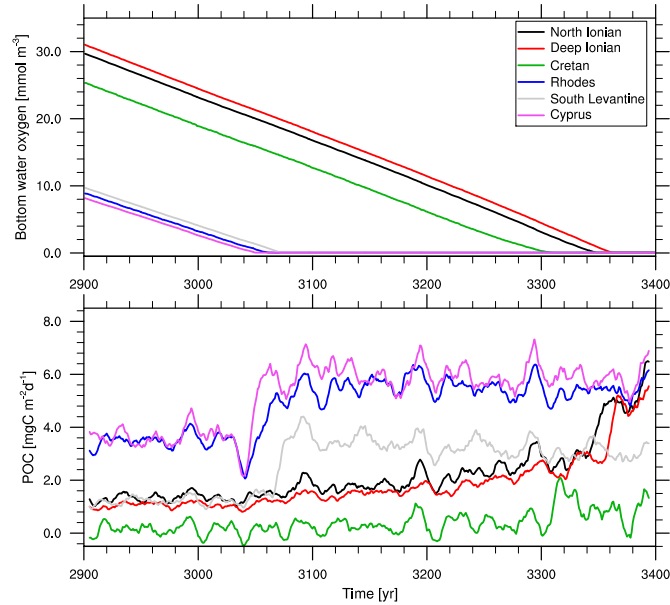


Figure 4.38: Bottom water annual mean dissolved oxygen concentration (upper panel) and annual mean sediment POC burial flux (lower panel) for the last 500 years of simulation of the IniGlac+3xNutri experiment at locations as indicated in Figure 2.1. POC flux was smoothed by applying a 10-year running mean.

In all locations depicted in Figure 4.37, the oligotrophic Baseline and IniGlac experiments show a relatively small drift of their POC sediment burial fluxes. In contrast, the eutrophication scenarios all show a much stronger drift of the POC sediment burial flux. While the well ventilated 3xNutri experiment shows a decreasing POC burial flux after the first peak everywhere, the stagnation scenarios show a drift towards higher fluxes (except for the Nile experiment at Cyprus). A comparison between the POC export production (Fig. 4.22) and the sediment POC burial flux (Fig. 4.37) shows that locations of high export production do not always translate into high POC burial fluxes, which emphasizes the role of other processes shaping the sediment POC burial flux. The dominating processes determining the POC sediment burial flux differ among the locations, while they are the same in-between the experiments at all locations. The North Ionian, Deep Ionian, Rhodes, and Cyprus locations are dominated by the biological remineralization within the sediment (not shown). In contrast, the Cretan and

southern Levantine locations are more erosion dominated (not shown).

The interannual variability of the POC flux among the experiments is mainly controlled by the POC export production, therefore, the eutrophicated experiments show the highest interannual variability.

Figure 4.39 shows maps of the sediment POC burial flux superimposed with observations from sediment cores for the pre-sapropel time slice for all experiments, and for the sapropel time slice only for the anoxic IniGlac+3xNutri experiment. As in the CTRL simulation, all experiments show a high small-scale variability of the POC burial flux. The model simulates a too strong erosion in particular in shallow water areas of the Adriatic Sea, the Aegean Sea, the Sicilian-Tunisian Platform, and the Nile delta zone. Therefore, we concentrate our interpretation to the deep basin below 1500 m depth.

The relatively warm Baseline simulation (compared to the IniGlac) shows the lowest POC burial fluxes everywhere. In contrast, the 3xNutri experiment, with the same physical circulation as the Baseline, shows an enhanced sediment POC burial flux compared to the Baseline experiment. However, the 3xNutri experiment is still drifting towards lower fluxes over large areas, hence, the map of the POC burial flux of the 3xNutri experiment should be interpreted with caution. High burial fluxes are simulated by the IniGlac+3xNutri experiment for both the pre-sapropel and sapropel period because the POC flux to the sediment is high, and the stagnating cold (anoxic during the sapropel) deep water limits the bacterial remineralization and physical erosion. A visual comparison with the observations highlights the oligotrophic IniGlac experiment as a most plausible pre-sapropel state. It shows higher POC burial fluxes than the Baseline simulation, with the same riverine nutrient regime but warmer deep water, and slightly lower POC burial fluxes than the Nile experiment with its eutrophication induced through the Nile river and the warmer stagnating deep water circulation. Nonetheless, the Nile experiment also shows a reasonable POC burial flux, over most of the deep basin. However, in the eastern Levantine, in the area of the Nile plume, the simulated POC burial flux of the Nile experiment is too high, induced by the strong Nile riverine nutrient input in this experiment. This indicates that the Nile riverine nutrient load is too high. Since the Baseline simulation shows a rather too low POC burial flux, and the Nile experiment only overestimates the burial flux in the eastern Levantine, this might indicate that the pre-sapropel eastern Mediterranean was basin-wide moderately eutrophicated. However, since the IniGlac shows a good accordance with the POC burial flux observations, the deep water temperature, modulating the remineralization rate, is highly important in shaping the POC burial flux.

Figure 4.40 compares the observed versus the modeled POC fluxes. The temporal variability and spatial small-scale variability of the simulations overweights the temporal variability within the sediment core time slice observations, and are highest in the shallower locations. While the Baseline simulation shows a reasonable agreement with

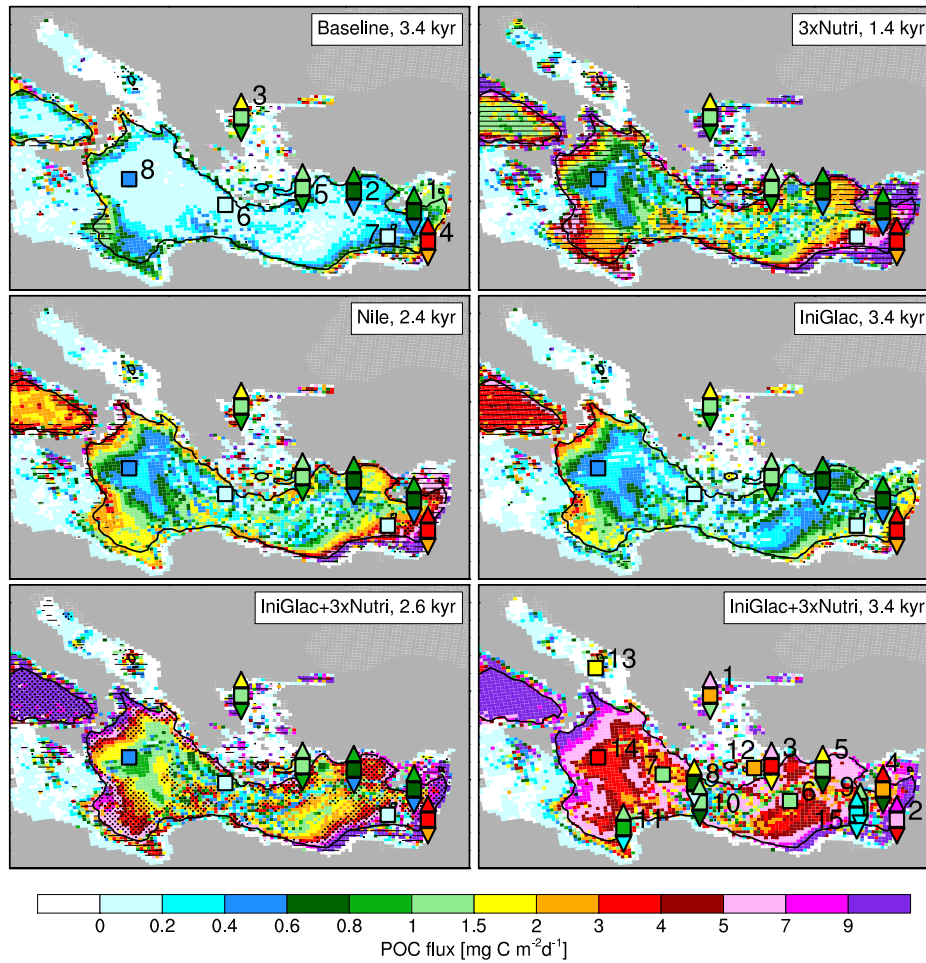


Figure 4.39: Sediment POC burial flux of indicated model experiment time slices (e.g. 3.4 kyr averaged between 3301-3400) superimposed with sediment POC burial flux data from sediment cores for the pre-sapropel time slice averaged between 10.5 to 11.5 kyr BP, and the sapropel time slice averaged between 6.5 to 9.5 kyr BP (sapropel observations only shown in subfigure IniGlac+3xNutri, 3.4 kyr). Squares show mean values, triangle pointing upward maximum, and triangles downward minimum value from sediment core data measurements of the corresponding time slices. The black line represents the 1500 m contour line. Line shaded regions show areas where the trend of POC burial flux is on average lower than  $-0.05 \text{ mgC m}^{-2} \text{ d}^{-1}$  over the last 500 years of simulation, and point shades areas where this trend is higher than  $0.05 \text{ mgC m}^{-2} \text{ d}^{-1}$ . Note that in IniGlac+3xNutri, 3.4 kyr no trends are illustrated because the simulation does not cover 500 years of deep anoxia (sapropel). Core labels for allocation of cores in Figure 4.40. Sediment core data for pre-sapropel time slice taken from sites: MD84-641 (Fontugne and Calvert 1992), Geo-Tü SL119 (Milker et al. 2006), ODP site 160-970 (Meyers and Bernasconi 2009), Geo-Tü SL114 (Schmidt 2007), Geo-Tü SL148, Geo-Tü SL112, Geo-Tü SL123 (Kuhnt 2008), SL 71 (Möbius et al. 2010). Sediment core data for sapropel time slice taken from sites: Geo-Tü SL148, Geo-Tü SL112, Geo-Tü SL123 (Kuhnt 2008), Geo-Tü SL114 (Schmidt 2007), Geo-Tü SL119 (Milker et al. 2006), BC19, SL114 (Slomp et al. 2002), SL60, MD90-917 (Slomp et al. 2004), ODP site 160-970 (Meyers and Bernasconi 2009), MD84-641 (Fontugne and Calvert 1992), SL 71, #569, #563, #562 (Möbius et al. 2010).

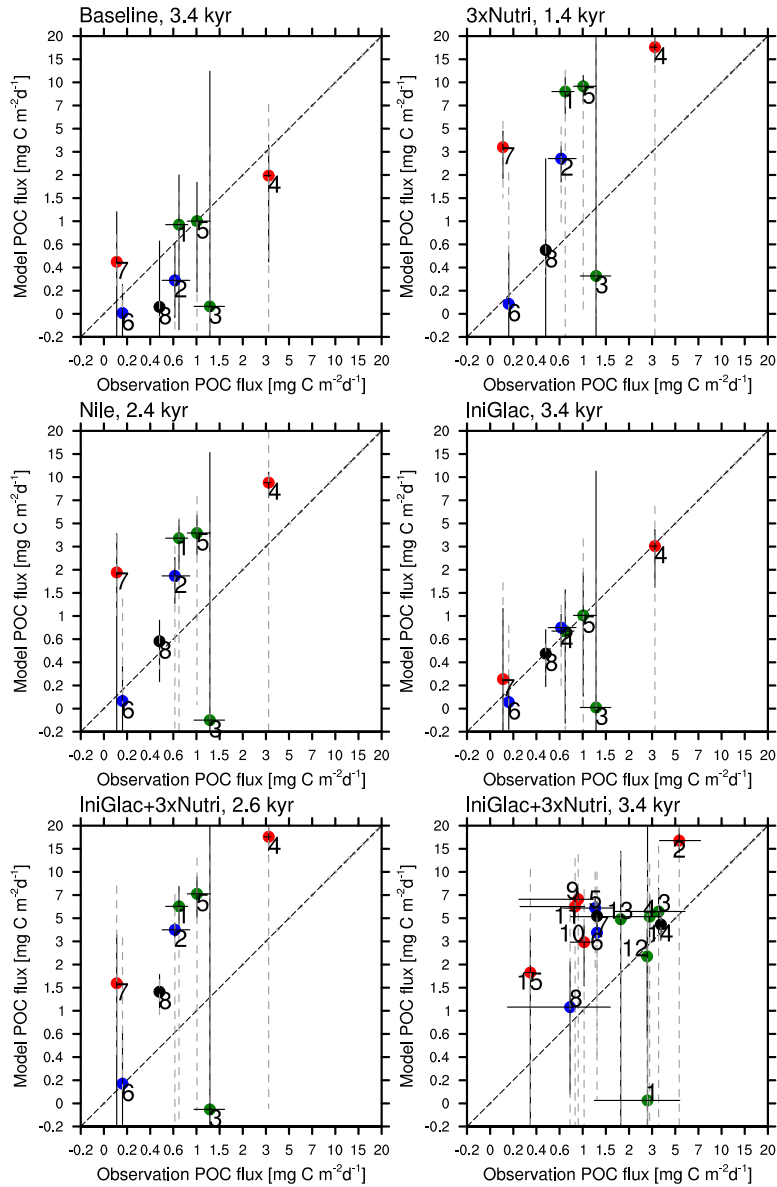


Figure 4.40: Sediment POC burial flux versus modeled POC burial flux of the indicated model experiment time slices (e.g. 3.4 kyr averaged between 3301-3400). Points represent the averaged observed flux of the sediment cores versus 100-year averaged modeled flux. Black horizontal lines represent the maximum temporal variation of the observations between 10.5 to 11.5 kyr BP for the pre-sapropel and 6.5 to 9.5 kyr BP for the sapropel period (only shown in IniGlac+3xNutri, 3.4 kyr). The black vertical lines shows  $\pm 1$  standard deviation of the interannual variability within the model time slices. Grey dashed vertical lines represent the maximum small-scale spatial variation of mean values within a  $2 \times 2$  gridbox window around the original core location. Colors indicate the water depth of the model gridbox at the core locations: green  $< 1000$  m,  $1000 \text{ m} \leq \text{red} < 2000$  m,  $2000 \text{ m} \leq \text{blue} < 3000$  m, black  $\geq 3000$  m. Sediment core labels as in Figure 4.39. Note the nonlinear axes scales, and that the plot size does not always cover the full data range of the temporal and spatial variations of model results on every point.

the observations, the Nile, 3xNutri, and IniGlac+3xNutri (pre-sapropel) experiments deviate more strongly from the 1:1 line in their mean fluxes, particularly above 2000 m. The best agreement between the observations and the model shows the IniGlac experiment, with only one site, in the northern Aegean Sea, being strongly underestimated by the mean output of the model. In section 3.3.5.1 we discussed that the model has problems to simulate the POC burial flux along marginal areas, which might explain the poor representation of the northern Aegean site. Nevertheless, for the time prior to the onset of the sapropel, we identify the IniGlac experiment, with its cold stagnating deep water circulation and its oligotrophic regime to be the most plausible scenario. This is further corroborated by benthic foraminifera indicating low organic matter availability at the sea floor prior to S1 deposition (Schmidt 2007; Kuhnt 2008). Given the high temporal variability of the POC burial flux of the sediment core observations during the sapropel formation, the IniGlac+3xNutri experiment might be slightly more realistic for the time of the sapropel formation. Yet, this might indicate that during the time of sapropel formation there was a transition to a more eutrophic regime.

#### 4.3.5.2 Sediment pore water $\delta^{13}\text{C}$ isotopes

In this section we focus on the simulated sediment pore water  $\delta^{13}\text{C}$  DIC. Through the comparison of our model results with sediment observations of benthic foraminifera  $\delta^{13}\text{C}$ , we aim to assess a plausible circulation and nutrient regime describing the early Holocene sapropel formation. The sediment pore water  $\delta^{13}\text{C}$  DIC is explicitly simulated by the model, and can be directly compared to benthic foraminifera  $\delta^{13}\text{C}$  records. The processes that determine the  $\delta^{13}\text{C}$  distribution are detailed in chapter 3.

In the Baseline simulation, surface  $\delta^{13}\text{C}$  DIC values (not shown) in the Ionian, Levantine and Adriatic Sea are around 0.1‰ heavier than in the pre-industrial CTRL simulation. Even though the atmospheric  $\text{CO}_2$  concentration in the early Holocene is lower, the enhanced seasonal cycle of the SST as well as the enhanced wind speed lead to a higher  $\text{CO}_2$  solubility and transfer velocity. The closed Bosphorus leads to a shutdown of the  $^{13}\text{C}$ -depleted surface waters from the Black Sea, and the reduced LIW formation mixes less  $^{13}\text{C}$ -depleted water towards the surface. Even though the biological production is reduced over most of the basin in the Baseline compared to the CTRL simulation, the overall  $\delta^{13}\text{C}$  values are slightly higher in the Baseline simulation. In the 3xNutri experiment, the biological production is everywhere enhanced (Fig. 4.20), thus, the surface  $\delta^{13}\text{C}$  are slightly heavier than in the Baseline simulation. In the IniGlac experiment the surface  $\delta^{13}\text{C}$  values are also heavier than in the Baseline simulation, since the development of the strong pycnocline in the IniGlac experiments reduces the upwelling of  $^{13}\text{C}$ -depleted deep water. Even though the biological produc-

tion is reduced, the overall  $\delta^{13}\text{C}$  values are slightly higher in the IniGlac compared to the Baseline simulation. Overall, the differences between the early Holocene and the pre-industrial CTRL upper ocean  $\delta^{13}\text{C}$  values are small, which is in accordance with epipelagic and mesopelagic  $\delta^{13}\text{C}$  for the time prior and after the S1 deposition (Casford et al. 2003).

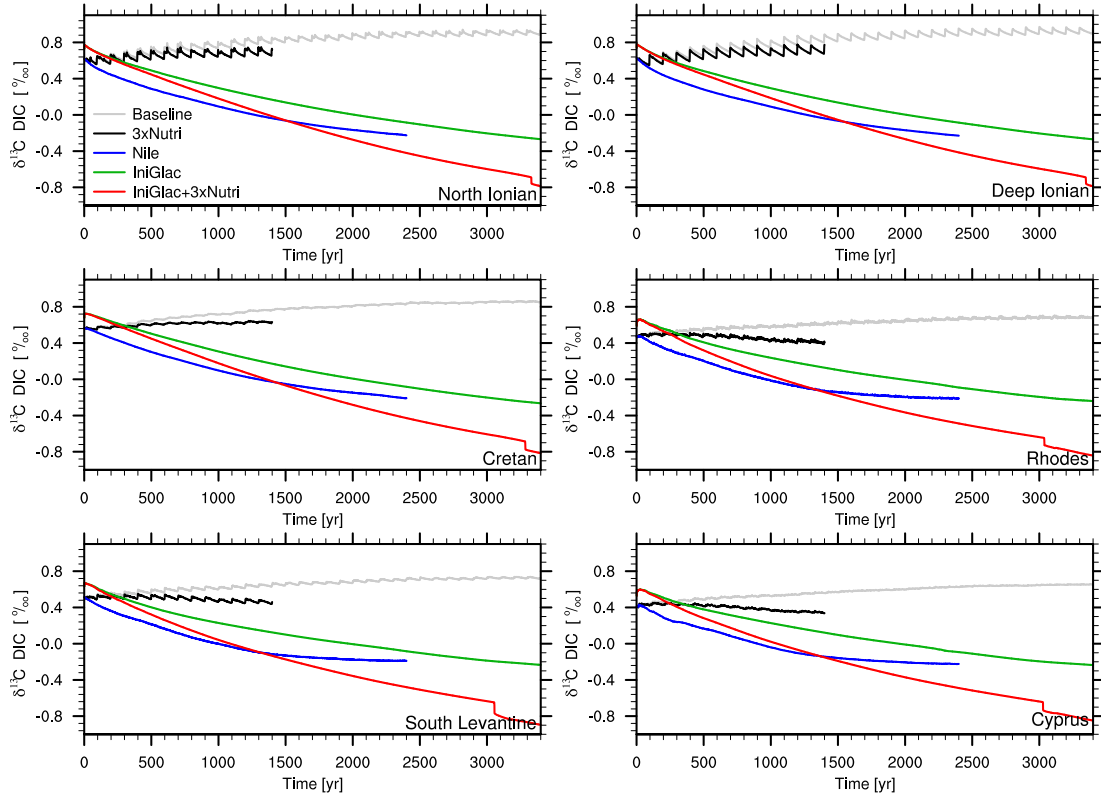


Figure 4.41: Sediment pore water  $\delta^{13}\text{C}$  DIC averaged between 1.2–2 cm depth at locations as indicated in Figure 2.1.

Figure 4.41 shows the time evolution of the sediment pore water  $\delta^{13}\text{C}$  DIC at various locations throughout the eastern Mediterranean Sea. While the Baseline simulation shows a stable  $\delta^{13}\text{C}$  DIC throughout time, all other simulations show a drift towards more depleted values. In the 3xNutri experiment, the drift towards more depleted values increases from west to east, indicating that the Ionian Sea is predominantly influenced by deep water formation, while the Levantine Sea accumulates relatively more excess  $^{12}\text{C}$  through the remineralization of the enhanced POC fallout. In both, the IniGlac and IniGlac+3xNutri simulation, the initialization with the cold deep water limits the remineralization, and thus, the release of the light  $^{12}\text{C}$  isotope, which overall

initially increases the  $\delta^{13}\text{C}$  DIC values compared to the Baseline simulation. Over time, both the IniGlac and IniGlac+3xNutri simulation show a flattening of the  $\delta^{13}\text{C}$  DIC depletion, indicating the slow erosion of the density gradient with a continuous increasing imprint of surface enriched  $\delta^{13}\text{C}$  DIC water. In contrast, the Nile experiment shows an initially strong depletion at all sites, which flattens more rapidly after  $\sim 1300$  years of simulation. With its warmer deep water mass compared to the IniGlac experiment, the Nile experiment shows a more efficient remineralization of the organic material in the sediment. Thus, even though its sediment POC burial flux is lower than the POC burial flux of the IniGlac+3xNutri experiment (Fig. 4.37), the more efficient remineralization within the warmer deep water mass leads to a stronger  $\delta^{13}\text{C}$  DIC depletion. Over time, the deep water stagnation of the Nile experiment weakens more strongly than in the IniGlac+3xNutri experiment. Therefore, the  $\delta^{13}\text{C}$  DIC enriched water from the surface imprints more strongly on the pore water  $\delta^{13}\text{C}$  DIC in the Nile than in the IniGlac+3xNutri simulation. With the onset of the deep water anoxia in the IniGlac+3xNutri experiment, after more than  $\sim 3000$  years, the pore water  $\delta^{13}\text{C}$  DIC is initially rapidly depleted, which is a model artifact due to the contemporaneous release of the light  $^{12}\text{C}$  isotope during the overlapping period of aerobic and anaerobic remineralization. Due to the high nitrate concentrations, the denitrification processes is initially very strong, releasing almost similar concentrations of the light  $^{12}\text{C}$  isotope.

The geographical distribution of the pore water  $\delta^{13}\text{C}$  DIC is illustrated in Figure 4.42. In the Baseline simulation, on the one hand, the slightly heavier surface  $\delta^{13}\text{C}$  DIC signal is transferred to the deep Ionian sediment pore water via deep water formation, and on the other hand, the relatively lower export production leads to a reduced release of the light  $^{12}\text{C}$  isotope during remineralization at depth compared to the CTRL simulation. Likewise to the CTRL simulation, EMDW formation leads to a rapid increase of the sediment pore water  $\delta^{13}\text{C}$  DIC due to the entrainment of isotropically enriched upper ocean waters. The amplitude of the  $\delta^{13}\text{C}$  enrichment during EMDW formation events is decreased from west to east (Fig. 4.41). Along the Israeli coast, in the Nile plume area, the enhanced export production of the Baseline leads to a slightly higher pore water  $\delta^{13}\text{C}$  DIC depletion of around 0.1 ‰ compared to the CTRL simulation. The major difference between the CTRL and Baseline simulation is in the northern Aegean Sea, where the  $\delta^{13}\text{C}$  DIC values are rather high compared to the CTRL as well as to the pre-sapropel observations. While the difference to the CTRL simulation is expected due to the missing inflow of nutrient-rich and  $^{13}\text{C}$  DIC depleted water from the Black Sea, the difference to the observations might be explained by the input of light dissolved organic carbon from terrestrial sources in the northern Aegean (Aksu et al. 1999; Kuhnt et al. 2008), due to enhanced precipitation in the northern borderlands starting to intensify at around 11 kyr BP (Rohling and Hilgen 1991; Kotthoff et al. 2008).

In the 3xNutri experiment the general pattern is similar to the Baseline simulation,

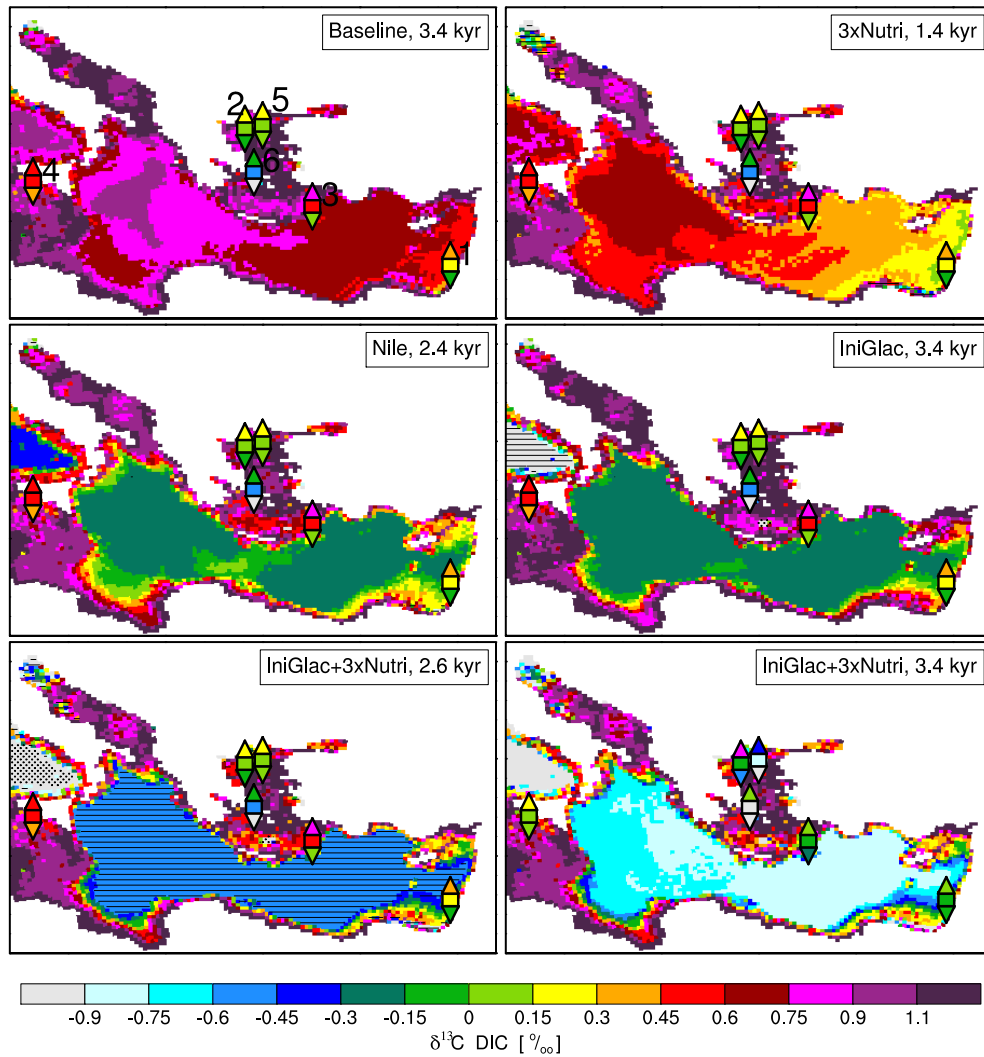


Figure 4.42: Sediment pore water  $\delta^{13}\text{C}$  DIC averaged between 1.2–2 cm depth of the model experiment time slices (e.g. 3.4 averaged between 3301–3400) superimposed with observed  $\delta^{13}\text{C}$  of shallow infaunal benthic *Uvigerina mediterranea* averaged between 10.5 to 11.5 kyr BP for the pre-sapropel and 6.5 to 9.5 kyr BP for the sapropel period (only shown in IniGlac+3xNutri, 3.4 kyr). Squares show mean values, triangle pointing upward maximum and triangles pointing downward minimum values of  $\delta^{13}\text{C}$  from sediment core data of the corresponding time slices. Line shaded regions show areas where the trend of  $\delta^{13}\text{C}$  DIC values are on average lower than  $-0.02$  ‰ over the last 500 years of simulation, and point shades areas where this trend is higher than  $0.02$  ‰. Note that in IniGlac+3xNutri, 3.4 kyr no trends are illustrated because the simulation does not cover 500 years of deep anoxia (sapropel). Core labels for allocation of cores in Figure 4.43. Sediment core data of pre-sapropel and sapropel time slice taken from cores: Geo-Tü SL148, Geo-Tü SL112, Geo-Tü SL123 (Kuhnt 2008), SL78 (Schmiedl unpublished data), SL-31, SL-A9 (Abu-Zied 2001).

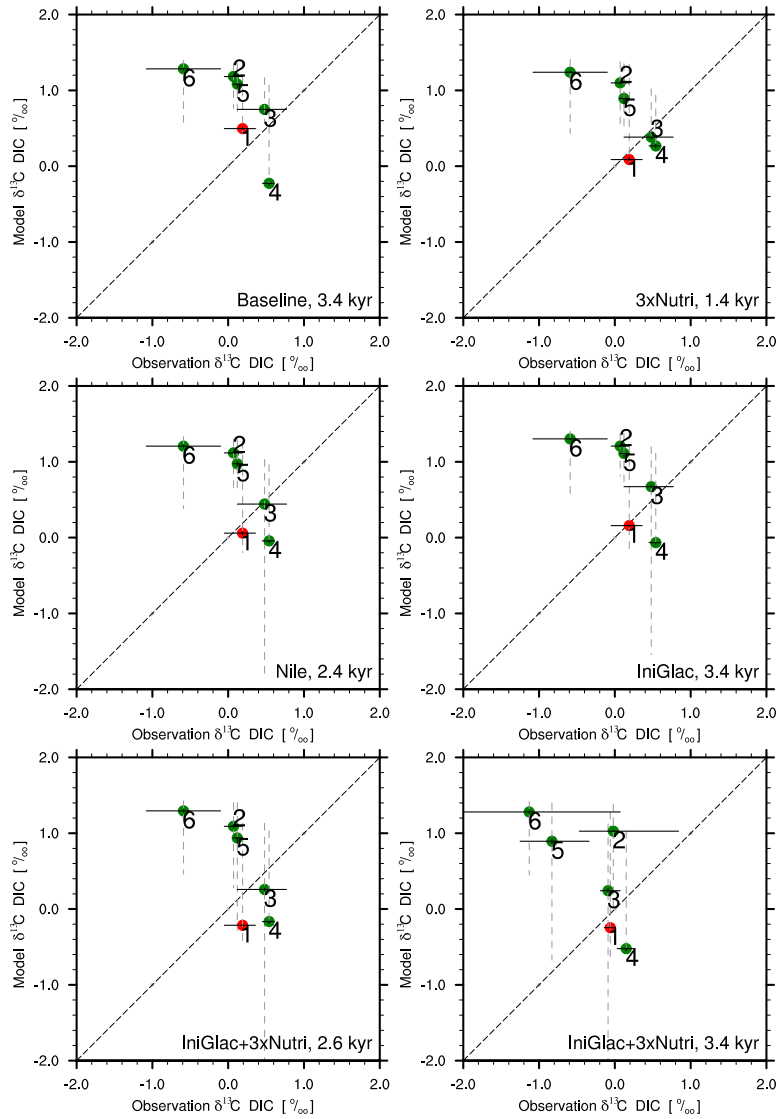


Figure 4.43: Observed  $\delta^{13}\text{C}$  of shallow infaunal benthic *Uvigerina mediterranea* versus modeled sediment pore water  $\delta^{13}\text{C}$  DIC averaged between 1.2–2 cm depth. Points show averaged observed  $\delta^{13}\text{C}$  of benthic foraminifera in the sediment cores between 10.5 to 11.5 kyr BP for the pre-sapropel, and between 6.5 to 9.5 kyr BP for the sapropel period (only shown in IniGlac+3xNutri, 3.4 kyr) versus 100-year averaged  $\delta^{13}\text{C}$  DIC of the model simulations. Black horizontal lines represent the maximum temporal variation of the observations in the corresponding time slices. Black vertical lines represent  $\pm 2$  standard deviation of the interannual variability within the model time slices. Grey dashed vertical lines represent the maximum small-scale spatial variation of 100-year mean modeled values within a  $2 \times 2$  gridbox window around the original core location. Colors indicate the water depth of the model gridbox at the core locations: green  $< 1000$  m,  $1000 \text{ m} \leq$  red  $< 2000$  m. Sediment core labels as in Figure 4.42.

however, the pore water  $\delta^{13}\text{C}$  DIC is more depleted due to the enhanced remineralization of the increased organic matter production. The strong eutrophication of the eastern Levantine through the Nile river is directly transferred to the sediment pore water  $\delta^{13}\text{C}$  DIC, so in total the east-west gradient of the deep eastern Mediterranean is stronger in the 3xNutri experiment than in the Baseline.

In contrast, there is no spatial gradient of the pore water  $\delta^{13}\text{C}$  DIC of the deep basin in the stagnating deep water circulation experiments. The reason that the Nile and IniGlac experiment show very similar pore water  $\delta^{13}\text{C}$  DIC throughout the deep basin is simply due to the 1000 year shorter simulation period of the Nile experiment. The trend of the Nile experiment depletes the pore water  $\delta^{13}\text{C}$  DIC slower than the IniGlac experiment (Fig. 4.41). The IniGlac+3xNutri shows the strongest trend of  $\delta^{13}\text{C}$  DIC depletion in the deep basins.

Figure 4.43 shows the observed  $\delta^{13}\text{C}$  of shallow infaunal benthic *Uvigerina mediterranea* versus the modeled pore water  $\delta^{13}\text{C}$  DIC. A direct comparison of the simulated pore water  $\delta^{13}\text{C}$  DIC with the benthic  $\delta^{13}\text{C}$  signal observed in sediment cores does not highlight any particular simulation. Anyhow, a model observation comparison is rather crude, concerning the sparse data coverage concentrated along the basin margins, where the model simulates the steepest  $\delta^{13}\text{C}$  gradients.

## 4.4 Discussion and Summary

The sapropel S1 formation implies the development of a deep water oxygen deficiency in the eastern Mediterranean Sea. Commonly, the S1 oxygen depletion was proposed to be triggered by an enhanced humidity over the broader Mediterranean area, in particular, over Africa during the African humid period (AHP), fueling enhanced riverine runoff and/or nutrient load. Both of these processes could have provoked a stagnating deep water circulation and/or enhanced biological productivity, and consequently would have initiated the S1 oxygen depletion. Also a stagnating deep water circulation in response to the warming and freshening of the Mediterranean Sea during the last glacial-interglacial transition period was proposed to have triggered S1 formation. Here we present a set of ocean biogeochemical model simulations covering a purely riverine induced eutrophicated scenario (3xNutri), the AHP climatic induced enhanced Nile runoff and nutrient load (Nile), as well as the climatic changes associated with the last glacial-interglacial transition period combined with a low (IniGlac) and high riverine nutrient input scenario (IniGlac+3xNutri). From these simulations we infer the major mechanisms leading to the sapropel S1 formation.

Our simulations show, irrespective of the imposed climate scenarios, a shallowing of the pycnocline by around  $\sim 50$  to  $250$  m in the Levantine compared to the pre-industrial CTRL simulation, and a strongly reduced LIW formation. This is partly in accordance with Myers et al. (1998), who also reported a reduction of the LIW formation, however, a considerably shallower position of the pycnocline, suggesting that it would have the potential to fuel enhanced biological production in the form of a DCM. In our simulations, the nutrient availability in the euphotic layer is largely controlled by the external nutrient input, while the intermediate and deep circulation play only a minor role. Compared to a well-ventilated ocean, a stagnating deep water circulation reduces the POC export production by  $\sim 8\%$  since nutrients are trapped in the deep stagnating water body, which limits the biological productivity. In contrast, a tripling of the riverine nutrient input under a given circulation scenario increases the POC export production by  $\sim 66\%$ , with much of the additional production concentrated close to river mouths.

For the early Holocene control climate (Baseline simulation), the model simulates a similar to present-day well-ventilated stable circulation and biogeochemical cycles. The same circulation field, combined with a strong eutrophication scenario (3xNutri experiment), leads to an enhanced oxygen consumption. However, the continuous strong deep water ventilation prevents the evolution of deep water anoxia within a realistic time frame for S1 formation. In fact, it seems that the enhanced oxygen utilization and the deep ventilation will equilibrate at a still highly oxygenated state. Based on these findings we exclude the enhanced biological productivity hypothesis as a plausible sce-

nario for S1 formation. Bianchi et al. (2006) performed a similar experiment, in which they imposed eutrophication scenarios on the present-day physical conditions in a 1D marine ecosystem model. Likewise to our deep water oxygen evolution in the 3xNutri simulation, their results did not show considerable effects of a strong eutrophication on the deep water oxygen profile within the well-ventilated deep water.

Physical ocean-only modeling studies showed that an enhanced Nile river runoff, as a consequence of the AHP climate, induces a density stratification inhibiting deep water formation. Myers (2002) presented a simulation with the Nile runoff enhanced by 2.5 times with respect to the pre-industrial discharge, and reports a reduction of the deep water formation penetration depth to 1500 m. Due to the short simulation of 100 years conducted by Myers (2002), it remained open how the simulated deep circulation behaves in the long term. Adloff (2011) showed 1.5 kyr of a simulation with the Nile runoff enhanced by 2.7 times with respect to the Baseline discharge and reported a recovery of the deep water circulation after a few centuries. Similarly to the findings of Meijer and Dijkstra (2009), we show that the stability of a density stratification is strongly dependent on the mixing parameterization. We further show that the model setup applied by Adloff (2011) is rather diffusive, which strongly erodes the Nile freshwater induced density stratification. Through a series of sensitivity experiments we significantly reduce the strength of the mixing in the model (Appendix A.1). We re-ran the physical ocean-only enhanced Nile discharge experiment presented by Adloff (2011) with our changed mixing parametrization and included the marine biogeochemical model. In our Nile simulation the deep water formation is effectively inhibited during the entire simulation period of 2.4 kyr. The enhanced Nile nutrient load fuels basin-wide enhanced biological production, with the highest production in the area of the Nile plume in the Levantine Sea. Within the stagnating deep water, the oxygen draw-down progresses nearly linearly, with a rate of  $40 \text{ mmolO}_2 \text{ m}^{-3}$  per 1 kyr. Initialized with a well-ventilated deep water mass ( $220 \text{ mmolO}_2 \text{ m}^{-3}$ ), no deep water anoxia develops in the frame of the Nile simulation. Trends of the oxygen consumption indicate 5 to 6 kyr until the onset of deep water anoxia would occur, supposed, however, that the stagnation was not further weakened. Yet, over time the interface between the well-ventilated upper ocean and the deep stagnating ocean progressively deepens down to  $\sim 2000$  m by the end of the simulation. The downward propagation velocity of the ventilation front suggests that the Nile simulation might reventilate after  $\sim 3.5$  kyr. Therefore, the time frame required for complete oxygen depletion exceeds the time frame of persistent deep water stagnation, so overall, the Nile simulation has no potential to develop deep water anoxia. The pre-sapropel deep-sea sediment POC burial flux is in accordance with the observed flux over large areas, however, the POC burial flux is too large in the area of the Nile plume along the eastern and northern Levantine Sea. This indicates that a basin-wide moderately strong eutrophication might be a plausible scenario for S1 formation, however, the Nile riverine nutrient load enhanced by 2.7 times with respect to

the Baseline simulation is localized too high for the Levantine Sea. A less eutrophicated Nile river simulation would reduce the biological productivity, and correspondingly the oxygen consumption rate, which would even more decrease the likelihood of developing deep water anoxia. The large time frame for the development of deep water anoxia exceeds the time frame between the onset of the AHP (14.8 kyr BP) and the onset of S1 deposition (10 kyr BP). We conclude that the AHP climate causes strong changes to the circulation and biogeochemical cycles, however, solely it cannot explain the S1 formation.

Immediately, this leads to the hypothesis that the required stagnation for S1 formation in the eastern Mediterranean Sea started early in time than the AHP, possibly during the onset phase of the last glacial-interglacial transition period.

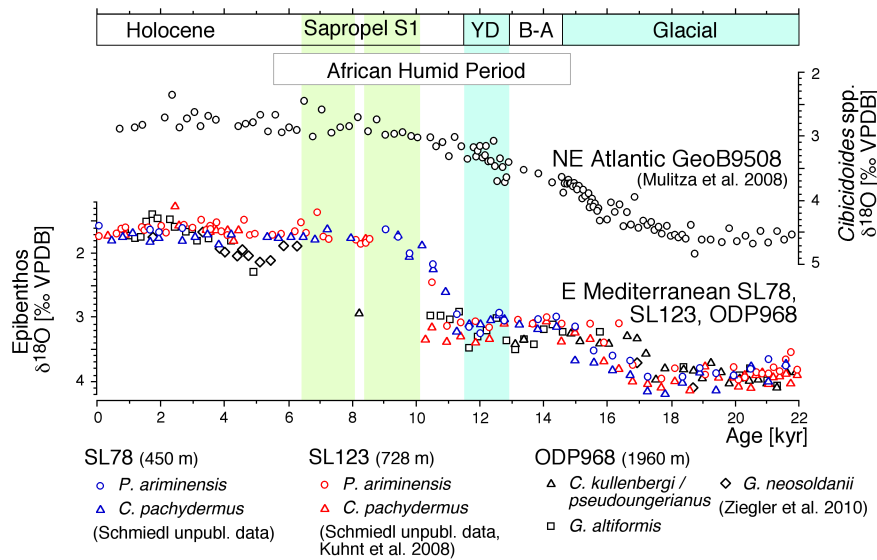


Figure 4.44: Northeastern Atlantic  $\delta^{18}\text{O}$  record (Mulitza et al. 2008), and epibenthos derived  $\delta^{18}\text{O}$  from the eastern Mediterranean at the indicated sites. Intervals shaded in blue and green represent the Younger Dryas and the time window of the eastern Mediterranean sapropel S1 formation, respectively. Duration of the African humid period after DeMenocal et al. (2000). Figure adapted from Schmiidl (personal communication).

The latest findings of epibenthic deep-sea foraminifera isotopes support the hypothesis of a stagnation being triggered during the early phase of the last deglaciation period (Fig. 4.44).  $\delta^{18}\text{O}$  values of eastern Mediterranean deep-sea benthic foraminifera show a decoupling from the global trend, with constant values between 16 kyr BP until the onset of sapropel deposition. The deepest core shows constant  $\delta^{18}\text{O}$  values proceeding into the sapropel deposition. In contrast, the trend in the northern Atlantic Ocean shows a continuous lightening of the  $\delta^{18}\text{O}$  values between  $\sim 18$  kyr BP and the early

Holocene. The continuous  $\delta^{18}\text{O}$  depletion in the deep north Atlantic Ocean reflects the release of light  $^{16}\text{O}$  isotopes with melt waters during the decay of the Laurentide and Fennoscandian ice sheets. Therefore, the constant  $\delta^{18}\text{O}$  values of the deep eastern Mediterranean may reflect stagnant deep water conditions, effectively isolating the deep eastern Mediterranean Sea from the global signal throughout the deglaciation period.

Our simulation of the deglaciation climate (IniGlac experiment) triggers a stronger and over time more persistent stagnation of the deep water circulation than the AHP climate. Throughout the simulation, the ventilation-stagnation interface deepens with a velocity of around 180 m per 1 kyr, resulting in a ventilation depth of 1600 m after 3.4 kyr of simulation. We estimate that deep reventilation will be developed after  $\sim 9$  kyr.

The strongly eutrophicated IniGlac+3xNutri experiment develops complete basin-wide deep water anoxia after  $\sim 3$  kyr of simulation. In the Levantine Sea, the simulation shows a nearly synchronous onset of anoxia below  $\sim 1700$  m to 1800 m depth. In the Ionian Sea, an OMZ develops at  $\sim 1600$  m to 1700 m depth and expands to the seafloor within a time frame of  $\sim 250$  years. The spatial onset of the simulated deep water anoxia is in accordance with the synchronous onset of anoxia inferred from proxy records (dating precision  $\pm 200$  years) (De Lange et al. 2008; Schmiedl et al. 2010). Below the intermediate anoxic OMZ, the POC flux increases relative to the time prior to the onset of anoxia since the remineralization of the POC flux is strongly reduced within the anoxic layer. This pattern is in accordance with the abundant and low diverse benthic ecosystem right before the onset of the S1 deposition, which indicates enhanced food supply for those few species who could survive under the extreme oxygen stress (Schmidt 2007; Kuhnt et al. 2007, 2008). In general, the dynamical evolution of deep water anoxia is dependent on the position of the ventilation front, the strength of the vertical stratification, and the oxygen consumption rate. The oligotrophic IniGlac simulation shows a less pronounced OMZ in the Ionian Sea. Hypothetically, if it became anoxic at the same time as the IniGlac+3xNutri within the simulation, then the onset would be basin-wide synchronously. Despite of developing basin-wide deep water anoxic conditions, the IniGlac+3xNutri simulation is an unrealistic scenario for describing the S1 formation, since it shows a strong overestimation of the sediment POC burial flux throughout the pre-sapropel period. Accordingly, deep-sea ecosystem reconstruction indicate a low productive marine environment for the time prior to the sapropel deposition, with indications of eutrophication restricted to marginal areas and close to river sources (Schmidt 2007; Kuhnt 2008).

In contrast, the oligotrophic IniGlac experiment shows a basin-wide very good representation of the deep-sea sediment POC burial flux. The deep-sea oxygen consumption totals  $\sim 130 \text{ mmol m}^{-3}$  over the 3.4 kyr of simulation. The strong deep water stagnation shows a similar oxygen utilization rate as the basin-wide moderately eutrophicated and stagnating Nile experiment, which clearly demonstrates the high sensitivity of the deep

water oxygen concentration even with respect to strongly reduced ventilation. The trend of the oxygen utilization suggests a potential development of deep water anoxia in  $\sim 6.5$  kyr, supposed that the strength of the stagnation remains unchanged. Since the stagnation-ventilation interface progressively deepens over time, the potential onset of anoxia after 6.5 kyr would be at  $\sim 2200$  m depth. Therefore, to match the reconstructed basin-wide S1 deposition below 1800 m (De Lange et al. 2008; Schmiedl et al. 2010), a restrengthening of the deep water stagnation is required in our simulation, which could be given by the enhanced Nile runoff during the AHP. Certainly, when the timing is right, other freshwater sources such as increased precipitation and river runoff from the northern borderland (Shaw and Evans 1984; Rossignol-Strick 1987; Cramp et al. 1988; Kallel et al. 1997; Rossignol-Strick 1999; Kallel et al. 2000; Kotthoff et al. 2008) can additionally strengthen the deep water stagnation (Meijer and Tuenter 2007; Adloff 2011). The reconnection with the Black Sea (Ryan et al. 1997; Sperling et al. 2003), could further contribute to hold the stagnation (Lane-Serff et al. 1997; Matthiesen and Haines 2003; Adloff 2011), and possibly fuel an enhanced biological productivity, similar to the present-day Mediterranean Sea (Chapter 3).

In summary, using a set of ocean biogeochemical model simulations, we show that the sapropel S1 formation cannot be explained through the AHP climate. We demonstrate that the Mediterranean deep water was pushed into an extreme oxygen deficiency by a strong and persistent deep water stagnation, triggered by the climatic changes of the last glacial-interglacial transition, and possibly restrengthened by an additional freshwater input. We further show that under this deglaciation scenario a particular strongly enhanced biological productivity, such as induced through a tripled riverine nutrient load, is an unrealistic assumption.

#### 4.4.1 Uncertainties in simulating the sapropel S1 formation

Here we discuss the robustness of our conclusions to sources of error in the assumptions, the mixing parametrization and time slice model setup, as well as the nutrient input data.

The correlation of the Quaternary sapropel sequence to insolation driven changes of the strength of the African monsoon (Rossignol-Strick 1985), with correspondingly enhanced Nile river discharge and nutrient load (Rossignol-Strick et al. 1982; Rohling 1994; Rohling et al. 2002; Scrivner et al. 2004; Osborne et al. 2008), has placed this scenario as the most widely used hypothesis to explain sapropel formation. In particular, sapropel formation during glacials seem difficult to explain without a strong source of freshwater from the African continent. Pliocene and Pleistocene sapropels show a tendency of being mainly controlled by productivity fluctuations, although preservation played a role (Warning and Brumsack 2000; Gallego-Torres et al. 2007). In a highly productive environment, a Nile river freshwater induced deep water stagnation might

be sufficient to induce sapropel formation. The early Holocene S1 formation occurred under a low productive environment (Kuhnt et al. 2007, 2008; Schmiedl et al. 2010). Inevitably, the development of a deep water oxygen deficiency under a low productive biological regime implies a strong and persistent stagnating deep water circulation, reducing ventilation to a minimum over a long period.

The strength and duration of a deep water stagnation depends on the magnitude of the initial perturbation (e.g. a freshwater induced density gradient) and the strength of the mixing eroding this perturbation. Both, the magnitude of the perturbation and the mixing are highly uncertain. In our set of experiments, we investigate two extreme examples of perturbation. If we now consider that mixing in our simulation is too strong, then the stagnating deep water circulation resulting from the enhanced Nile river discharge during the AHP might be strong enough for the evolution of deep water anoxia. However, then it would be unclear how the much denser LGM water, and the stable stratification resulting from the climatic changes associated with the last glacial-interglacial transition period, was eroded beforehand, and did not contribute to the overall oxygen depletion. The strength of mixing might be assessed by evaluating the deep turnover time, which is estimated to be 125 years for the present-day Mediterranean Sea (Roether and Schlitzer 1991). Our early Holocene Baseline simulation, with its well-ventilated deep ocean, shows a continuous slow-down of the deep turnover time from initially  $\sim 150$  year to  $\sim 600$  years by the end of the simulation. The Baseline and CTRL simulation, parametrized with stronger mixing, show a rather constant deep water turnover time of 150 to 200 years (Fig. A.5), which is more closely to the present-day estimate. Thus, the slow-down of the overturning in the model setup parametrized with reduced mixing might imply the underestimation of the strength of mixing. However, stronger mixing in the model does not lead to S1 oxygen depletion under neither of the presented climatic perturbation scenarios (Fig A.4). Considering, that we might just slightly underestimate the strength of mixing in the presented simulation, then the time frame needed for complete oxygen depletion would be prolonged compared to the oxygen depletion rates in our simulations. Yet, this model uncertainty would even enforce our main finding in that the S1 formation requires a long and persistent stagnating deep water circulation, which was triggered by the climatic changes associated with the last glacial-interglacial transition period.

With our time slice simulation approach, in particular, the time variability of the climatic changes associated with the glacial-interglacial transition could not be captured (IniGlac simulation), which possibly bears implications for the strength of the stagnation and its vertical extent throughout the eastern Mediterranean Sea. To mimic the glacial-interglacial climatic signal in our IniGlac simulation, we initialized the model with LGM water conditions, and imposed the early Holocene Atlantic hydrography, sea level, and atmosphere. The imposed sea-level rise of  $\sim 100$  m between the LGM and the early Holocene rapidly enhances the simulated exchange rate at the Strait of Gibraltar

by a factor of 2 compared to the LGM exchange rate (Mikolajewicz 2011). The increase of the exchange rate under the high sea level leads to a decrease of the salinity difference between the Atlantic Ocean and the Mediterranean Sea, so overall the Mediterranean experiences a freshening in response to the initialized high Holocene sea level. In addition, the imposed early Holocene atmosphere is warmer than during the LGM, and the prescribed Atlantic inflow fresher since the major ice sheets largely decayed and released their freshwater to the global ocean during the deglaciation period. Therefore, the simulated upper anti-estuarine overturning cell in the Mediterranean Sea rapidly establishes warm and fresh early Holocene characteristics, which strongly contrast the initialized cool and salty LGM deep water conditions. Consequently, the simulation establishes a strong vertical density gradient, which is slowly eroded by cross-isopycnal mixing over time. In reality, however, during the glacial-interglacial transition period a strongly variable progressive climate warming and decay of the major ice sheets translated into a variable freshening rate of the Atlantic inflow, and a variable increase of the exchange rate at the Strait of Gibraltar (Fairbanks 1989; Bryden and Stommel 1984; Shakun et al. 2012). Since the Mediterranean deep water with its long residence time possibly lagged behind the relatively fast changes of the water properties at the surface, it has been proposed that a vertical density gradient was established (Thunell and Williams 1989; Troelstra et al. 1991; Béthoux and Pierre 1999). Yet, the real vertical density stratification during the deglaciation period was most likely never as strong as in the initial phase of our simulation. Moreover, compared to our IniGlac simulation, in reality the position of the maximum vertical density gradient was possibly located in shallower depth, dependent on the sea level, which influenced the vertical extent of the upper anti-estuarine circulation cell (Mikolajewicz 2011). A shallower position of the ventilation-stagnation interface than simulated in our IniGlac experiment is in accordance, for instance, with the reconstructed hydrographic changes in the Aegean Sea that started  $\sim 6$  kyr prior to S1 deposition (Casford et al. 2002), and the epibenthic foraminifera  $\delta^{18}\text{O}$  records presented in Figure 4.44.

Another source of uncertainty is given by the nutrient regime during the time of S1 formation. First, the riverine nutrient input is highly uncertain. Under a given circulation scenario the external nutrient input determines the strength of the biological productivity, and consequently the sediment POC burial flux. In turn, under a given nutrient regime the circulation determines the biological productivity, and the erosion and water temperature the remineralization capacity of the sediment POC. The cold bottom water of the IniGlac+3xNutri experiment limits the sediment POC remineralization, and thus this simulation shows a basin-wide overestimation of the sediment POC burial flux. In contrast, the relatively warm bottom water of the 3xNutri and the Nile experiment overestimate the sediment POC burial flux only in the area of the Nile plume in the eastern and northern Levantine Sea, while over large areas the simulated POC burial flux is in the range of the observed fluxes for the pre-sapropel

period. Nonetheless, the 3xNutri experiment shows no potential to develop deep water anoxia due to the continuous deep ventilation. In contrast, the Nile experiment could develop deep water anoxia within 5 to 6 kyr, supposed that the strength of the stagnation remains unchanged, which, for example, might be achieved by a restrengthening of the stagnation through enhanced freshwater input from the northern borderland. However, the required time frame of the Nile experiment for complete oxygen depletion would still exceed the temporal extent of the AHP. Thus, our main conclusion that the S1 formation requires a long and persistent deep water stagnation triggered during the deglaciation period before the onset of the AHP still endures, even though a basin-wide spatially evenly distributed eutrophication scenario might be a realistic scenario for S1 formation.

Second, the initial conditions of the nutrient concentrations are uncertain. The LGM was possibly characterized by high nutrient concentrations in the eastern Mediterranean deep water (Kuhnt 2008), accumulated by the same processes as salinity due to the reduced exchange rate between the Atlantic Ocean and the Mediterranean Sea at times of low sea level. Since we initialize the IniGlac simulation from the oligotrophic Baseline simulation, we do not account for high LGM deep water nutrient concentrations. Initially, the POC export production is reduced in the IniGlac simulation, since the rapidly established deep water stagnation leads to a strong nutrient exhaustion of the upper ocean limiting the biological productivity. Over time, this simulation shows a trapping of nutrients in the deep stagnating water. Thus, the simulated biological production is slowly enhanced by receiving traces of highly nutrient-enriched deep water through cross-isopycnal upward mixing. A simulation, initialized with LGM nutrient-enriched deep water might initially not (not strongly) reduce the export production, and over time even fuel higher biological production compared to the simulated POC export. Thus, our IniGlac simulation, initialized with nutrient-poor deep water, possibly underestimates the strength of the biological production and oxygen depletion. This assumption could explain the  $\sim 500$  year time offset between the derived 6.5 kyr required for complete oxygen depletion in the IniGlac simulation, and the  $\sim 6$  kyr as indicated by the epibenthic deep-sea foraminifera  $\delta^{18}\text{O}$  (Fig. 4.44).

In summary, the simulation of the S1 formation involves a number of uncertainties, such as, the mixing parameterization of the model, the time slice setup of the simulations, the riverine nutrient loads, and the initialization of the deep water nutrients. With our set of simulations we could constrain a large part of these uncertainties. Overall, we find a strong robustness of our main conclusions in that the S1 formation was triggered by the climatic changes associated with the glacial-interglacial transition, which involved no particularly strong riverine induced eutrophication scenario.

# Chapter 5

## Conclusions and Outlook

We simulated scenarios leading to the eastern Mediterranean early Holocene sapropel formation using a regional ocean general circulation model coupled to a biogeochemical model, including a sediment model (MPIOM/HAMOCC), forced by atmospheric data derived from a coarse resolution global climate model (MPIOM/ECHAM/LPJ) for the early Holocene time slice.

### 5.1 Conclusions

To conclude our findings, we re-visit the research questions posed in the introduction.

- (1) Is the sapropel S1 formation caused by an enhanced biological productivity, or is a stagnating deep water circulation a prerequisite?

An enhanced biological production and corresponding increased oxygen utilization cannot exceed the effect of continuous ventilation via deep water formation. No deep water deficiency can evolve under a purely enhanced biological production scenario. We conclude that a stagnating deep water circulation is a prerequisite for S1 formation.

- (2) Is the climate of the African humid period (AHP), implying a particularly enhanced Nile river discharge and nutrient load, a plausible scenario explaining the sapropel S1 formation?

No. Our simulation with an 2.7 times enhanced Nile river runoff and nutrient load with respect to the early Holocene Baseline simulation shows no potential to develop deep water anoxia from a well-ventilated initial state. The enhanced Nile discharge establishes a density stratification, inhibiting deep water ventilation over the entire simulation period of 2.4 kyr. Within the stagnating water column the oxygen is progressively depleted. The simulated strength of the stagnating deep water circulation weakens over time, and the trend of this weakening suggests that this simulation will start to reventilate before deep water anoxia would be developed. The simulated eutrophication through the enhanced Nile river nutrient load translates into a good representation of

the deep-sea sediment POC burial flux, except for the Nile plume area, where the sediment POC burial flux is too large compared to observations of the pre-sapropel period. A lower Nile river nutrient load would translate into a lower oxygen consumption rate, which would even less likely lead to the development of deep water anoxia. We conclude that the relatively short temporal extent of the AHP cannot explain the required time frame for the evolution of deep water anoxia. This implies that the onset of the deep water stagnation and correspondingly oxygen depletion was not triggered through an enhanced Nile river runoff during the AHP, but earlier in time.

- (3) Did the climatic changes associated with the last glacial-interglacial transition period trigger the sapropel S1 formation?

Yes. Our IniGlac simulation shows that the climatic changes associated with the last glacial-interglacial transition trigger a stable stratification in the eastern Mediterranean Sea, inhibiting deep water formation throughout the entire simulation period of 3.4 kyr. Under a low productive oligotrophic regime the simulated sediment POC burial flux is in accordance with the sediment core observations of the pre-sapropel period. Due to the short time frame of the simulation with respect to the temporal extent of the deglaciation period, no deep water anoxia evolves. The oxygen depletion progresses nearly linearly throughout the simulation, with the trend of the oxygen depletion suggesting at least 6.5 kyr for the development of deep water anoxia. This time frame is in accordance with records of epibenthic deep-sea foraminifera  $\delta^{18}\text{O}$ , which indicate that the stagnation of the deep water circulation in the eastern Mediterranean Sea started approximately 6 kyr before the onset of S1 deposition. The simulated trend of the strength of the deep water stagnation indicates that a restrengthening of the density stratification is required to meet the reconstructed spatial extent (basin-wide below 1800 m) and duration (3.5 kyr) of the S1 deposition. We conclude that the stagnating deep water circulation initiating the S1 oxygen depletion was triggered by the climatic changes associated with the last glacial-interglacial transition, and was restrengthened through an additional contribution of enhanced freshwater input. Furthermore, we conclude that this scenario requires no particularly strong basin-wide eutrophication scenario, as would be induced through a tripled riverine nutrient input.

- (4) What are the main uncertainties in simulating the formation of the sapropel S1?

Previously we concluded that the S1 deep water oxygen deficiency developed under a strong and persistent stagnating deep water circulation, triggered by the climatic changes associated with the last glacial-interglacial transition, which required no particularly strong basin-wide eutrophication scenario fueled by tripled riverine nutrient input. Both, the parameterization of the strength of mixing and the nutrient input, however, are highly uncertain, thus, they might affect on the robustness of our main conclusion.

The strength and duration of a deep water stagnation depends on the magnitude of the initial perturbation (e.g. a freshwater induced density gradient) and the strength of the mixing eroding this perturbation. Both, the magnitude of the perturbation and the strength of the mixing are highly uncertain. With our set of experiments we investigate two extreme examples of perturbation. The freshwater forcing from the AHP might be sufficient for a long-term stagnation if the strength of the mixing was much lower than in our model. However, then it would be unclear how the much denser LGM water, and the stable stratification resulting from the climatic changes associated with the last glacial-interglacial transition period, was eroded beforehand, and did not contribute to the overall oxygen depletion. In turn, we show that stronger mixing in the model will not lead to S1 oxygen deficiency under neither of the climatic perturbation scenarios.

Furthermore, the nutrient regime required for S1 formation is highly uncertain. Since both, the 3xNutri and Nile experiment shows a good representation of the deep-sea sediment POC burial flux over large areas except of the Nile plume region, a spatially evenly distributed basin-wide eutrophication might be in the range of being a realistic scenario for S1 formation. During the last glacial-interglacial transition period a basin-wide enhanced biological productivity was possibly fueled by high nutrient concentrations accumulated during the glacial due to the reduced exchange rate at the Strait of Gibraltar under the lower sea level. Therefore, the IniGlac simulation, which is initialized with nutrient-poor deep water, possibly underestimates the strength of the biological production, and hence oxygen depletion. Since the IniGlac experiment takes at least 6.5 kyr until deep water anoxia will be developed, and proxy records suggest only  $\sim 6$  kyr of stagnation before the onset of S1 deposition, an accelerated oxygen consumption due to moderately enhanced biological productivity fueled by higher initial nutrient concentrations seems a plausible scenario. We conclude that even though the simulated strength of the oxygen depletion is highly sensitive to the mixing parameterization and nutrient regime, these uncertainties do not affect on the robustness of our main conclusions.

- (5) Can we infer from the reconstructed temporal and spatial synchronous onset of the sapropel S1 deep water oxygen deficiency a circulation and/or nutrient regime that governs this pattern?

Yes. A basin-wide synchronous onset of the S1 deep water oxygen deficiency implies a homogenized oxygen depth profile, which is given by a stagnating deep water column that is internally weakly stratified. In the range of the dating precision of sediment core data ( $\pm 200$  years), also an OMZ downward propagation scenario results in a 'synchronous' onset of the simulated deep water anoxia, since an intermediate anoxic OMZ preserves the POC flux throughout the anoxic layer and accelerates the oxygen consumption below. The simulations show that the development of a pronounced OMZ at intermediate depth requires an eutrophication scenario and a strong vertical strat-

ification. Benthic ecosystem reconstructions for S1 formation (Schmidt 2007; Kuhnt 2008) favor the OMZ downward propagation scenario, which implies a shallow position of the stagnation/ventilation interface and a well-stratified water column, considering the oligotrophic nature of the eastern Mediterranean Sea during the early Holocene.

## 5.2 Outlook

The most promising simulation, the deglaciation climate preconditioning of the circulation combined with an oligotrophic regime, was not simulated long enough to study how it will behave in the long term. It would be interesting to continue this simulation, and finally, combine it with the AHP scenario. Also the reconnection with the Black Sea seems a promising scenario for the restrengthening of the density stratification, as well as a source for enhanced nutrient input, which could trigger an enhanced productivity.

Even more interesting than combining time slice simulations would be to simulate the last deglaciation period in a transient setup, coupled to a regional atmospheric model. A transient simulation would provide valuable insight into the timing of climatic events triggering and restrengthening the deep water stagnation.

All simulations show very strong differences in their pore water  $\delta^{13}\text{C}$  DIC in the deep basin. It is well established that the carbon isotopes correlate with phosphate concentration (Broecker and Maier-Reimer 1992), and can be used as a proxy for the strength of the deep water circulation (Vergnaud-Grazzini and Pierre 1991; Kuhnt et al. 2008; Schilman et al. 2001). A continuous benthic foraminifera  $\delta^{13}\text{C}$  record from the deep basin could be used to understand both, the time evolution of the stagnation, possibly also the timing of specific climatic changes, as well as the strength of the biological productivity. For a successful model versus observation comparison, a deep-sea benthic  $\delta^{13}\text{C}$  record is highly desirable since such a record could be used to precisely reconstruct the evolution of the S1 deep water oxygen deficiency.

The model results are rather sensitive to the parametrization of the mixing. We showed that the model has a relatively high implicit diffusion in the advection scheme. Obviously, also the parameterization of the Richardson number dependent mixing term is not optimally tuned for the cases with very stable stratification. The sapropel S1 formation, offers a good test bed for studying and testing mixing parametrizations, since both the initial perturbation and time scales for the development of the deep water oxygen deficiency are restricted, which quite strongly constrains the parameter space for mixing parametrizations.

# List of Abbreviations

|          |  |
|----------|--|
| ADW      | Adriatic deep water  |
| $age_D$  | Apparent water age deviation                                 |
| $age_M$  | Apparent water age   |
| AHP      | African humid period   |
| AIW      | Aegean intermediate water                                    |
| Baseline | Early Holocene control simulation                            |
| BFN      | Benthic foraminiferal number                                 |
| C        | Carbon   |
| CTRL     | Pre-industrial control simulation                            |
| DCM      | Deep chlorophyll maximum                                     |
| DIC      | Dissolved inorganic carbon                                   |
| DOC      | Dissolved organic carbon                                     |
| E        | Evaporation  |
| ECHAM    | Atmospheric general circulation model developed by the MPI-M |
| EMDW     | Eastern Mediterranean deep water                             |
| EMT      | Eastern Mediterranean Transient                              |
| HAMOCC   | Hamburg ocean carbon cycle model                             |
| HIM      | Holocene insolation maximum                                  |
| IIW      | Ionian intermediate water                                    |
| IniGlac  | HIM forced simulation initialized with LGM water properties  |
| kyr BP   | Kilo year before present                                     |
| LGM      | Last glacial maximum   |
| LIW      | Levantine intermediate water                                 |
| LPJ      | Dynamic global simulation model of vegetation biogeography   |
| MAW      | Modified Atlantic water                                      |
| MPIOM    | Max Planck Institute ocean model                             |
| N        | Nitrate  |
| NAdDW    | Northern Adriatic deep water                                 |
| $O_2$    | Dissolved oxygen   |
| OMS      | Oxygen minimum structure                                     |
| OMZ      | Oxygen minimum zone  |
| P        | Dissolved phosphate, or precipitation                        |
| $pCO_2$  | Carbon dioxide partial pressure                              |
| POC      | Particulate organic carbon                                   |

## LIST OF ABBREVIATIONS

|                   |  |
|-------------------|--|
| ppm               | Dimensionless unit [parts per million]   |
| PR                | Pre-industrial   |
| ptanox            | Time until full anoxia evolves relative to the year 1 of the simulation              |
| R                 | Rivers   |
| S                 | Salinity   |
| Sv                | Unit of measure of volume transport [ $1\text{Sv} = 10^6 \text{m}^3 \text{s}^{-1}$ ] |
| S1                | Most recent deposited sapropel layer (6.5–10 kyr BP)                                 |
| T                 | Temperature  |
| 3xNutri           | HIM forced simulation with tripled riverine nutrient input                           |
| $\sigma_{\Theta}$ | Potential density anomaly [ $\text{kg m}^{-3}$ ]                                     |

# Appendix A

## Additional remarks: The early Holocene sapropel formation

### A.1 Sensitivity of the deep water circulation to the mixing parameterization

We showed that sapropel S1 formation requires a stagnating deep ocean circulation. In general, the duration of a deep water stagnation is determined by the magnitude of the initial perturbation, and the strength of the mixing eroding the perturbation. In this study, we have chosen to simulate rather extreme examples of perturbation experiments (section 4.2). Nonetheless, running these perturbation experiment using the default model configuration reveals that the model is unable to hold a deep water stagnation longer than a few centuries, which makes it thus unsuitable for the simulation of the early Holocene sapropel. To understand the model's inability to simulate a full and over Millennia persistent deep water stagnation, we focus on the mixing parameterization in MPIOM, which erodes the stability of a stagnation.

In general, mixing in the ocean is induced through convection, advection, diffusion, tidal mixing, wind induced mixing, eddy induced mixing, internal wave breaking, and other minor sources of mixing. In the GCM MPIOM, the mixing of tracers within unresolved mesoscale eddies is parametrized after Gent et al. (1995). The vertical eddy viscosity and diffusivity is parametrized by the so-called PP-scheme (Pacanowski and Philander 1981). The total vertically diffusivity is given by:

$$k = k_{ri} + k_{bg}, \quad (\text{A.1})$$

where  $k_{ri}$  is a Richardson number dependent mixing term, and  $k_{bg}$  is the background mixing term, which accounts mainly for the breaking of internal waves. In the default model setup,  $k_{bg}$  is set to a constant value of  $0.2 \text{ cm}^2 \text{ s}^{-1}$ . Since the PP-scheme in its classical form underestimates the turbulent mixing close to the surface, an additional wind mixing parameterization  $k_{wind}$  is included in Eq. A.1. In the presence of static instability, convective overturning is parametrized by greatly enhanced vertical diffusion to a value of  $50 \text{ cm}^2 \text{ s}^{-1}$ . The advection equation in MPIOM is realized through

## APPENDIX A THE EARLY HOLOCENE SAPROPEL FORMATION

Table A.1: Setup of mixing sensitivity experiments (Exp.), imposed perturbation (Pertu. (section 4.2)), mixing parameterization (mix. para.), number of vertical layers (vert. layers) and change of salinity after 700 years of simulation averaged over the Ionian Sea at 2000 m depth.

| Exp.            | Pertu.  | Mixing para.                  | vert. layers | Change of S [%] |
|-----------------|---------|-------------------------------|--------------|-----------------|
| bgcLR           | IniGlac | const. $k_{bg}$               | 29           | 55.6            |
| bgpLR           | IniGlac | profile $k_{bg}$              | 29           | 45.7            |
| bgp             | IniGlac | profile $k_{bg}$              | 46           | 3               |
| bgpLR-T         | IniGlac | profile $k_{bg}, notides$     | 29           | 40.3            |
| bgpLR-T-Ri      | IniGlac | profile $k_{bg}, notides, Ri$ | 29           | 40.1            |
| bgpLR: Nile     | Nile    | profile $k_{bg}$              | 29           | 12              |
| bgp: Nile       | Nile    | profile $k_{bg}$              | 29           | 1               |
| bgpLR: Baseline | -       | profile $k_{bg}$              | 29           | 0               |
| bgp: Baseline   | -       | profile $k_{bg}$              | 46           | 0               |

a  $2^{nd}$  order total variation diminishing scheme (Sweby 1984). This advection-scheme is using weighted averages of both the central-differences and upstream method. The central-differences scheme has the disadvantage of producing numerical spurious tracer sources and sinks, thus, its weights are put in such a way that it is preferably used for weak flows, reducing its disadvantage of producing tracer overshoots. The upstream-scheme involves an implicit diffusive term, which leads to a smoothed representation, and hence, is preferably applied to steep gradients with a stronger flow. Since the implicit diffusive term of the upstream-scheme increases with increasing vertical layer thickness, an increase of the vertical resolution decreases its impact.

To asses the model’s sensitivity towards the mixing parameterization, we conduct a series of simulations, in which we impose a perturbation leading to a stagnating ocean circulation. Successively we reduce some of the individual mixing terms (Table A.1). The parameterization of mixing by unresolved eddies is not included in all simulations. Our default setup (bgcLR) uses the mixing parameters as described above, and is the same, as has been used in a previous report by Adloff (2011) for the simulation of a stagnating deep water circulation in the eastern Mediterranean during the early Holocene. In the first sensitivity experiment (bgpLR), we replace the constant background diffusion term through a depth dependent profile, with the diffusivity reduced to molecular diffusion below 1500 m (Fig. A.1) to reduce the effect of internal wave breaking, since in a stagnating ocean this parameterization is likely to be overestimated. To understand the impact of the other mixing processes, we additionally switch off the tides (bgp-NT), and finally we switch off the Richardson number dependent term (bgp-NT-Ri). In case of water column instability, we still apply the convection adjustment procedure. Although the latter two sensitivity experiments appear rather unrealistic,

## A.1 SENSITIVITY OF THE DEEP WATER CIRCULATION TO THE MIXING PARAMETERIZATION

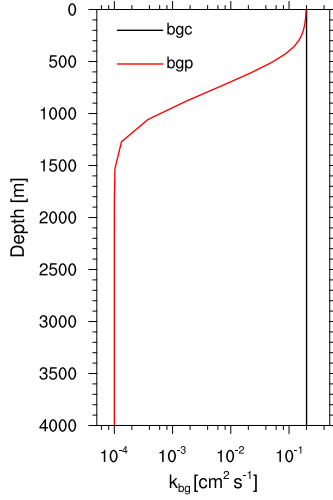


Figure A.1: Background diffusion profiles for bgc (constant default parametrization) and bgp (depth dependent background diffusion profile).

they can be used to assess the impact of the individual mixing terms on the stability of a stagnating ocean circulation. As additional sensitivity experiment, we increase the vertical resolution of the background diffusion profile (bgp) simulations, to reduce the effect of the implicit diffusion of the upstream advection-scheme.

Each mixing sensitivity simulation was run for at least 700 years, initialized with the Baseline circulation field after 1600 years. While we impose the IniGlac perturbation to achieve a stagnating deep water circulation in all mixing sensitivity experiments, we assess the sensitivity towards the mixing parameterization of the Nile freshwater perturbation only through the increased vertical resolution setup.

Figure A.2 shows the salinity averaged over the Ionian Sea at 2000 m depth. In the IniGlac experiments, with the default model setup (bgcLR) the initially imposed salinity perturbation erodes fastest and most efficiently by 55.6 % (Table A.1). Reducing the effect of internal wave breaking (bgpLR) reduces the salinity erosion to 45.7 %, while the mixing by tides and the Richardson number dependent mixing term show only modest additional changes to the deep ocean mixing. In contrast, the increase of the vertical resolution from 29 to 46 vertical layers (bgp) reduces the erosion of the salinity perturbation to 3 %, and thus, significantly improves the stability of the stagnation over a long period. In the Nile freshwater induced stagnation experiment, the low resolution setup (bgp: NileLR) changes the deep salinity by 12 %, while the high resolution Nile experiment (bgp: Nile) shows only a 1 % reduction in the deep water salinity. In the case of the well-ventilated Baseline simulations, there is no change of salinity over the

## APPENDIX A THE EARLY HOLOCENE SAPROPEL FORMATION

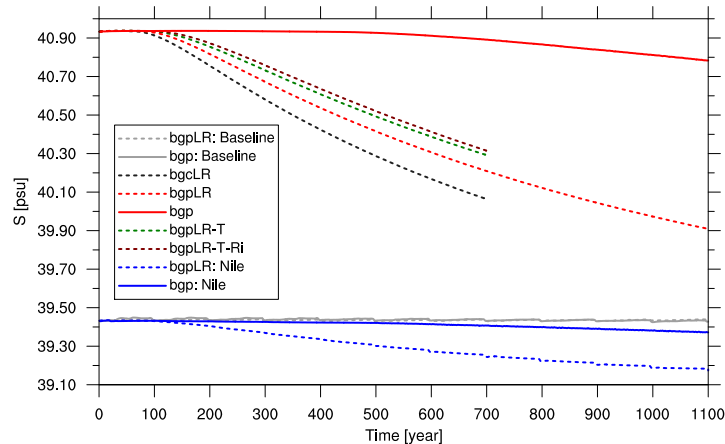


Figure A.2: Time series of salinity at 2000 m depth averaged over the Ionian Sea for the indicated experiments.

entire period of simulation when increasing the vertical resolution, indicating that a well-ventilated ocean seems insensitive to the vertical resolution.

Instead of increasing the vertical resolution to reduced the numerical diffusion term, we could simply use a less diffusive advection-scheme, such as a  $3^{rd}$  order advection-scheme. Unfortunately, a  $3^{rd}$  order advection-scheme is currently not available as parallelized code version for MPIOM, nor does it include the bottom boundary layer transport scheme for tracer advection, and the advection of the HAMOCC tracers. Especially the unparallelized code version makes the  $3^{rd}$  order advection-scheme in terms of computational load not applicable for the high horizontal resolution needed to simulate the Mediterranean Sea. Nonetheless, to quantify the lower diffusivity of the  $3^{rd}$ -scheme with respect to the  $2^{nd}$  order advection-scheme we run both advection schemes in a global low resolution model setup (TP  $6^\circ \times 6^\circ$ ). We run a 50 year spinup of the global model using the  $2^{nd}$  order advection-scheme, initialized with the levitus climatology (Levitus et al. 1998), and forced it with the OMIP climatological atmospheric forcing (Röske 2006). In the year 51, we added +2 psu globally below 1275 m, and run it for another 50 years with the  $2^{nd}$  order advection-scheme, and in an additional experiment with the  $3^{rd}$  order advection-scheme.

The results of the salinity time evolution averaged over various ocean basins at 2000 m depth within both experiments is shown in Figure A.3. In all ocean basins the  $3^{rd}$  order advection-scheme reduces the imposed salinity perturbation slower, with the largest difference among these experiments in the northern Atlantic, where there is the formation of North Atlantic Deep Water, and thus, a strong deep flow. In this case, the  $2^{nd}$

## A.1 SENSITIVITY OF THE DEEP WATER CIRCULATION TO THE MIXING PARAMETERIZATION

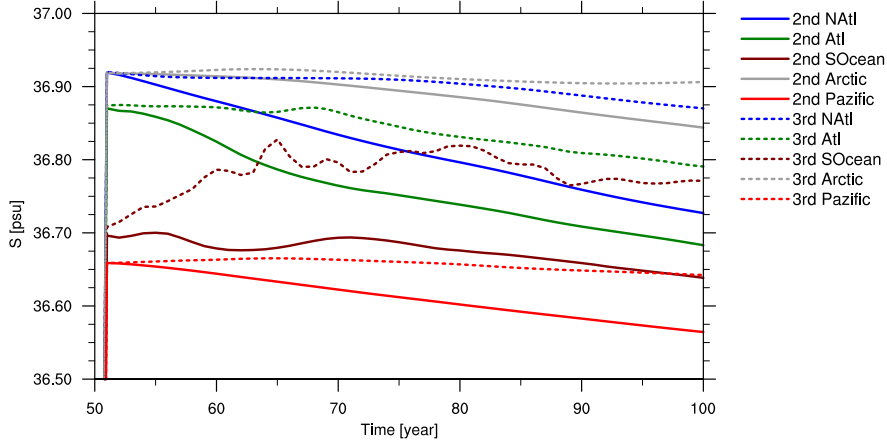


Figure A.3: Time series of salinity at 2000 m depth averaged over the indicated ocean basins in the global model for the  $2^{nd}$  order advection-scheme (solid lines) and the  $3^{rd}$  order advection-scheme (dashed lines).

order advection-scheme puts its weights towards the upstream-scheme, which implies a higher implicit diffusion. These results confirm the lower diffusivity of the  $3^{rd}$  order advection-scheme, which might be in the future also an appropriate model configuration choice for the simulation of the early Holocene sapropel formation.

In summary, the elimination of individual explicit mixing parametrizations within the computationally cheaper low vertical resolution setup can only moderately improve the stability of a stagnating deep water circulation, since the implicit diffusion of the  $2^{nd}$  order advection-scheme erodes the stability of the stagnation most efficiently. Thus, the low vertical resolution is not suitable for the simulation of a full and over Millennia persisting stagnating deep water circulation. In contrast, the high vertical resolution model setup, which reduces the implicit diffusion of the  $2^{nd}$  order advection-scheme, shows the ability to hold a stagnating deep water circulation for several millennia. Thus, the high vertical resolution model setup is an appropriate model configuration for the simulation of the early Holocene sapropel formation. In the future, however, the incorporation of a  $3^{rd}$  order advection-scheme seems promising, since its computational load is similar to the  $2^{nd}$  order advection-scheme, while producing a less diffusive result.

### A.1.1 Additional remarks: Sensitivity of the deep water circulation to the mixing parameterization

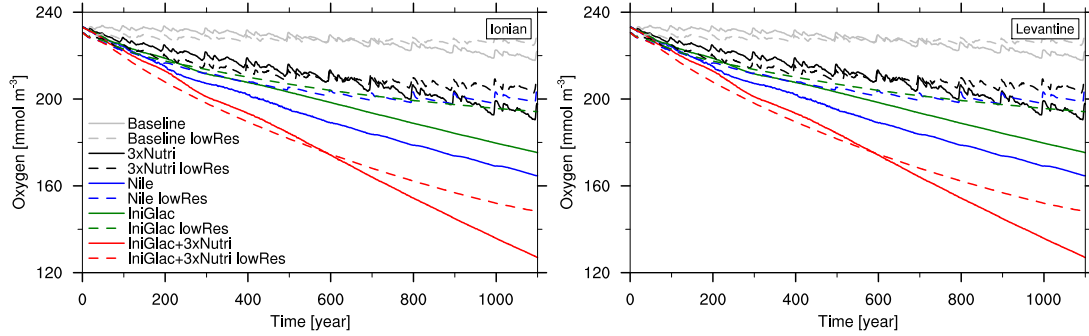


Figure A.4: Time series of the oxygen concentration averaged over the Ionian Sea (left panel) and Levantine Sea (right panel) for the indicated model simulations in 1800 m for experiments with 29 vertical levels (dashed lines) and 46 vertical levels (solid line). Higher vertical resolution implies less diffusion. For longer time scales compare also to Figure 4.24.

## A.1 SENSITIVITY OF THE DEEP WATER CIRCULATION TO THE MIXING PARAMETERIZATION

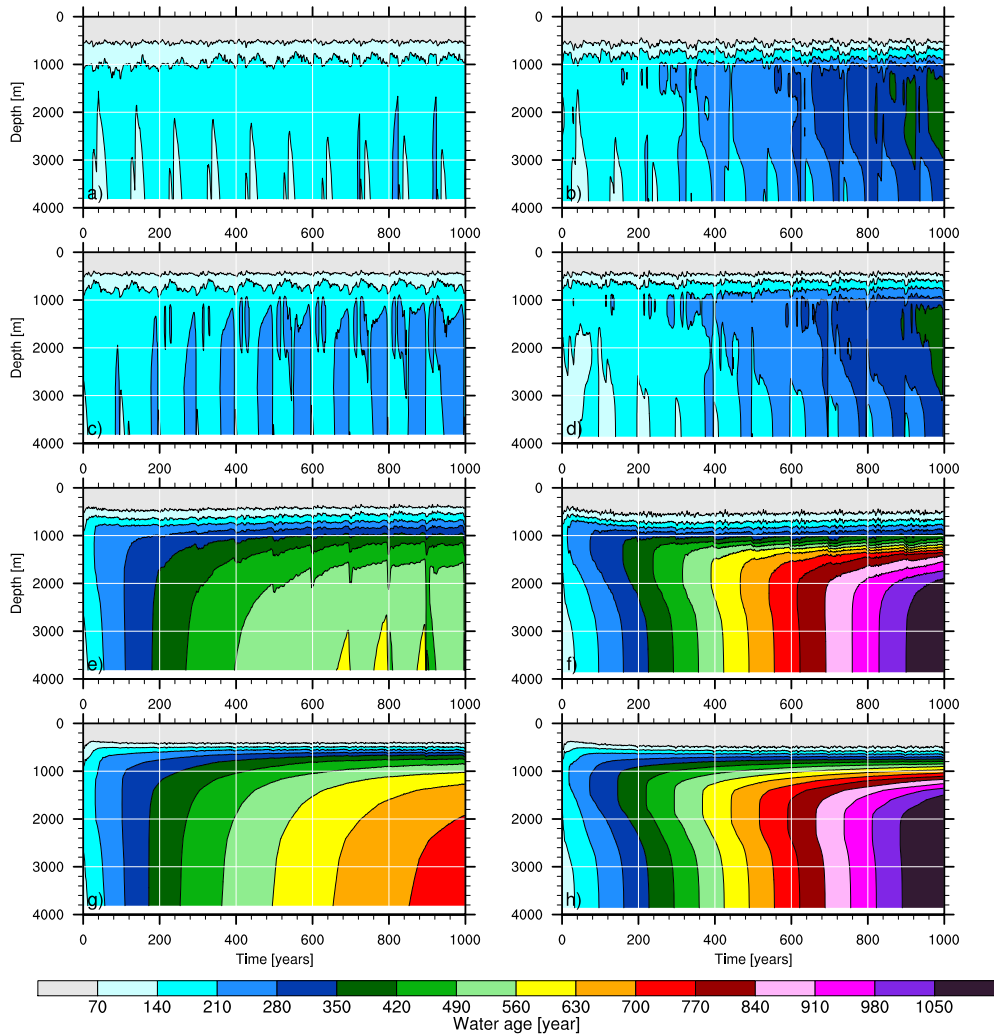


Figure A.5: Hovmöller diagram of the water age ( $age_M$ , Eq. 3.5) averaged over the Ionian Sea for low vertical resolution setup (left column) and high vertical resolution setup (right column) for the pre-industrial CTRL simulation (a, b), the Baseline (c, d), the Nile (e, f), and the IniGlac (g, h) experiments. Higher vertical resolution implies less implicit diffusion.

## A.2 Additional remarks: General circulation

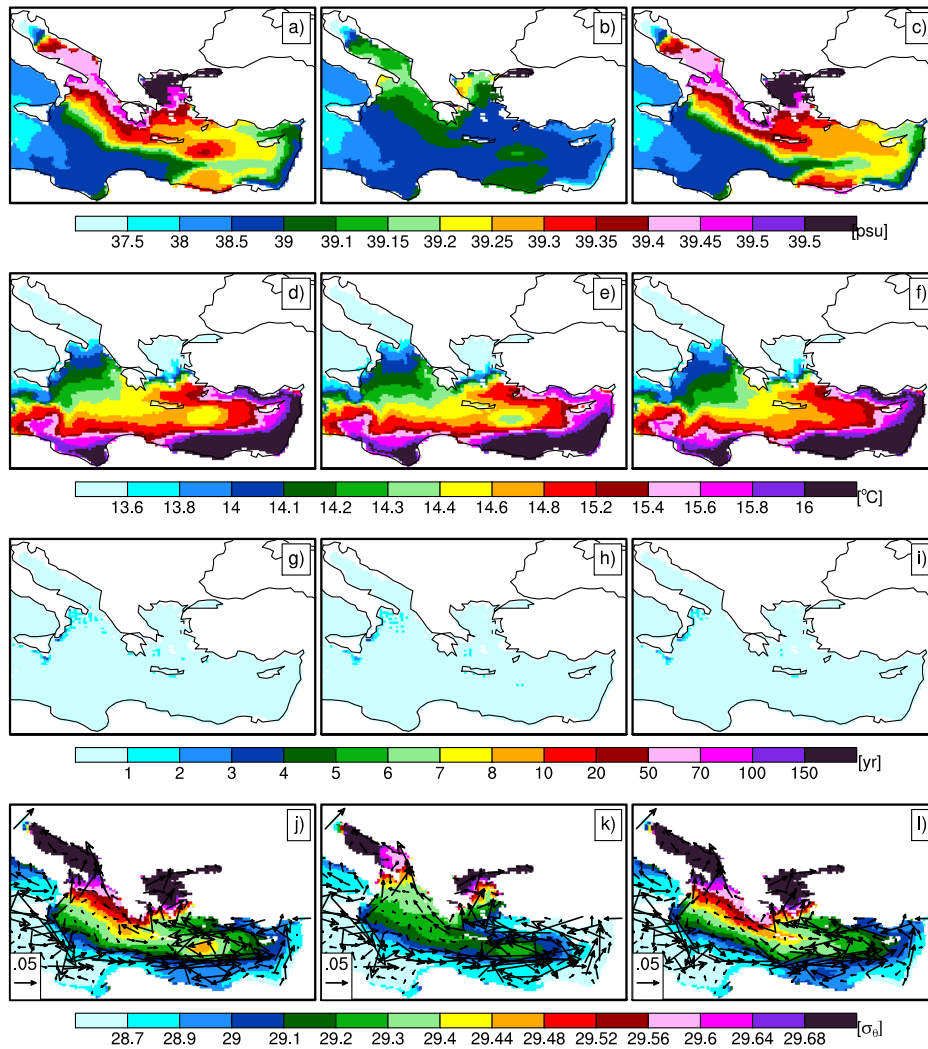


Figure A.6: Water properties at 25 m depth. a) to c) salinity; d) to f) temperature; g) to i) water age; j) to l)  $\sigma_{\theta}$  superimposed with circulation, vector represent both speed and direction of circulation.

## A.2 ADDITIONAL REMARKS: GENERAL CIRCULATION

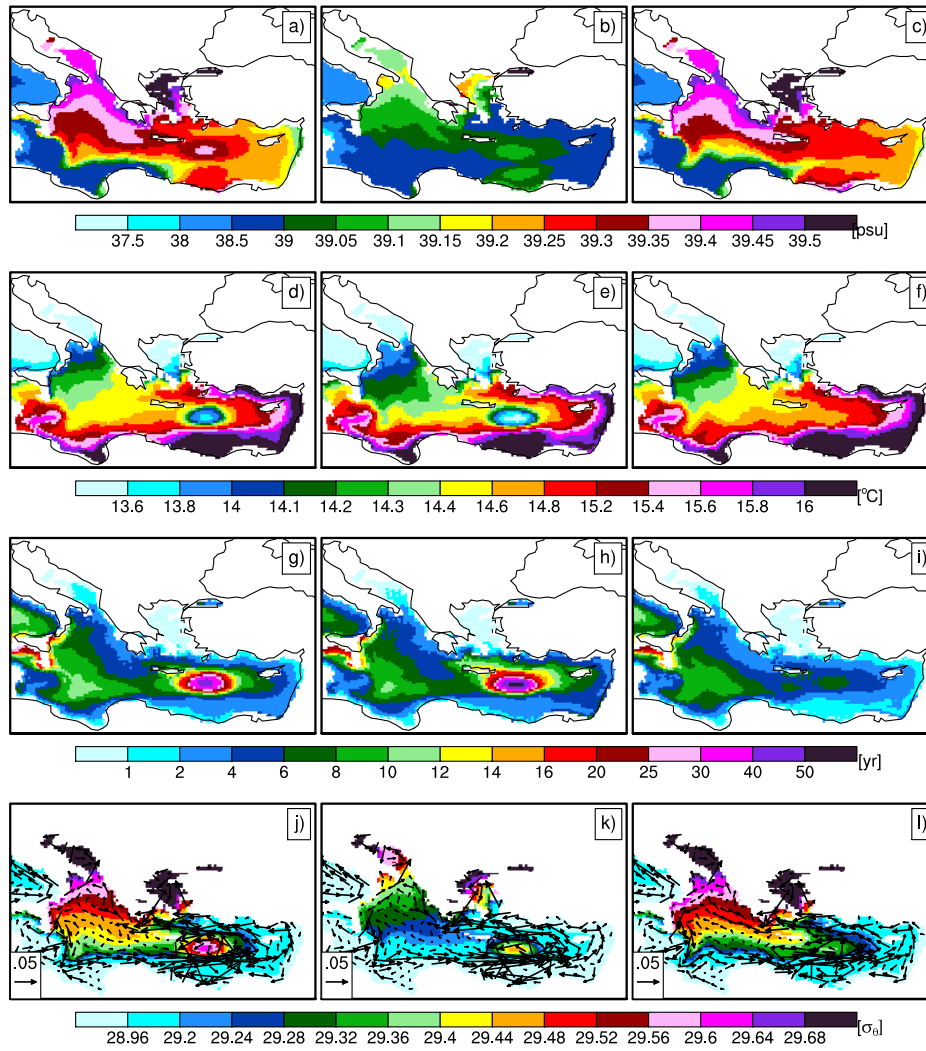


Figure A.7: Water properties at 113 m depth. a) to c) salinity; d) to f) temperature; g) to i) water age; j) to l)  $\sigma_\theta$  superimposed with circulation, vector represent both speed and direction of circulation.

APPENDIX A THE EARLY HOLOCENE SAPROPEL FORMATION

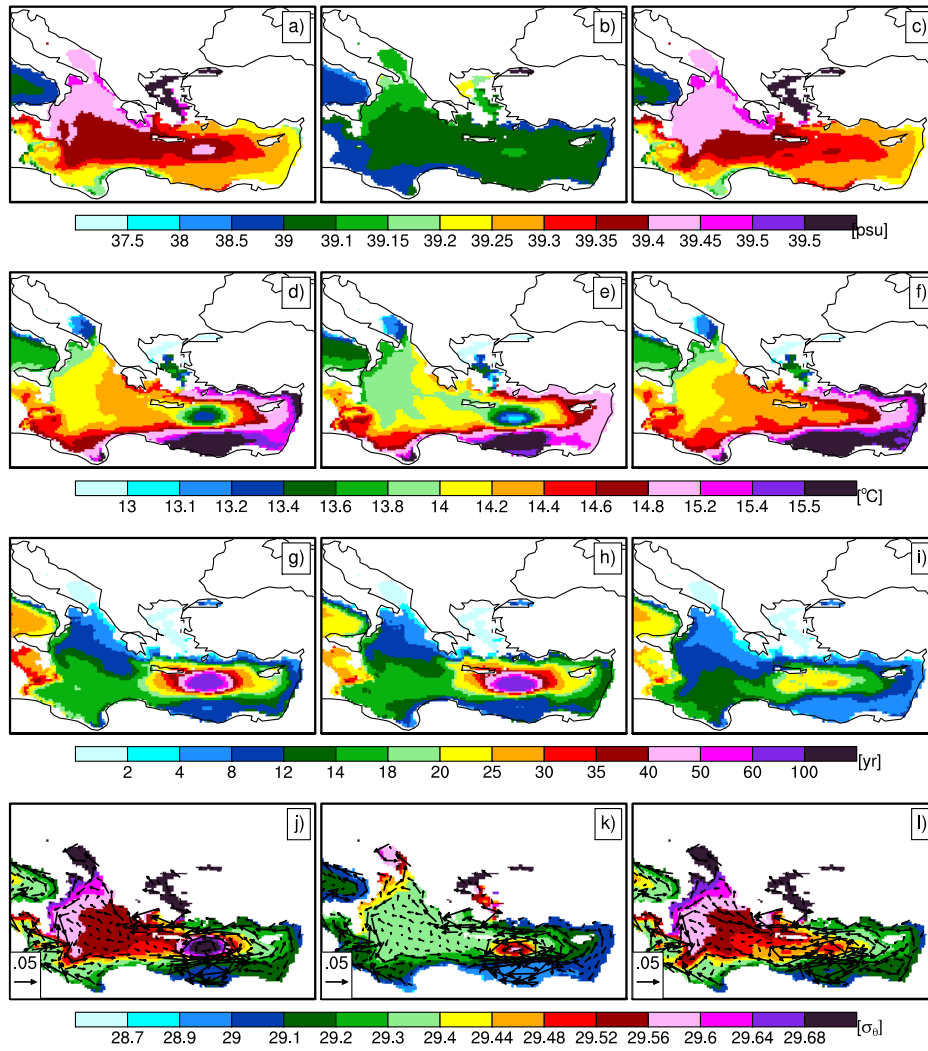


Figure A.8: Water properties at 197m depth. a) to c) salinity; d) to f) temperature; g) to i) water age; j) to l)  $\sigma_\theta$  superimposed with circulation, vector represent both speed and direction of circulation.

## A.2 ADDITIONAL REMARKS: GENERAL CIRCULATION

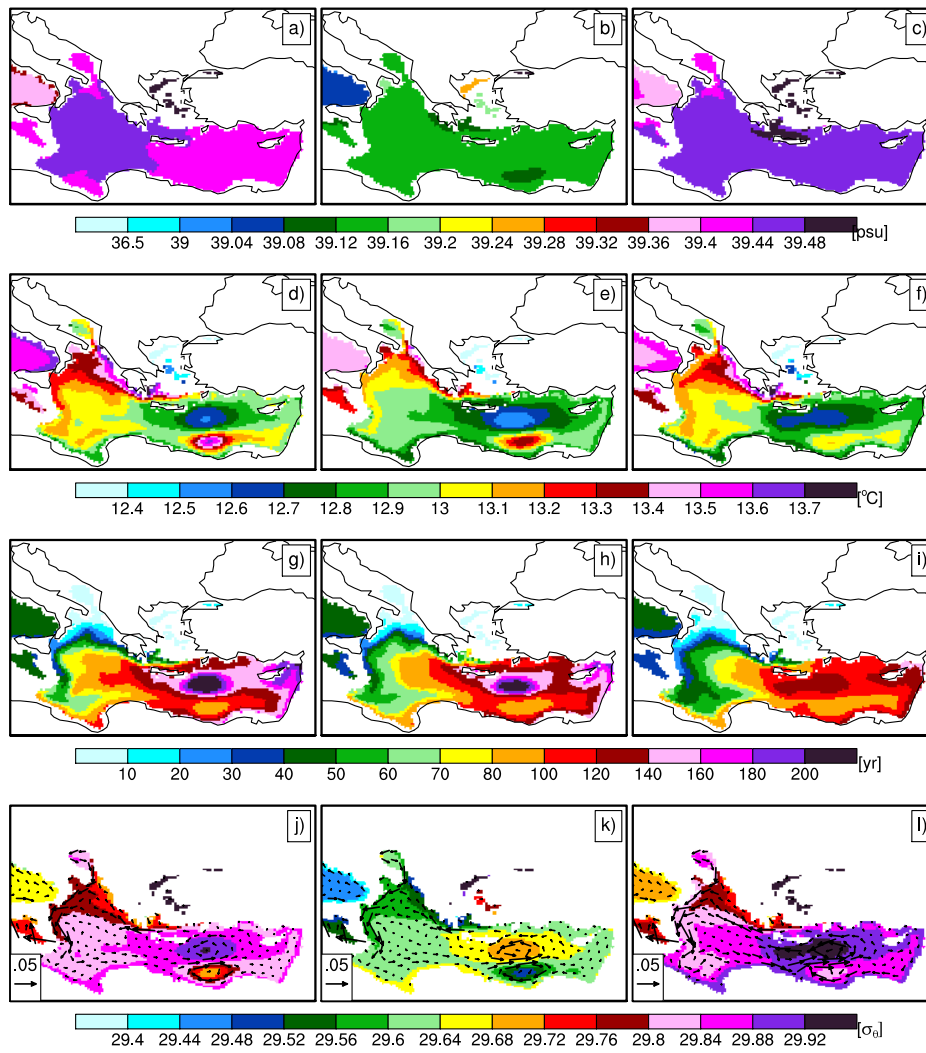


Figure A.9: Water properties at 445 m depth. a) to c) salinity; d) to f) temperature; g) to i) water age; j) to l)  $\sigma_\theta$  superimposed with circulation, vector represent both speed and direction of circulation.



## Bibliography

- Abu-Zied, R. H. (2001). *High resolution LGM-Present paleoceanography of the N.E. Mediterranean: a benthic perspective*. PhD thesis, University of Southampton.
- Adloff, F. (2011). *Early Holocene Eastern Mediterranean ocean climate and the stability of its overturning circulation*. PhD thesis, University of Hamburg.
- Adloff, F., Mikolajewicz, U., Kucera, M., Grimm, R., Maier-Reimer, E., Schmiedl, G., and Emeis, K. (2011). Upper ocean climate of the Eastern Mediterranean Sea during the Holocene Insolation Maximum - a model study. *Climate of the Past*, 7(3):1457–1509.
- Aksu, A., Abrajano, T., Mudie, P., and Yasar, D. (1999). Organic geochemical and palynological evidence for terrigenous origin of the organic matter in Aegean Sea sapropel S1. *Marine Geology*, 153(1-4):303–318.
- Aksu, A. E., Hiscott, R. N., Yasar, D., Isler, F. I., and Marsh, S. (2002). Seismic stratigraphy of Late Quaternary deposits from the southwestern Black Sea shelf: evidence for non-catastrophic variations in sea-level during the last 10 000 yr. *Marine Geology*, 190(1-2):61–94.
- Arakawa, A. and Lamb, V. R. (1977). Computational design of the basic dynamical process of the UCLA general circulation model. *Methods in Computational Physics*, 17:173–265.
- Artegiani, a., Paschini, E., Russo, A., Bregant, D., Raicich, F., and Pinardi, N. (1997). The Adriatic Sea general circulation. Part I: Air-sea interactions and water mass structure. *Journal of Physical Oceanography*, 27(8):1492–1514.
- Bahr, A. (2007). Age and stable isotopes of sediment core GeoB7608-1.
- Bartoli, G., Migon, C., and Losno, R. (2005). Atmospheric input of dissolved inorganic phosphorus and silicon to the coastal northwestern Mediterranean Sea: Fluxes, variability and possible impact on phytoplankton dynamics. *Deep Sea Research Part I: Oceanographic Research Papers*, 52(11):2005–2016.
- Bethoux, J. P. (1989). Oxygen consumption, new production, vertical advection and environmental evolution in the Mediterranean Sea. *Deep Sea Research Part A. Oceanographic Research Papers*, 36(5):769–781.

## BIBLIOGRAPHY

- Béthoux, J.-P. and Pierre, C. (1999). Mediterranean functioning and sapropel formation: respective influences of climate and hydrological changes in the Atlantic and the Mediterranean. *Marine Geology*, 153(1-4):29–39.
- Beuvier, J., Sevault, F., Herrmann, M., Kontoyiannis, H., Ludwig, W., Rixen, M., Stanev, E., Béranger, K., and Somot, S. (2010). Modeling the Mediterranean Sea interannual variability during 1961-2000: Focus on the Eastern Mediterranean Transient. *Journal of Geophysical Research*, 115(C8):1–27.
- Bianchi, D., Zavatarelli, M., Pinardi, N., Capozzi, R., Capotondi, L., Corselli, C., and Masina, S. (2006). Simulations of ecosystem response during the sapropel S1 deposition event. *Palaeogeography, Palaeoclimatology, Palaeoecology*, 235(1-3):265–287.
- Box, M. R., Krom, M., Cliff, R., Almogi-Labin, A., Bar-Matthews, M., Ayalon, A., Schillman, B., and Paterne, M. (2008). Changes in the flux of Saharan dust to the East Mediterranean Sea since the last glacial maximum as observed through Sr-isotope geochemistry. *Mineralogical Magazine*, 72(1):307–311.
- Broecker, W. S. and Maier-Reimer, E. (1992). The influence of air and sea exchange on the carbon isotope distribution in the sea. *Global Biogeochemical Cycles*, 6(3):315–320.
- Bryden, H. L. and Stommel, H. M. (1984). Limiting processes that determine basic features of the circulation in the Mediterranean Sea. *Oceanologica Acta*, 7(3):289–296.
- Calvert, S. E., Nielsen, B., and Fontugne, M. R. (1992). Evidence from nitrogen isotope ratios for enhanced productivity during formation of eastern Mediterranean sapropels. *Nature*, 359(6392):223–225.
- Casford, J., Rohling, E., Abuzied, R., Fontanier, C., Jorissen, F., Leng, M., Schmiedl, G., and Thomson, J. (2003). A dynamic concept for eastern Mediterranean circulation and oxygenation during sapropel formation. *Palaeogeography, Palaeoclimatology, Palaeoecology*, 190:103–119.
- Casford, J. S. L., Rohling, E. J., Cooke, S., Fontanier, C., Leng, M., and Lykousis, V. (2002). Circulation changes and nutrient concentrations in the late Quaternary Aegean Sea: A nonsteady state concept for sapropel formation. *Paleoceanography*, 17(2):1–11.
- Castellari, S., Pinardi, N., and Leaman, K. (2000). Simulation of water mass formation processes in the Mediterranean Sea: Influence of the time frequency of the atmospheric forcing. *Journal of Geophysical Research*, 105:157–181.

- Cita, M. B., Vergnaud-Grazzini, C., Robert, C., Chamley, H., Ciaranfi, N., and D'Onofrio, S. (1977). Paleoclimatic record of a long deep sea core from the eastern Mediterranean. *Quaternary Research*, 8(2):205–235.
- Cramp, A., Collins, M., and West, R. (1988). Late Pleistocene-Holocene sedimentation in the NW Aegean Sea: A palaeoclimatic palaeoceanographic reconstruction. *Palaeogeography, Palaeoclimatology, Palaeoecology*, 68(1):61–77.
- Cramp, A. and O'Sullivan, G. (1999). Neogene sapropels in the Mediterranean: a review. *Marine Geology*, 153(1-4):11–28.
- De Lange, G. J., Thomson, J., Reitz, A., Slomp, C. P., Speranza Principato, M., Erba, E., and Corselli, C. (2008). Synchronous basin-wide formation and redox-controlled preservation of a Mediterranean sapropel. *Nature Geoscience*, 1(9):606–610.
- DeMenocal, P., Ortiz, J., Guilderson, T., Adkins, J., Sarnthein, M., Baker, L., and Yarusinsky, M. (2000). Abrupt onset and termination of the African Humid Period: rapid climate responses to gradual insolation forcing. *Quaternary Science Reviews*, 19(1-5):347–361.
- D'Ortenzio, F., Iudicone, D., de Boyer Montegut, C., Testor, P., Antoine, D., Marullo, S., Santoleri, R., and Madec, G. (2005). Seasonal variability of the mixed layer depth in the Mediterranean Sea as derived from in situ profiles. *Geophys. Res. Lett.*, 32(12):L12605.
- Ediger, D. and Yilmaz, A. (1996). Characteristics of deep chlorophyll maximum in the Northeastern Mediterranean with respect to environmental conditions. *Journal of Marine Systems*, 9(3-4):291–303.
- Ehrmann, W., Schmiedl, G., Hamann, Y., Kuhnt, T., Hemleben, C., and Siebel, W. (2007). Clay minerals in late glacial and Holocene sediments of the northern and southern Aegean Sea. *Palaeogeography, Palaeoclimatology, Palaeoecology*, 249(1-2):36–57.
- Emeis, K., Struck, U., Schulz, H., Rosenberg, R., Bernasconi, S., Erlenkeuser, H., Sakamoto, T., and Martinez-Ruiz, F. (2000). Temperature and salinity variations of Mediterranean Sea surface waters over the last 16,000 years from records of planktonic stable oxygen isotopes and alkenone unsaturation ratios. *Palaeogeography, Palaeoclimatology, Palaeoecology*, 158(3-4):259–280.
- ETOPO5 (1988). Data Announcement 88-MGG-02, digital relief of the surface of the Earth. NOAA, National Geophysical Data Center, Boulder, Colorado.

## BIBLIOGRAPHY

- Fairbanks, R. G. (1989). A 17,000-year glacio-eustatic sea level record: influence of glacial melting rates on the Younger Dryas event and deep-ocean circulation. *Nature*, 342(6250):637–642.
- Fontugne, M. R. and Calvert, S. E. (1992). Late Pleistocene variability of the carbon isotopic composition of organic matter in the eastern Mediterranean: monitor of changes in carbon sources and atmospheric CO<sub>2</sub> concentrations. *Paleoceanography*, 7(1):1–20.
- Gallego-Torres, D., Martínez-Ruiz, F., Paytan, A., Jiménez-Espejo, F., and Ortega-Huertas, M. (2007). Pliocene-Holocene evolution of depositional conditions in the eastern Mediterranean: Role of anoxia vs. productivity at time of sapropel deposition. *Palaeogeography, Palaeoclimatology, Palaeoecology*, 246(2-4):424–439.
- Gent, P. R., Willebrand, J., McDougall, T. J., and McWilliams, J. C. (1995). Parameterizing eddy-induced tracer transports in ocean circulation models. *Journal of Physical Oceanography*, 25(4):463–474.
- Griffies, S. M. (1998). The Gent-McWilliams skew flux. *Journal of Physical Oceanography*, 28(5):831–841.
- Hayes, A., Kucera, M., Kallel, N., Saffi, L., and Rohling, E. J. (2005). Glacial Mediterranean sea surface temperatures based on planktonic foraminiferal assemblages. *Quaternary Science Reviews*, 24(7-9):999–1016.
- Heinze, C., Hupe, A., Maier-Reimer, E., Dittert, N., and Ragueneau, O. (2003). Sensitivity of the marine biospheric Si cycle for biogeochemical parameter variations. *Global Biogeochemical Cycles*, 17(3):12–1–12–21.
- Hense, I. and Beckmann, A. (2008). Revisiting subsurface chlorophyll and phytoplankton distributions. *Deep Sea Research*, 55(9):1193–1199.
- Herut, B. (2000). The seasonal dynamics of nutrient and chlorophyll a concentrations on the SE Mediterranean shelf-slope. *Oceanologica Acta*, 23(7):771–782.
- Herut, B., Zohary, T., Krom, M., Mantoura, R., Pitta, P., Psarra, S., Rassoulzadegan, F., Tanaka, T., and Fredthingstad, T. (2005). Response of East Mediterranean surface water to Saharan dust: On-board microcosm experiment and field observations. *Deep Sea Research Part II: Topical Studies in Oceanography*, 52(22-23):3024–3040.
- Hilgen, F. J. (1991). Astronomical calibration of Gauss to Matuyama sapropels in the Mediterranean and implication for the geomagnetic polarity time scale. *Earth and Planetary Science Letters*, 104:226–244.

- Hong, X., Hodur, R. M., and Martin, P. J. (2007). Numerical simulation of deep-water convection in the Gulf of Lion. *Pure and Applied Geophysics*, 164(10):2101–2116.
- Howell, M. W. and Thunell, R. C. (1992). Organic carbon accumulation in Bannock Basin: Evaluating the role of productivity in the formation of eastern Mediterranean sapropels. *Marine Geology*, 103(1-3):461–471.
- Jerlov, N. G. (1976). *Marine optics*, volume 14. Elsevier, Amsterdam.
- Kallel, N., Duplessy, J.-C., Labeyrie, L., Fontugne, M., Paterne, M., and Montacer, M. (2000). Mediterranean pluvial periods and sapropel formation over the last 200000 years. *Palaeogeography, Palaeoclimatology, Palaeoecology*, 157(1-2):45–58.
- Kallel, N., Paterne, M., Duplessy, J.-C., Vergnaud-Grazzini, C., Pujol, C., Labeyrie, L., Arnold, M., Fontugne, M., and Pierre, C. (1997). Enhanced rainfall in the mediterranean region during the last sapropel event. *Oceanologica acta*, 20(5):697–712.
- Kemp, A. E. S., Pearce, R. B., Koizumi, I., Pike, J., and Rance, S. J. (1999). The role of mat-forming diatoms in the formation of Mediterranean sapropels. *Nature*, 398(6722):57–61.
- Klein, B., Roether, W., Manca, B. B., Bregant, D., Beitzel, V., Kovacevic, V., and Luchetta, A. (1999). The large deep water transient in the Eastern Mediterranean. *Deep-Sea Research*, 46(1999):371–414.
- Kotthoff, U., Pross, J., Müller, U. C., Peyron, O., Schmiedl, G., Schulz, H., and Bordon, A. (2008). Climate dynamics in the borderlands of the Aegean Sea during formation of sapropel S1 deduced from a marine pollen record. *Quaternary Science Reviews*, 27(7-8):832–845.
- Kress, N. and Herut, B. (2001). Spatial and seasonal evolution of dissolved oxygen and nutrients in the Southern Levantine Basin (Eastern Mediterranean Sea): chemical characterization of the water masses and inferences on the N:P ratios. *Deep-Sea Research Part I: Oceanographic Research Papers*, 48(11):2347–2372.
- Krom, M. D., Brenner, S., Kress, N., Neori, A., and Gordon, L. I. (1992). Nutrient dynamics and new production in a warm-core eddy from the Eastern Mediterranean Sea. *Deep Sea Research Part A. Oceanographic Research Papers*, 39(3-4):467–480.
- Kuhnt, T. (2008). *Reconstruction of late Quaternary deep-sea ecosystem variability in the eastern Mediterranean Sea based on benthic foraminiferal faunas and stable isotopes*. Doctoral thesis, Universtiy of Leipzig, Germany.

## BIBLIOGRAPHY

- Kuhnt, T., Schmiedl, G., Ehrmann, W., Hamann, Y., and Andersen, N. (2008). Stable isotopic composition of Holocene benthic foraminifers from the Eastern Mediterranean Sea: Past changes in productivity and deep water oxygenation. *Palaeogeography, Palaeoclimatology, Palaeoecology*, 268(1-2):106–115.
- Kuhnt, T., Schmiedl, G., Ehrmann, W., Hamann, Y., and Hemleben, C. (2007). Deep-sea ecosystem variability of the Aegean Sea during the past 22 kyr as revealed by Benthic Foraminifera. *Marine Micropaleontology*, 64(3-4):141–162.
- Kutzbach, J. E. and Street-Perrott, F. A. (1985). Milankovitch forcing of fluctuations in the level of tropical lakes from 18 to 0 kyr BP. *Nature*, 317(6033):130–134.
- Lane-Serff, G. F., Rohling, E. J., Bryden, H. L., and Charnock, H. (1997). Postglacial connection of the Black Sea to the Mediterranean and its relation to the timing of sapropel formation. *Paleoceanography*, 12(2):169–174.
- Lascazatos, A. (1993). Estimation of deep and intermediate water mass formation rates in the Mediterranean Sea. *Deep Sea Research Part II: Topical Studies in Oceanography*, 40(6):1327–1332.
- Lascazatos, A., Williams, R. G., and Tragou, E. (1993). A mixed-layer study of the formation of Levantine Intermediate Water. *Journal of Geophysical Research*, 98(C8):14739–14749.
- Lavelle, J. W., Mofjeld, H. O., and Baker, E. T. (1984). An in situ erosion rate for a fine-grained marine sediment. *Journal of Geophysical Research*, 89(C4):6543–6552.
- Levitus, S., Boyer, T., Conkwright, M., Johnson, D., O'Brien, T., Antonov, J., Stephens, C., and Gelfield, R. (1998). *World Ocean Database 1998, vol. 1, Introduction. NOAA Atlas NESDIS 18*, pages 1–346.
- Ludwig, W., Meybeck, M., and Abousamra, F. (2003). Riverine transport of water, sediments and pollutants to the Mediterranean Sea.
- Maier-Reimer, E., Kriest, I., Segschneider, J., and Wetzell, P. (2005). The Hamburg ocean carbon cycle model HAMOCC5.1.
- Manca, B., Burca, M., Giorgetti, A., Coatanoan, C., Garcia, M., and Iona, A. (2004). Physical and biochemical averaged vertical profiles in the Mediterranean regions: an important tool to trace the climatology of water masses and to validate incoming data from operational oceanography. *Journal of Marine Systems*, 48(1-4):83–116.
- Marshall, J. and Schott, F. (1999). Open-ocean convection: Observations, theory, and models. *Reviews of Geophysics*, 37(1):1–64.

- Marsland, S., Haak, H., Jungclaus, J., Latif, M., and Röske, F. (2003). The Max-Planck-Institute global ocean/sea ice model with orthogonal curvilinear coordinates. *Ocean Modelling*, 5(2):91–127.
- Martinez-Ruiz, F., Kastner, M., Paytan, A., Ortega-Huertas, M., and Bernasconi, S. M. (2000). Geochemical evidence for enhanced productivity during S1 sapropel deposition in the eastern Mediterranean. *Paleoceanography*, 15(2):200.
- Matthiesen, S. and Haines, K. (2003). A hydraulic box model study of the Mediterranean response to postglacial sea-level rise. *Paleoceanography*, 18(4):1084.
- McGill, D. (1969). A budget for dissolved nutrients salts in the Mediterranean Sea. *Cahiers Océanographiques*, 21:543–554.
- Medar-Medatlas (2002). Mediterranean and Black Sea database of temperature salinity and bio-chemical parameters. *Climatological Atlas. IFREMER Edition (4 Cdroms)*.
- Meijer, P. and Dijkstra, H. (2009). The response of Mediterranean thermohaline circulation to climate change: a minimal model. *Climate of the Past*, 5(4):713–720.
- Meijer, P. and Tuenter, E. (2007). The effect of precession-induced changes in the Mediterranean freshwater budget on circulation at shallow and intermediate depth. *Journal of Marine Systems*, 68(3-4):349–365.
- Mercone, D., Thomson, J., Croudace, I. W., Siani, G., Paterne, M., and Troelstra, S. (2000). Duration of S1, the most recent sapropel in the eastern Mediterranean Sea, as indicated by accelerator mass spectrometry radiocarbon and geochemical evidence. *Paleoceanography*, 15(3):336–347.
- Mertens, C. and Schott, F. (1998). Interannual variability of deep-water formation in the northwestern Mediterranean. *Journal of Physical Oceanography*, 28(7):1410–1424.
- Meybeck, M. and Ragu, A. (1996). *River Discharges to the oceans: An assessment of suspended solids, major ions, and nutrients*. United National Environmental Programme, Nairobi.
- Meyers, P. A. and Bernasconi, S. M. (2009). Carbon contents and isotopic compositions from the ODP Hole 161-974C near the center of the Tyrrhenian Basin (Table 1).
- Mikolajewicz, U. (2011). Modeling Mediterranean ocean climate of the last glacial maximum. *Climate of the Past*, 7:161–180.
- Milker, Y., Ehrmann, W., and Schmiedl, G. (2006). *Spätquartäre Sedimentationsgeschichte im östlichen Mittelmeer*. Diploma thesis, University of Leipzig, Germany, Leipzig.

## BIBLIOGRAPHY

- Möbius, J., Lahajnar, N., and Emeis, K.-C. (2010). Diagenetic control of nitrogen isotope ratios in Holocene sapropels and recent sediments from the Eastern Mediterranean Sea. *Biogeosciences Discussions*, 7(1):1131–1165.
- Moodley, L., Middelburg, J. J., Herman, P. M., Soetaert, K., and de Lange, G. J. (2005). Oxygenation and organic-matter preservation in marine sediments: Direct experimental evidence from ancient organic carbon-rich deposits. *Geology*, 33(11):889.
- Moutin, T. and Raimbault, P. (2002). Primary production, carbon export and nutrients availability in western and eastern Mediterranean Sea in early summer 1996 (MINOS cruise). *Journal of Marine Systems*, 33-34:273–288.
- Mulitza, S., Prange, M., Stuut, J.-B., Zabel, M., von Dobeneck, T., Itambi, A. C., Nizou, J., Schulz, M., and Wefer, G. (2008). Sahel megadroughts triggered by glacial slowdowns of Atlantic meridional overturning. *Paleoceanography*, 23(4):PA–206.
- Myers, P. G. (2002). Flux-forced simulations of the paleocirculation of the Mediterranean. *Paleoceanography*, 17(1):1–7.
- Myers, P. G., Haines, K., and Rohling, E. J. (1998). Modeling the paleocirculation of the Mediterranean: The last glacial maximum and the Holocene with emphasis on the formation of sapropel S1. *Paleoceanography*, 13(6):586–606.
- Myers, P. G. and Rohling, E. J. (2000). Modeling a 200-yr interruption of the Holocene sapropel S1. *Quaternary Research*, 53(1):98–104.
- Nixon, S. W. (2003). Replacing the Nile: are anthropogenic nutrients providing the fertility once brought to the Mediterranean by a great river? *Ambio*, 32(1):30–9.
- Ollausson, E. (1961). Studies of deep-sea cores: Report of the Swedish Deep-Sea Expedition, 1947-1948. 8:323–438.
- Osborne, A. H., Vance, D., Rohling, E. J., Barton, N., Rogerson, M., and Fello, N. (2008). A humid corridor across the Sahara for the migration of early modern humans out of Africa 120,000 years ago. *Proceedings of the National Academy of Science of the United States of America*, 105(43):16444–16447.
- Pacanowski, R. C. and Philander, S. G. H. (1981). Parameterization of vertical mixing in numerical models of tropical oceans. *Journal of Physical Oceanography*, 11(11):1443–1451.
- Peltier, W. (2004). Global glacial isostasy and the surface of the ice-age Earth: the ICE-5G (VM2) model and GRACE. *Annual Review of Earth and Planetary Sciences*, 32(1):111–149.

- Pinardi, N. and Masetti, G. (2000). Variability of the large scale general circulation of the Mediterranean Sea from observations and modelling: a review. *Palaeogeography, Palaeoclimatology, Palaeoecology*, 158(3-4):153–173.
- POEM-Group (1992). General circulation of the eastern Mediterranean. *Earth Science Reviews*, 32:285–309.
- Prell, W. L. and Kutzbach, J. E. (1987). Monsoon variability over the past 150,000 years. *Journal of Geophysical Research*, 92(D7):8411–8425.
- Psarra, S., Tselepidis, A., and Ignatiades, L. (2000). Primary productivity in the oligotrophic Cretan Sea (NE Mediterranean): seasonal and interannual variability. *Progress In Oceanography*, 46:187–204.
- Ridame, C. and Guieu, C. (2002). Saharan input of phosphate to the oligotrophic water of the open western Mediterranean Sea. *Limnology and Oceanography*, 47(3):856–869.
- Roeckner, E., Buml, G., Bonaventura, L., Brokopf, R., Esch, M., Giorgetta, M., Hagemann, S., Kirchner, I., Manzini, L. K. E., Rhodin, A., Schlese, U., Schulzweida, U., and Tompkins, A. (2003). The atmospheric general circulation model ECHAM5. *Tech. Rep. 349, Max Planck Institute for Meteorology, Hamburg*.
- Roether, W., Manca, B. B., Klein, B., Bregant, D., Georgopoulos, D., Beitzel, V., Kovacevic, V., and Luchetta, A. (1996). Recent changes in eastern Mediterranean deep waters. *Science*, 271:333–335.
- Roether, W. and Schlitzer, R. (1991). Eastern Mediterranean deep water renewal on the basis of chlorofluoromethane and tritium data. *Dynamics of Atmospheres and Oceans*, 15(3-5):333–354.
- Rohling, E. J. (1994). Review and new aspects concerning the formation of eastern Mediterranean sapropels. *Marine Geology*, 122(1-2):1–28.
- Rohling, E. J. and Bryden, H. L. (1994). Estimating past changes in the eastern Mediterranean fresh-water budget, using reconstructions of sea-level and hydrography. *Proceedings of the Koninklijke Nederlandse Akademie Van Wetenschappen-Biological Chemical Geological Physical and Medical Sciences*, 97(2):201–217.
- Rohling, E. J., Cane, T. R., Cooke, S., Sprovieri, M., Bouloubassi, I., Emeis, K. C., Schiebel, R., Kroon, D., Jorissen, F. J., and Lorre, A. (2002). African monsoon variability during the previous interglacial maximum. *Earth and Planetary Science Letters*, 202(1):61–75.

## BIBLIOGRAPHY

- Rohling, E. J. and Gieskes, W. W. C. (1989). Late Quaternary changes in Mediterranean intermediate water density and formation rate. *Paleoceanography*, 4(5):531–545.
- Rohling, E. J. and Hilgen, F. J. (1991). The eastern Mediterranean climate at times of sapropel formation - a review. *Geologie en Mijnbouw*, 70(3):253–264.
- Röske, F. (2006). A global heat and freshwater forcing dataset for ocean models. *Ocean Modelling*, 11:235–297.
- Rossignol-Strick, M. (1985). Mediterranean Quaternary sapropels, an immediate response of the African monsoon to variation of insolation. *Palaeogeography, Palaeoclimatology, Palaeoecology*, 49(3-4):237–263.
- Rossignol-Strick, M. (1987). Rainy periods and bottom water stagnation initiating brine accumulation and metal concentrations: 1. The late Quaternary. *Paleoceanography*, 2(3):333–360.
- Rossignol-Strick, M. (1999). The Holocene climatic optimum and pollen records of sapropel 1 in the eastern Mediterranean, 9000-6000 BP. *Quaternary Science Reviews*, 18(4-5):515–530.
- Rossignol-Strick, M., Nesteroff, W., Olive, P., and Vergnaud-Grazzini, C. (1982). After the deluge: Mediterranean stagnation and sapropel formation. *Nature*, 295(5845):105–110.
- Ryan, W. B. F., III, W. C. P., Major, C. O., Shimkus, K., Moskalenko, V., Jones, G. A., Dimitrov, P., Gorür, N., Sakiñç, M., and Yüce, H. (1997). An abrupt drowning of the Black Sea shelf. *Marine Geology*, 138(1-2):119–126.
- Sachs, J. P. and Repeta, D. (1999). Oligotrophy and nitrogen fixation during eastern Mediterranean sapropel events. *Science*, 286(5449):2485–2488.
- Salihoglu, I., Saydam, C., Bastürk, O., Yilmaz, K., Göçmen, D., Hatipoglu, E., and Yilmaz, A. (1990). Transport and distribution of nutrients and chlorophyll-a by mesoscale eddies in the northeastern Mediterranean. *Marine Chemistry*, 29(0):375–390.
- Schilman, B., Almogi-Labin, A., Bar-Matthews, M., Labeyrie, L., Paterne, M., and Luz, B. (2001). Long- and short-term carbon fluctuations in the Eastern Mediterranean during the late Holocene. *Geology*, 29(12):1099–1102.
- Schilman, B., Almogi-Labin, A., Bar-Matthews, M., and Luz, B. (2003). Late Holocene productivity and hydrographic variability in the eastern Mediterranean inferred from benthic foraminiferal stable isotopes. *Paleoceanography*, 18(3).

- Schlitzer, R., Roether, W., Oster, H., Junghans, H., Hausmann, M., Johannsen, H., and Michelato, A. (1991). Chlorofluoromethane and oxygen in the Eastern Mediterranean. *Deep Sea Research Part A. Oceanographic Research Papers*, 38(12):1531–1551.
- Schmidt, A. (2007). *Deep sea ecosystem variability in the eastern Levantine basin during the late Quaternary as revealed by benthic foraminifera and stable isotopes*. Diploma thesis, Universität Leipzig.
- Schmiedl, G., Hemleben, C., Keller, J., and Segl, M. (1998). Impact of climatic changes on the benthic foraminiferal fauna in the Ionian Sea during the last 330,000 years. *Paleoceanography*, 13(5):447–458.
- Schmiedl, G., Kuhnt, T., Ehrmann, W., Emeis, K.-C., Hamann, Y., Kotthoff, U., Dulski, P., and Pross, J. (2010). Climatic forcing of eastern Mediterranean deep-water formation and benthic ecosystems during the past 22000 years. *Quaternary Science Reviews*, 29(23-24):3006–3020.
- Schmiedl, G., Pfeilsticker, M., Hemleben, C., and Mackensen, A. (2004). Environmental and biological effects on the stable isotope composition of recent deep-sea benthic foraminifera from the western Mediterranean Sea. *Marine Micropaleontology*, 51(1-2):129–152.
- Scrivner, A. E., Vance, D., and Rohling, E. J. (2004). New neodymium isotope data quantify Nile involvement in Mediterranean anoxic episodes. *Geology*, 32(7):565–568.
- Shakun, J. D., Clark, P., He, F., Marcott, S., Mix, A., Liu, Z., Otto-Biesner, B., Schmittner, A., and Bard, E. (2012). Global warming preceded by increasing carbon dioxide concentrations during the last deglaciation. *Nature*, 484(7392):49–54.
- Shaw, H. F. and Evans, G. (1984). The nature, distribution and origin of a sapropelic layer in sediments of the Sicilia Basin, northeastern Mediterranean. *Marine Geology*, 61(1):1–12.
- Sheng, P. Y. and Lick, W. (1979). The transport and resuspension of sediments in a shallow lake. *Journal of Geophysical Research*, 84(C4):1809–1826.
- Slomp, C. P., Thomson, J., and De Lange, G. J. (2002). Enhanced regeneration of phosphorus during formation of the most recent eastern Mediterranean sapropel (S1). *Geochimica et Cosmochimica Acta*, 66(7):1171–1184.
- Slomp, C. P., Thomson, J., and De Lange, G. J. (2004). Controls on phosphorus regeneration and burial during formation of eastern Mediterranean sapropels. *Marine Geology*, 203(1-2):141–159.

## BIBLIOGRAPHY

- Soulet, G., Menot, G., Lericolais, G., and Bard, E. (2011). A revised calendar age for the last reconnection of the Black Sea to the global ocean. *Quaternary Science Reviews*, 30(9-10):1019–1026.
- Sperling, M., Schmiedl, G., Hemleben, C., Emeis, K. C., Erlenkeuser, H., and Grootes, P. M. (2003). Black Sea impact on the formation of eastern Mediterranean sapropel S1? Evidence from the Marmara Sea. *Palaeogeography, Palaeoclimatology, Palaeoecology*, 190(0):9–21.
- Spötl, C., Nicolussi, K., Patzelt, G., and Boch, R. (2010). Humid climate during deposition of sapropel 1 in the Mediterranean Sea: Assessing the influence on the Alps. *Global and Planetary Change*, 71(3-4):242–248.
- Stratford, K., Williams, R. G., and Myers, P. G. (2000). Impact of the circulation on Sapropel formation in the eastern Mediterranean. *Global Biogeochemical Cycles*, 14(2):683.
- Strobl, R. O., Somma, F., Evans, B. M., and Zaldívar, J. M. (2009). Fluxes of water and nutrients from river runoff to the Mediterranean Sea using GIS and a watershed model. *Journal of Geophysical Research*, 114(G3).
- Strohle, K. and Krom, M. D. (1997). Evidence for the evolution of an oxygen minimum layer at the beginning of S-1 sapropel deposition in the eastern Mediterranean. *Marine Geology*, 140(3-4):231–236.
- Sweby, P. (1984). High resolution schemes using flux limiters for hyperbolic conservation laws. *SIAM Journal on Numerical Analysis*, 21(5):995–1011.
- Thunell, R. C. and Williams, D. F. (1989). Glacial-Holocene salinity changes in the Mediterranean Sea: hydrographic and depositional effects. *Nature*, 338(6215):493–496.
- Thunell, R. C., Williams, D. F., and Belyea, P. R. (1984). Anoxic events in the Mediterranean Sea in relation to the evolution of late Neogene climates. *Marine Geology*, 59(1-4):105–134.
- Troelstra, S., Ganssen, G., Klaas, V., and A, D. (1991). A late Quaternary stratigraphic framework for eastern Mediterranean sapropel S1 based on AMS <sup>14</sup>C dates and stable oxygen isotopes. *Radiocarbon*, 33:15–21.
- Vergnaud-Grazzini, C. and Pierre, C. (1991). High fertility in the Alboran Sea since the last glacial maximum. *Paleoceanography*, 6(4):519–536.

- Vergnaud-Grazzini, C., Ryan, W. B. F., and Cita, M. B. (1977). Stable isotopic fractionation, climate change and episodic stagnation in the eastern Mediterranean during the late Quaternary. *Marine Micropaleontology*, 2(0):353–370.
- Vörösmarty, C., Fekete, B., and Tucker, B. (1998). Global river discharge, 1807-1991. *Version. 1.1 RivDIS Data set.*, Available online [<http://www.daac.ornl.gov>] from Oak Ridge National Laboratory Distributed Active Archive Center, Oak Ridge, Tennessee, U.S.A.
- Wallace, M. and Gutzler, D. (1981). Teleconnections in the geopotential height field during the northern Hemisphere winter. *Monthly Weather Review*, 109:784–812.
- Wang, X. J., Behrenfeld, M., Borgne, R. L., Murtugudde, R., and Boss, E. (2008). Regulation of phytoplankton carbon to chlorophyll ratio by light, nutrients and temperature in the equatorial Pacific Ocean: a basin-scale model. *Biogeosciences Discussions*, (5):3869–3903.
- Warning, B. and Brumsack, H.-J. (2000). Trace metal signatures of eastern Mediterranean sapropels. *Palaeogeography, Palaeoclimatology, Palaeoecology*, 158(3-4):293–309.
- WOA (2009). World Ocean Atlas 2009. *National oceanographic data center (NODC)*.
- Wu, P. and Haines, K. (1996). Modeling the dispersal of Levantine Intermediate Water and its role in Mediterranean deep water formation. *Journal of Geophysical Research*, 101(C3):6591–6607.
- Yacobi, Y., Zohary, T., Kress, N., Hecht, A., Robarts, R., Waiser, M., Wood, A., and Li, W. (1995). Chlorophyll distribution throughout the southeastern Mediterranean in relation to the physical structure of the water mass. *Journal of Marine Systems*, 6(3):179–190.
- Zohary, T. and Robarts, R. D. (1998). Experimental study of microbial P limitation in the eastern Mediterranean. *Limnology and Oceanography*, 43(3):387–395.



# Acknowledgements

First, I wish to thank my advisor Dr. Ernst Maier-Reimer for his patient support, for his confidence and encouragement, for granted scientific freedom, and his ever open door whenever I had questions or felt the need for discussions. I especially would like to thank my co-advisor Dr. Uwe Mikolajewicz for his great support, his academic advice, for sharing his excellent ideas, for keeping me on track, and for encouraging me all the way throughout this thesis. I also would like to thank my panel chair Prof. Dr. Gerhard Schmiedl for his fantastic interest in my work, his always very encouraging words, his steady support, sharing his data and guiding me through the interpretation, and the many inspiring meetings. I wish to thank Prof. Dr. Nadia Pinardi for the warm and friendly welcome at the University of Bologna/Ravenna, for giving me this excellent and very intensive scientific support, and for introducing me to many experts of various fields during my three month stay in her group. A special thanks also to Prof. Dr. Kay Emeis for many discussions.

I would like to thank the people of the Ocean Biogeochemistry group, Dr. Tatiana Ilyina, Dr. Joachim Segschneider, Mathias Heinze, Dr. Matthias Gröger, Dr. Irene Stemmler, and in particular, Dr. Katharina Six, for her great advice in many aspects, for sharing her excellent understanding of the ocean biogeochemical processes, and for encouraging me throughout my PhD time.

Many thanks to the members of the Ocean Physics group for entirely adopting me as an additional group member and many fruitful discussions, Laura Niederdrenk, Dr. Alfredo Izquierdo, Florian Ziemen, Dr. Christian Roderhake, Dr. Fanny Adloff, Dr. Alberto Elizalde, Dr. Dmitry Sein.

Many thanks also to all the proof readers, Dr. Katharina Six, Dr. Nils Fischer, Mathias Heinze, Dr. Florian Rauser, Florian Ziemen, and Dr. Michael Brüdgram.

I would like to thank all members of the Ocean Department of the MPI-M, and the IMPRS-ESM, in particular Antje and Conni. Thanks to all the people with whom I had such a great time throughout my PhD especially Dr. Florian Rauser, Dr. Nils Fischer, Iris Ehlert, Laura Niederdrenk, Werner Bauer, Dr. Juliane Otto, Dr. Malte Heinmann, Dr. Mario Krapp, Mathias Heinze, Dr. Aiko Voigt, Dr. Michael Brüdgram, Florian Ziemen, Dr. Alfredo Izquierdo, Dr. Freja Vamborg, Vera Schemann, Dr. Dirk Notz, Dr. Julia Pongratz, Peter Düben, Philipp Griewank, Dr. Ronny Petrik, Sebastian Sonntag, Nils Brüggemann, Kevin Sieck, Swantje Preuschmann, Thomas Raub, and Christine Radermacher.

## ACKNOWLEDGEMENTS

I also thank the German Research Foundation (DFG) for financial support for this thesis in the framework of the INTERDYNAMIK priority program. The model integrations were performed in the German Climate Computation Center (DKRZ). And many thanks also to the members of the Central IT Services for helping me with technical support.

Last but not least, I would like to thank my parents and my brothers for always being there for me.

